Organization, dynamics and adaptation of the photosynthetic machinery in cyanobacteria

Thesis submitted in accordance with the requirements of the University of Liverpool for the degree of Doctor in Philosophy by Selene Casella

September 1, 2017

UNIVERSITY OF LIVERPOOL
Department of Functional and comparative genomics, school of biological science, Institute of integrative biology

Abstract

Cyanobacteria are the oldest oxygenic phototrophs on Earth. In the cyanobacterial cell, oxygenic photosynthesis typically takes place in the specialised intracellular membranes, namely thylakoid membranes (TMs), analogous to higher plants. The cyanobacterial photosynthetic machinery embedded in thylakoid lipid bilayers typically consists of a series of membrane integral multi-subunit complexes, including photosystem I (PSI), photosystem II (PSII), cytochrome (Cyt) b_6f and ATP synthase (ATPase) complexes. Cyanobacterial thylakoid membranes also act as the site that harbours the components of respiratory electron transport chains, comprising type-I NAD(P)H dehydrogenase-like complex (NDH-1), succinate dehydrogenase (SDH), Cyt oxidase and alternative oxidase. Remarkable macromolecular crowding and close protein-protein contacts within the cyanobacterial thylakoid membrane result in the dense packing of photosynthetic components. Nowadays, information about the structures and functions of individual supercomplexes, in both photosynthetic and respiratory chains, are available. However, their spatial organization and dynamics have not been well understood experimentally. Here, we study the native organisation and mobility of PSI, PSII, ATPase and Cyt b_6f complexes in the TMs from the cyanobacterium *Synechococcus elongatus* PCC 7942. We also describe the interferences on these dynamics from external (red light, temperature) or internal parameters (supramolecular organization, protein size) *in vivo*.

We first, determined the native arrangement and dense packing of PSI, PSII and Cyt b_6f within the thylakoid membrane using atomic force microscopy. We calculated that the 75% of the TMs is composed of proteins, in which PSI and PSII complexes appear interspersed. Then, we fused fluorescent proteins to the complexes of interest, maintaining the expression of genes under the control of their endogenous promoters. Genetic, biochemical, structural and functional characterisation of the mutants were carried out, confirming the functional tagging. Live-cell fluorescence imaging using total internal reflection fluorescence and confocal microscopy were performed to study the global distribution of the supercomplexes. We revealed that, in normal growth conditions, PSI, ATPase and Cyt b_6f have a higher heterogeneous distribution compared with PSII along the TMs. From the fluorescence pictures, we extracted the relative quantification of the photosynthetic complexes. We visualised for the first time the reorganization in defined patches of ATPase and Cyt b_6f complexes upon red light illumination. We also characterised in detail the distinct rearrangement of PSI and PSII complexes. Using fluorescence recovery after photobleaching (FRAP), we monitored the movement of the complexes within the crowded thylakoid membrane environment. This work revealed that in normal growth conditions, the photosynthetic complexes are mobile within a time frame of 90 s. It also showed that the velocity of diffusion of PSI, PSII and Cyt b_6f can be reduced by red light. On the other hand, we observed that in red light adapted cells, the PSII complex arranges in discrete patches which are highly mobile within a time frame of 13 min. Lastly, we provide a quantitative description of the interference of temperature, supramolecular organisation and protein size on the *in vivo* diffusion dynamics of photosynthetic complexes.

Our findings provide evidence about the clustering distribution and mobility of the photosynthetic complexes, and indicate the differential responses of photosynthetic complexes to the same environmental stimulus. Knowledge of the cyanobacterial thylakoid membranes could be extended to other cell membranes, such as chloroplasts, given the close evolutionary links between chloroplasts and cyanobacteria, as well as mitochondrial membranes. Understanding the organisation and dynamics of photosynthetic membranes is essential for rational design and construction of artificial photosynthetic systems to underpin bioenergy development.

Acknowledgement

I would like to start this thesis by acknowledging the people who one way or another contributed to the success of this work.

I warmly thank all the people of the Bioscience building where I have spent four years performing research for this thesis.

I gratefully thank all my co-authors for making an impact on this work and sharing their expertise with me. Especially Tchern Lenn and Conrad Mullineaux to provide support during my stay at Queen Mary University.

I thank the University staff including Paul Loughnane, Jean Wood, Alison Beckett from the EM Unit and the CCI members, in particular, Dave Mason for the patience showed during my data analysis development.

I would like to express my gratitude to all my colleagues in the Liu lab for the useful scientific discussions and the infinite talks about the meaning of life, namely Yaqi Sun, Yi Fang, Greg Dykes, Matthew Faulkner, Zimeng Zhang, Leanne Miller, Mengru Yang, Fang Huang, Jorge Rodriguez-Ramos, Taiyu Chen. I am also in serious debt to Jorge who helped me with statistics and in improve my self-confidence skills.

Special thanks go to Rebecca Donnelly, Hanna Rees, Jenny Francis, Sipko Van Dam, Marco Marcello and Linda D'Amore for creating and maintaining a cheerful atmosphere during my PhD studies.

I am very much indebted to my supervisor Luning Liu, for his support and guidance during these years. Being a PhD supervisor for the first time is a challenging experience which requires patience and flexibility, qualities of which I'm very grateful.

Furthermore, I thank Prof Mark Caddick for being not only my assessor but also an excellent guide during these years.

Many thanks to all my friends who have been around these four years, who have been helping me on different occasions and in one way or another have influenced this thesis.

Finally, I would like to thank my parents, their endless phone calls helped me to feel at home everyday.

However, it is difficult to recall every person that has assisted, contributed or more importantly encouraged me to pursue these studies, and I hope that being in a hurry or sometimes stressed did not prevent me for thanking them at the appropriate moment during the last four years.

Liverpool, 2017 *Selene Casella*

Publications and Author's contributions

The majority of Chapter 1 of this dissertation make up a book's chapter entitled:

Adaptation and regulation of photosynthetic apparatus in response to light. Casella S, Huang F, Liu LN. Handbook of Photosynthesis, Third Edition. CRC Press, US, edited by Mohammad Pessarakli. 2016, 53-63.

The content Chapters 3 and 4 are based on a recently published article entitled:

Dissecting the native architecture and dynamics of cyanobacterial photosynthetic machinery. Casella S, Huang F, Mason D, Zhao GY, John GN, Mullineaux CW, Liu LN*. Molecular Plant, 2017, 10(11): 1434–1448. DOI:http://dx.doi.org/10.1016/j.molp.2017.09.019. (Cover article). Featured in Media: University News, Weixin (cn).

I acknowledge the following contribution of collaborators to the results described in these chapters. Unless specified below, all work was completed by the Author.

Luning Liu University of Liverpool, UK	AFM imaging of thylakoid membranes
Conrad Mullineaux Queen Mary University, UK	Choice of appropriate analysis for the one-dimensional protein diffusion
David Mason University of Liverpool, UK	Development of a script in Matlab to analyse FRAP data
Giles N. Johnson University of Manchester, UK	Acquisition of the $P700^+$ re-reduction kinetics
Tchern Lenn Queen Mary University, UK	Assistance for the 77K fluorescence spectroscopy
Jorge Rodriguez-Ramos University of Liverpool, UK	Assistance for data analysis

Other publications produced during my PhD studies but not included in my thesis:

- Direct characterization of the native structure and mechanics of cyanobacterial carboxysomes.
  Faulkner M, Rodriguez-Ramos J, Dykes GF, Owen SV, Casella S, Simpson DM, Beynon RJ, Liu LN*.
  Nanoscale, 2017, 9(30): 10662-10673, DOI:10.1039/C7NR02524F. *Featured in Media:* ScienceDaily, ScienceNewsLine, Nano Magazine, Phys.org, EurekAlert!, University News.

In this manuscript, I generated the TEM images of β-carboxysome fragments by electron microscopy.

- Light modulates the biosynthesis and organisation of cyanobacterial carbon fixation machinery through photosynthetic electron flow.

Sun Y, Casella S, Fang Y, Huang F, Faulkner M, Barrett S, Liu LN*.
Plant Physiology, 2016, 171(1): 530-541. DOI:10.1104/pp.16.00107. *Featured in Media:* ScienceDaily, ScienceNewsLine, NanoWerk, Phys.org, SpectroscopyNow, University News.

In this manuscript, I carried out all the thin-section electron microscopy images of Synechococcus 7942 cells.

The work described in Chapter 5 is unpublished. All work was completed by the Author.

Contents

List of figures

List of tables

Abbreviations

1-D	one dimensional
2-D	two dimensional
ACA	Aminocaproic acid
ADP	adenosine diphosphate
AFM	atomic force microscopy
APS	ammonium persulphate
ATP	adenosine-5'-triphosphate
ATPase	ATP synthase
A_X	absorbance at X (nm) wavelength
BisTris	bis (2-hydroxyethyl)-imino-tris(hydroxymethyl) methane
BN	blue-native
bp	base pairs
BSA	bovine serum albumin
CCA	complementary chromatic adaptation
Chl	chlorophyll
AChl	chlorophyll a
Cyt *b6f*	cytochrome b6f complex
D	diffusion coefficient
DCBQ	2,6 dichloro-p-benzoquinone
DCMU	3-(3,4-dichlorophenyl)-1,1-dimethylurea
DMSO	dimethyl sulfoxide
DNA	2'-deoxyribonucleic acid
EDTA	ethylenediaminetertraacetic acid
EM	electron microscopy
EtOH	ethanol
FRAP	fluorescence recovery after photobleaching
GFP	green fluorescent protein
IPTG	isopropyl-ß-D-thiogalactopyranoside
kb	kilobase pairs
kDa	kilo Dalton
kV	kilo Volt
LB	Luria-Bertani medium
LHC	Light-harvesting complexes
M	molar
MetOH	methanol
Mf	mobile fraction
MW	molecular weight
NADP+	oxidised β-nicotinamide adenine dinucleotide phosphate
NADPH	reduced β-nicotinamide adenine dinucleotide phosphate
NDH	NADPH-dehydrogenase complex
o.n.	overnight
OD_X	optical density at X (nm) wavelength
P680	primary electron donor of photosystem II

P700	primary electron donor of photosystem I
PAGE	polyacrylamide gel electrophoresis
PBsomes	phycobilisomes
PC	plastocyanin
PCC	Pasteur Culture Collection
PCR	polymerase chain reaction
PDB	protein data bank
PE	phycoerythrins
PQ	plastoquinone
PSI	photosystem I
PSII	photosystem II
RCs	reaction centres
RNaseA	ribonuclease A
rpm	rounds per minute
RT	room temperature
Rubisco	ribulose 1,5-biphosphate carboxylase/oxygenase
SDS	sodium dodecyl sulphate
Syn7942	Synechococcus elongatus PCC7942
TEM	transmission electron microscopy
TEMED	N-N-N'-N'-tetramethylethylenediamine
TES	N-tris[hydroxymethyl]methyl-2-aminoethanesulfonic acid
TIRF	Total internal reflection fluorescence microscopy
TM	thylakoid membrane
Tris	2-amino-2-hydroxy-methylpropane-1,3-diol
UV	ultraviolet
WT	wild-type
X-Gal	5-bromo-4-chloro-3-indolyl-β-D-galactopyranoside
β-DM	n-dodecyl-β-D-maltoside
ΔpH	proton gradient

Chapter 1

Structure and regulation of photosynthetic apparatus in response to the light

1.1 Introduction

Solar light can be efficiently captured and converted into chemical energy by all phototrophs, including photosynthetic bacteria, cyanobacteria, algae and vascular plants, through their specific photosynthetic machinery. Photosynthesis typically takes place in specialised intracellular membranes, called thylakoid membranes (TMs), where the photosynthetic complexes are located. The structure of the TMs, the type of the photosynthetic complexes and their spatial organisation present great difference among taxa, still preserving similar or the same function. One of the major environmental challenges to photosynthetic organisms is the light variability (especially the intensity and wavelength distribution), which during the evolution promoted the formation of complex regulatory systems. One of the mechanisms to cope and respond with rapidly fluctuating light conditions is to reorganise the complexes promptly on the TMs. Substantial information about the structures and functions of individual photosynthetic components has been available. However, the spatial organisation and dynamics of photosynthetic complexes in the cyanobacterial thylakoid membrane have yet to be well understood experimentally.

Having an advanced understanding of the dynamics and adaptive mechanisms developed by photosynthetic organisms will inform the bioengineering of phototrophs to enhance the utilisation of solar energy, for the production of biofuel and commodity products from light, CO_2 and water. In this chapter, we will summarise the recent studies on the molecular basis underlying the composition, organisation and physiological adaptation of the photosynthetic machinery towards irradiance variation, focusing in particular on cyanobacteria.

1.2 The relevance of studying photosynthesis

The basis for the majority of life on Earth is the oxygen (O_2) present in the atmosphere. It is highly reactive and has a relatively short atmospheric lifetime [1], so it was almost certainly nonexistent in Earth's early atmosphere. Nevertheless, O_2 has constituted ~10 to 30% of the atmospheric volume for 500 million years [2, 3]. It began to accumulate after cyanobacteria developed the oxygenic photosynthesis in which O_2 is continuously produced [4]. It is commonly accepted that, during the evolution, an endosymbiotic event led cyanobacteria to be encapsulated within a host cell. The evolution of this fusion then became the progenitor of all photosynthetic eukaryotes, including algae and higher plants [5-7]. Molecular phylogenetic analyses show evidence supporting the prokaryotic origins of chloroplasts [8]. It has been estimated that worldwide cyanobacteria convert solar energy into biomass-based chemical energy at a rate that is higher than the total power used by humans [9]. The interest in exploiting solar irradiation as a clean and renewable energy resource has stimulated research into utilisation of cyanobacteria for generating renewable biofuels and at the same time fixing CO_2 from the atmosphere [10, 11]. During the past century artificial photosynthesis, which uses chemical processes to mimic the natural photosynthetic system, has had extensive development and brought about the creation of the modern solar panels [12-14]. However, in recent years, synthetic biology appears to be the emerging discipline. It aims to redesign existing biological systems or create artificial life focusing the attention on simple model organisms such as *Escherichia coli*, yeast and photosynthetic microbes [15]. Despite promising progress, in-depth knowledge of how nature designed photosynthetic machinery is a prerequisite for the development and improvement of high-efficiency solar energy conversion into chemical energy.

1.3 Photosynthetic Apparatus: Composition and Organization

The primary reactions of photosynthesis are mediated by a series of photosynthetic complexes associated to or embedded in the photosynthetic membranes. These pigment-protein complexes can be classified into several groups according to their functions: light-harvesting antenna complexes, photosynthetic reaction centres, the cytochrome (Cyt) complex and ATP synthase (ATPase). They are structurally and functionally linked in order through the photosynthetic electron transport chain (Figure 1-1). Light energy captured by the light-harvesting antenna is rapidly and efficiently transferred to the reaction centres to drive the transmembrane charge separation. The electrons are then transferred to the (plasto)quinone pool (PQ) and subsequently to the Cyt enzymes. The electron transfer reactions are coupled to the formation of an electrochemical gradient across the photosynthetic membranes, which is essential for driving ATP synthesis. The photosynthetic electron transport is also used to produce NADPH (an energy carrier). Both ATP and NADPH are required as energy input into the Calvin-Benson cycle for the fixation of the CO_2. The cyanobacterial photosynthetic machinery typically consists of an antenna complex which captures the light, then a series of membrane integral multi-subunit complexes, including photosystem I (PSI), photosystem II (PSII), cytochrome (Cyt) b_6f and ATP synthase (ATPase) complexes (Figure 1-2). Several small electron transport molecules, such as plastoquinones, plastocyanins and Cyt c6, serve as electron carriers to shuttle electrons between distinct photosynthetic complexes and promote physiological coordination [16]. PSII catalyses light-driven electron transfer from water to PQ, producing O_2 as a waste product [17].

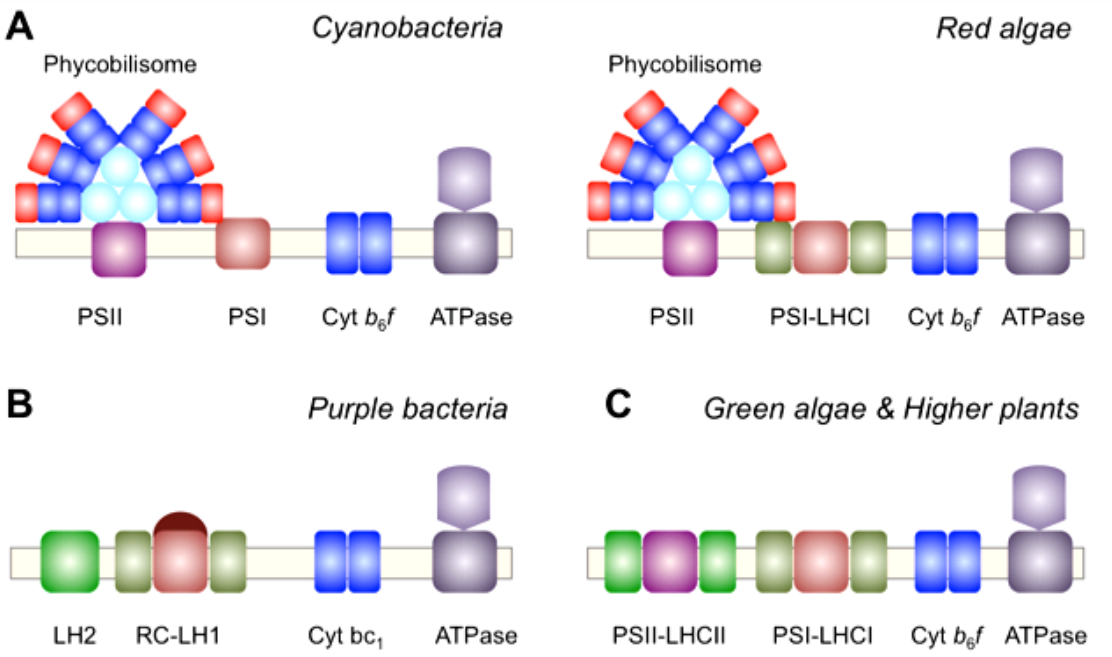

Figure 1-1 Variety of the photosynthetic apparatus in different photosynthetic organisms. (A) Cyanobacterial and red algal photosynthetic apparatus are composed of light-harvesting phycobilisomes, PSII and PSI, Cyt b_6f and ATPase. Typical phycobilisomes consist of a central core subcomplex with several rods radiating from the core. (B) Purple bacteria contain type II reaction centres with two major types of membrane light-harvesting complexes LH1 and LH2. (C) The photosynthetic apparatus of green algae and higher plants consists of PSI and PSII with their membrane-embedded antennae LHCI and LHCII, respectively, as well as Cyt b_6f and ATPase.

Electrons from mobile PQ are transferred to the cytochrome Cyt b_6f complex that is also located within proximity to PSII and PSI. Cyt b_6f can reduce PSI and the Cytochrome c oxidase (COX). PSI is a light-driven oxidoreductase that transfers the electron to ferredoxin. This process supplies electrons for subsequent reduction of $NADP^+$ to NADPH by the ferredoxin-$NADP^+$ reductase (FNR). Cyanobacterial thylakoid membranes also act as the site that harbours the components of respiratory electron transport chains, comprising type-I NAD(P)H dehydrogenase-like complex (NDH-1), succinate dehydrogenase (SDH), Cyt oxidase and alternative oxidase [18-21].

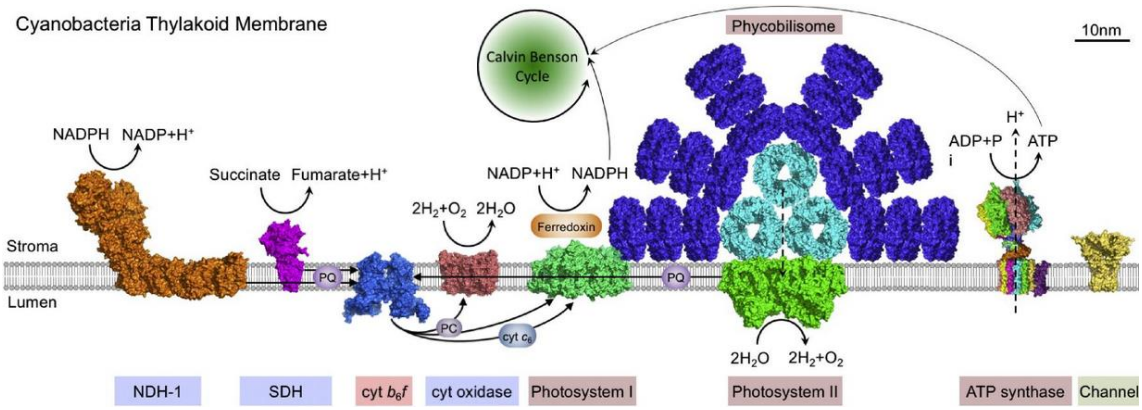

Figure 1-2 Simplified scheme of electron transport pathways in cyanobacteria. See text for description of the electron flows. Abbreviations: ADP, adenosine diphosphate; ATP, adenosine triphosphate; Cyt b_6f, cytochrome b_6f; Ox, terminal oxidase; NADP(H), nicotinamide-adenine dinucleotide phosphate (reduced form); NDH-1, type 1 NADPH dehydrogenase; PC, plastocyanin; PQ, plastoquinone; SDH, succinate dehydrogenase. Arrows indicate the electron flow. Representation scheme from [22].

1.3.1 Light-harvesting complexes (LHC)

The first step in the process of photosynthesis is the absorption of light photons by an array of antenna pigment-protein complexes, termed light-harvesting complexes (LHCs). The spectral properties and macromolecular conformations of photosynthetic antenna complexes vary dramatically depending on the different origins (Figure 1-1). The photosynthetic apparatus of the anoxygenic purple bacteria present the simplest configurations [23-25]. Most purple photosynthetic bacteria synthesise two types of light-harvesting (LH) complexes classified according to their *in vivo* absorbance, B875 (LH1) and B800-850 (LH2) complexes. Such antenna complexes are generally composed of two polypeptides (α and β subunits), two or three *BChl* molecules and some carotenoids (Figure 1-1B). Green algae and higher plants contain integral LHC I and II as the peripheral antenna proteins associated with PSI and PSII supercomplexes, respectively [26] (Figure 1-1C). The migration of LHCs between PSII and PSI in the thylakoid

membrane is essential to balancing the excitation energy between the two photosystems during state transitions [27].

Phycobilisomes (PBsomes) are the major light-harvesting antennae complexes in cyanobacteria and red algae [28-31] (Figure 1-3). They are aggregations of water-soluble phycobiliproteins (PBPs) and linker polypeptides [29], and serve as external antenna macrocomplexes associated with the stromal surfaces of thylakoid membranes [32, 33]. Red algae also have an intrinsic antenna LHCI-like complex, functionally associated with PSI [34].

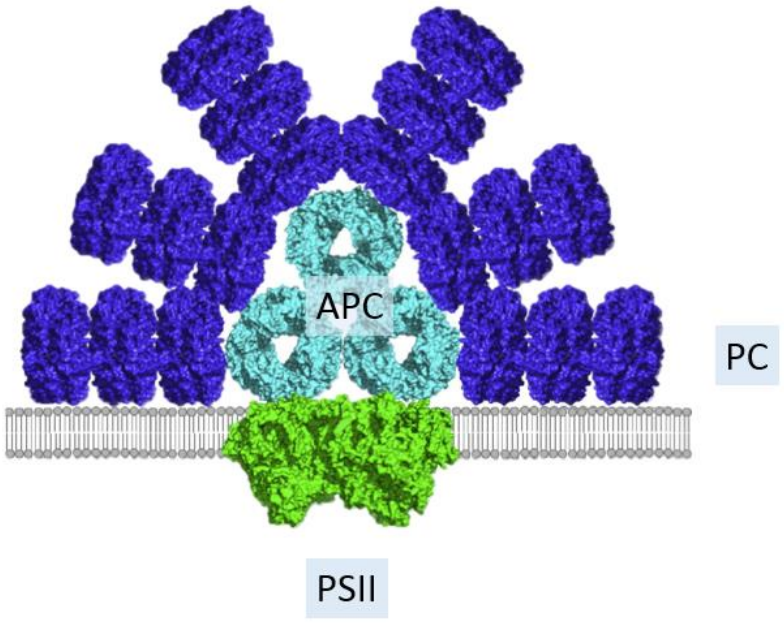

Figure 1-3 Simplified model of cyanobacterial phycobilisome (*Synechocystis* 6803). The protein structures are achieved from PDB database: allophycocyanin, PDB ID: 1KN1, phycocyanin, PDB ID: 3O18. (Adapted from [35]).

PBsomes consist of two structural domains: the inner domain contains three cylinders that are arranged in a triangular PBsome core, and the peripheral domain contains six rod-like structures that radiate from the core. Both the core and the rods of the PBsome are composed of stacked PBP hexamers. In typical PBsomes, this domain is composed predominantly of allophycocyanins (APC), whereas the peripheral rods are mainly composed of phycocyanins (PC) and

phycoerythrins (PE) (Figure 1-1A). In freshwater unicellular cyanobacteria *Synechocystis* PCC 6803 and *Synechococcus* 7942, the PBsomes rods contain just PC while APC is the major PBP of the core (Figure 1-3).

Energy transfer in PBsomes is expected to progress from PE (λ_{max} = 545~565 nm) [36] stepwise to PC (λ_{max} = 620 nm), APC (λ_{max} = 650 nm) and eventually to chlorophylls (*Chls*). It is evident that the presence of PBsomes extends the absorbance range covered by PSII and PSI. The stepwise energy transfer within the PBsomes may probably also play a photoprotective role [37]. A key physiological importance of PBsomes is reflected in light-state transitions, which will be discussed in detail below.

1.3.2 Reaction centres (RCs)

Photosynthetic RCs are pigment-protein complexes that convert the excitation energy from antenna complexes into chemical potential energy [38]. The key reactions of photosynthesis occur in two homologous types of RCs: (1) RCI type in some anoxygenic photosynthetic bacteria, such as green sulfur bacteria and heliobacteria; (2) RCII type in other anoxygenic photosynthetic bacteria, for instance purple bacteria and green filamentous bacteria; (3) coexistence of both RCI and RCII in all oxygenic photosynthetic organisms, i.e. cyanobacteria, algae, and plants [39] (Figure 1-1). These two types of RCs probably share a common evolutionary ancestor because of their similar structures and cofactor arrangements of the electron-transfer domains [40].

PSI is the most abundant photosystem in cyanobacteria, and its function is to transfer electrons to NADPH during the linear electron transport. PSI is a multisubunit pigment-protein complex composed by 12 subunits (named Psa), 96 chlorophyll *a* (*AChl*) molecules, 22 L-carotenes, two phylloquinones, four lipids and three iron-sulfur proteins that serve as intermediate redox carriers. The 12 polypeptide subunits of PSI are named from PsaA to PsaF, from PsaI to PsaM, and PsaX [41]. PsaA and PsaB are the two central subunits of the RC core which harbour the

primary electron donor P700 (a dimer of *AChl* molecules) [42]. The PsaL subunit was identified as essential for the formation of PSI trimers (see section 5.1) [43]. In cyanobacteria, the PSI complexes are present mostly in the form of monomers and trimers [44] while in higher plants and algae PSI is present only as a monomer [45].

PSII catalyses the oxidation of water with the release of molecular oxygen. In cyanobacteria and green plants, PSII contains at least 17 subunits: proteins D1 (PsbA) and D2 (PsbD); the subunits CP43 (PsbC) and CP47 (PsbB); cytochrome b-559 (PsbE and PsbF); and other smaller subunits PsbH, PsbI, PsbJ, PsbK, PsbL, PsbM, PsbN and PsbX [46]. The heart of the PSII reaction centre is formed by the subunits D1 and D2 where is located the primary electron donor P680, an *AChl* [47]. In cyanobacteria and plants, PSII is present in both monomeric and dimeric form [46, 48].

1.3.3 Cytochrome (Cyt) and ATP synthase (ATPase)

Various cytochromes are mainly responsible for the electron transfer released from the primary processes of charge separation in reaction centres. The Cyt b_6f complex is a dimeric membrane-intrinsic complex located in the TMs (Figure 1-2). It is essential for both photosynthetic and respiratory electron transfer chains [49]. In the linear electron transfer scheme of oxygenic photosynthesis, Cyt b_6f receives electrons from PSII by plastoquinol and passes them to PSI by reducing plastocyanin or Cyt c_6. This results in proton release in the lumen, generating a proton electrochemical gradient across the membrane. Cyt b_6f can switch from linear electron transfer between both photosystems to a cyclic mode of electron transfer around PSI [50]. The Cyt b_6f complex contains four large subunits which are involved in electron transport (cytochrome f, cytochrome b_6, the Rieske iron-sulfur protein, and subunit IV); it also includes four small subunits which are involved in the stabilisation of the complex (PetG, PetL, PetM, and PetN) [51]. The cytochrome *c* oxidoreductases (Cyt bc_1) are multi-subunit enzymes existing in a broad variety of

organisms, including the purple non-sulfur photosynthetic bacteria [49]. They are components of both cyclic photosynthetic and mitochondrial-like linear respiratory electron transport chains.

The ATP synthase (ATPase) is a large protein complex. It catalyses the synthesis of ATP from ADP and inorganic phosphate using a flux of protons across the membrane. The movement of the protons is driven by the proton gradient generated by electron transfer. ATPases are located in the plasma membrane and photosynthetic membrane of bacteria, the chloroplast thylakoid membrane in algae and plants, and the mitochondrial inner membrane in plants and animals.

1.3.4 Diversity of photosynthetic apparatus organisation

The physiological arrangement and functional coordination of these photosynthetic constituents are fundamental for efficient light capture and energy transfer mechanisms. In order to adapt to the diverse habitats, photosynthetic organisms have developed distinct photosynthetic machinery to regulate the energy conversion, as shown in Figure 1-1. Purple photosynthetic bacteria contain one type of RC and two types of LH complexes, LH1 and LH2. Cyanobacteria, red algae, green algae and higher plants consist of PSI, PSII and various membrane or extra-membrane light-harvesting antennae complexes. Distinct from green algae and higher plants, cyanobacteria and red algae utilise PBsomes to capture light for PSI and PSII.

1.4 Light Effects on the Photosynthetic Stoichiometry

1.4.1 Light intensity

The ratio of antenna quantity to photosynthetic RC has been demonstrated to depend on light intensity during cell growth. To retain the efficient light absorbance to RC, additional 30% PBsome antennae complexes are synthesised under low-light condition compared to high-light condition (Figure 1-4) [32]. Similarly, in the photosynthetic membranes from the purple

photosynthetic bacterium *Rhodospirillum* (*Rsp.*) *photometricum* adapted to high light, ~3.5 LH2 are present per core complex, whereas under low-light condition ~7 LH2 per core were observed and the moderate-light-adapted membranes have an intermediate LH2/core ratio of 4.8 [52, 53].

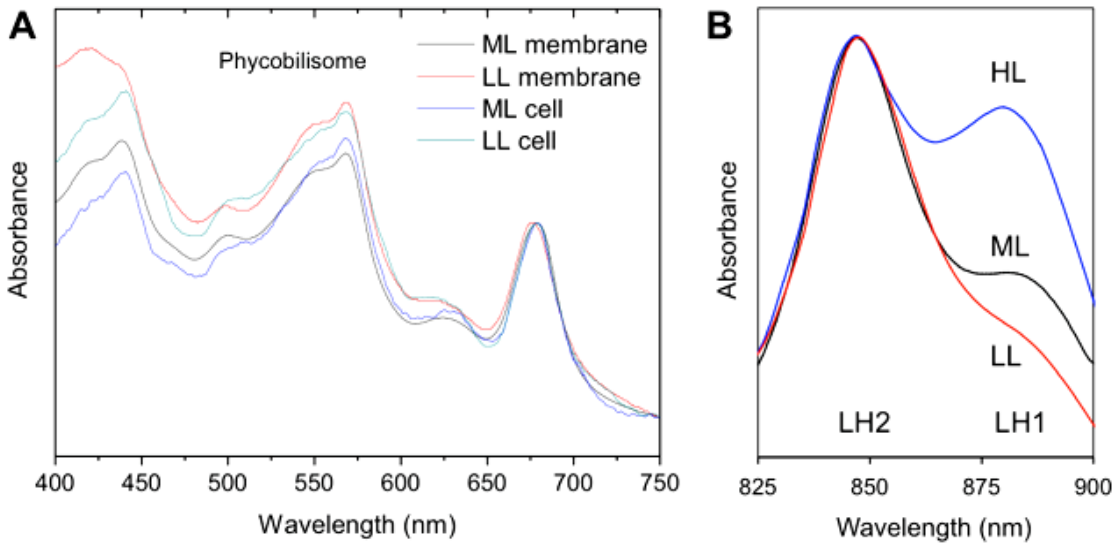

Figure 1-4 Light Effects on the Photosynthetic Stoichiometry. (A) Room temperature absorption spectra of whole cells and isolated PBsome-thylakoid membranes from the unicellular red alga *Porphyridium cruentum* grown under low light (LL, 6 watts/m^{-2}) and moderate light (ML, 15 watts/m^{-2})[32]. Spectra were normalised to the chlorophyll absorption band at 682 nm. It showed the amount of PBsomes (500–650 nm) is dependent upon the light intensity. (B) The absorption spectrum of purple photosynthetic membranes adapted to high light (HL), moderate light (ML) and low light (LL). The absorption ratios of LH2 (845 nm) to core complex (LH1, 880 nm) are 1.16, 1.86 and 2.6, respectively [52, 53]. It indicated that the ratio of antenna to RC varies according to the light intensity. Similar phenomena are observed as a general response of phycobilisome-containing organisms, including cyanobacteria [54].

In cyanobacteria, the ratio of PSII to PSI is variable towards the light intensity and spectral quality. The switch from low light to high light suppresses the PSI biosynthesis, increasing PSII/PSI ratio. This responsive effect has been shown to be triggered by the redox state of the electron transport chain [55]. Furthermore, two genes have been implicated in the regulation of the PSII/PSI ratio. Inactivation of a gene encoding for a putative sensory histidine kinase, *rppA*, leads to phenotypic changes consistent with a role in transducing redox signals to changes in PSII and PSI gene expression [56]. Inactivation of *pmgA* specifically abolishes the PSII/PSI ratio

change in response to high light [57]. Both RppA and PmgA are excellent candidates for redox signal transduction proteins.

1.4.2 Light quality

The acclimation of photosynthetic organisms to changes in light wavelength is ubiquitous and may be best characterised by the complex process of complementary chromatic adaptation (CCA) [58, 59]. In many freshwaters, marine, and soil cyanobacteria whose PBsomes contain both PE and PC, the ratio of PC to PE in PBsomes varies in response to light spectra (Figure 1-5). Green light (optimally 540 nm) promotes the PE biosynthesis, whereas red light (optimally 650 nm) elevates the PC biosynthesis. The CCA leads to the optimised absorbance of PBsomes to capture the most abundant wavelength of light in the green-to-red spectral region.

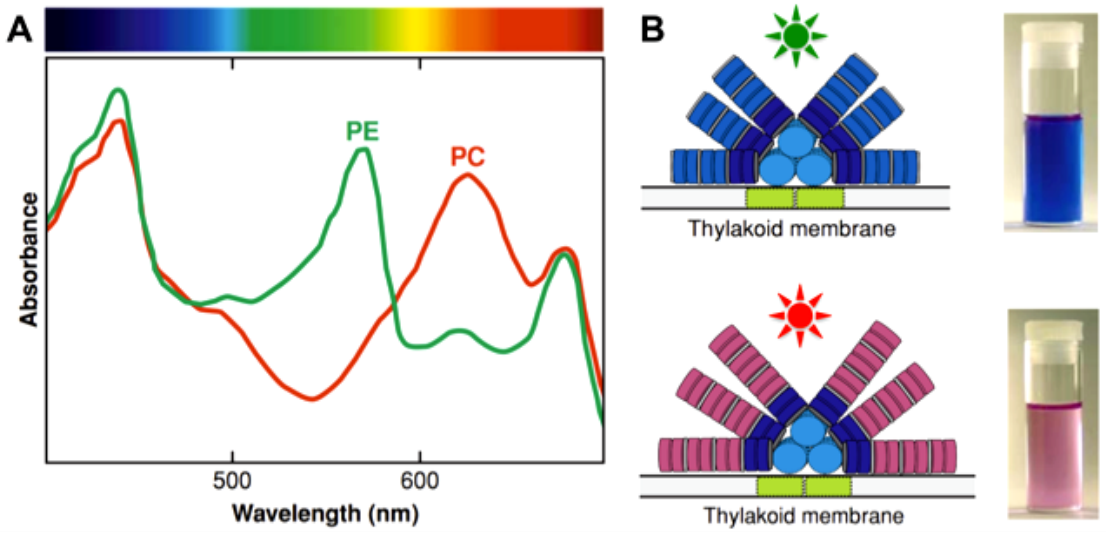

Figure 1-5 Acclimation of photosynthetic organisms to changes in light wavelength. (A) Whole-cell absorption spectra of the cyanobacterium *Fremyella diplosiphon* cells grown in green and red light. The phycoerythrin (PE) and phycocyanin (PC) absorption peaks were indicated [58]. (B) Changes of *Fremyella diplosiphon* PBsomes in composition and structure induced by green and red light.

CCA regulation of PC and PE synthesis is predominantly at the transcriptional level for PE and PC genes (*cpeBA* and *cpc2*). The β and α subunits of PE are encoded by the *cpeBA* operon which is

highly upregulated by green light [60]. The β and α subunits of “inducible PC” as well as three corresponding linker proteins are encoded by a large transcription unit *cpc2* (*cpcB2A2H2I2D2*)[61]. Its expression is highly upregulated by red light. Maintaining the expression of these operons is not essential once steady-state CCA is obtained [62]. The changes in RNA levels of PBsome components after an inductive light treatment are relatively rapid [63]. *cpc2* RNA reaches a maximum level, two hours after a shift from green to red light, and drops to undetectable levels two hours after a shift from red to green light. While *cpeBA* RNA reaches a maximum level, eight hours after a shift from red to green light, and drops to undetectable levels more than 14 hours after a shift from green to red light. In contrast to the rapid response at the transcriptional level, PE and PC protein levels altered more slowly, requiring a few days to fully shift between the red- and green-light steady states. The regulatory mechanisms governing these responses are different for *cpc2* versus *cpeBA*. Two light-response pathways controlling the PBsome biosynthesis during CCA, a Rca system and a Cgi system, have been identified [58]. The light sensor in the Rca system is a photoreceptor called RcaE. In the presence of red light, RcaE modulates the transcription factors involved in the activation of PC genes and the repression of the PE genes (transcriptional regulation).

The second mechanism to control the CCA response is the Cgi system which is much less understood. Its initial light signalling for CCA is not well characterised. A phytochrome would be a potential candidate for a red-light sensor. However, the phytochrome responding to green light has not been found. If CCA is controlled by a single photoreceptor, it should contain a novel pigment or another green-absorbing chromophore. There is a precedent in the purple photosynthetic bacterium *Rhodospirillum centenum* for a phytochrome-like protein that binds a second pigment [64]. Alternatively, a second photoreceptor, possibly a rhodopsin, could be involved [65]. The Cgi system is known to regulate the expression of PE (CpeC genes) by repressing CpeC in red light (post-transcriptional regulation) [66, 67].

1.4.3 Light-dark cycle

The daily light-dark cycle controls rhythmic changes in the behaviour and physiology of most species, such as cyanobacteria, plants, animals and fungi. The so-called circadian rhythm displays an endogenous and entrainable oscillation of about 24 hours. Cyanobacteria exhibit a self-sustained circadian rhythm that results in temporal changes in gene expression patterns, even in the absence of environmental cues [68-70]. Correct circadian regulation maximises photosynthesis, which is carried out specifically in plant chloroplasts, and productivity by increasing *Chl* content, modifying the stoichiometry of photosynthetic complexes, and enhancing photosynthetic carbon fixation [71]. A recent study has described how the nuclear-encoded clock regulates the expression of key chloroplast associated genes [72]. Based on observations of rhythms in the delayed fluorescence [73], a readout of the chemical state of PSII, the clock likely to be having profound effects on the structure and function of thylakoid membranes. However, how the circadian clock controls the photosynthetic performance at the biochemical and structural level remains uncharacterized.

1.5 Light Effects on the Organization of Photosynthetic Machinery

Light variability not only determines the optimisation of photosynthetic stoichiometry but also results in inevitably the reconfiguration of photosynthetic apparatus organisation, for regulating the energy transduction under diverse light conditions. The adaptation of the light-harvesting apparatus is just one example in which the protein diffusion plays an important role. Other events that require protein diffusion are the turnover and repair of the photosynthetic complexes [74] and the control of the electron transport chains by lateral segregation [75, 76]. With improved knowledge of the localisation, velocity of diffusion and conditions that determine these, it will be possible to draw a detailed model of the thylakoid membrane functions. In the

following sections, we will discuss the effect of the light on the organisation of the photosynthetic complexes.

1.5.1 Photoadaptation of the photosynthetic apparatus

To understand the dynamic organization of photosynthetic complexes and the mechanisms of photosynthetic processes, it is essential to assess the *in situ* assembly and distribution of membrane proteins in native photosynthetic membranes under their physiological conditions. Recently, atomic force microscopy (AFM) has matured as a unique and powerful tool for directly assessing the supramolecular organisation of photosynthetic complexes in their native environment at submolecular resolution [24] (see section 1.9.3). The tight arrangement of LHC has been observed in AFM topographs of the photosynthetic membranes in a unicellular red alga *Porphyridium* (*P.*) *cruentum* (Figure 1-6)[32]. Under moderate light, PBsomes are randomly distributed and tightly clustered on photosynthetic membranes. In contrast, under low light increasing amounts of PBsomes form densely packed rows on the membrane surface. The presence of dense antenna domains might be a general regulatory mechanism for light trapping when photons are relatively rare. Such structural constraints would enhance photosynthetic electron transfer under diverse light conditions [52].

A similar response has also been recorded in the thylakoid membrane of higher plants [77, 78]. Electron microscopy data on the dark- and light-adapted *Arabidopsis thaliana* thylakoids indicated that the granal thylakoid lumen significantly expands in the light stress [79]. This light-induced expansion may moderate the restrictions imposed on protein diffusion in the lumen in the dark.

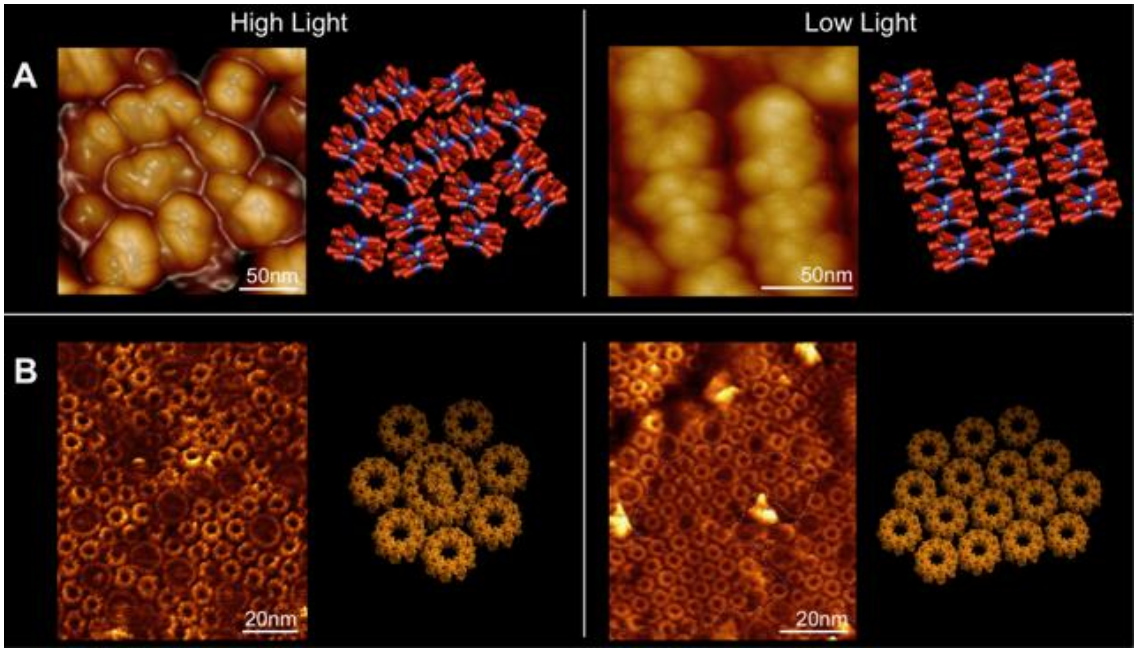

Figure 1-6 AFM topographs of LHC arrangement in high light and low light. (A) AFM images presenting the adaptation of the organisation of PBsomes on the red algal thylakoid membrane [32]. The PBsomes show a random distribution and clustering in high light, whereas low-light illumination induces the synthesis of more PBsomes and facilitates the formation of parallel rows. The structural models of the photosynthetic apparatus are based on the AFM topographs. (B) AFM images showing the organisation of photosynthetic membranes from the purple photosynthetic bacterium *Rhodospirillum photometricum* adapted to high light and low light. LH2-rich antenna membrane domains were observed in the low-light-adapted photosynthetic membrane of *Rsp. photometricum* [24, 53].

AFM imaging has also characterised comprehensively how the organisation of *Rhodospirillum photometricum* photosynthetic membrane is modulated towards light variation [52, 53]. In high-light-adapted membranes, ~3.5 LH2 are present per core complex, whereas after low-light growth ~7 LH2 per core were recorded. Two different types of protein assemblies in the bacterial photosynthetic membranes were identified: core–LH2 domains and paracrystalline LH2-rich domains (Figure 1-6). Additional LH2 incorporated into the membrane segregated in paracrystalline antenna domains, whereas the domains with core seemed architecturally unaffected. The two domains have distinct roles to optimise the photosynthetic activity during light intensity change: core–LH2 domains maintain efficient harvesting, trapping, and transmission of solar energy; LH2-rich domains enhance light capture when only few photons are available but do not perturb the photosynthetically active core assemblies. The membrane

adapted to medium-light conditions exhibited the intermediate composition and organisation of photosynthetic apparatus [52]. Similar protein assembly patterns have been found in other species, for instance, *Phaeospirillum molischianum* [80], *Rhodopseudomonas* (*Rps.*) *palustris* [81] and *Rhodobacter sphaeroides* [82]. In *Rps. palustris* photosynthetic membranes of high-light-adapted cells, the core complexes also segregate into hexagonally packed paracrystalline domains, reminiscent of the assembly found in *Blastochloris viridis* [83]. The dense packing of the large paracrystalline LH2 domains may limit quinone diffusion and, therefore, favour quinone distribution in the proximity of the cores.

1.5.2 Light-state transitions

State transitions are rapid adaptive responses to changes in light quality. Illumination conditions which lead to excess excitation energy of PSII compared to PSI induce a transition to State 2, in which more absorbed excitation energy is diverted to PSI. When PSI is over-excited relative to PSII it induces a transition to State 1, in which more energy is transferred to PSII. Thus, state transitions act as a mechanism to balance excitation of the two photosystems under changing light regimes. State transitions have been extensively characterized in green alga *Chlamydomonas reinhardtii* and higher plant *Arabidopsis thaliana*. The processes of the state transitions involve the LHCII migration, the molecular reorganization of photosystem supercomplexes, the identification of LHCII kinase, mapping phosphorylated residues in LHCII, and the involvement of Cyt b_6f in the control of LHCII phosphorylation [27](Figure 1-7). It has been shown that the state transitions are regulated by the redox state of plastoquinone (PQ), an electron carrier located between two photosystems [84], and involve post-translational modifications by phosphorylation of LHCII. Under certain light conditions, for example when PSII is excited, the redox state of PQ pool is more reduced. The more reduced PQ pool induces the activation of an LHCII kinase and LHCII phosphorylation, resulting in its movement from PSII to PSI (state 2). Conversely, when the PQ pool is oxidized, the LHCII kinase is inactive, and LHCII is

dephosphorylated by phosphatase and moves back from PSI to PSII (state 1). Thus, the PQ redox regulated-reversible phosphorylation of LHCII promotes state transitions and acts to redistribute absorbed excitation energy in response to different light conditions.

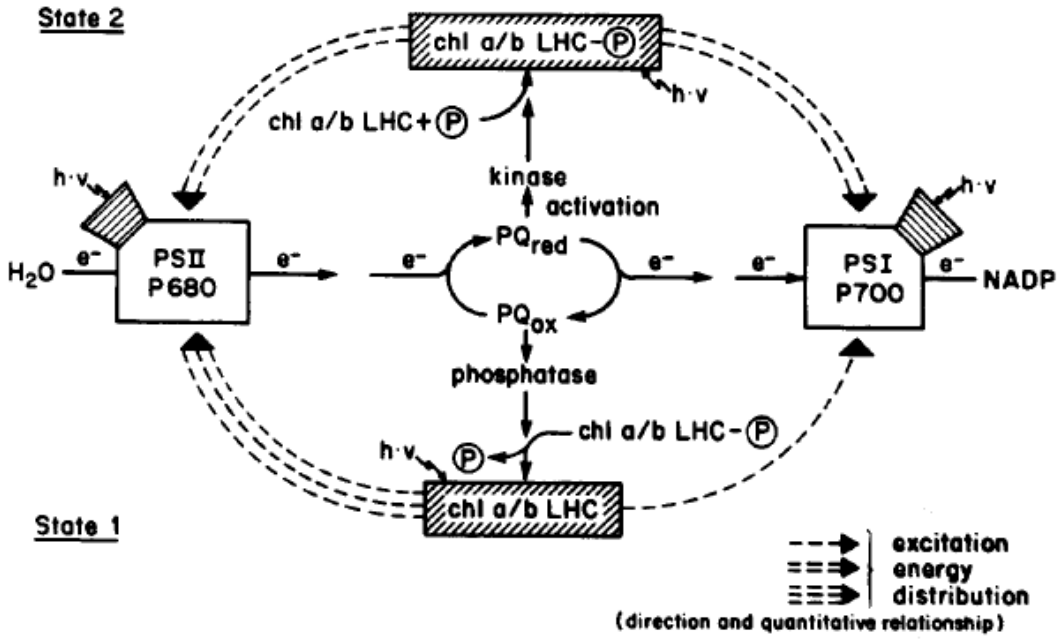

Figure 1-7 Control of the state transition in chloroplasts. The PQ redox state controls the state transition by a feedback mechanism. Excessive excitation of PSII induce a transition from State 1 to State 2 causing a reduction of the PQ pool. This lead a kinase to phosphorylate the LCHII which detaches from PSII and attaches to PSI. This mechanism diverts the more absorbed energy toward PSI. On the contrary the state 1 is induced by the oxidation of the PQ pool [85]. See text for more details. Diagram from [86].

In cyanobacteria, there is no specific light-harvesting antenna for PSI, and the PBsomes serve as the major antenna for both photosystems. State transitions regulate the excitation energy transfer from the PBsomes to PSII or PSI. The structural basis of state transitions in cyanobacteria is still controversial (Figure 1-8). One hypothesis is “mobile PBsomes”, which suggests that state transitions may involve the physical association and disassociation of PBsomes between PSII and PSI, and thus the energy redistribution between PSII and PSI [87]. About 80% of all PBsomes were found to connect with PSI and energy is transferred via PBsomes independently to PSII and PSI [88]. Another model is “energy spillover”, which proposed that PBsomes could only associate

with PSII and excess *A*Chl absorbed excitation energy may be redistributed from PSII to PSI [89, 90]. The redistribution of excitation energy absorbed by *Chl* is independent of the redistribution of excitation energy absorbed by the PBsomes. Both changes are triggered by the same environmental light conditions. An updated model described that PBsomes are capable of physically interacting with both PSII and PSI. Instead of the long-range movement, redistribution of PBsomes between PSI and PSII in the local membrane region might be essential to the state transitions [91].

Studies using Fluorescence Recovery after Photobleaching (FRAP) (see section 1.9.1) based on live-cell imaging have indicated that the PBsomes are mobile along the surface of thylakoid membrane [92], and the diffusion of PBsomes from RC to RC is required for state transitions [93] and non-photochemical quenching (NPQ)[94]. A recent study further demonstrated that state transitions have an important regulatory function in mesophilic red algae, but this process is replaced by non-photochemical quenching in thermophilic red algae [95]. However, FRAP experiments have revealed a partial fluorescence recovery in wholly-bleached cells of the red alga *P. cruentum*, and more interestingly, immobilised PBsome complexes *in vitro* [96]. The observations might suggest that the fluorescence recovery recorded during FRAP experiments could be ascribed to the intrinsic photophysics of the bleached PBsomes *in situ*, rather than the diffusion of PBsome complexes on the thylakoid membranes. Furthermore, AFM images on the native thylakoid membrane of *P. cruentum* showed significant crowding of PBsome complexes (Figure 1-6)[32]. Under such crowd circumstance, the rapid and long-range movement of PBsomes may be significantly restricted by steric hindrance, taking into account the large size of individual PBsomes, their dense lateral packing membrane surface as well as the limited free vertical spacing between opposite thylakoid layers. In addition, given the fact that PSII and PSI are mixed in the thylakoid membrane [97], the dense coverage of PBsomes on the thylakoid membranes may denote the structural association between the PBsomes and both photosystems underneath.

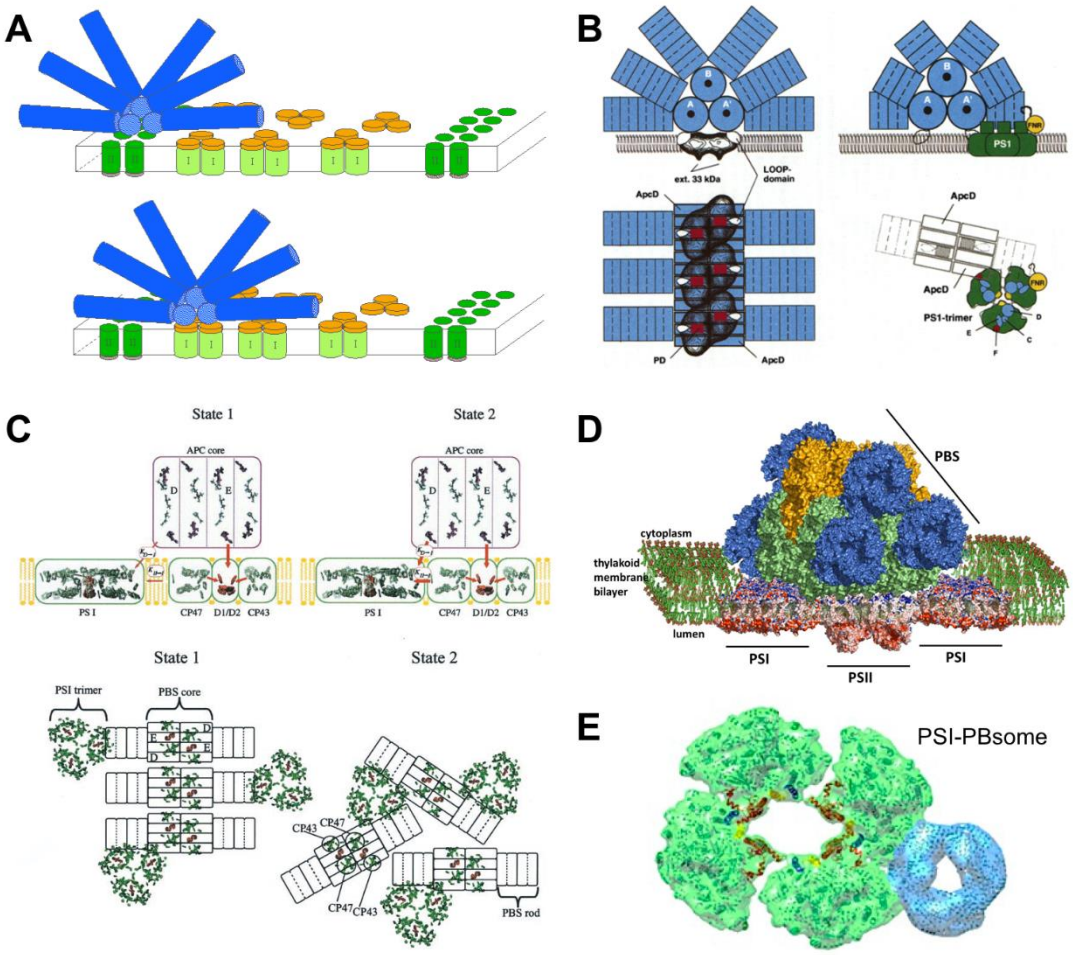

Figure 1-8 Models of the association between PBsome and PSI, PSII. (A) Mobile PBsomes, suggesting that PBsomes have loose association with PSI and PSII, and the movement of PBsomes between the two photosystems is essential to state transitions [92]. (B) Possible coupling of PBsome with PSII and PSI. PBsome core can contact PSII dimer. Tilted packing of PBsomes and PSII is essential to driving the connection. PBsomes can also interaction with PSI trimmers through the rods, to form a PSI-PBsome supercomplex under "state 2" condition. The model is adapted from [98]. (C) A schematic model showing the organization of cyanobacterial thylakoid membrane, showing possible associations between the PBsome core, PSII and PSI complexes in states 1 and 2 [91]. Energy transfer from the core to PSII occurs from the ApcE subunit to D1/D2. Energy transfer from the core to PSI is via the ApcD subunit. Energy "spillover" from PSII to PSI is assumed to occur from CP47 to PSI. APC core cylinders are associated with PSII dimers and PC rods interact with PSI trimers. In state 2, trimeric PSI is in close contact with both CP47 of PSII and the ApcD subunits of the core. In state 1, the PBsome-PSII supercomplexes are organized into rows. One PBsome-PSII supercomplex is shown to remain coupling with one PSI trimer via ApcD, to form the PBsome-PSII-PSI supercomplex. (D) A structural model of the PBsome-PSII-PSI photosynthetic megacomplex, depicting that the PBsome core fully covers and close couples with the PSII dimer, whereas the PSI is associated with ApcD through a side-on orientation [99]. (E) A structural model of the PBsome-CpcL-PSI supercomplex isolated from the

cyanobacterium *Anabaena* [100], describing the CpcL–PBsome rods specifically bind at the periphery of the PSI tetramers.

Recently, the existence of PBsome-photosystem supercomplexes has been proved (Figure 1-8). Using a chemical cross-linking strategy, a protein megacomplex composed of a PBsome, PSII, and PSI from a cyanobacterium *Synechocystis* sp. PCC6803 has been isolated [99]. This provided evidence about the presence of PBsome–PSII–PSI supercomplexes *in vivo*. Time-resolved fluorescence spectroscopy further demonstrated that the PBsome could deliver excitations to the RCs of either PSI or PSII, although the energy transfer from the PBsome to PSII is efficient whereas that from the PBsome to PSI is slow. Another work characterised a supercomplex PBsome–CpcL–PSI isolated from a cyanobacterium *Anabaena* [100]. Within the supercomplex, PSI is organized into tetramers (a dimer of dimers). The PBsome subcomplex, CpcL–PBsome rods, specifically bind at the periphery of the PSI pseudotetramers.

1.6 Regulation of Electron Transport Pathways

The organisation of photosynthetic complexes regulates the electron transport pathway and efficiency. All photosynthetic membranes that have been analysed exhibit a dense-packing of multicomponent photosynthetic complexes [24]. On the one hand, protein crowding is favourable for excitation energy transfer between complexes; on the other hand, it significantly reduces the lipid content and space between protein complexes, and as a consequence probably membrane fluidity that is required for the diffusion of hydrophobic electron/proton transport carriers (i.e., quinone molecules). Therefore, it represents an obstacle for efficient cyclic electron transduction between RCs and Cyt bc_1 complexes in membranes. Analysis of the molecular environment and long-range protein organisation proposed a continuous 'lipid area network' for long-range quinone diffusion throughout the photosynthetic membrane of the purple photosynthetic bacterium *Rsp. photometricum* [52]. Recent studies on the distribution and

dynamics of respiratory components in the plasma membrane of *Escherichia coli* revealed that respiratory complexes are concentrated in mobile domains in the membrane [101]. Different complexes are concentrated in separate domains, with no significant co-localisation and therefore no supercomplexes. This is another indication about a rapid and long-range quinone diffusion that serves to shuttle electrons between islands of distinct electron transport complexes in the membrane.

Photosynthetic electron transfer induced by light excitation modulates the redox state of electron transport components. Several cyanobacterial responses are known to be triggered by changes in the redox state of PQ or the Cyt b_6f complex, and thioredoxin that accepts electrons from PSI. Light-harvesting regulation can act to control the balance of linear and cyclic electron transport, and therefore the balance of proton-motive force and reducing power as photosynthetic outputs. Switches that remove electrons from the photosynthetic electron transport chain are also known as “electron valves”: they serve to prevent dangerous over-reduction of the electron transport chain [21]. There is scope for short-scale post-translational mechanisms to switch between cyclic and linear electron transport. One example is the regulation of cyclic electron transport pathway involving Complex I under different light intensities [21]. Fluorescence microscopy images on the fluorescently tagged Complex I in *Synechococcus elongatus* PCC7942 showed that the large-scale distribution of Complex I in the thylakoid membrane is controlled in response to a redox switch triggered by light intensity changes. Oxidation of the PQ pool induces the clustering of Complex I in segregated thylakoid membrane zones, whereas reduction of the PQ pool induces a post-translational switch in the distribution of respiratory complexes to a state in which it is more evenly dispersed in the membrane. Complex II (succinate dehydrogenase) showed a similar change in distribution under the same conditions. This switch in the distribution of respiratory complexes correlates with a major change of the probability that electrons from the respiratory complexes are transferred to a PSI rather than to a terminal oxidase [21]. It provided a mechanism to promote cyclic

electron transport when the reduction of the PQ pool indicates an adequate supply of electrons in the cell. Although many questions about the mechanism remain to be addressed, the observation indicates that the distribution of electron transport complexes in the membrane at the sub-micron scale is under physiological control, and plays a crucial role in controlling pathways of electron flux.

Another example of cyanobacterial "electron valves" is the flavodiiron (Flv) proteins Flv1–4: they are cytoplasmic proteins that take electrons from the photosynthetic electron transport chain and divert them to alternative acceptors. Flv1 and Flv3 form a heterodimer that takes electrons from the acceptor side of PSI and uses them to reduce oxygen [102]. A Flv2/Flv4 heterodimer takes electrons from the acceptor side of PSII, passing them to an unknown acceptor [103]. The regulation of the activities of Flv proteins is not known, and they presumably act only as an electron transport switch on slow timescales.

1.7 Photoprotection

Light is not only the basic driving force for photosynthesis but can also be destructive, mainly when the light-harvesting antenna capture excess photons after photosynthetic electron transport saturates. The photosynthetic apparatus has developed appropriate physiological mechanisms to modulate the absorbance of excitation energy while avoiding the potentially phototoxic effects of excess photons [104].

1.7.1 Non-photochemical quenching (NPQ) and orange carotenoid protein (OCP)

High levels of solar radiation can increase the production of reactive oxygen species and cause damage to photosynthetic membranes and pigment-protein complexes. Cyanobacteria have evolved a protective mechanism, NPQ, to dissipate excess PBsome-absorbed energy as heat

[105]. In contrast to plants and eukaryotes, cyanobacteria lack both pH-dependent quenching or the xanthophyll cycle [106]. NPQ in cyanobacteria is triggered by strong blue light, which excites both PBsomes and *Chls*. Recent studies have shown that the NPQ in cyanobacteria is mediated by a 35 kDa water-soluble orange carotenoid protein (OCP) [107-109]. As a high-light sensor, OCP is directly involved in the fluorescence quenching of PBsomes and possibly in the regulation of energy transfer between the PBsomes and photosystems [109]. OCP contains a single bound carotenoid (3'-hydroxyechinenone), which can change the conformation between its orange (OCP^O) and red forms (OCP^R)[109]. The photoactivated OCP^R binds to the PBsome core, where it takes excitation energy from the phycobilins and converts it to heat to prevent photodamage of the reaction centres at high light. The reversal of OCP-induced energy quenching (conversion of OCP^R back to OCP^O) depends on a second cytoplasmic protein, the fluorescence recovery protein (FRP), which binds to the OCP and weakens its association with the PBsome [110].

1.7.2 Photoprotection of PBsomes

The photoprotection of PBsomes to excess excitation energy remains poorly characterised. A study using single-molecule spectroscopy imaging on purified PBsomes from the red alga *P. cruentum* elucidated an energetic decoupling in PBsomes with respect to intense light (Figure 1-9)[37]. Strong green light was able to induce the fluorescence decrease of PBsomes and the fluorescence increase of the peripheral PE in the PBsome at the first stage of photobleaching. It indicated that excess photon energy can be dissipated from the peripheral PE in the PBsome to minimise the photodamage of RCs. This process may serve as a photoprotective mechanism ascribed to the PBsomes under strong light illumination. It is corroborated by high-light-induced reorganisation [111, 112] and photodegradation of PBsomes [113]. The photoprotective role of PE has also been characterised in marine cyanobacteria [114]. The chromophore variety and increasing abundance extend the absorbance spectrum and enhance the absorption capacity,

enabling the photosynthetic organisms to survive in various environments. The energetic decoupling of PBsomes occurred under high light indicates a novel physiological role of the chromophore variety: creating a multi-step photoprotection to effectively prevent photodamage of photosynthetic RCs in response to excess excitation energy [37].

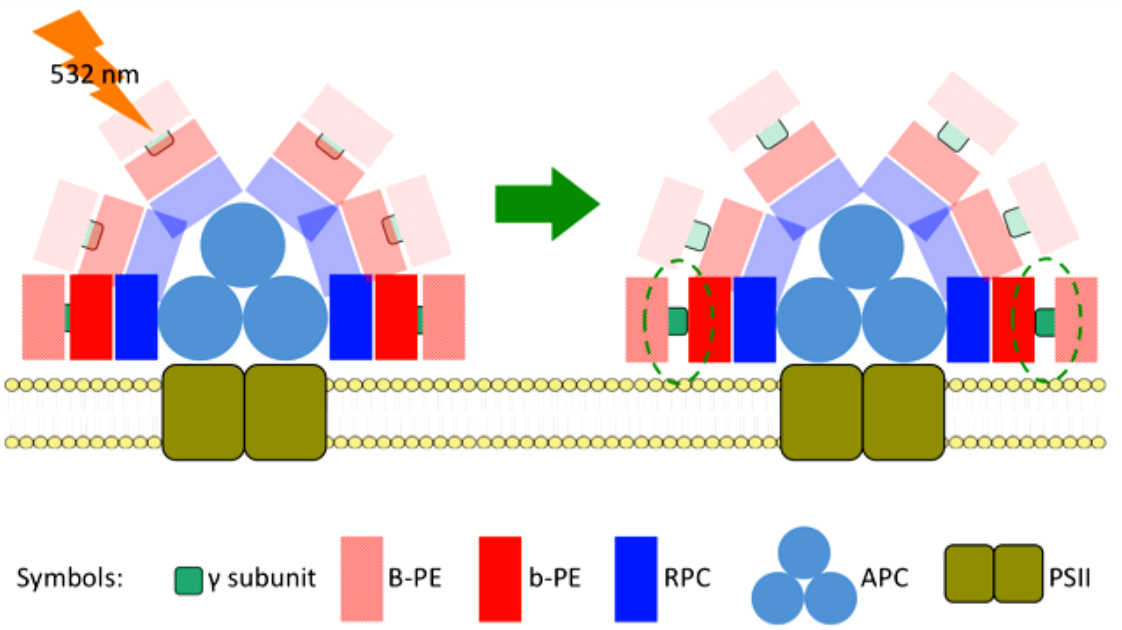

Figure 1-9 The photoprotection of Phycobilisomes. Schematic model of light-induced decoupling of PBsomes, indicating a possible photoprotective mechanism of the PBsome. Green open circles present the potential decoupling sites within the PBsome.

1.8 Cyanobacteria and the model organism *Synechococcus elongatus* PCC 7942 (previously known as Anacystis nidulans R2)

Cyanobacteria, formerly known as blue-green algae, are the oldest oxygenic phototrophs on Earth. Due to special structure and chemical composition of cell wall they belong to the class of gram-negative prokaryotes. They are a group of great structural diversity which include solitary and colonial unicellular, and filamentous species [115]. However, the cells of most cyanobacteria

have some distinctive features: bilayered wall and cell membrane, photosynthetic membranes knowns as thylakoid membranes (except for Gloeobacter, discussed below), photosynthetic electron chain, antenna complexes in an extrathylakoidal location (phycobilisomes), polyhedral organelles fixing CO_2 (carboxysome) (Figure 1-11) [116]. Detailed descriptions of cyanobacterial features such as vesicles, membrane structure and inclusion bodies are available in the literature [117-119]. The thylakoid membranes (TMs) are specialised membranes which harbour the photosynthetic apparatus. In cyanobacteria, they are structured in regular series of flat membranes, in contrast, complex organisation in granal stacks are typical of chloroplasts (Figure 1-10) [120].

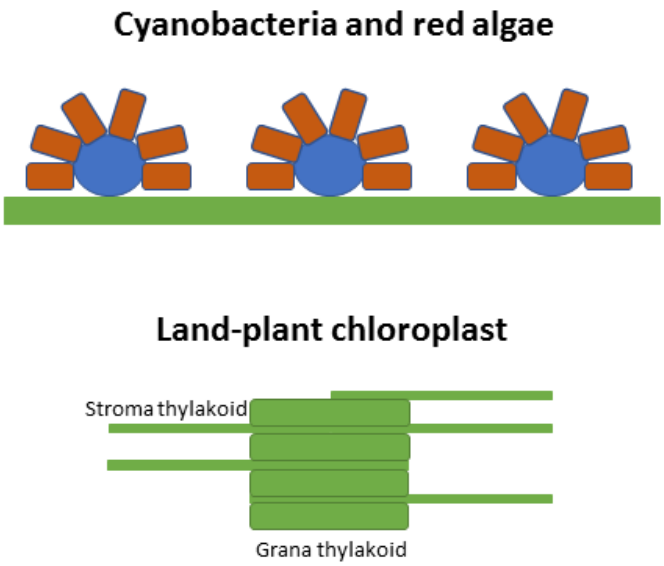

Figure 1-10 Schematic representation of thylakoid membranes in cyanobacteria and plants. On top a typical structure of cyanobacterial TMs (green) with no membrane stacking and the presence of phycobilisomes in an extrathylakoidal location. PSI and PSII have an interspersed distribution. On the bottom the TMs (green) in plants arranged in grana stacks and stroma thylakoids. PSI and PSII are segregated in stroma thylakoids and grana thylakoids respectively and LHCII. Adapted from [120].

The presence of intracellular membrane system is one of the distinguishing features of all the photosynthetic organisms. The cyanobacterium Gloeobacter violaceus is the only cyanobacteria

performing oxygen photosynthesis lacking TMs, where both photosynthetic and respiratory apparatuses are located on the plasma membrane. However, the efficiency of energy conversion during photosynthesis is lower than regular cyanobacteria, highlighting the importance of TMs as the ideal environment for the photosynthetic energy transduction [121].

Cyanobacteria, on the contrary of purple and green bacteria, contain just a specific form of chlorophyll called chlorophyll *a* (*AChl*) in their photosynthetic pigment apparatus and perform oxygenic photosynthesis similarly to plants [116]. Cyanobacteria grow faster than plants [15] and can be cultivated in bioreactors in arid or unfarmable land which minimises the competition with food crops for future applications [122]. Importantly, cyanobacteria can take up extraneous DNA and incorporate it into the genome by homologous recombination [123], simplifying the mutation or deletion of specific genes. Conversely, no comparable methodology is available in higher plants. For these characteristics, cyanobacteria are excellent model systems and have been used to investigate biological issues that are more challenging in eukaryotes (e.g. photosynthetic light reaction, carbon fixation, circadian gene expression, acclimation to environmental stress). The most popular organisms among cyanobacteria are *Synechocystis* sp. PCC 6803 and *Synechococcus elongatus* sp. PCC 7942 (Syn7942) which provided stable protein complexes for structural investigations [46, 124]. Among all cyanobacterial species, Syn7942 is one of the preferred systems to study proteins dynamics (see section 1.9.1) because of its elongate cells and regular thylakoid membrane topology [125]. Its entire genome has been sequenced (US Department of Energy Joint Genome Institute: http://genome.jgi-psf.org/draft_microbes/synel/synel.home.html) and has strong similarities with the plant chloroplast [8]. The TMs in Syn7942 are symmetrically and equally spaced around the centre of the cell forming cylindrical-like structures (Figure 1-11). PSI and PSII are localised and interspersed in the TMs (Figure 1-11B) giving the characteristic green colour due to the chlorophyll pigment [126].

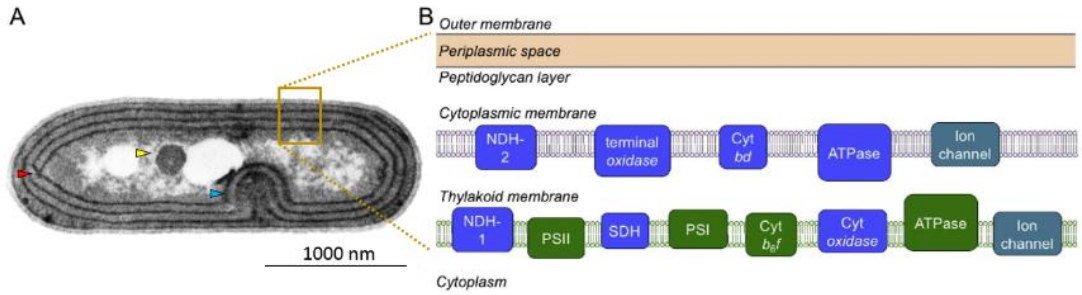

Figure 1-11 Structure and organisation of thylakoid membranes in Syn7942 cells. (A) Thin-section electron microscopy image of a wild-type *Synechococcus* 7942 cell. The distance between each TMs is around 68 nm. The red arrowhead indicates a common TM's perforation which permits the connection between the layers [118]. The yellow arrowhead shows a carboxysome, and the blue one shows a TM invagination. (B) Localization of the major components of cyanobacterial electron transport pathways. Represented in blue are the respiratory electron transport components, in green the photosynthetic complexes, although cytochromes have a role in both electron transport chains. Abbreviations: ATPase — ATP synthase, cyt *bd* — cytochrome *bd* oxidase, NDH-1 and -2 — type I and II NADPH dehydrogenase, terminal oxidase — cytochrome terminal oxidase [22, 127].

1.9 The theory behind the imaging techniques

1.9.1 The confocal fluorescence microscopy and the importance of FRAP

Fluorescence microscopy has become an essential tool in biology to observe structures and processes in fixed or living cells and tissues [128]. It makes use of fluorophores, molecules that can re-emit light (fluorescence) upon light excitation. Fluorophores can be naturally present in the photosynthetic complexes (such as Chl and PBsomes), or alternatively, the protein of interest can be labelled with a fluorescent tag (Green fluorescence protein and its derivatives [129], chemical tags [130]). A conventional fluorescence microscope (i.e. wild-field) is equipped with a light source that illuminates at the same time all the parts of the sample and a photosensitive camera which captures the resulting fluorescence to generate a micrograph. The fluorescence image, in this case, also includes a significant amount of unfocused background with a decrease of the achievable resolution and contrast for weak fluorescence signals or small

samples [131]. Improvements in optical resolution have been obtained with the invention of the confocal laser scanning microscopy (CLSM) which, due to the presence of a point illumination and a pinhole, receives signals just from a small section of the sample. The block of the out-of-focus light helps to obtain a better optical resolution than a wide-field microscope [132], which is optimal for imaging in cyanobacterial cells.

Together with the microscopy, the fluorescence imaging methods have been developed and improved to visualise better the localisation of proteins, to quantify their abundance, to assess their dynamic properties and to analyse their interactions in living cells. Imaging methods commonly used include fluorescence correlation spectroscopy (FCS) [133], fluorescence resonance energy transfer (FRET) [134] and fluorescence recovery after photobleaching (FRAP) [135]. FCS is a single molecule-based analysis used to assess molecular movements within single cells. This technology involves monitoring signals emitted from single fluorescent molecules to quantify protein concentration, complex formation and molecular diffusion rates [136, 137]. FRET is another fluorescence microscopy method which studies the protein-protein interactions. In a typical experiment, two proteins of interest are tagged either with a donor or an acceptor fluorophore. When the proteins are interacting, upon excitation of the donor, energy is transferred to the acceptor which will emit photons [138].

FRAP is a well-established technique to examine the mobility of molecules in either cytoplasm or membranes [139]. Due to its relative simplicity, it will be the approach used to probe the dynamics of cyanobacterial photosynthetic membranes in the next chapters. FRAP exploits the property of a fluorophore (e.g. GFP) to be photobleached (i.e. permanently unable to fluoresce) if overexcited by an intense light source (laser). This technique consists of a first phase where an intense laser bleaches a small area of the cell. In the second phase, if the fluorescent-tagged protein is mobile, the pool of still fluorescent molecules will migrate in the bleached area, and all or part of the bleached molecules will move out. These rearrangements will lead to a recovery of the fluorescence signal over the time in the bleached area.

The movement of a protein through a medium is considered as a diffusive phenomenon and is described by the **Fick's laws** of diffusion. The first Fick's law postulates that the flux of particles (J) is proportional to the concentration gradient ($\frac{dC}{dx}$).

$J=-D\frac{dC}{dx}$

The flux is intended as the number of particles that passes per unit area and unit time [C/(m^2*s)]. The D value is the diffusion coefficient or diffusivity [m^2/s]. C is the fluorescence intensity. X is the position between two adjacent points along the cell, [m]. The parameter that characterises the fluorescence recovery is the diffusion coefficient. FRAP can, therefore, be used to identify changes in mobility due to binding between the fluorescent protein of interest and unknown (or unlabelled) binding partners [140].

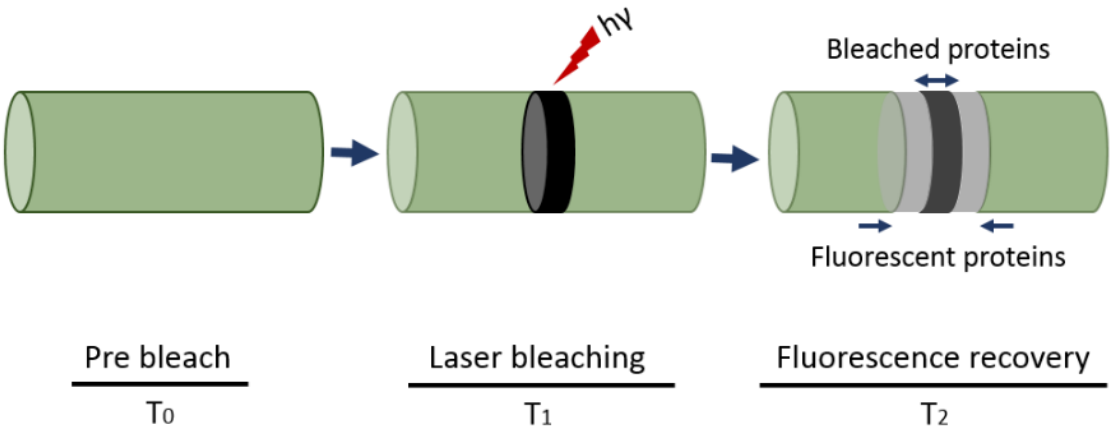

Figure 1-12 Fluorescence recovery after photobleaching. In the TMs of Syn7942, comparable to an elongated cylinder (T_0), a small region is bleached (T_1) by scanning a high-intensity laser (hγ). If the fluorescent proteins are mobile, they diffuse laterally together with the bleached proteins causing the bleached region to become broader and shallower with the time (T_2).

One of the fundamental requirements, to perform FRAP and obtain accurate diffusion coefficient values, is that the environment is uniform over the area of the measurement. In the case of photosynthetic transmembrane proteins, this means that the TMs must lack convoluted structures. By far the most regular TMs are found in Syn7942, which are TMs are symmetrically

and equally spaced around the centre of the cell forming cylindrical-like structures (Figure 1-11), thus designating Syn7942 as a suitable model to perform FRAP experiments (Figure 1-12) [20, 141]. In order to visualise the fluorescence recovery, a series of images are recorded before and after the bleaching, and the fluorescence plotted against the time (Figure 1-13). Then, D can be calculated by fitting the recovery curve with an appropriate equation, which considers the geometry of the system and the shape of the bleached area [142]. However, another approach to calculate D is available, which derives the estimated FRAP curve by a simulation and compare it with the experimental curve. The last method corrects the permanent loss of fluorophores during the bleaching phase (which cannot be neglected in small cells). Thus it is the most appropriate for application in little organisms such as the cyanobacterial cells.

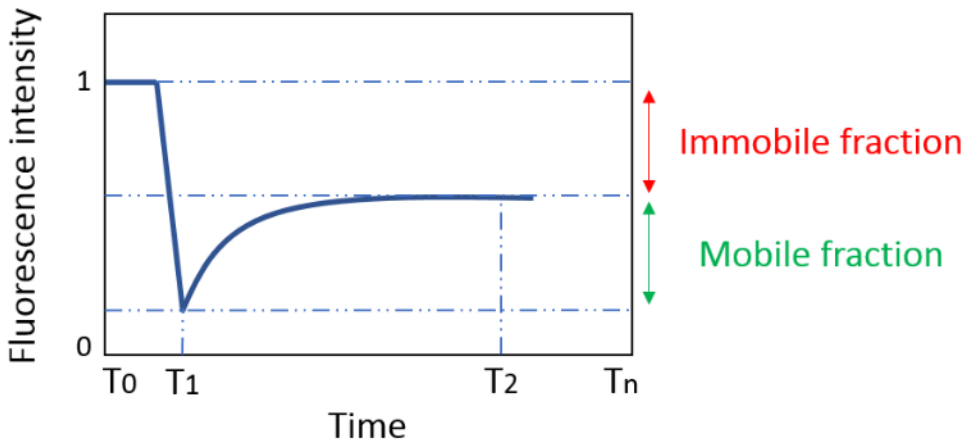

Figure 1-13 Quantification of fluorescence signal in a FRAP sequence. When a fluorescence area is bleached, its initial fluorescence (T_0) decreases (T_1). Due to the diffusion of the tagged proteins (mobile fraction), the fluorescence signal recovers over the time until it reaches a steady state (T_2). If some of the proteins are immobilised in the bleached area (immobile fraction), there will be an incomplete recovery (fluorescence in T_2 < fluorescence in T_0).

1.9.2 Total internal reflection fluorescence microscopy (TIRF)

Total internal reflection fluorescence microscopy (TIRF) microscopy provides a means to restrict the excitation and detection of fluorophores only near the thin region of cell membranes adherent to the glass surface (about 100 nm thick) while minimizing fluorescence from intracellular regions [143]. It does not only offer a higher signal-to-noise ratio and spatial

resolution compared to conventional confocal microscopy, but also allow for the visualisation of thylakoid membranes from only one side of the cell (with a bias to the outer membrane layers), which potentially facilitates the exploration of heterogeneous protein distribution in the membrane. In a brief description (Figure 1-14), TIRF uses an excitation laser beam to generate an evanescent wave and excite fluorophores in a restricted region of the sample (the one adjacent to the coverslip). The evanescent wave is obtained when the angle of the incident laser and the coverslip is greater than a specific value (the critical angle [143]). Due to the different physical properties of the glass (coverslip) and the water (sample), the incident waves travel along the interface between the two materials (a phenomenon called total internal reflection), rather than propagate into the sample. Therefore, only the fluorophores located in close proximity of the coverslip will be excited, and their fluorescence detected.

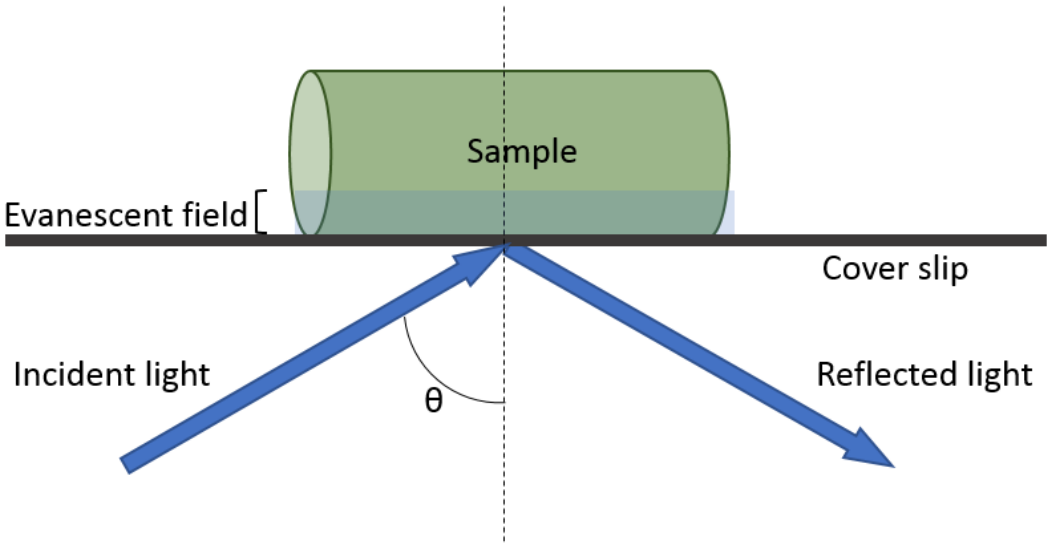

Figure 1-14 The physical basis of TIRF illumination. The excitation beam travels through the coverslip to the sample at an incident angle θ. The angle is measured from the normal. The excitation beam is then reflected by the cover slip-sample interface creating an evanescent field in the sample. Only fluorophores located in the evanescent field are excited.

1.9.3 Atomic force microscopy (AFM)

Membrane proteins (such as PSI, PSII, ATPase and Cyt b_6f) are extremely hydrophobic and are naturally inserted in a lipid bilayer. Traditional methods to study these proteins often impose the extraction from their membranes and detergent treatments to maintain the protein functionality. However, it is uncertain if these data accurately reflect the protein behaviours under native conditions. Atomic force microscopy (AFM) is a technique that allows the visualisation of membrane proteins under physiologically relevant conditions (embedded in the lipid bilayer and a buffer solution) which preserve their native properties [144].

AFM is a technique invented in 1986 [145], but just recently it has been used in the field of bioscience to analyse biological membranes. AFM provides high resolution images (in the order of one nanometer) and at the same time does not require elaborated sample preparation. Sample imaging can be performed in air or, in more physiological conditions, in a buffer solution [146].

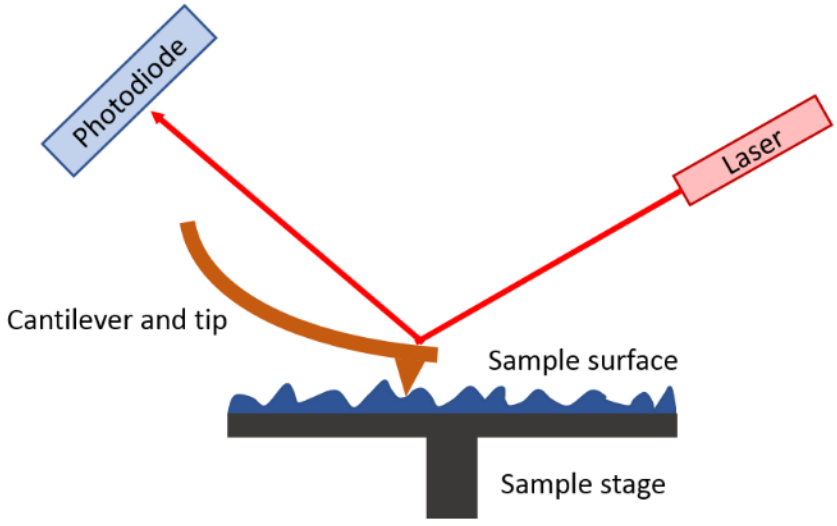

Figure 1-15 Main components of an atomic force microscope. Biological samples are immobilised on a solid substrate. While the tip scans the sample surface, the deflection of the laser is detected by a photodiode. The data are then collected to build a 3D image (see Figure 1-6, Figure 3-10).

A typical microscope consists in a fine probe, attached to a flexible cantilever, that mechanically scan the surface of the sample. As the tip approaches the surface, the cantilever will vertically and laterally deflect following the features of the surface. A laser beam reflecting on the cantilever is detected by a photodiode, and its changes in position are recorded. The recorded movements will be analysed and displayed as a topographic map to produce the final 3D image.

1.9.4 Transmission electron microscopy (TEM)

The transmission electron microscope (TEM) is a microscopy technique that illuminates the sample making use of a high voltage electron beam to produce a high resolution image. The electron beam is shone through a very thin sample which presents clear parts and other that scatters the electrons. The electron beam emerging from the sample is collected and magnified by an objective lens system [147]. TEM essentially operate on the same principle of the light microscopy with the advantage of a greater resolution due to the use of electrons (rather than photons) in the beam. Since the TEM works in vacuum, the water from the sample must be removed. To obtain thin-section electron micrographs, biological samples (e.g. cells, membranes, proteins) contain large quantities of water, so they often require a long process before the imaging (see section 2.7.9 for details). To avoid disruption due to the loss of water, the tissue is firstly preserved with different fixatives (formaldehyde and glutaraldehyde, osmium tetroxide). The tissue is then dehydrated (in alcohol or acetone) and embedded in a hard resin block [148]. Finally, the block is cut into thin sections of around 70 nm that can be studied under the electron beam to produce the image (Figure 1-11).

1.10 Aims

The adaptation of cyanobacteria to several ecosystems is due to appropriate coordination between photosynthesis and other metabolic pathways [149] in response to external stimuli. Fluctuating parameters of the environment include light quality and quantity, temperature and nutrient concentrations. Among the multiple mechanisms to regulate the photosynthetic pathway, the physical mobilisation of transmembrane proteins in the TMs is a common strategy (sections 1.5 and 1.6). The balance of photosynthetic outputs is fundamental for the physiology of the cell. Thus protein mobility must be a highly regulated and a necessary process to understand and control. *In vivo* visualisation of naturally fluorescent pigment-protein complexes has already provided some insights about phycobilisomes and PSII dynamics. However, limited information is available about non-fluorescence components since they require a fluorescent tag in a functional complex.

From here, this thesis aims to extend what is known of the (re)distribution and dynamics of the central photosynthetic transmembrane complexes (PSI, PSII, ATPase, Cyt b_6f) and the timescales on which they occur.

In order to achieve this aim the following objectives were defined and addressed in the respective section as follow:

- Determine the protein density of the transmembrane proteins of the TMs in native conditions and calculate the relative abundance of each photosynthetic complex (section 3.3 and 3.4.2);
- Construct fluorescence-tagged complexes that retain their function (sections 3.2.1, 3.2.2 and 3.2.3);

- Visualise the localisation of the complexes in standard growth conditions (30 °C and 50 µE/(m^2 *s)), and their redistribution in response to red light;
- Determine the photosynthetic complexes dynamic features in standard growth conditions and their adjustable diffusion in response to intense red light (section 0), reduced protein size, temperature increase and supramolecular alteration (section 5.2.3).

Chapter 2
Materials and Methods

2.1 Introduction

In this chapter, we will describe in detail all the techniques used for the construction of the fluorescence-tagged strains and the methods to collect information about Syn7942 cells physiology. The first sections (2.2 - 2.6) will introduce the cell biology and the molecular biology techniques used. Then, the optical techniques will be explained in section 2.7, and the data analysis is elucidated in section 2.8.

2.2 Bioinformatic analysis

All the crystal structures were retrieved from the Protein Data Bank (PDB), and were visualised using Pymol Molecular Graphics System, Version 1.2r3pre, Schrödinger, LLC. All the genes sequences for primers construction were deduced from KEGG database (http://www.genome.jp/kegg/). Clone manager and SnapGene were used for mapping and the construction of primers. Fiji software was used for image visualization and analysis [150]. Origin (OriginLab, Northampton, MA) was mainly used for data representation and Stats direct for statistical analysis. Routines in Matlab and Sigmaplot (see appendix C-D) were used to process FRAP data and obtain mobile fraction and diffusion coefficient values.

2.3 Reagents

All reagents were purchased from Sigma-Aldrich unless otherwise specified.

2.4 *E. coli* strains and growth conditions

The *E. coli* DH5α strain (Thermofisher Scientific) was used to amplify plasmid DNA before the DNA isolation procedure. The BW25113 strain [151] was used to perform insertion of double-stranded PCR products via the lambda red recombination system [152, 153].

E. coli cells were grown aerobically in either liquid or solid Luria-Bertani medium (LB) on an orbital shaker at 30 or 37 °C. Medium supplements were used where appropriate at the following final concentrations: ampicillin 100 µg·ml^{-1}, chloramphenicol 10 µg·ml^{-1}, apramycin 50 µg·ml^{-1}, spectinomycin 50 µg·ml^{-1} and arabinose 100 µM. Cell suspensions were supplemented with 15 % glycerol, frozen in liquid nitrogen and stored at -80 °C.

2.5 Cyanobacterial strains and growth conditions

Synechococcus elongatus PCC 7942 (Syn7942) strains were grown photoautotrophically in BG11 medium [154] at 30°C under constant white illumination (40-50 µE/(m^2*s)) and shaking. For growth on plates, the medium was supplemented with TES buffer pH 8.2 (22.9% w/w of $C_6H_{15}NO_6S$) and sodium thiosulphate (0.3% w/w of $Na_2S_2O_3$), then solidified by addition of 1.5% (w/v) agar. The eGFP mutants were cultured in the presence of 50 µg/mL of apramycin. The KO strain was cultured in the presence of spectinomycin (50 µg·ml^{-1}). Strains on plates were transferred to new ones every 2-4 weeks.

Table 2.1 Cyanobacterial strains produced in this work

#	Strain name	Description	Antibiotic resistance
1	**WT**	PCC 7942 wild-type strain	none
2	**PsaE:eGFP**	WT strain in which a C-terminal GFP tag was added to the *1322* gene, part of the PSI complex	apramycin

3	**CP47:eGFP**	WT strain in which a C-terminal GFP tag was added to the *0697* gene, part of the PSII complex	apramycin
4	**Atpβ:eGFP**	WT strain in which a C-terminal GFP tag was added to the *2315* gene, part of the ATPase complex	apramycin
5	**Atpε:eGFP**	WT strain in which a C-terminal GFP tag was added to the *2316* gene, part of the ATPase complex	apramycin
6	**Atpγ:eGFP**	WT strain in which a C-terminal GFP tag was added to the *0337* gene, part of the ATPase complex	apramycin
7	**Subf:eGFP**	WT strain in which a C-terminal GFP tag was added to the *1231* gene, part of the Cyt b_6f complex	apramycin
8	**CP47:eGFP/ΔPsaL**	CP47:eGFP strain in which the gene 2342 was disrupted and substituted by a spectinomycin-resistance cassette	Apramycin, spectinomycin
9	**PsaE:eGFP/ΔPsaL**	PsaE:eGFP strain in which the gene 2342 was disrupted and substituted by a spectinomycin-resistance cassette	Apramycin, spectinomycin
10	**Atpβ:eGFP/ΔPsaL**	Atpβ:eGFP strain in which the gene 2342 was disrupted and substituted by a spectinomycin-resistance cassette	Apramycin, spectinomycin
11	**Subf:eGFP/ΔPsaL**	Subf:eGFP strain in which the gene 2342 was disrupted and substituted by a spectinomycin-resistance cassette	Apramycin, spectinomycin

For long-term storage cell suspension were supplemented with 8 % DMSO, frozen in liquid nitrogen and kept at -80 °C. The derivative strains produced in this study are listed in Table 2.1.

2.6 Molecular biology

2.6.1 Generation of plasmid constructs and recombinant DNA techniques

The production of GFP fusion genes and the KO were made through the λ RED recombination system as previously done [155]. This method uses a plasmid (pIJ790) contained in *E. coli* BW25113 [156] that encodes for three enzymes under the control of an inducible arabinose promoter.

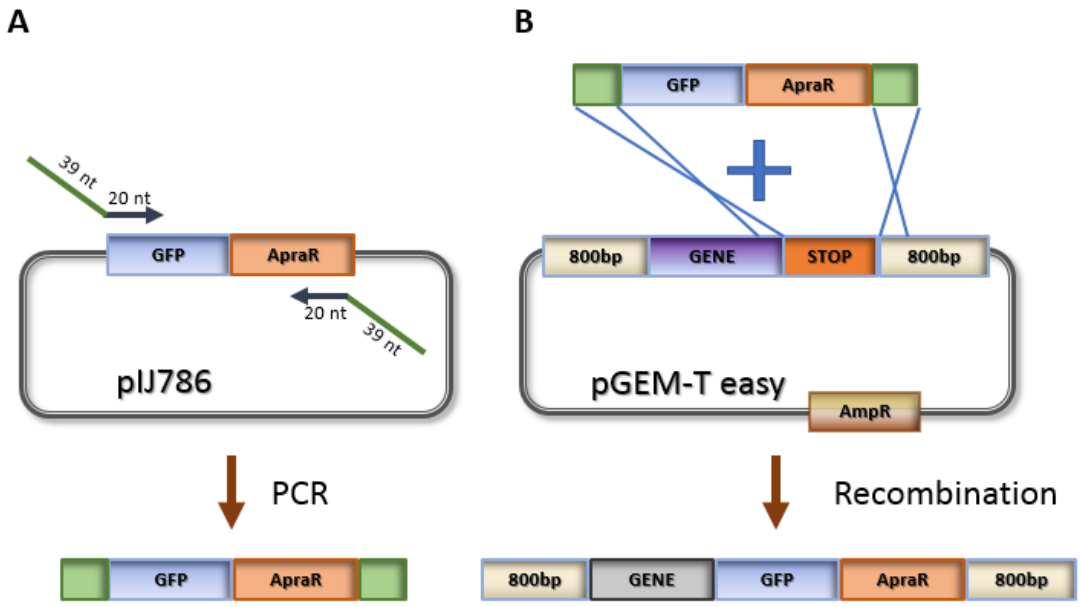

Figure 2-1 GFP mutant construction strategy. (A) Amplification of the GFP cassette with 39 bp of homology before and after the stop codon of the gene. (B) Overview of the recombination mediated by the Lambda Red recombination system. The amplified GFP cassette replace the stop codon of the gene.

These enzymes enhance the homology-dependent recombination events occurring between DNA filaments that share 50 bp of homology [157, 158]. The primer design to perform this technique is made as follow.

The GFP cassette primers will amplify the region containing the GFP and the apramycin resistance on the pIJ786 plasmid. GFP cassette primers are also designed to have 39 bp of homology before (forward primer) and after (reverse primer) the stop codon of the gene to tag (Figure 2-1A). The PCR product obtained will be able to replace the STOP codon, of the gene, with the GFP coding sequence (Figure 2-1B). The STOP codon of the GFP will be situated just after the GFP sequence without interruptions. In order to produce in-frame deletion to remove the whole gene, the spectinomycin cassette will contain homology with the initial and the final sequence of the gene.

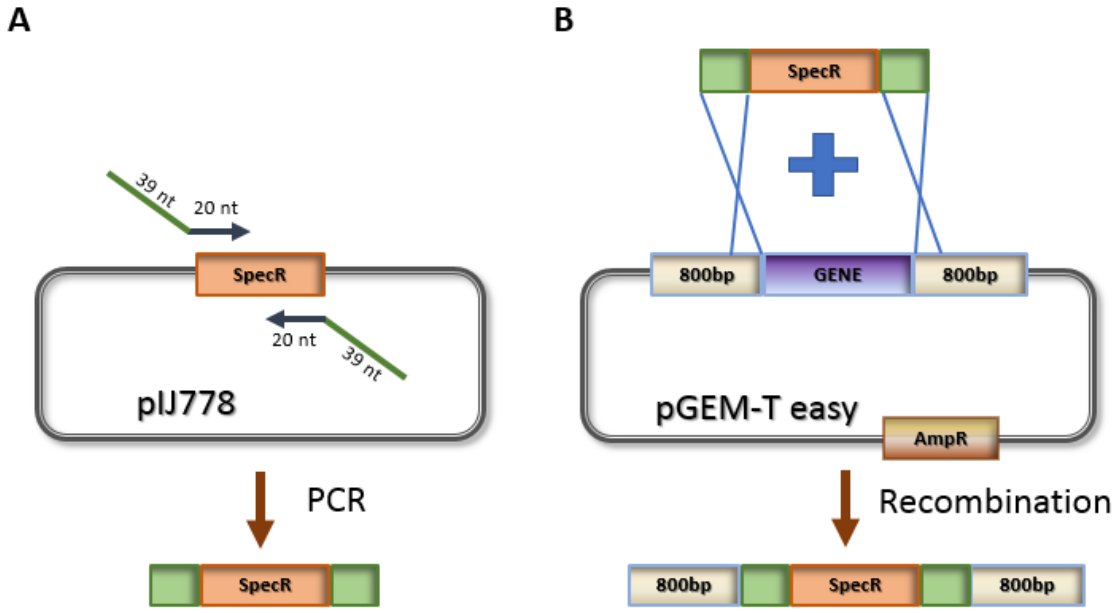

Figure 2-2 KO mutant construction strategy. (A) Amplification of the spectinomycin resistance with 39 bp of homology before and after the sequence of the gene. (B) The recombination mediated by the Lambda Red recombination system replaces the sequence of the gene with the amplified KO cassette.

In particular, the forward primer will contain the 36bp before start +3 bp start codon of the gene sequence; the reverse primer will have 36bp after stop +3 bp stop codon of the gene sequence (Figure 2-2). The whole process consists of two PCR steps. In the first step, a fragment containing the gene of interest and 800-1000 bp flanking sequence is amplified and inserted in the pGEM-T easy vector. With the second PCR, GFP or spectinomycin cassette are amplified. The resulting fragment is inserted in the *E. coli* host. BW25113 contains the pGEM-T easy vector previously made and a second plasmid (pIJ790) which in the presence of arabinose promotes a double crossing-over between overlapping sequences. In the case of the GFP tag, the GFP cassette will replace the STOP codon of the gene in order to produce a fused protein-GFP. In the case of KO, the spectinomycin will replace the entire gene of interest [152, 153]. The final plasmids obtained were verified by PCR and sequencing and used to transform Synechococcus cells following the method described earlier [159] (Figure 2-3**Error! Reference source not found.**).

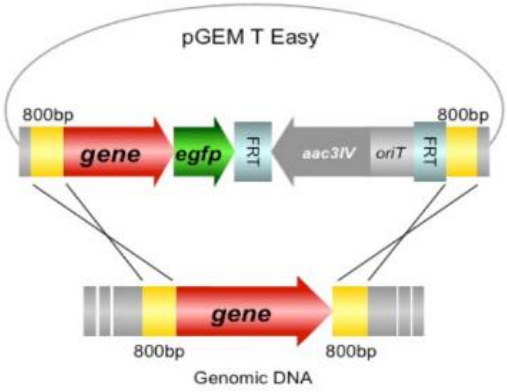

Figure 2-3 Natural transformation of Syn7942. The grey dashed lines show the site of homologous recombination between pGEM T-Easy and the Syn7942 DNA fragment with the gene. Blue arrows show the binding site of segregation primers. When the strains are fully segregated, the FRT sequences can be used to excise the antibiotic resistance cassette.

The capability of Syn7942 of natural transformation and homologous recombination was exploited to produce genetic substitution. It is known that Syn7942 is oligoploid, which implies the presence of 3-4 genome copies per cell [160]. Usually, just few gene replacements happen during the 1st recombination event, so further antibiotic selections in plate are needed to obtain full segregation of the gene replacement [123]. The segregation process is the time needed under antibiotic selection to obtain the replacement of all the WT genes with the fragment of interest. The efficacy of the recombination between the plasmid and the genomic DNA (gene

replacement) and the full segregation in Syn7942 was confirmed by PCR. Candidate colonies were screened by colony PCR with primers that flanked the recombination sites (segregation PCR).

2.6.2 Vectors and recombinant plasmids

The vectors used in this work are listed in Table 2.2. The pGEM-T easy vector was used to clone the gene of interest then transferred in the *E. coli* DH5α to produce a high copy number of the plasmid. The pIJ786 plasmid is used as template to amplify the GFP cassette which will take the place of the STOP codon of the gene. The pIJ778 plasmid is employed to amplify the spectinomycin cassette that will replace the target genes to produce knockout strains. The pIJ790 plasmid increases the recombination events occurring between double strands of DNA sharing 50 bp of homology.

Table 2.2 *E. coli* vectors used in this work

Vector	Purpose	Antibiotic-resistance cassette
pGEM-T easy	cloning	ampicillin
pIJ786	Amplify GFP cassette	apramycin
pIJ778	Amplify spectinomycin cassette	spectinomycin
pIJ790	Expression of homologous recombination systems	chloramphenicol

2.6.3 DNA transformation of cells

2.6.3.1 Preparation of chemically competent *E. coli* DH5α cells

A single *E. coli* colony was inoculated into a 10 mL liquid LB medium and incubated overnight (o.n.) at 37 °C. In the following day, 100 µL of the culture was inoculated in 40 mL liquid LB medium and was shaken at 37 °C for 3-3.5 h, until they reached an optical density at 700 nm (OD_{700}) between 0.5 and 0.6 (exponential growth). The cell suspension was then pelleted by centrifugation (4500 *g*, 4 °C, 3 min), suspended in 5 mL $MgCl_2$ solution (100mM) and kept in ice for 5 min. The cell suspension was centrifuged again (4500 *g*, 4 °C, 3 min), the pellet resuspended in 1 mL $CaCl_2$ solution (100 mM) and stored in ice for 30 min. Cells were now ready to be used in the transformation step or frozen in liquid nitrogen for future use [161].

2.6.3.2 Transformation of chemically competent *E. coli* DH5α cells (heat shock)

Ten µL of DNA (from a ligation mixture) were added to 100 µL of chemically competent *E. coli* cells and incubated in ice for 30 min. The cells were heated shocked for 2 min at 42 °C then placed in ice for 2 min. One mL of liquid LB medium was added to the mixture and shaken at 37 °C for at least 1.5 h. Afterwards, 200 µL of the mixture was plated on LB agar plates supplemented with ampicillin selection, Isopropyl β-D-1-thiogalactopyranoside (IPTG) and 5-bromo-4-chloro-3-indolyl-β-D-galactopyranoside (X-Gal). The plates were incubated overnight together with a negative control. The following day after a blue/white screening, only the white colonies were PCR tested for the presence of the plasmid and the pGEM plasmid will be extracted from the positive colonies.

2.6.3.3 Preparation of competent BW25113 *E. coli* cells for first electroporation

A single *E. coli* colony was inoculated into a 10 mL liquid LB medium and incubated overnight at 30 °C. In the following day, 100 µL of the culture was inoculated in 30 mL liquid LB medium

supplemented with chloramphenicol and shaken at 30 °C for 3-3.5 h, until they reached OD_{700} between 0.5 and 0.6 (exponential growth). The cell suspension was then pelleted by centrifugation (4500 *g*, 4 °C, 3 min), and resuspended in 2 mL of 10 % ice cold glycerol. This last step was repeated 3 times to remove the ions from the solution. Afterwards, the pellet was suspended in 100 µL of 10 % glycerol and placed in ice for 10 min.

2.6.3.4 Transformation of competent *E. coli* BW25113 cells (first electroporation)

Fifty µL of competent cells were mixed with 5 µL of pGEM plasmid containing the gene of interest and placed into a pre-cooled 2 mm gap electroporation cuvette. The electroporation was performed in 4.8-5 ms, with a Biorad electroporation system (Biorad Gene Pulser equipped with a pulser controller and a capacitance extender module), setting the following parameters: 2500 V, 25 µF of capacitance, 200 Ω of resistance. Then the mixture was added to 1 mL of liquid LB and incubated for more than 1 h at 30°C degree to give time for a new generation of *E. coli*. The suspension was spun down (13,000 rpm, 1 min), resuspended in 100 µL of LB media, spread onto a plate with ampicillin and chloramphenicol selection and incubated overnight at 30°C. The next day the largest colonies were tested with PCR for the presence of the pGEM plasmid.

2.6.3.5 Preparation of competent BW25113 *E. coli* cells with pIJ790 plasmids

Competent cells were prepared from the BW25113 *E. coli* strain derived from the first electroporation. The cells were grown in 10 mL of liquid LB, supplemented with chloramphenicol and ampicillin, overnight at 30 °C. The next day 100 µL of BW25113 cell suspension was inoculated in 10 ml of liquid LB supplemented with antibiotics and arabinose (0.02 M), which can stimulate the gene ExoGambet essential for the recombination process. When the cell suspension reached OD_{700} between 0.5 and 0.6, 30 µL of cell suspension was collected (5,000 rpm, 2 min, 4 °C), washed in 10% glycerol and resuspended in 100 µL of 10% glycerol. Then the competent cells were ready for the second electroporation step.

2.6.3.6 Transformation of competent BW25113 *E. coli* cells with pIJ790 plasmids (second electroporation)

50 µL of competent cells were mixed with 10 µL of redirect products (see paragraph 2.6.6.1) in a pre-cooled 2 mm gap electroporation cuvette. The second electroporation process was performed as described earlier in section 2.6.3.4. However, this time soon after the electrical pulse, liquid LB supplemented with 0.2 M of arabinose was added to the cells. Then the cell suspension was shaken for at least 2 h to allow the recombination between the gene in the pGEM plasmid and the double strand of DNA containing either the GFP cassette or just the spectinomycin resistance cassette. The next day the largest colonies were screened with PCR for the presence of the GFP/ KO cassette in the pGEM plasmid.

2.6.4 Transformation of Syn7942 strains

S. elongatus was transformed with the recombinant plasmid DNA according to the method described earlier [162]. Syn7942 cells were grown in 50 mL of BG-11 and harvested in exponential growth phase by centrifugation (5,000 *g,* 30 °C, 10 min). The pellet was washed 3 times with fresh BG-11 and finally resuspended in 1-2 mL of BG-11. Successively, 40 µL of recombinant plasmid was added to 100 µL of cells and incubated for 24 h at 30 °C under illumination. The following day the transformation mix was spread in BG-11 agar plates supplemented with the appropriate antibiotic. The resistant colonies appeared after 2-3 weeks, then were transferred at least three times in a new BG-11 plate to allow the complete replacement of the WT genes through natural recombination.

2.6.5 Extraction and purification of DNA

Plasmid preparation from *E. coli* cells was carried out using the GeneJET Plasmid Miniprep kit (Fisher Scientific UK Ltd) according to the manufacturer's instructions. Purifications of DNA fragments from 1 % agarose gels were performed with a GeneJET Gel Extraction Kit (Fisher

Scientific UK Ltd) following the manufacturer's instruction. Genomic DNA from *S. elongatus* was extracted with PureLink Genomic DNA Mini Kit (Fisher Scientific UK Ltd) by the protocol provided. The concentration and quality of the DNA were evaluated with a Nanodrop ND-100 Spectrophotometer at a wavelength of 260 nm (A_{260}). The presence of contaminations was determined by measuring the A_{260}/A_{280} ratio, where values lower than 1.8 were indicating the presence of contaminants from the extraction process. The DNA solutions were then stored at -20 °C.

2.6.6 DNA manipulations

2.6.6.1 Amplification of DNA fragments by polymerase chain reaction (PCR)

In order to find the optimum amplification of the gene of interest, a gradient PCR program was used. It was consistent in an initial denaturing step at 94 °C (2 min), then 15 cycles of melting, annealing and elongation steps respectively at 94 °C (45 s), from 48 to 65 °C (45 s) and 72 °C (4 min). To amplify the GFP and spectinomycin cassette, and also to verify the segregation of the new Syn7942 strains a Redirect PCR program was used (calling Redirect product the DNA obtained). It had an initial denaturing step at 94 °C (2 min), then 30 cycles of 94 °C (45 s), 50/55 °C (45 s), 72 °C (1 min). In the case of screening of whole Syn7942 cells, the initial denaturing step at 94 °C was extended to 10 min. The DNA oligonucleotides used in this work are shown in Table 2.3.

Table 2.3 Oligonucleotide primers used in this work. All nucleotide primers used were purchased from Eurofins Genomics. Primers 1, 2, 7, 8, 13, 14, 19, 20, 25 and 26 were used to amplify the gene of interest. Primers 3, 4, 9, 10, 15, 16, 21 and 22 were used to amplify the GFP cassette. Primers 27 and 28 were used to amplify the spectinomycin cassette. Primers with the suffix *–seg* were used to test the full segregation of the new cyanobacterial strains.

#	Primer		Sequence
1	PSI	FpsaE	CGAGGTAGCGCGACAGATAG
2		RpsaE	GCCATAGACCCACGCTTGAC
3		RFpsaEGFP	GAAGCAGAATTACAAGTGGTTGCAGCAGCCGCCAAAAAACTGCCGGGCCCG GAGCTGCC
4		RRpsaEGFP	GTAGCCGTTTCAGGAACCTCTTGTGAAGACAGAAGCAGTATTCCGGGGATC CGTCGACC
5		FpsaEseg	CGCGTGGTGATAAGGTTCGG
6		RpsaEseg	GAGTAAGACTTCGCCACCTG
7	PSII	FCP47	CTACAAAGCGCTGCGGATGG
8		RCP47	AATCCCGCACGCCTCGAAAC
9		RFCP47GFP	CAGAAATTGGGTGACCCGACCACTCGGAAAACAGCCGCTCTGCCGGGCCCG GAGCTGCC
10		RRCP47GFP	GAATGAGCATCACCCAAACCGCTCTAACCATTCACAACCATTCCGGGGATCC GTCGACC
11		FCP47seg	GCGTGGCTGGTTCACCTTTG
12		RCP47seg	GCTGTAGGCCAGTTGTAGCG
13	Cyt b_6f	FpetA	GTTTGGGCAACTCTATCTGG
14		RpetA	CCTGCACTAAAGCTCACTAC
15		RFpetAGFP	AAACAAGTCGAGAAAGTGCAAGCTGCTGAGCTGAACTTCCTGCCGGGCCCG GAGCTGCC
16		RRpetAGFP	GGCCCGCCCTCTCTCTTGCAACCGTTACTGCAACCAGATATTCCGGGGATCC GTCGACC
17		FpetCseg	CGCTGACCAACGATCCGAAC
18		RpetCseg	GAGGCCATACCAACGGATGC

19	**ATPase sub β**	FatpB	GAAGCGGCTTGACGAATCAG
20		RatpB	TCTCCACCGATGAGTCCTAC
21		RFatpBGFP	GAAGCCATCGAAAAAGGCGCCAAGCTGAAAGCTGAATCCCTGCCGGGCCCG GAGCTGCC
22		RRatpBGFP	GCGGGGCTGCGATCGCAACCCCACCAAAGTCAGCCAAACATTCCGGGGATC CGTCGACC
23		FatpBseg	CCTTCTTCGTGGCTGAAGTG
24		RatpBseg	TGACCCGGCAAGATACCGAG
25	**ATPase sub ε**	FatpE	ACTCGAAAGTGGCCTTGGTC
26		RatpE	GATGCTGTGGCCATGATCGG
27		RFatpEGFP	CGGGCACGCTTGCAGGCTGCGGGTGGTCTAGTCAGCGTTCTGCCGGGCCCG GAGCTGCC
28		RRatpEGFP	GCGATCGCAGCCTCTGCAAACTTAAGAAGGCATTCAGGAATTCCGGGGATC CGTCGACC
29		FatpEseg	GTTGGTCAACGCTGCTGAAC
30		RatpEseg	CCAAGCCGAATCTTCCCAAC
31	**ATPase sub γ**	FatpG	CGGCAACGCTGCAATACCTG
32		RatpG	CTTCGACGTAGGCGACGTTC
33		RFatpGGFP	CTGCTGGAAGTTGTGGCTGGCGCCGAAGCGCTGAACGGCCTGCCGGGCCC GGAGCTGCC
34		RRatpGGFP	CCGAATTCACTCAAGCGCGGCCTCTGTTTCGGGAAGAACATTCCGGGGATCC GTCGACC
35		FatpGseg	AGTTGTTGCGGGCCTTGCAG
36		RatpGseg	AAGAGGCCGGCAGATCAACG
37	**PsaL**	FPsaL	ACTGTGGCCAAGCTAGTCTG
38		RPsaL	GAAGCGGTAATCACTCGCTG
39		RFPsaL	CTATCACTGCACTATTGTCCTATTCGGAGTTCTGCAATGATTCCGGGGATCCG TCGACC

40		RRPsaL	CTTGTAAGGAACGAGGTGGAATTAATCAGATCGGACTTATGTAGGCTGGAG CTGCTTC
41		FPsaLseg	TCGCGTAGCAGCAGCACTTC
42		RPsaLseg	ACACCAGCATCCAGCCAGAG

2.6.6.2 DNA polymerase enzymes

The polymerases used in this study were the Q5 Hot Start High-Fidelity DNA polymerase (New England Biolabs) and the DreamTaq Green DNA Polymerase (Thermo Scientific). The DreamTaq polymerase was used for gradient PCR, routine screening of *E. coli* colonies and Syn7942 segregation. The Q5 hot start polymerase was employed to amplify DNA fragments for high fidelity cloning.

2.6.6.3 A-tailing

PCR products obtained by the high-fidelity polymerase are blunt double-stranded DNA molecules that require an A-tailing prior the cloning in a T-vector (such as pGEM-T easy vector). Clean-up of the amplified DNA was made on 1% agarose gel, cutting-out the gel band of interest and purifying the DNA with a gel extraction kit (GeneJET Gel Extraction Kit, Thermofisher). After the clean-up, a reaction with the following components was set up: PCR product, Dream Taq polymerase (0.2 µL), 10X DreamTaq buffer (5 µL), 1mM dATP (10 µL), DNAse free water, for a total reaction volume of 50 ul. The mixture was then incubated at 72 °C for 20 minutes and then used during the ligation progress.

2.6.6.4 Ligation

DNA fragments with 3´ terminal deoxyadenosines to both ends were inserted into pGEM-T Easy accordingly to the manufacturer's instructions (Promega). A reaction mixture was produced with

pGEM-T Easy vector (1 µL), 2X ligase buffer (5 µL), DNA product (3 µL), and T4 ligase (1 µL). Then it was incubated at R.T. overnight.

2.6.7 Analysis of Syn7942 strains

2.6.7.1 Spot assay

Cyanobacterial strains were inoculated in liquid BG11 medium and incubated with constant shaking at 30°C for 2-3 days. The cell cultures in logarithmic phase were then diluted to OD_{750} 0.2 and the drops allowed to dry for 15 min at room temperature inoculated in a BG11 plate. Afterwards, plates were incubated at 30 °C under constant illumination with white light at 50 µmol photons m^{-2} s^{-1} for approximately four days.

2.6.7.2 Crude Thylakoid membrane isolation

TMs preparation was done accordingly to Zhang et al. [163]. Syn7942 cells during the exponential phase were pelleted by centrifugation (4000 rpm, 8 min) from a 50 mL culture, washed twice with washing buffer (50 mM HEPES-NaOH, pH 7.5, and 30 mM $CaCl_2$) then concentrated in 300-400 µL of resuspension buffer (50 mM HEPES-NaOH, pH 7.5, 30 mM $CaCl_2$, 800 mM sorbitol, 1 mM Aminocaproic acid) with the addition of 3 µL DNase (Promega) and 5 µL protease inhibitors. Cells were disrupted with four cycles of 1 min with a Mini-bead beater, after the addition of 400 µg of glass beads (212-300 µm, 50-70 U.S. sieve) under constant refrigeration.

Glass beads and unbroken cells were removed by low-speed centrifugation (3000 *g*, 5 min) and the supernatant collected in a new tube. The TM-rich supernatant was further centrifuged (14000 rpm, 1 h) to collect the broken membranes. The pellet was then resuspended in storage buffer (50 mM Tricin·NaOH, pH 7.5, 600 mM sucrose, 30 mM $CaCl_2$, 1 M glycine betaine) for chlorophyll measurements.

2.6.7.3 SDS-PAGE and immunoblot analysis

The TMs isolated were solubilised by the addition of SDS sample buffer (0.06 M TRIS HCl pH 6.8, 10% glycerol, 2% SDS, 0.1% bromophenol blue, 1.5% dithiothreitol) and heating at 95°C for 10 minutes. Proteins were separated by 12.5% denaturing SDS-PAGE and electrotransferred to PVDF membrane using a wet-electroblotting system (90 V, 45 min) in transfer buffer (glycine 0.29% w/w, TRIS 0.58% w/w, SDS 0.037% w/w, methanol 20% v/v). The PVDF membranes were washed in TBS buffer (20 mM TRIS HCl pH 7.5, 0.15 M NaCl,), washed twice in TTBS buffer (TBS with 0.1% tween 20) and incubated with blocking buffer (TBS with 5% [w/v] Marvel milk powder) overnight at 4°C. Subsequently, the membranes were incubated for 4 h at 4°C using the primary antibody diluted in blocking buffer (see Appendix A for antibodies type and concentrations). The membrane was then incubated for 1.5 h at 25°C with a secondary antibody. Finally, antibody-bound proteins were detected using the Clarity Western ECL substrate (Bio-Rad) and visualised by ImageQuant LAS 4000 (GE Life Sciences).

2.6.7.4 Blue Native Polyacrylamide Gel Electrophoresis (BN-PAGE)

Isolated TMs were washed with washing buffer (330 mM sorbitol, 50 mM BisTris pH 7.0), then resuspended in 50% resuspension buffer (see appendix B) and 50% of solubilization buffer (see appendix B), left on ice for 30 min to solubilise the membranes and release the protein complexes. After 15 min centrifuge (14000 rpm, 4°C) the supernatant was loaded with 1/10 loading buffer (0.5% servaG, 0.5 M 6-aminocaproic acid, 50 mM BisTris-HCl pH 7.0, 30% sucrose) and separated in 3-12% linear gradient blue native gel (Invitrogen, Native page) as previously done [163].

The samples were calibrated by *AChl* concentration for comparison (see section 2.7.1). The A*Chl* content was determined by extraction into methanol and absorption measurement taken at 666 and 750 nm as previously done [164].

GFP signal was detected through a luminescent image analyser (Image Quant 4000, GE Healthcare Life Science, excitation blue epi-RGB, filter detector for GFP). Samples were loaded with a final *AChl* concentration of 5 µg/mL. The BN-gel was also used for western blot analysis.

2.6.7.5 Oxygen evolution measurements

O_2 evolution measurements of cell cultures were performed in a 506 Clarke-type oxygen electrode (OxyLab 2; Hansatech). The temperature in the chamber was maintained at 30°C by a circulating water bath. Before measuring different samples, the electrode and membrane were calibrated accordingly to the manufacturer's instructions. The electrode chamber was filled with one millilitre of cell suspension at the *Chl* concentration of 20 µM (see section 2.7.1) and sealed from the atmosphere. After stabilization of the signal in the dark for 2 min, the oxygen consumption rate was recorded. Then, the cell suspension was exposed to saturating red light, and the value of oxygen production was recorded.

2.7 Optical techniques

2.7.1 Cell growth, absorption spectra and Chlorophyll *a* concentration

The growth of the cells was monitored by turbidity at 750 nm with a UV/Vis spectrophotometer (Jenway 6300, UK). Absorbance spectra of intact cells or TMs suspensions were carried out at room temperature with a microplate reader (SpectraMax 340, Molecular Devices, US) between the wavelengths of 400 nm and 750 nm. *AChl* content was determined by methanol extraction method), as previously described [164]. 5 µL of TMs in storage buffer (obtained as described in section 2.6.7.2) were added to 995 µL of methanol in a 1.5 mL Eppendorf tube. After 5 min, the suspension was centrifuged (2 min, max speed in a top bench centrifuge) and the pellet collected and poured in a cuvette. Absorption measurements were taken at 666 and 750 nm using a

UV/Vis Spectrophotometer (Jenway 6300, UK). *AChl* concentration (µg/mL) was calculated as shown in equation:

$$(OD_{666} - OD_{750})12.6 * 200$$

Where 12.6 is the A*Chl* molar extinction coefficient and 200 is the dilution factor.

2.7.2 Photosynthetic efficiency of Photosystem II (Quantum Yield)

The efficiency of PSII (QY) was measured in triplicate using 4 mL culture aliquots from biological replicates at exponential phase in cells dark adapted for three minutes as described previously [165] using an AquaPen-C fluorometer (Photon Systems Instruments, Brno, Czech Republic) with 620 nm excitation provided by a LED. Data were collected using the proprietary AquaPen-C software package. The QY in dark-adapted samples is calculated as follow:

$$QY = \frac{F_m - F_0}{F_m}$$

Where QY is the maximum quantum yield of PSII in dark-adapted state, Fm is the maximal fluorescence intensity of PSII in dark-adapted state, F_0 is the minimum fluorescence of PSII in dark-adapted state. The difference $F_m - F_0$ correspond to the maximal variable fluoresence (Fv) [166].

2.7.3 77K fluorescence spectroscopy

Cells were harvested during the exponential growth phase. Mutants and wild-type samples were adjusted to equal absorbance at 435 nm. Samples were dark adapted to state 2 and then transferred in a glass capillary (5 mm diameter) with one end sealed. The capillaries were frozen in a liquid nitrogen. Steady-state fluorescence emission spectra at 77 K were measured in the

intact cells as described previously [167, 168]. Data of emission spectra were recorded from 620 nm to 800 nm with excitation wavelength at 435 and 600 nm.

2.7.4 $P700^+$ Re-reduction Measurements

Cells were illuminated with 5 s pulses of red light (lmax=623nm; I = 2000 µmol/(m^2*s)) repeated at 30 s intervals. Then the changes in absorbance at 830 nm were recorded. Each curve represents the mean of 10 accumulations from each of 2 separate aliquots of cells. Curves were normalised to the absorbance of WT following illumination for 5 s. After correction of the baseline, data of emission spectra with excitation at 435 nm, were deconvoluted into plural components bands using the curve fitting tool in ORIGIN. Each band was assumed to have a Gaussian distribution [169-171].

2.7.5 Confocal Fluorescence microscopy

Cells grown on liquid BG11 media in exponential phase were immobilised on 1.5% agarose plates (w/v in BG11), letting them dry for 15 min. The agar was then cut and placed on a 0.17 mm coverslip. The temperature during all the experiments was kept constant at 30°C. Images were acquired on a Zeiss LSM710 or LSM780 inverted confocal microscope using an Argon laser at 488 nm as excitation wavelength, a 100x oil-immersion objective (1.45 N.A.) and 2 um pinhole. Images were captured using Zen 2010 and analysed using ImageJ. GFP and chlorophyll fluorescence were detected between 500-520 nm and 670-720 nm respectively. All images were captured with all pixels below saturation. Exposure to red light treatments was performed scanning the cells using a 633 nm laser at 5% power for 1.5 min; similar treatment was previously described by Sarcina et al. [172].

2.7.6 Total Internal Reflection Fluorescence (TIRF)

Samples immobilised in agar plates were imaged with TIRF illumination [173] in a Zeiss LSM880 providing laser excitation at 488 nm and 561 nm for GFP and chlorophyll respectively by a 100x oil objective lens (numerical aperture 1.46) with an additional 1.6x optovar magnifying lens in the emission lightpath. Fluorescence emission was imaged by an Evolve 512 Delta EMCCD Camera (Photometrics). GFP and chlorophyll fluorescence were detected between 510-555 nm and 581-679 nm respectively. The focal plane was set at 79 nm from the glass coverslip surface to image the TMs surface of the cyanobacterium. The incident angle of the laser was maintained at 68.3° ± 1.

2.7.7 Fluorescence recovery after photobleaching (FRAP)

The methodology used to carry out the FRAP experiments was set as follow. The cells of interest were positioned with its long axis in the Y direction. Then, a series of images were captured with a low power excitation laser before performing any bleach. The same setting was also used after the bleach. After the initial scanning, a small area, in the middle of the cell, was bleached using a 100 % laser power (488 nm or 633 nm laser) for 200 iterations. To follow the GFP diffusion a series of images were taken until the recovery (if present) in the bleached area reached a steady state (usually 90 s). A whole cell was bleached, and the fluorescence recorded during the 90 s to check the irreversible bleaching of the GFP. The frames stacks were aligned with ImageJ software.

2.7.8 Atomic force microscopy (AFM)

Membrane fractions previously prepared (Par. 2.6.7.2) were further purified in a step sucrose gradient (1.6 M, 1.4 M, 1.2 M, 1.0 M, 0.8 M) and centrifuged at 40,000 rpm in Beckman 70Ti for 1 hour at 4°C. Lower and upper bands were collected separately and stored in their sucrose

solution at 4°C to prepare the sample for AFM measurements. Then, the samples were diluted in adsorption buffer (10 mM Tris-HCl pH 7.2, 150 mM KCl, 25 mM MgCl2). Five µl of thylakoid membrane samples were adsorbed onto freshly cleaved mica surface with 40 µl of adsorption buffer at room temperature for more than 1 hour. After adsorption, the sample was carefully rinsed five times with imaging buffer (10 mM Tris-HCl pH 7.2, 150 mM KCl). AFM imaging [174] was performed in peak force tapping mode in liquid using a Bruker Multimode 8.0 equipped with a J-scanner with NanoScope V controller (Bruker, Santa Barbara, US). AFM tips with the spring constant of 0.4 N·m−1 (ScanAssyst Air HR, Bruker, Santa Barbara, US) were used for high-resolution imaging, and the tip spring constant was routinely calibrated. The average imaging force was ∼100 pN. The area occupied by the proteins, in the TMs, was calculated using the Masks function based on Gwyddion software (see appendix E).

2.7.9 Transmission electron microscopy (TEM)

Syn7942 cells were grown in liquid BG-11 medium until the culture reached an OD750 of 1. A 10-ml aliquot of the culture was harvested (4,000 *g*, 10 min, 4 °C) and the cell pellet rinsed three times with electron microscopy buffer (EM buffer; 0.05 M sodium cacodylate buffer pH = 7.2). Cells were fixed in 2% (v/v) glutaraldehyde and 2% (v/v) paraformaldehyde in EM buffer for 60 min. Cells were then post-fixed with 1% (v/v) osmium tetroxide for 1.5 h and dehydrated with a series of increasing alcohol concentrations (30%, 60%, 70%, 80% and 100%). After dehydration, the samples were embedded stepwise in Transmit EM resin (TAAB Laboratories Equipment, UK) (acetone/Transmit (1:1) for 20 min and acetone/Transmit (1:2) for 4 h). After the next 6 h incubation, the pure Transmit was changed three times. Subsequently, the samples were left to polymerise for 48 h at 70 °C. Thin sections of 70 nm were cut with a diamond knife (Diatome 45° ultra, Agar Scientific) and poststained with 4% uranyl acetate and 3% lead citrate. Images were recorded using an FEI Tecnai G2 Spirit BioTWIN transmission electron microscope.

2.8 Data analysis

2.8.1 Localization (standard deviation)

The uneven distribution of the photosynthetic complexes was quantified by extracting with Image J line profiles of fluorescence intensity along the thylakoid membranes (Figure 2-4). Then, the fluorescence standard deviation (SD) was calculated and normalised against the mean fluorescence intensity for each cell. SD values among different strains were used as an index of fluctuation of the signal; higher SD values correspond to a less uniform fluorescence distribution.

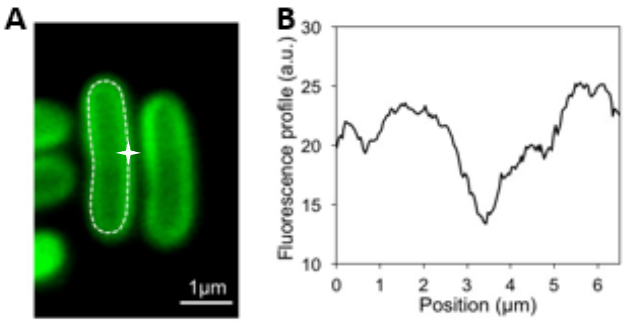

Figure 2-4 GFP fluorescence profile analysis of the distribution of photosynthetic complexes in the thylakoid membrane. (A) An example of GFP fluorescence profile of PSI:eGFP Syn7942 cells. (B) Normalized fluorescence profiles of the tracing lines in A starting clockwise from the white cross in A.

2.8.2 Stoichiometry analysis

For the stoichiometry calculations, the total GFP and chlorophyll fluorescence signals of a single cell were corrected by extracting fluorescence background, divided by its length and its chlorophyll intensity per length. The same procedure was applied for all the tagged photosynthetic complexes in at least three biological repeats, and the ATPase fluorescence was taken as a reference to obtain the fluorescence ratio.

2.8.3 FRAP data analysis

ImageJ was used to align the fluorescence images and extract the fluorescence profile along the Y-axis of the cell, the background and the non-bleached region values.

The mobile fraction (Mf) was determined by the formula:

$$Mf = \frac{\text{final fluorescence} - \text{post bleach fluorescence}}{\text{scaled pre bleach fluorescence} - \text{post bleach fluorescence}}$$

Then, in order to calculate the diffusion coefficient (D), the experimental fluorescence recovery curve underwent to a series of normalisations. Then the experimental recovery curve was compared with a simulated recovery curve to establish the diffusion coefficient value.

The assumptions taken into account for this calculations were as follow [175]:

- The bleached area is always the same size and shape, in the centre of the cell, perpendicular to long axes of the cell;
- The diffusion occurs just in 1D;
- The diffusion during the bleaching period is negligible;

More in details, the fluorescence signal along the long axis of the cell was collected, and the pixel values in the X direction were summed. All the fluorescence profiles were normalised against an unbleached cell of reference to minimise fluctuations due to the equipment (laser power) and to take into account the decreasing of fluorescence intensity due to each laser scan. Then, a background fluorescence intensity was subtracted from all the fluorescence profiles to decrease noise in the data collected. The total fluorescence before and after the bleaching was calculated by the sum of all the fluorescence values in each profile, then the difference between total pre and post-bleach fluorescence (scaled pre-bleach profile) was calculated to know the final total fluorescence intensity value assuming that all the GFP-fused proteins are mobile. Furthermore, the difference between pre-bleach and post-bleach profile (difference profile) versus cell length was plotted to find the minimum value (assumed as the centre of the bleaching

area in the x-axes). The fluorescence value at the centre of the bleached area was then recorded versus time to obtain the experimental fluorescence recovery curve.

At the same time, knowing the fluorescence profile just after bleaching and the final one, it was possible to predict the evolution of the fluorescence profile. For this purpose, an iterative computer routine running in SigmaPlot 10.0 (Jandel Scientific) was used (appendix D). A typical fluorescence profile evolution, for a mobile protein, during the time is illustrated in Figure 2-5.

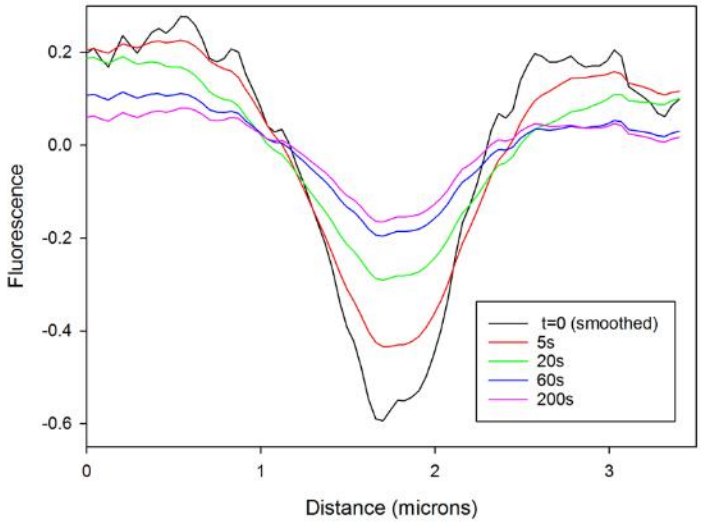

Figure 2-5 Evolution of the fluorescence difference profile during the time for mobile proteins. Once a small area across the cell is bleached, the fluorescence profile will evolve during the time reducing the depth and increasing the amplitude. This phenomenon is due to the movement of the transmembrane proteins along the thylakoids membranes. Representation kindly provided by Prof. Conrad Mullineaux (Queen Mary, London).

The routine takes the experimental difference bleaching profile and predicts how it will evolve in small time increments, according to the basic diffusion equation:

$$\frac{dC}{dt} = D\frac{\delta^2 C}{\delta X^2}$$

The routine estimates (δ^2 C)/(δX^2) at each time point. This value is then multiplied by a factor related to the diffusion coefficient and used to predict the increment in C at that point.

Where the mobile fraction is less than 1, the routine calculates the "mobile profile" and predicts how it will evolve. Once obtained a simulated fluorescence recovery (mobile profile), its diffusion coefficient was changed to fit with the experimental recovery curve. Once the overlay of the two curves was reached, the diffusion coefficient of the simulation was recorded.

Finally, the data were normalised by the average of each pre-bleach value obtaining all the pre-bleached values with a value of 100%.

Chapter 3

Spatial distribution and mobility of PSI, PSII, ATPase and Cyt b_6f in the cyanobacterial thylakoid membrane

3.1 Introduction

Remarkable macromolecular crowding and close protein-protein contacts within the cyanobacterial thylakoid membrane result in the dense packing of photosynthetic components [22, 176]. Cyanobacterial thylakoid membranes also act as the site that harbours the components of respiratory electron transport chains, comprising type-I NAD(P)H dehydrogenase-like complex (NDH-1), succinate dehydrogenase (SDH), Cyt oxidase and alternative oxidase [18-21]. The heterogeneity in the composition and localisation of photosynthetic proteins in cyanobacterial thylakoid membranes has been reported in previous studies using proteomics, immuno-electron microscopy and fluorescence microscopy based on their natural fluorescent properties [177-180]. By using hyperspectral confocal fluorescence microscopy, previous studies showed the physical segregation of photosynthetic complexes in the cyanobacterium Synechocystis sp. PCC 6803 (Synechocystis 6803): the enrichment of PSI in the inner thylakoid regions and the preferential localisation of phycobilisomes and PSII in the peripheral thylakoid layers [178, 179]. By contrast, results from immuno-electron microscopy indicated that the outer thylakoid layer of the cyanobacterium Synechococcus sp. PCC 7942 (Syn7942) contains mainly ATPase and PSI, whereas PSII and Cyt b_6f are located in both the outer and inner thylakoid layers [180]. Nevertheless, it appears that the cyanobacterial thylakoid membrane possesses confined regions that allow for the accommodation and coordination of different photosynthetic components. The lateral segregation of thylakoid membranes could be functionally imperative to the enhancement of photosynthetic performance.

The architecture of cyanobacterial thylakoid membranes is highly dynamic [181, 182], which is of paramount importance for the formation and maintenance of functional photosynthetic machinery involving de novo synthesis, turnover and repair of photosynthetic complexes, as well as crosstalk between components. Confocal fluorescence microscopy and FRAP have been previously performed to visualise the mobility of photosynthetic complexes in cyanobacterial thylakoid membranes [181]. The major supramolecular light-harvesting antenna, phycobilisomes, were shown to be mobile on the stromal surface of the thylakoid membrane [92]. It was further demonstrated that the phycobilisome mobility is required for state transitions [93] and non-photochemical quenching [94]. In contrast, the membrane-integral PSII complexes exhibit much restricted lateral mobility within the thylakoid membrane, as illustrated by tracking chlorophyll fluorescence [172]; whereas lipid molecules and the IsiA, another chlorophyll-binding membrane protein that is postulated to bind with photosystems and respond to iron deficiency, were determined to be mobile in the thylakoid membrane [183, 184]. It is conceivable that the protein organisation and specified membrane environment play essential roles in determining the diffusion dynamics of photosynthetic complexes in the thylakoid membrane.

Here, we present a direct observation of the native arrangement of photosynthetic complexes in isolated thylakoid membranes from the model cyanobacterium Syn7942, using high-resolution AFM. Then, we characterise the in vivo distribution and mobility fingerprints of these photosynthetic complexes in Syn7942 by live-cell TIRF microscopy imaging, confocal microscopy imaging and FRAP analysis.

3.2 Results

3.2.1 Selection of the fluorescence label sites

In our studies, the addition of the GFP cassette was preferred at the C-terminus of the protein. Tags at the N-terminal end are not recommended since in this region there are signal peptides important for the folding and the translocation of the proteins in the correct membrane system. Signal peptides in cyanobacteria are a positively charged sequence at the aminoterminal domain resembling an analogous sequence in chloroplast (named TLTD) [185].

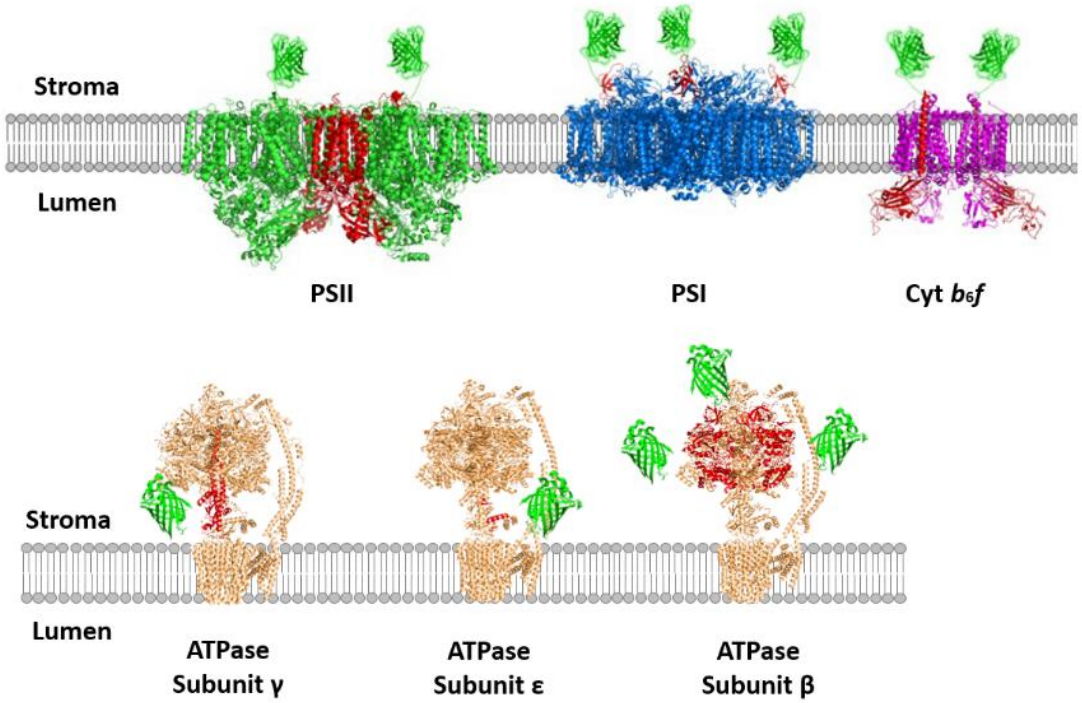

Figure 3-1 Fluorescence tagging of photosynthetic complexes in Syn7942. Localization of the GFP-tag to the C-terminus of targeted subunits in the four main photosynthetic complexes. The subunits chosen for tagging are CP47 (PsbB) of PSII (two copies per PSII dimer), PsaE of PSI (three copies per PSI trimer), Cyt f (PetA) of Cyt b_6f (two copies per Cyt b_6f dimer), the subunit γ (AtpG) of ATPase (one copy per ATPase), the subunit ε (AtpE) of ATPase (one copy per ATPase) and the subunit β (AtpB) of ATPase (three copies per ATPase). The GFP tags are exposed to the thylakoid stromal membrane surface.

Conserved protein sorting-mechanisms called Sec or Tat pathway transport proteins [186] can guide protein precursors to the TMs. Afterword, the membrane proteins are inserted by an SRP

pathway [187]. Signal peptides also have the function of retard the folding of proteins until they reach the right compartment. Thus, in our work GFP was fused to the C-terminus of selected protein subunits: PsaE for PSI, CP47 for PSII, Sub β, δ, ε for ATPase and Sub f for Cyt b_6f. We also positioned the GFP-tag on the stromal side of the TMs. According to a previous study [188], the stable integration of the membrane proteins in the TMs is more likely to occur when the tagged extremity of the peptide does not need to cross the membrane.

Finally, it is important to choose the correct subunit to label in order to minimise the perturbation of the system. A list of potential targets was made according to successful recombinant complexes [51, 189-197] and unsuccessful ones [155] found in the literature. Then, the 3D structure of the whole complex was examined to choose a subunit far from the main active site. Crystallographic information was retrieved from the PDB database (Table 3.1), and the resulting labelled complexes are illustrated in Figure 3-1.

Table 3.1 Codes of PDB database of the three-dimensional structures of the photosynthetic complexes. The protein structures were achieved from PDB database. Structures from other organisms were used when not available from Syn7942.

Complex	PDB ID	Organism	Reference
PSI	1JB0 2.5 (Å)	Syn7942	[198]
PSII	1W5C 3.2 (Å) 5KAF 3.0 (Å) in dark state	Thermosynechococcus elongatus	[199] [200]
ATPase	5LQX (7.9 Å)	Pichia angusta	[201]
Cyt b_6f	2ZT9 (3.0 Å)	Nostoc sp. PCC 7120	[202]

3.2.1.1 PCR evaluation of genetic substitution in Syn7942

GFP-tagged mutants were produced exploiting the natural transformation capability of the Syn7942 cells. The gene of interest, together with the GFP sequence and a selectable marker (apramycin), was inserted in a donor plasmid, which contains around 1000 bp of flanking

sequence overlapping with the recipient chromosome of Syn7942 cells. The donor plasmid was incubated with the WT cells, without further treatment. This procedure promoted the replacement of the WT gene with the DNA sequence present in the donor plasmid.

Due to the polyploidy of cyanobacteria genome (Syn7942 strain contains 3-4 chromosome copies per cell), extra care was taken to check the segregation of the mutations. Typically, the gene replacement during the transformation step occurs in one of the chromosome copies. Apramycin-resistant transformants were grown through several generations until homozygous mutants were obtained [16]. The efficacy of the recombination between the plasmid and the genomic DNA and the full segregation in Syn7942 has been confirmed by PCR (Figure 3-2) using GFP segregation primers (see Table 2.3).

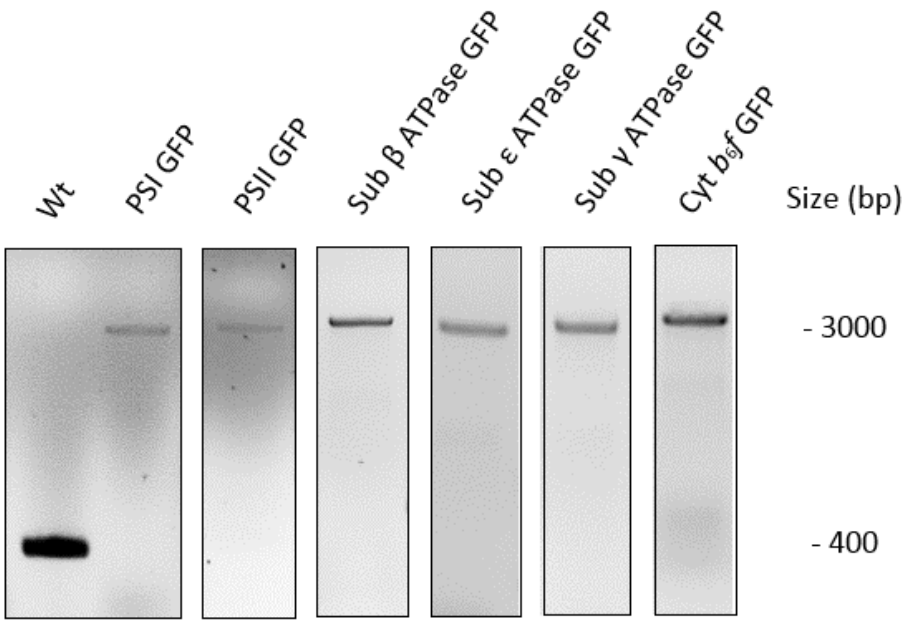

Figure 3-2 PCR verification of the full segregation of the mutants. Evaluation of the GFP fusion strains by segregation PCR (GFP segregation primers are listed in Table 2.3). All primer pairs have been tested on both WT and mutant DNA. The first line on the left shows the fragment amplified from using the PSI GFP segregation primers. The following lines show PSI:eGFP, PSII:eGFP, Cyt b_6f:eGFP, sub γ ATPase:eGFP, sub β ATPase:eGFP and sub ε ATPase:eGFP full segregated into the Syn7942 genome (see appendix F for original gels).

According to the primer design, a fragment with the size of 380 bp is expected for the WT genes. The fragment with the size of 3000 bp, if present alone, is an index of the successful substitution of all the WT gene copies with the GFP fusion gene. In the case of partial segregation, both bands (380 bp and 3000 bp) will be amplified at the same time. Once the GFP-tagged cells were obtained, we verified that the GFP could be usefully used as reporter gene without significant effects on the cell physiology. For this purpose, a series of tests were performed by comparing the GFP-tagged strains and the WT strain. Specifically, physiological and characterisation of the strains were carried out to quantify the pigments, structure and activity of the complexes.

3.2.2 Biochemical and structural integrity

The compositions of thylakoid membrane proteins from WT and GFP-tagged strains were separated using either SDS-PAGE or linear gradient BN-PAGE.

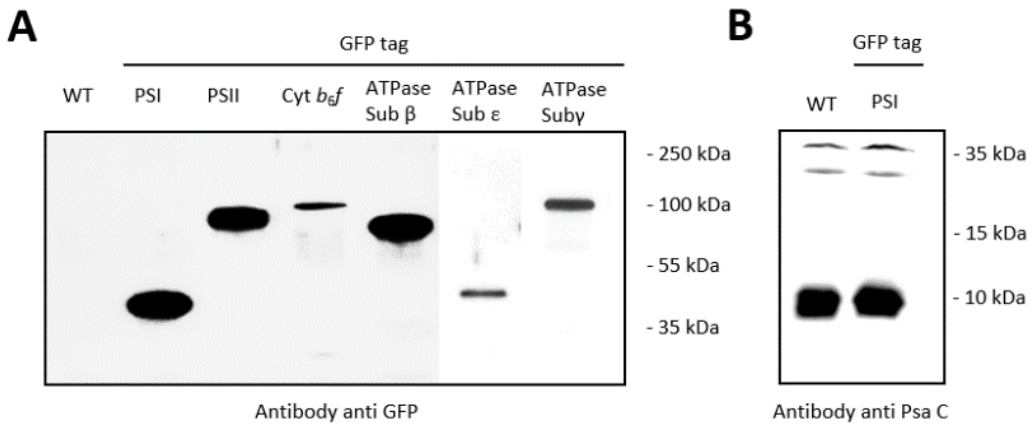

Figure 3-3 Characterization of the GFP fusion mutants with SDS page and immunoblot analysis. (A) Immunoblot on SDS-PAGE using anti-GFP antibody indicating the band size predicted for each eGFP-tagged subunit (detailed MW shown in Table 3.2). (B) Immunoblot with anti-Psa C (subunit of the PSI complex) antibody. The bands at 10 kDa show similar intensity proving a comparable expression level of the PSI complex in wild-type and GFP-tagged strains. Samples were loaded in equal protein amount. See appendix A for antibodies concentrations.

These techniques, in conjunction with immunoblot analyses, were used to verify the integrity of the GFP-fusion proteins and their supercomplexes. Transmembrane complexes were

disassembled in their respective subunits by SDS-PAGE. Then, immunoblot analysis was performed using an anti-GFP antibody (Figure 3-3A). The position of the resulting bands was compared with the size prediction listed (Table 3.2), confirming in all the strains the presence of the correct GFP-fused subunits.

Further westerns blots were done with specific antibodies to assess if the expression levels of the photosynthetic complexes were affected by the labelling. Figure 3-3B shows the immunoblot analysis using anti-PsaC (a subunit of the PSI complex) in which two equally strong bands of about 9 kDa are present in WT and PsaE-eGFP strains. Assuming that the amount of the PsaC subunit is proportional to the quantity of PSI, we deduce that the expression level of PSI did not seem to be noticeably affected by the labelling. Similar experiments were performed in the other mutants. However, the results presented unexpected bands of difficult interpretation (see appendix G).

Table 3.2 List of the subunits fused with eGFP and their estimated size. Nucleic acid sequences of the subunits were retrieved from KEGG (Kyoto Encyclopedia of Genes and Genomes). Molecular weights of the fused subunits were estimated using Protein Molecular Weight Calculator (https://www.bioinformatics.org/sms/prot_mw.html). The molecular weight of the Enhanced Green Fluorescent Protein is 26.9 kDa as stated previously [203].

Name subunit	Molecular weight (kDa)	Subunit fused with GFP (kDa)
PsaE (PSI)	8.14	35.04
PsbB (PSII)	55.77	82.67
PetA (Cyt b_6f)	34.46	61.36
Subunit β (ATPase)	52.22	79.12
Subunit ε (ATPase)	14.75	41.65
Subunit γ (ATPase)	34.81	61.71

The analysis of the oligomeric state of wild-type and GFP-tagged photosynthetic supercomplexes was monitored by BN-PAGE (Figure 3-4A). This method allows separating

complexes under non-denatured conditions to evaluate their aggregation states [204]. We simultaneously confirmed, by the in-gel GFP fluorescence detection (Figure 3-4B), the native assembly of the eGFP-tagged subunits in the respective functional complexes and their appropriate oligomerisation. It is possible to discern PSI monomer and trimer, PSII monomer and dimer and the bands matching with ATPase and Cyt b_6f monomers, proving that GFP is incorporated in complete supercomplexes.

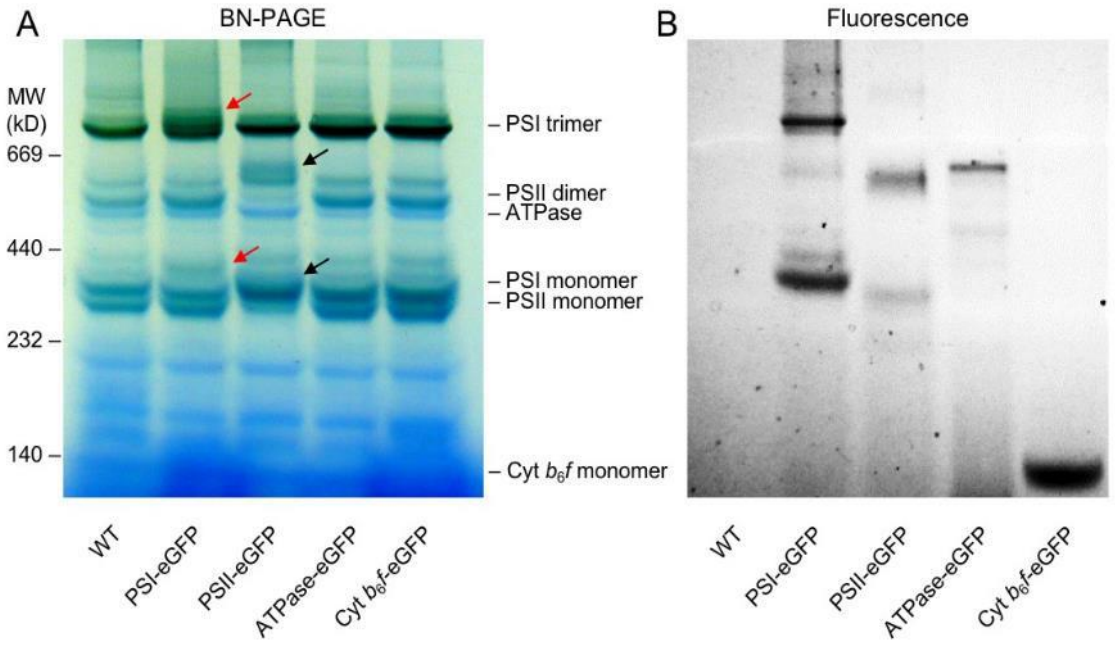

Figure 3-4 Structural integrity of the eGFP-labeled photosynthetic complexes. (A) Membrane protein complexes were separated by a gradient BN-PAGE for wild-type and eGFP tagged strains. Complexes were identified in their monomeric and/or multimeric forms. Shifting of protein bands due to the GFP tagging was indicated in PSI-eGFP (red arrows) and PSII-eGFP (black arrows) strains. (B) In-Gel GFP fluorescence detection of the BN-PAGE gel shown in A, using an ImageQuant LAS 4000. Additional immunoblots on BN-PAGE in appendix H.

Therefore, it is plausible to assume that the GFP tagging does not interfere with the complexes assembling and supercomplex formation. Note that the Cyt b_6f complex is known to be a dimer [51], although in the purification carried out in the present work it appears just under the form of a monomer. Still, we are confident this is not attributable to the GFP labelling since it is consistently observed in all the TMs preparation and for all the Syn7942 strains. Previous work reported the presence of Cyt b_6f mostly as monomers and just a limited amount of dimers [205].

The identification techniques they used were immune blot and mass spectrometry analysis that might be more sensitive than the GFP detector used in our studies. The increased MW of the chlorophyll-containing complexes, due to the insertion of the GFP, was visualised by BN-gels without any further treatment (Figure 3-4A). The protein complexes were identified accordingly to the purification made by Zhang et al. [163]. The typical wild-type pattern of thylakoid membrane protein complexes is shown in the first line. The green bands refer to PSI or PSII due to the presence of chlorophylls. It is possible to distinguish the PSI complex as monomer or trimer [206, 207], PSII as monomer or dimer [207, 208]. The shift of the PSI and PSII bands, due to the presence of the GFP tag, is indicated with black and red arrows and it is consistent with the position of the GFP fluorescence bands in Figure 3-4B. Finally, ATPase-eGFP and Cyt b_6f-eGFP strains show the same bands pattern of the wild-type cells, since the low abundance of these complexes does not permit the direct recognition of the bands in the gel. Further immunoblots on BN-PAGE were done with specific antibodies (appendix H), but the results presented unexpected bands of difficult interpretation.

3.2.3 Physiological assays

3.2.3.1 Growth and spectral characterization of the Syn7942 strains

The growth rate is an important characteristic of a bacterial population. It, in fact, reflects the coordination of gene expression and cells responses to the environment [209]. Therefore, we carried out a spot assay (for a more qualitative observation) and growth curves to examine the overall cell physiology of our GFP-tagged strains. In Figure 3-5A, a drop of liquid culture (OD_{750} = 0.2) was spotted on a BG-11 agar plate and incubated 4 days in the same light and temperature conditions. If the GFP labelling affects the metabolic activity, GFP-tagged strains will form fewer colonies or the pigments expressed could results different. By comparing the surviving cells in each spot (Figure 3-5A), we observed no decrease in cell survival or change of pigmentations

between mutants and WT cells. Although a further spot assay with serial dilutions could be used to compare the cell growth rate, we decided to proceed with the alternative turbidity-based method recording their growth curves. The comparison of the growth curves is an accurate method to highlight the possible differences in metabolic activity among the strains due to the effect of the GFP labelling. In Figure 3-5B we can observe that no substantial increment or decline in growth is occurring in the mutant strains compared to the WT strains.

The pigment composition of the Syn7942 strains was evaluated, more in depth, from their absorption spectra, which gives an overview of the type and amount of pigments absorbing in the visible light (Figure 3-5C).

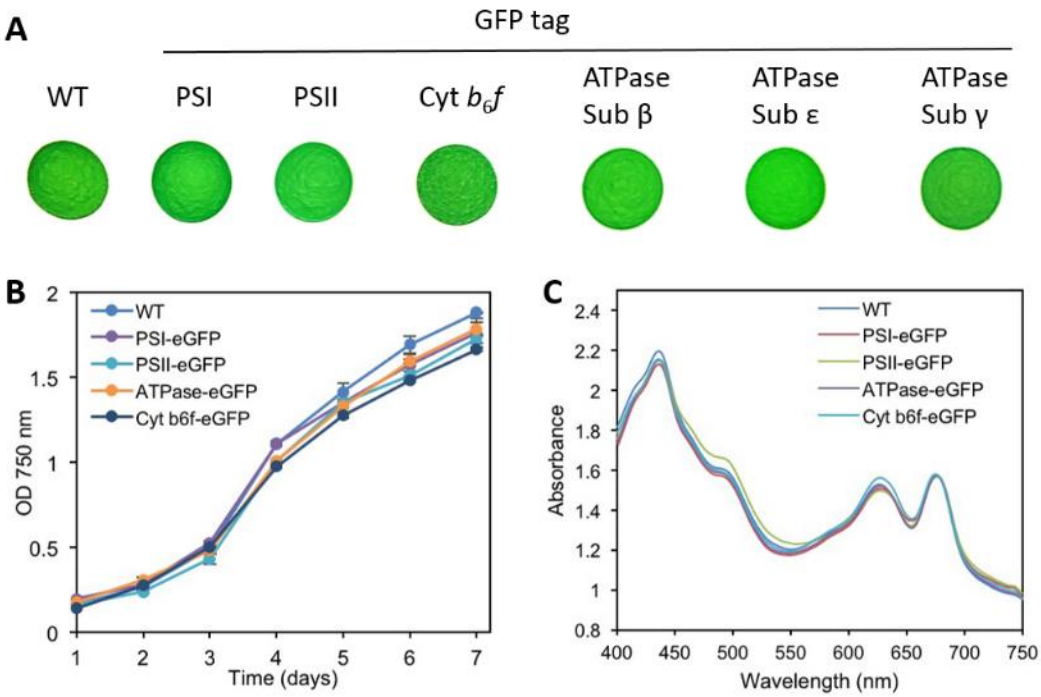

Figure 3-5 Growth and spectral characterization of WT and PSI:eGFP, PSII:eGFP, ATPase(subβ):eGFP, Cyt b_6f:eGFP cells. (A) Growth of WT and GFP-tagged strains on agar plates. Cells at late exponential phase were diluted to OD_{750} = 0.2 and spotted on autotrophic agar plates. Plates were incubated for 4 days at 50 $\mu E \cdot m^{-2} \cdot s^{-1}$. (B) Growth of WT and GFP-tagged strains in liquid BG11 medium. Growth was monitored by turbidity of cell suspensions at 750 nm. Results are a mean ± SD of three independent cultures. (C) Room-temperature absorption spectra of WT and GFP-tagged strains.

To visualise the pigments content per cell, the absorption spectra were normalised to the OD_{750} (which is proportional to the cells number of the suspension). In the spectra is possible to discern the peak at 620 nm, due to the absorbance of phycocyanin (PC) and allophycocyanin (APC) contained in the phycobilisomes [210]. APC also has the main peak at 650 nm. The peaks at 430 and 680 nm correspond to the *AChl* contained in both PSI and PSII. But it has been previously studied that in Synechocystis about 85% of all chlorophylls are bound to PSI [211]. The absorption at 520 nm is attributed to carotenoids. Collectively, no significant changes in the pigment composition of WT and GFP-fused mutants were observed.

The fluorescence emission spectra at 77 K were used to estimate the relative amounts and activities of the two photosystems. The low temperature is the only way to resolve the emission peaks of the chlorophylls belonging to the two photosystems. Cells were dark-adapted at 30 °C before freezing in liquid nitrogen then 77 K fluorescence emission spectra were recorded. The peak at 650-660 nm comes from PCs and APCs, and the peak at about 680 nm is from the long-wavelength terminal emitters of the phycobilisome core; the peak at 700-725 nm is from PSI; PSII contributes to the peak at 680-685 nm and an additional peak at about 695 nm [170].

When cells are excited at 435 nm, the energy is absorbed by the chlorophylls incorporated in PSI and PSII resulting in the fluorescence emission spectra of Figure 3-6A. The spectra show some differences, the PSI/PSII ratio is slightly lower in PSI-eGFP, ATPase (sub β)-eGFP and Cyt b_6f-eGFP strains, on the contrary, it is higher in PSII-eGFP and ATPase (sub ε+γ)-eGFP. However, to have a quantitative comparison, the spectra were resolved into their three components. In Figure 3-6B is represented a typical WT spectrum in which it is possible to discern the PSI and PSII resolved peaks (dashed lines). Then, the area under the two PSII bands and the one under the single PSI band were compared to estimate the abundance of the two photosystems in the cell (Table 3.3).

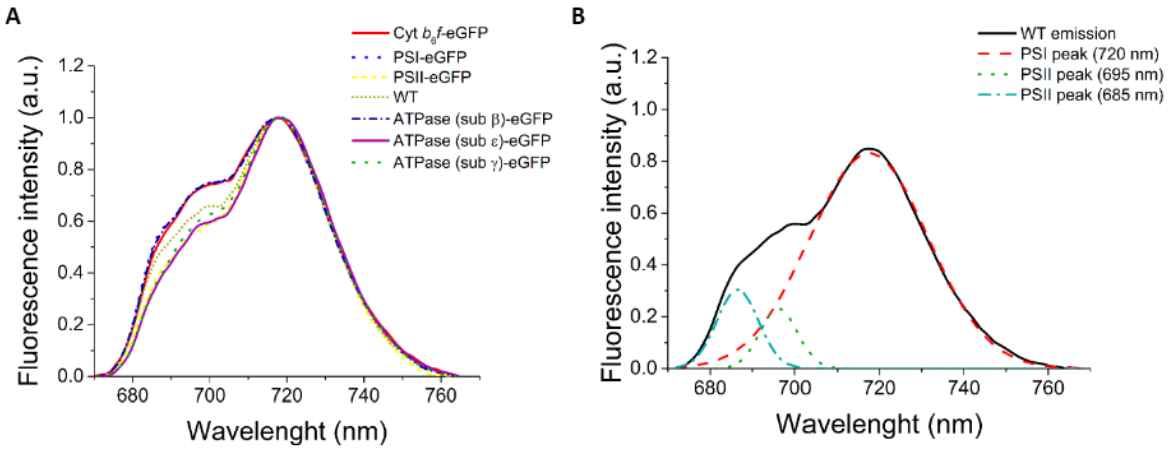

Figure 3-6 Steady-state 77K fluorescence emission spectra of intact cells with chlorophyll excitation at 435 nm. (A) Emission spectra after baseline correction and normalisation to the long-wavelength emission (mainly from PSI) at 720 nm. (B) Deconvolution pattern of a WT Syn7942 fluorescence emission spectrum. The solid line represents the real data points. The dashed lines are the deconvoluted bands. Bands with the maximum at 695 nm and 685 nm are due to PSII fluorescence, the peak at 720 nm is related to PSI fluorescence emission.

The results indicate that the PSI/PSII ratios, in all the strains, are on average 4.9±0.6. Technical repeats show an error between 0.06-5 % (data not shown). Thus, we can conclude that the strain Cyt b_6f-eGFP does not exhibit difference with the WT since it falls within the technical error. To sum up, we can say that PSI-eGFP, PSII-eGFP and ATPase (sub β)-eGFP show a negligible variation of the PSI/PSII ratio. This result is corroborated by the previous SDS-PAGE in PSI:eGFP strain, which did not show variation of PSI expression compared to the WT strain.

On the contrary, in the ATPase (sub ε)-eGFP and ATPase (sub γ)-eGFP strains, there is above 16% of difference, so the GFP labelling seem to affect somehow the PSI/PSII ratio due either to an increase of PSI or a decrease of PSII.

Table 3.3 Comparison of the component bands of the 77 K emission spectra at 435 nm. Analysis of the areas of the peaks based on the deconvoluted patterns. The areas under the two components of the PSII fluorescence emission were added together to represent the PSII amount. The estimated ratio PSI/PSII for each strain was compared with the WT and the percentage of difference is indicated.

	Strains name						
	WT	**PSI-eGFP**	**PSII-GFP**	**ATPase (sub β)-eGFP**	**ATPase (sub ε)-eGFP**	**ATPase (sub γ)-eGFP**	**Cyt*b*$_6$*f*-eGFP**
area peak PSI (720 nm)	29.31	29.05	27.24	30.07	30.14	29.46	31.32
area peak PSII (695 nm)	2.56	3.38	2.42	3.57	2.50	2.58	3.15
area peak PSII (685 nm)	3.76	3.38	2.95	3.65	3.11	2.59	3.36
PSII tot area	6.32	6.76	5.37	7.21	5.61	5.16	6.50
Ratio PSI:PSII	4.63	4.30	5.08	4.17	5.37	5.71	4.82
% difference with WT		-7.33	9.55	-10.04	15.96	23.12	3.93

The evaluation of energy transfer from phycobilisome to PSI and PSII was inferred by fluorescence emission spectra (Figure 3-7). Cells were excited by a wavelength of 600 nm (phycobilisome excitation) then fluorescence emission spectra were recorded to show the phycobilisome, PSI and PSII fluorescence emissions. The PSI and PSII emission peaks are related to the coupling with the phycobilisome and their cell amount: the higher the peak, the higher is the coupling or higher is the concentration of the chlorophyll pigments.

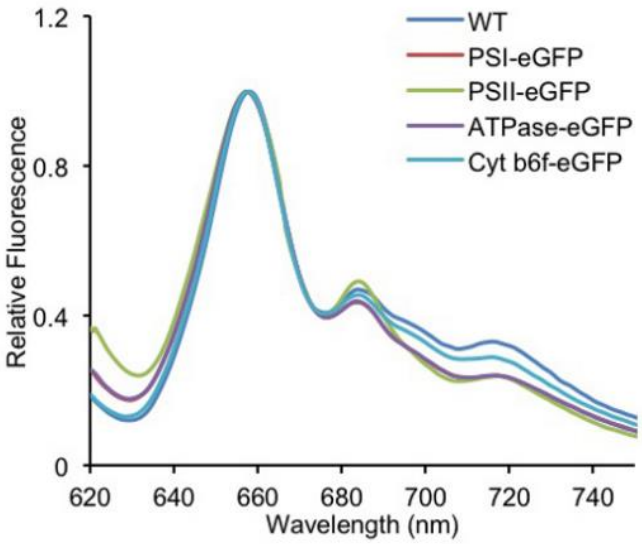

Figure 3-7 Steady-state 77K fluorescence emission spectra of intact cells with phycobilisome excitation at 600 nm. All measurements were carried out at 77K using cell suspension with the same chlorophyll concentration. Spectra were normalised to the phycocyanin fluorescence emission peak at 650nm. Bands with the maximum at 695 nm and 685 nm are due to PSII fluorescence, the peak at 720 nm is related to PSI fluorescence emission. GFP labelling of the ATPase-eGFP strain on subunit β.

The 77K fluorescence emission spectra (Figure 3-7) show only marginal differences between the wild-type and all the GFP mutants. In the case of an interrupted energy transfer from phycobilisomes to the photosystems the relative emission peak would be lost More in details, the coupling between phycobilisome and photosystems in PSI-eGFP, PSII-eGFP and ATPase (sub β)-eGFP strains is weaker than the wild-type cells. At the same time, the coupling in WT and Cyt b_6f-eGFP strains is very similar.

To sum up, we can say that mutant strains are still able to efficiently capture light and transfer energy from PBsomes to PSI and PSII is preserved. Given the proximity and overlap of the fluorescence peaks, a perusal of the emission spectra would require a deconvolution of the peaks and more biological repeats, but more specific analyses are beyond the purpose of this study.

3.2.3.2 $P700^+$ re-reduction, PSII activity and electron transport activities Syn7942 strains

The efficient electron transfer to PSI can be also monitored by measuring the $P700^+$ re-reduction kinetics (Figure 3-8A). As has been previously recognised by Weis et al. [17], absorbance changes around 830 nm give valuable information on the redox state of P700, the reaction centre chlorophyll of PSI.

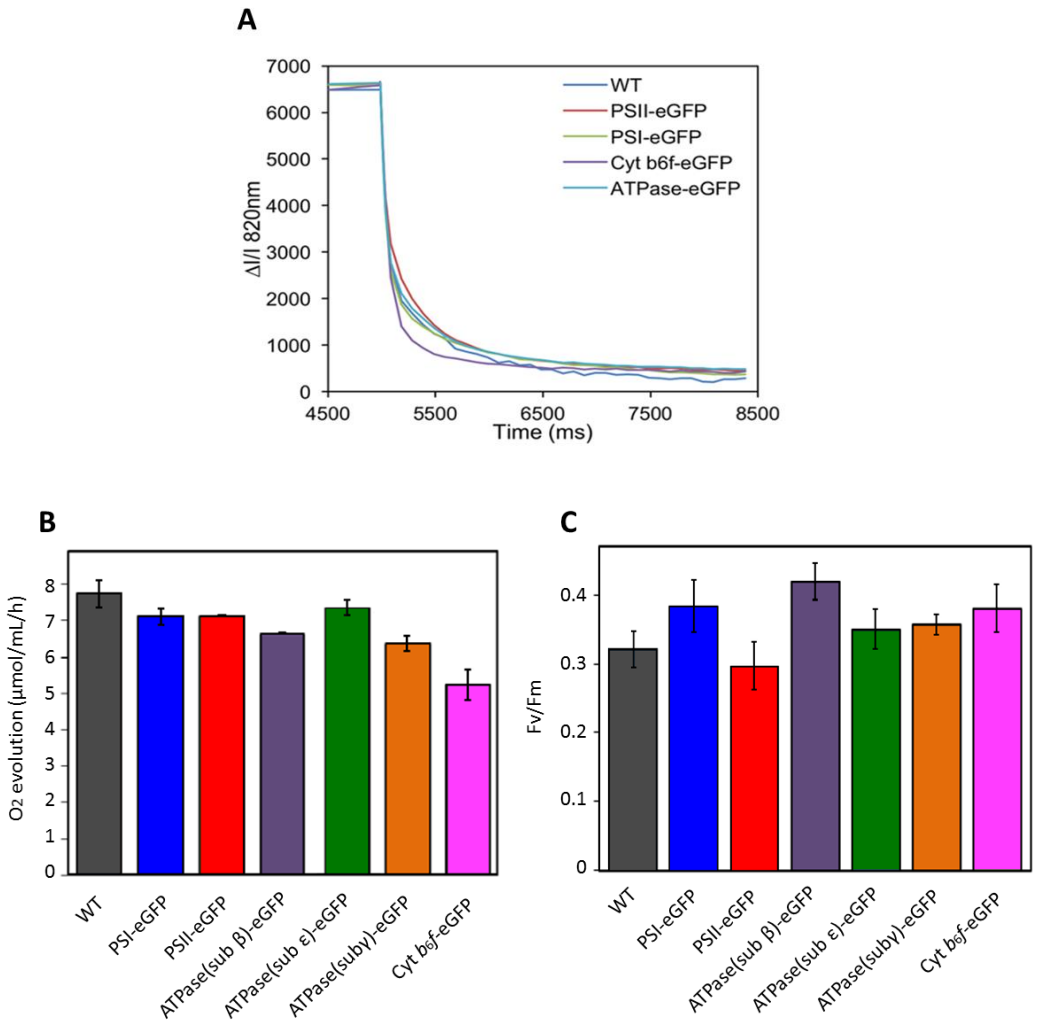

Figure 3-8 Characterization of $P700^+$ re-reduction, PSII activity and electron transport activities of WT and GFP-tagged Syn7942 cells. (A) Kinetics of the $P700^+$ re-reduction in WT and GFP-tagged strains. P700 reduction kinetics were determined at room temperature by analysis of flash-induced absorbance changes at 830 nm. Cells grown at late exponential phase in fresh BG-11 were illuminated by red light (623nm, 2000 $\mu E \cdot m^{-2} \cdot s^{-1}$) with 5 s pulses repeated at 30 s intervals. Each curve represents the mean of 10 accumulations from each of 2 separate aliquots of cells. Curves are normalized to the absorbance of WT. (B) Rates of oxygen evolution determined in saturated red-light illumination (n = 3). The oxygen evolution activities of PSI-eGFP, PSII-eGFP, ATPase (sub β,γ,ε) and Cyt b_6f were respectively 8%, 8%,5-15% and 32% less

than WT cells. (C) PSII activity (F_v/F_m) of cells grown at exponential phase (n = 3). The F_v/F_m (or QY) was 9-30% higher in PSI-eGFP, ATPase-eGFP and Cyt b_6f-eGFP than WT cells. The QY was 7% lower in PSI-eGFP than WT cells. Data are represented as mean ± SD. GFP labelling of the ATPase-eGFP strain on subunit β.

PSI donor pool consists of plastocyanin and the Cyt b_6f complex. The PSI donor pool becomes, however, re-filled by electrons originating from PSII, which are transferred by plastoquinol. In the dark-adapted state, P700 is reduced, when illuminated, P700 becomes more or less oxidized, depending on the intensity, wavelength and duration of illumination. When the cells were illuminated, the reaction centre of PSI released electrons, resulting in an increase of the $P700^+$ absorbance. Once the light was turned off, the $P700^+$ went through a definitive reduction, consisting in a fast and a slower phase, until it reached the lower oxidation state again. Except the Cyt b_6f-eGFP, all the strains had an oxidation/reduction rates comparable with wild-type cells. In the case of the Cyt b_6f-eGFP cells, the $P700^+$ reduction kinetic appears slightly faster due to increased efficacy of electron donors of PSI. Specifically, it was probably due to the increased electron donor efficiency of Cyt b_6f. The P700 measurements of all the strains showed good performance of the electron transport system around PSI. Additionally, the PSII activity was measured in terms of O_2 evolution rates and Quantum Yield (chlorophyll fluorescence measurements).

The quantification of the photosynthetic oxygen produced was used as a direct measurement of the water oxidation carried out at the lumenal side by PSII [212]. The activation of the PSII under a saturated red light led to an overproduction of oxygen which diffuses in the liquid solution and was detected by an electrode. The O_2 evolution rates in the eGFP-tagged strains (Figure 3-8B) show a slight decrease of O_2 production. In comparison to the WT cells, O_2 evolution activity was about 8% lower in the PSI-eGFP and PSII-GFP mutants. It was between 5-15% lower in the ATPase-eGFP strains while it was 32% less in Cyt b_6f-eGFP strain.

The activity of photosystem II was further checked by Flash Fluorescence analysis (measuring the quantum yield of PSII)(see section 2.7.2 for details). Contrary to the oxygen evolution activity, the PSII quantum yield was in general slightly higher in the GFP-labelled strains (Figure 3-8C). In comparison with the wild-type cells, the QY was around 9-30% higher in the PSI-eGFP, ATPase(sub β,γ,ε)-eGFP, Cyt b_6f-eGFP strains. Only the QY in PSII-eGFP mutant was 7% lower, compatible with the results for the oxygen evolution.

In short, O_2 evolution kinetics demonstrated that the GFP-labelled cells were able to increase the photosynthetic performance under saturating red light and in all the cases at least the 70% of the PSII activity was preserved. The O_2 production rate was slightly lower in the mutants, but this was contradictory with the PSII performance measured by QY which show an excellent PSII activity in all the strains. We could deduce that the discrepancies between the two results are due to natural photosynthetic fluctuations of the cell cultures and intrinsic technical errors. Furthermore, previous growth curves and native gels support the idea that the GFP-tagged cells do not have significant structural nor functional damage of PSII. In the case the GFP tag affected the interactions between complexes, this will be reflected in a lower PSII functionality, which in turn is linked with the efficiency of the photosynthetic electron transport.

Concluding and summarising this first part of the chapter, purification techniques revealed that the recombinant proteins were structurally incorporated into fully assembled photosynthetic multi-subunit complexes. Functional assays confirmed the preservation of the photosynthetic activity of PSI and PSII complexes in the mutants. However due to the high PSI:PSII ratio in the ATPase(sub γ,ε)-eGFP strains we will proceed our studies on the ATPase(sub β)-eGFP cells, hereafter just ATPase-eGFP. Taken all together, these observations lead us to assume that the following localisations and behaviours investigated using the tagged strains reflect the natural organisation of the WT strains.

3.3 AFM topography of native thylakoid membranes from Syn7942

In the present work, cyanobacterial thylakoid membranes from wild-type Syn7942 cells were isolated to study their native organization using high-resolution AFM imaging. After cell breakage by glass beads, a further centrifugation in a step sucrose gradient (without the addition of detergents) permitted to separate membrane fragments accordingly with their density. Thylakoid membranes were collected from the 1.6-1.4M fraction (Figure 3-9A). A BN-PAGE was used to reveals the structural integrity of isolated photosynthetic complexes extracted from TMs (treatment with 1.5% DDM) (Figure 3-9B). We visualised PSI monomers and trimers, PSII monomers and dimers, Cyt b_6f and ATPase, consistent with the previous result [213]. Then we conducted AFM imaging in solution to describe the large-scale organization of photosynthetic complexes in the isolated thylakoid membranes under near physiological conditions. During the whole procedure no detergents were used to treat the purified TMs, in order to avoid the disassembling or excision of the transmembrane complexes. Figure 3-9C shows an AFM topography images of isolated thylakoid fragments with two membrane bilayers. It is manifest that the thylakoid membrane contains a high content of membrane proteins. Cross section analysis illustrates that the heights of the single and double thylakoid membranes are 9.49 ± 0.40 (n = 5) and 18.01 ± 1.10 nm (n = 5), respectively. The thickness of a single thylakoid membrane spans the height of the lipid bilayer (4.5 nm), the stromal protrusion of PSI (2.6 nm), and the lumenal protrusion of PSII (4.0 nm)[124, 214, 215]. High-resolution AFM imaging on the large stacking thylakoid membranes enables us to determine the orientation and long-range distribution of photosynthetic complexes in thylakoid membranes from both stromal and lumenal surfaces. On the stromal surface (Figure 3-9D), trimeric structures (white triangles) were predominately observed, together with some dimeric features (light blue circles). The distribution of these complexes appears relatively random, rather than in regular patterns.

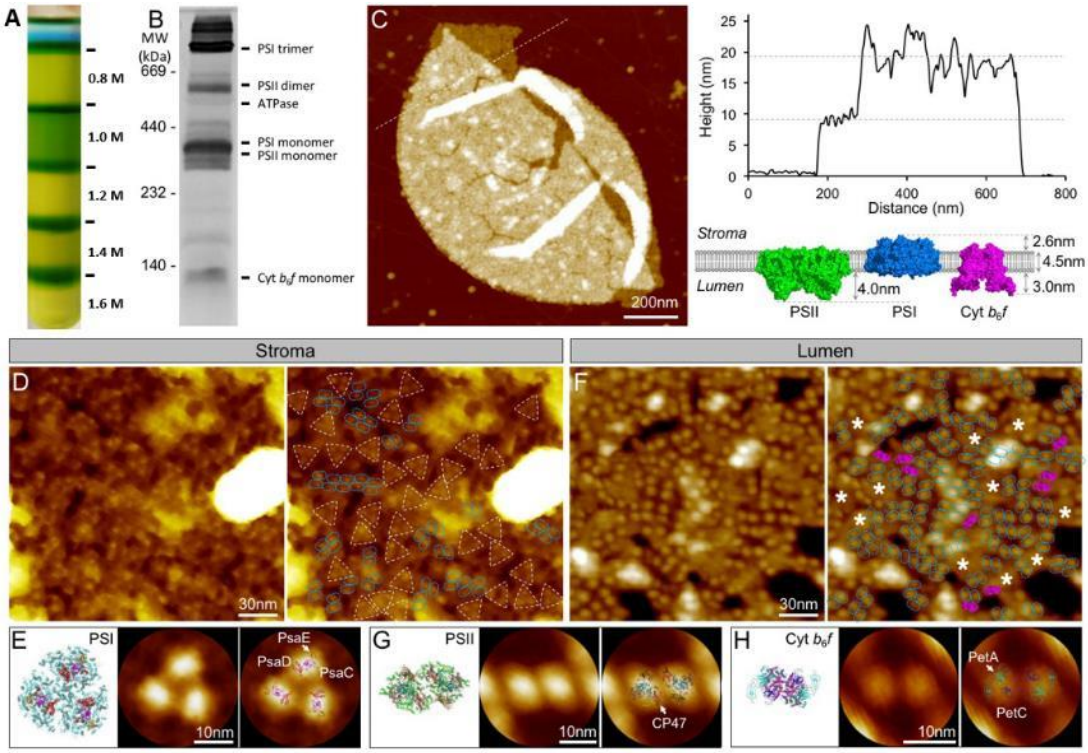

Figure 3-9 Isolation and AFM imaging of native thylakoid membranes from Syn7942. (A) Step sucrose gradient centrifugation of thylakoid membranes. The fraction between 1.6 M and 1.4 M containing large patches of thylakoid membrane was extracted for further analysis. (B) Blue-native gel of wild-type TMs stained with Coomassie Blue. Molecular markers are indicated to the left, and the assignment of the major protein complexes is given to the right, based on [213]. (C) AFM topography of isolated thylakoid membrane fragments in liquid solution. It is manifest that photosynthetic membrane complexes are densely packed in the thylakoid membrane. The cross-section profile of thylakoid membranes (from right to left), along the dashed line, reveals the height of thylakoid membranes. The structure model of the thylakoid membrane (side view) containing dimeric PSII, trimeric PSI, and dimeric Cyt b_6f. The thylakoid lipid bilayer is about 4.5 nm thick. Analysis of the crystal structures indicates that PSII and Cyt b_6f protrude from the lumenal membrane surface by 4.0 nm and 3.0 nm, respectively, whereas the protrusion of PSI complexes from the stromal membrane surface is 2.6 nm high. (D) High-resolution AFM image of the stromal surface of thylakoid membranes in liquid solution (left). Individual trimers (white) and dimers (blue) are deduced to be PSI and PSII complexes (right). (E) Atomic structure of the PSI complexes from the stromal surface (left, PDB ID: 1JB0); the three-fold symmetrized correlation average AFM topography of PSI from the stromal surface of thylakoid membranes (middle); AFM topography of PSI superimposed with its atomic structure (right). The protruded subunits of PSI from the stromal surface of thylakoid membranes, PsaC, PsaD, PsaE, are labelled. (F) High-resolution AFM image of the lumenal surface of thylakoid membranes in liquid solution (left). Individual dimers are speculated to be PSII (blue ovals) and Cyt b_6f (pink shadings) complexes (right), based on their protrusions from the lumenal membrane surface (right). White asterisks indicate the possible location of PSI trimers. (G) Atomic structure of PSII from the lumenal surface (left, PDB ID: 3WU2); the two-fold symmetrized correlation average topograph of PSII from the stromal surface (middle); AFM topography of PSII superimposed with its atomic structure (right). The CP47 subunit of PSII is labeled. (H) Atomic structure of Cyt b_6f from the lumenal surface (left, PDB ID: 4H13); the two-fold symmetrized correlation average topograph

of Cyt b_6f from the stromal surface (middle); AFM topography of Cyt b_6f superimposed with its atomic structure (right). The PetA and PetC subunits of Cyt b_6f are labeled.

AFM can acquire data with a lateral resolution of approximately 1 nm and a vertical resolution of 0.1 nm on membrane proteins [174]. Three-fold symmetrised correlation average AFM images of the trimeric structure match well the stromal side structure of PSI complexes (Figure 3-9E, PDB: 1JB0). The three protrusions of PSI trimers are separated by 10.65 ± 0.46 nm (n = 60), consistent with previous results [124, 216](Figure 3-10A-B). The surface protrusion of trimeric structures from the membrane bilayer on the stromal side is 2.66 ± 0.25 nm (n = 30, Figure 3-10C), in close agreement with the vertical dimension of PSI complexes (Figure 3-9C). Thus, these trimeric structures observed on the stromal surface are assigned to be PSI trimeric complexes. The dimeric objects, often forming arrays, are likely PSII dimers.

By contrast, dimeric structures were mostly seen on the lumenal surface of cyanobacterial thylakoid membranes (Figure 3-9F).

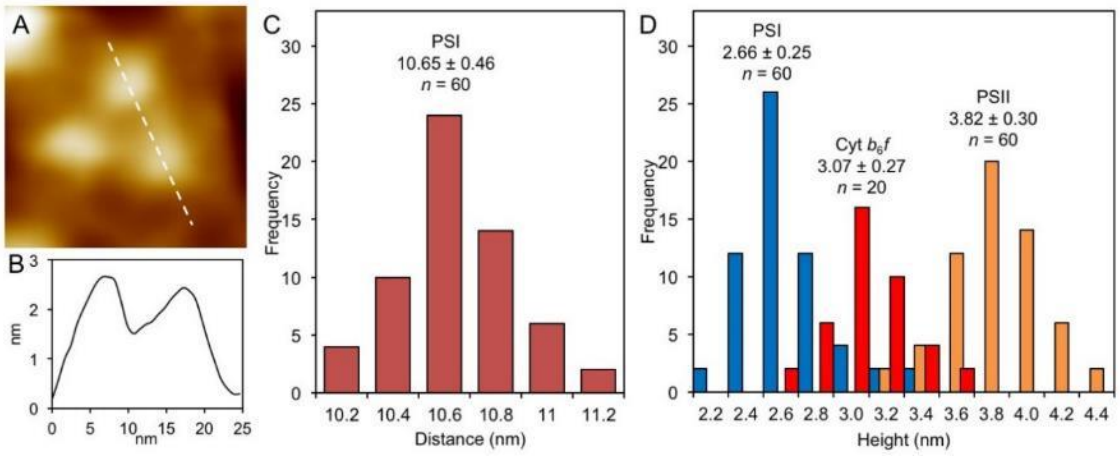

Figure 3-10 AFM analysis of photosynthetic complexes in native thylakoid membranes. (A) High-resolution AFM image of a single trimer, which is assigned to be a PSI complex. (B) Height profile analysis of the protrusions in the trimeric structure, along the dashed line shown in A. (C) Histogram of the lateral distance of monomers within a PSI trimer from the stromal surface of

thylakoid membranes, along the dashed line shown in A. (D) Histogram of the protrusion heights of PSI, PSII and Cyt b_6f complexes above the thylakoid lipid bilayer.

Surface protrusion analysis further revealed that these dimers could be divided into two groups, one has a higher vertical protrusion (3.82 ± 0.30 nm, n = 60, light blue) from the surface than the other (3.07 ± 0.27 nm, n = 20, purple)(Figure 3-10D), consistent with the vertical dimensions of PSII and Cyt b_6f, respectively (Figure 3-9C).

Two-fold symmetrised correlation average AFM topographs were overlaid with the top-view structures of PSII (Figure 3-9G, PDB: 3WU2) and Cyt b_6f complexes (Figure 3-9H, PDB: 4H13). The analysis suggests that the dimers with a higher vertical protrusion are PSII dimers, whereas the less-protruded dimeric features are tentatively identified as Cyt b_6f proteins, reminiscent of the PSII and Cyt b_6f structures observed in spinach grana thylakoids using AFM [217, 218]. It is worthy to note that, given the less than 1.0 nm difference in the vertical protrusions of PSII and Cyt b_6f particles and the architectural complexity on the lumenal surface, we could not accurately identify Cyt b_6f complexes in Figure 3-9F. There are also other particles that we could not easily determine due to the lack of unique topographic structures, i.e., monomers of PSII and Cyt b_6f complexes, ATPases and respiratory complexes. Nonetheless, AFM images of both surfaces of cyanobacterial thylakoid membranes illustrate explicitly a crowding membrane environment (see section 2.7.8), with proteins occupying about 75% of the thylakoid membrane area (see appendix E), comparable to the protein-occupied grana thylakoid area in higher plants [219].

3.4 Distribution of photosynthetic complexes in cyanobacterial thylakoid membranes

3.4.1 Imaging with total internal reflection fluorescence microscopy

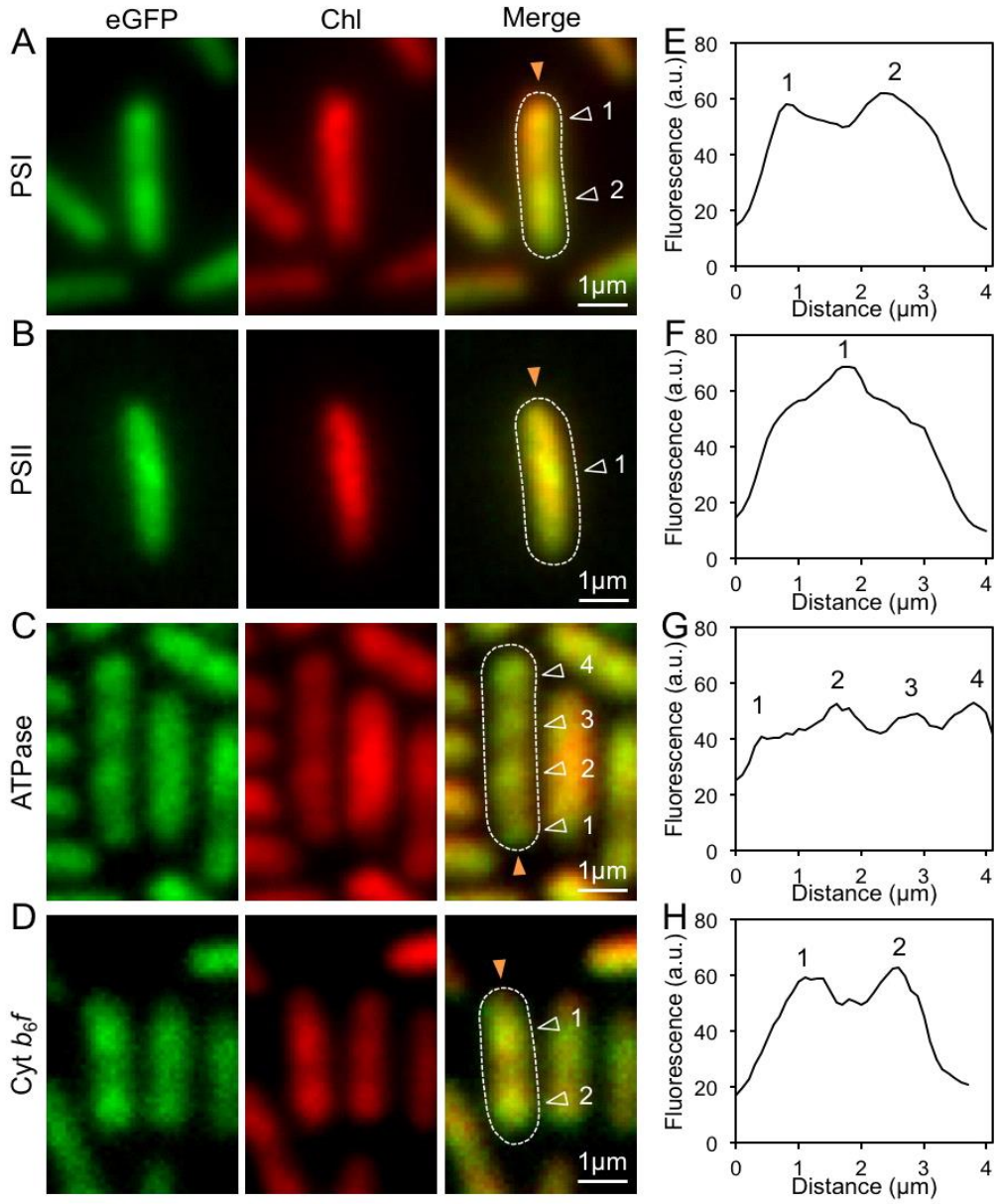

Figure 3-11 Localization of photosynthetic complexes in Syn7942 by TIRF microscopy. (A-D) Single near-TIRF image frames (150 ms exposure) of PSI:eGFP, PSII:eGFP, ATPase:eGFP and Cyt b_6f:eGFP Syn7942 cells. The GFP and *Chl* fluorescence were recorded simultaneously. In the merged channel, the distinct fluorescent patches were indicated (white triangles), and cell body borders were outlined based on bright-field images (white dashed lines). (E-H) Normalized

fluorescence profiles of GFP-tagged cells, taken along the orange arrows indicated in A-D. Additional images in appendix I.

To study the spatial organisation of photosynthetic complexes in cyanobacteria, we visualised eGFP distribution in live Syn7942 cells from exponentially growing cultures using TIRF (Figure 3-11). While eGFP fluorescence was seen throughout the cell membranes, all four eGFP-fused cells present heterogeneous distribution of photosynthetic complexes. For example, the PSI-eGFP cell shown in Figure 3-11A has two large membrane patches, and the PSII-eGFP cell in Figure 3-11B possesses one observable membrane patch in the middle of the cell. More distinct spots of fluorescence were observed in the ATPase-eGFP (Figure 3-11C) and Cyt b_6f-eGFP (Figure 3-11D) cells, indicating the uneven distribution of ATPase and Cyt b_6f complexes. Fluorescence profile analysis along the longitudinal axis of the cell verifies the lateral segregation of photosynthetic complexes, representing the specific compartmentalisation of cyanobacterial thylakoid membranes (Figure 3-11 E to H).

3.4.2 Imaging with confocal fluorescence microscopy

The global distribution of photosynthetic complexes in Syn7942 was further characterised using laser-scanning confocal fluorescence microscopy (Figure 3-12). The pinhole, in our studies, was set up to obtain 2.0 μm optical section in the Z-direction and collect fluorescence from the whole cell. The four photosynthetic complexes (GFP fluorescence) were located in thylakoid membranes (*Chl* fluorescence), confirming the functional tagging. The distribution inhomogeneity of the four photosynthetic complexes in whole cells was also observed (Figure 3-12, arrows). PSI and PSII complexes tend to aggregate into large membrane regions. By contrast, the ATPase and Cyt b_6f complexes exhibit more spotty distribution, in line with TIRF results (Figure 3-11). The inhomogeneity of GFP fluorescence was further quantified using line profile analysis along the thylakoid membrane and standard deviation (SD) calculation (Figure

3-13), as previously described [155]. The profile analysis in Figure 3-13 shows that the PSI, ATPase and Cyt b_6f complexes exhibit relatively higher inhomogeneity (higher standard deviation) of the lateral distribution in thylakoid membranes in contrast to PSII (lower standard deviation).

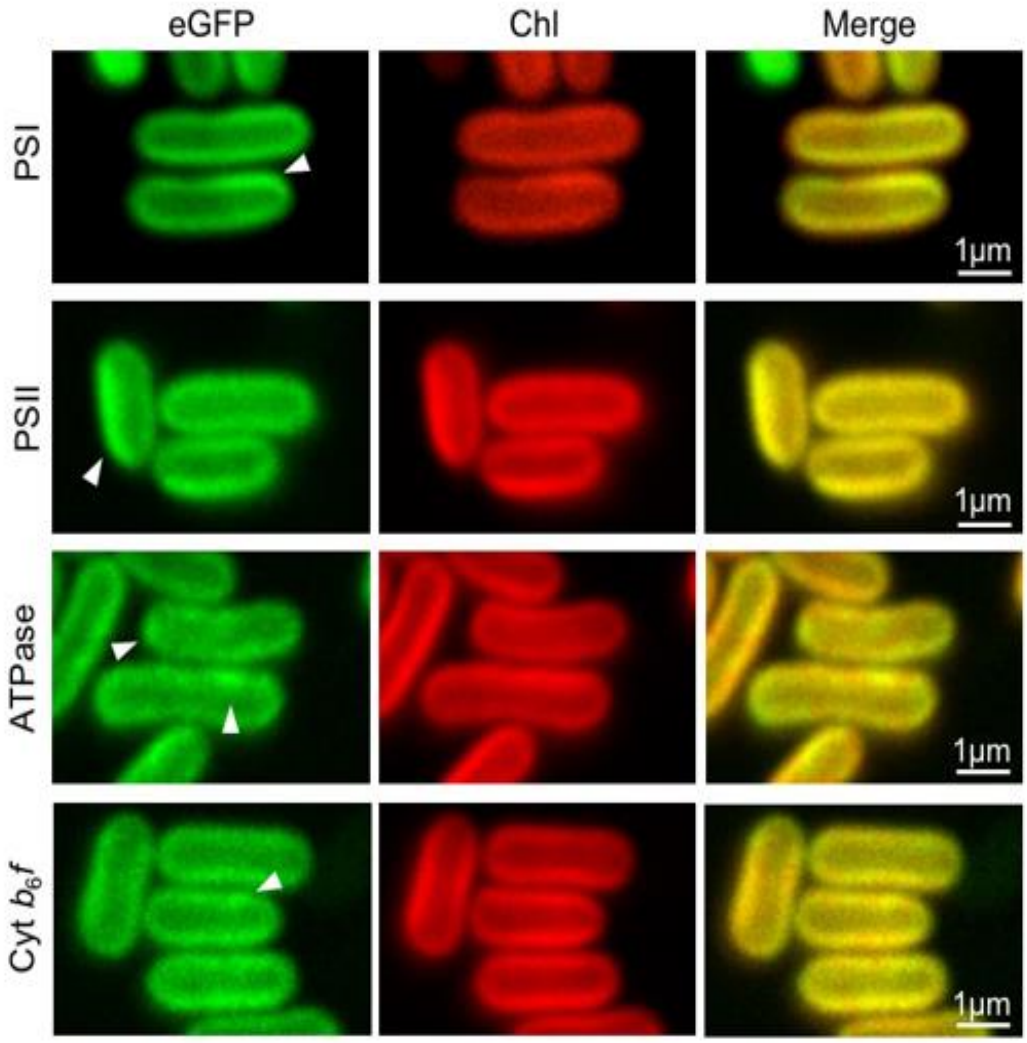

Figure 3-12 Distribution of photosynthetic complexes in Syn7942 by confocal microscopy. Confocal microscopy images of PSI:eGFP, PSII:eGFP, ATPase:eGFP and Cyt b_6f:eGFP Syn7942 cells. Fluorescence spots of photosynthetic complexes, as indicated by white arrows, illustrate the heterogeneous distribution of photosynthetic complexes in thylakoid membranes.

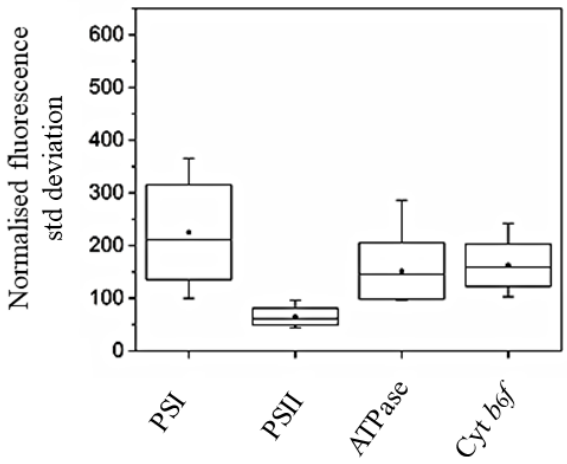

Figure 3-13 GFP fluorescence profile analysis of the distribution of photosynthetic complexes in the thylakoid membrane. Fluorescence profile standard deviations (SDs) of eGFP-fused Syn7942 cells. The box shows the standard deviation, the whisker shows data from 5 to 95% range, the dot represents the average, the line is the median value. Fluorescence profiles were collected and normalised as described in Figure 2-4. The method to calculate the standard deviation is explained in section 2.8.1.

Table 3.4 Mobility parameters and stoichiometry of photosynthetic complexes. Diffusion coefficient, mobile proportion and stoichiometry of photosynthetic complexes per cell measured using confocal fluorescence microscopy and FRAP in this work.

Complex	Diffusion coefficient (D, $\times 10^{-10}$ cm$^2 \cdot$s^{-1})	Mobile proportion	Complex Ratio	
PSI	0.83 ± 0.27 (n = 35)	60 ± 17% (n = 30)	PSI/PSII	4.47
PSII	0.98 ± 0.27 (n = 45)	75 ± 12% (n = 45)	PSI/ATPase	10.06
ATPase	0.83 ± 0.29 (n = 30)	76 ± 18% (n = 35)	PSI/Cyt b_6f	4.76
Cyt b_6f	1.62 ± 0.91 (n =30)	78 ± 15% (n = 30)	PSII/ATPase	2.25
			PSII/Cyt b_6f	1.16
			Cyt b_6f/ATPase	1.93

Moreover, the physiological tagging of eGFP allows us to assess the stoichiometry of photosynthetic complexes at the single-cell level. The relative abundance of GFP molecules per cell was estimated by measuring the brightness of GFP fluorescence in different eGFP-fused cells imaged with the same microscope settings after background subtraction (Figure 3-14). The

PSI:PSII ratio is calculated to be 4.47 (Table 3.4), slightly higher than the previous data based on the spectroscopic analysis [220]. It could be ascribed to the variable PSI content under different growth conditions. The PSII:Cyt b_6f ratio is 1.16, in good agreement with the previous estimation of 1.0 to 1.38 [221, 222]. The PSII:ATPase ratio is 2.25, similar to the ratio examined from immunoblotting results of *Synechocystis* 6803 [222].

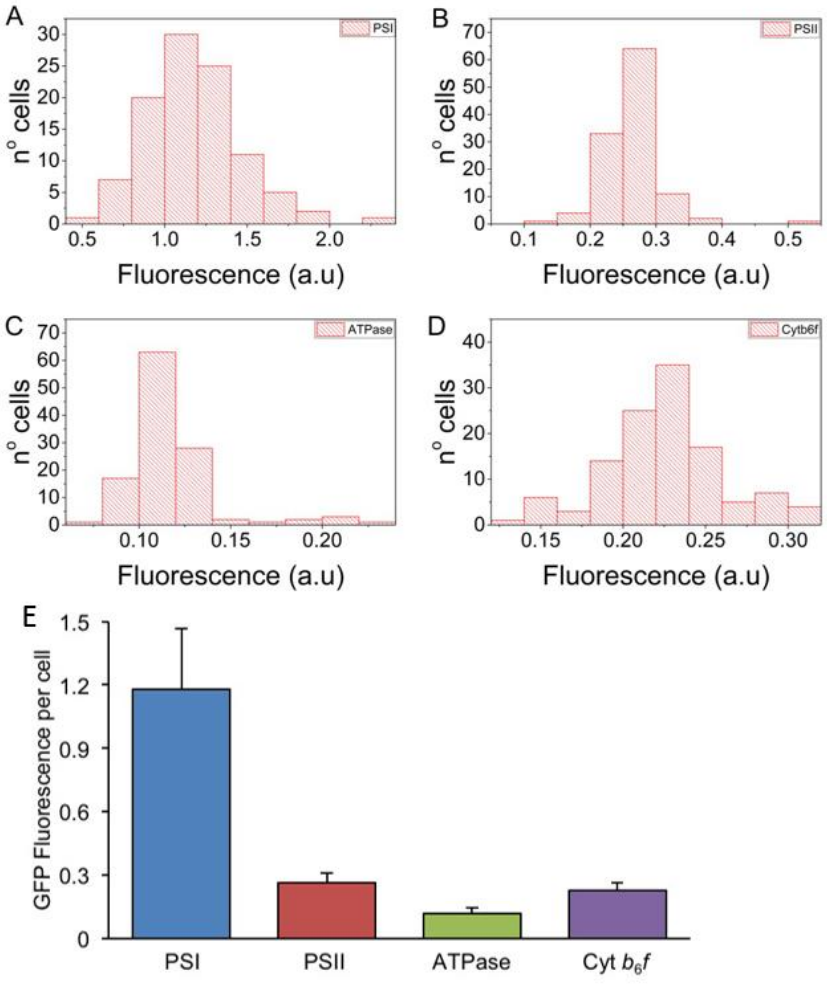

Figure 3-14 Quantification of total GFP fluorescence intensities per cell of GFP-tagged transformants. GFP fluorescence intensity of cells was determined by measuring the total GFP fluorescence of individual cells and extracting background fluorescence of empty regions with the same area. GFP fluorescence intensity per cell was normalized to the cell length and chlorophyll intensity. (A) Histogram of total GFP fluorescence intensities per cell of PSI-eGFP. (B) Histogram of total GFP fluorescence intensities per cell of PSII-eGFP. (C) Histogram of total GFP fluorescence intensities per cell of ATPase-eGFP. (D) Histogram of total GFP fluorescence intensities per cell of Cyt b6f-eGFP. (E) Quantification of total GFP fluorescence intensities per cell of PSI:eGFP (n = 100), PSII:eGFP (n = 120), ATPase:eGFP (n = 120) and Cyt b6f:eGFP (n = 120) strains as in A. Data are represented as the mean ± standard deviation (SD).

3.5 Mobility of photosynthetic complexes in cyanobacterial thylakoid membranes

The diffusion dynamics of photosynthetic complexes in the eGFP-fused cells was investigated using confocal FRAP measurement with 488 nm excitation. Syn7942 cells have regular and elongated thylakoid membranes that form a set of concentric cylinders aligned along the long axis of the cell, representing an ideal system for FRAP analysis [135]. During FRAP measurements, cells were immobilized on the surface of BG11 agar plates at 30^0 C. The confocal laser spot was used to bleach a line across the centre of the cell, using 100% laser power (Figure 3-15A). For pre- and post-scanning, 7% of the laser power was applied and eGFP fluorescence was detected between 500-520 nm. Figure 3-15A to 3-15D show typical FRAP image sequences of eGFP fluorescence in the four eGFP-labelled strains. Diffusion of photosynthetic components, monitored by repeatedly imaging the same cell and recording the spread and recovery of the bleached line, leads to partial fluorescence recovery in the bleached zone [181, 223].

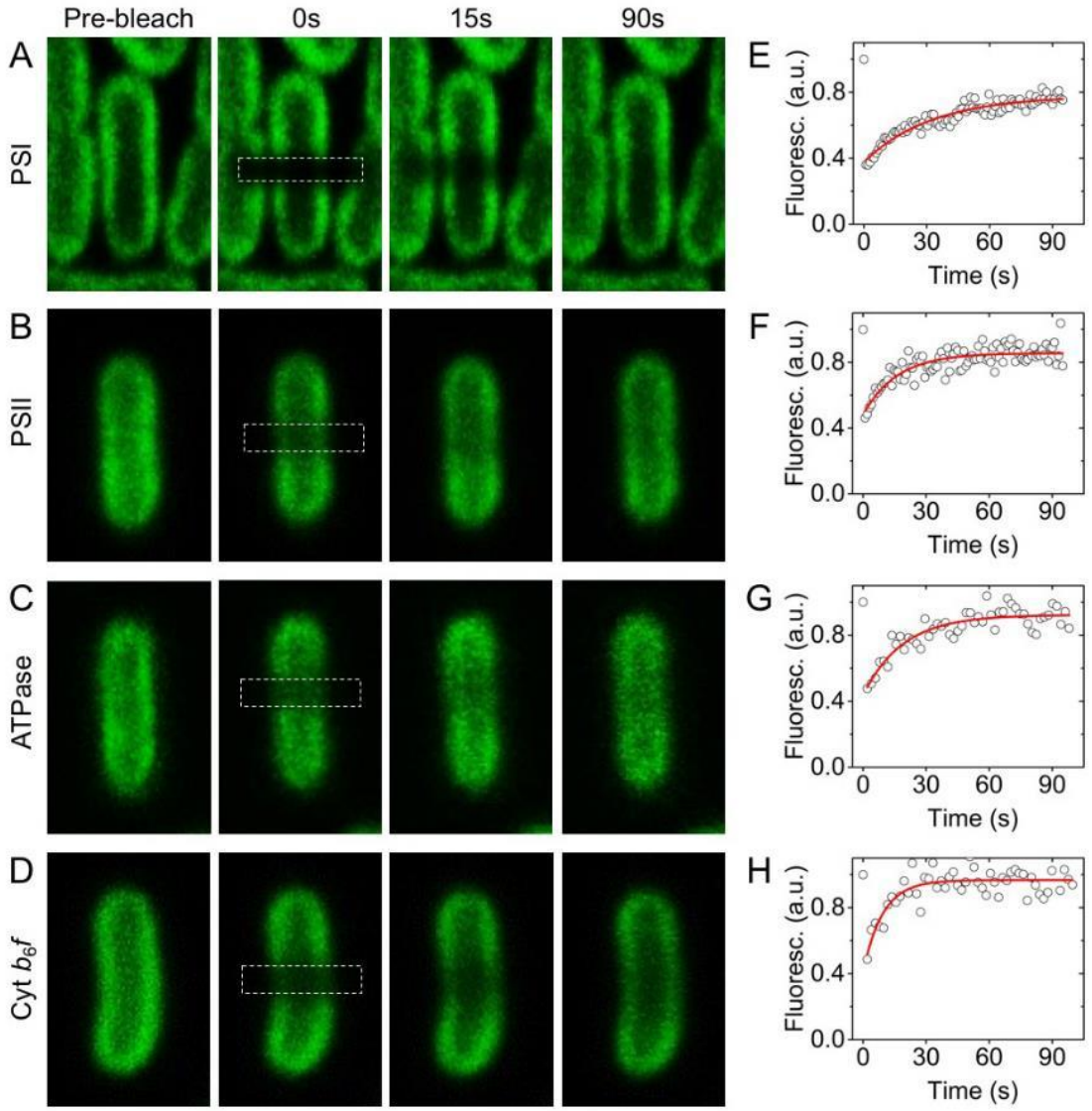

Figure 3-15 FRAP analysis of GFP fluorescence in individual GFP-tagged Syn7942 cells. (A-D) Representative FRAP sequence images of PSI:eGFP, PSII:eGFP, ATPase:eGFP and Cyt b_6f:eGFP cells. (E-H) Time course of fluorescence recovery of the bleached cell regions (white squares as shown in A-D) for GFP fluorescence. Fluorescence values (in arbitrary unit) are relative to fluorescence prior to the bleach. The recovery of GFP fluorescence is presented as circles and fitted to an exponential function (red lines).

The fluorescence recovery curves in the bleached cellular region are depicted in Figure 3-15E to 3-15H (open circles) and adequately fitted to a single exponential function (red lines).

By tracking the evolution of fluorescence intensity in the bleached regions, the *in vivo* mobility features of photosynthetic complexes were investigated in-depth, including the mobile/immobile proportions within 90 seconds and the mean diffusion coefficients of mobile

complexes (Figure 3-15 and Figure 3-16, Table 3.4). A common character of the photosynthetic membrane is the exceptional macromolecular crowding [22, 174, 176]. The high density of photosynthetic membrane complexes in cyanobacterial thylakoid membranes was confirmed by our AFM analysis (Figure 3-10). Interestingly, the FRAP data reveals that large fractions of photosynthetic complexes are mobile within the crowding membrane environment in 90 seconds (Figure 3-16A).

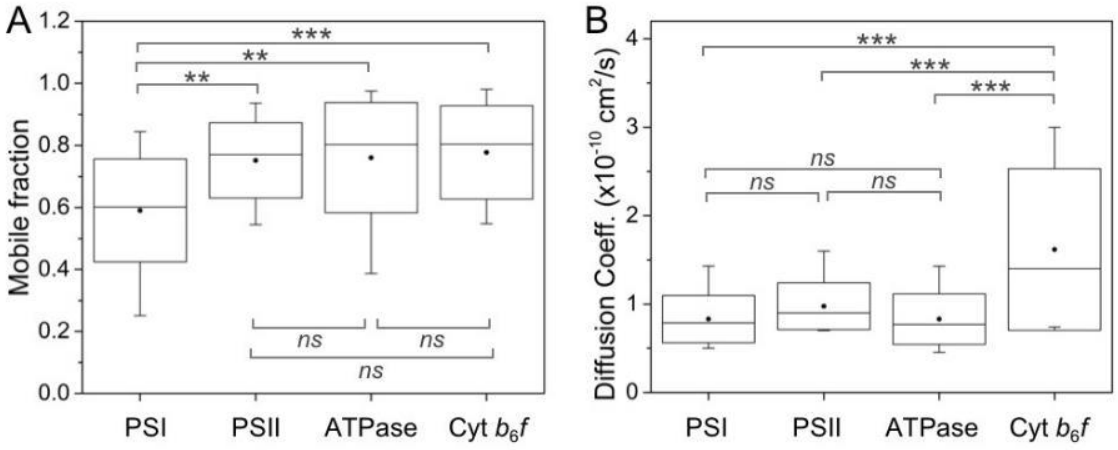

Figure 3-16 Mobility features of photosynthetic complexes in thylakoid membranes of Syn7942. (A) Quantification of the mobile fractions of PSI (*n* = 30), PSII (*n* = 45), ATPase (*n* = 35) and Cyt b_6f (*n* = 30) in individual GFP-fused cells within 90 seconds after photobleaching. Data are represented as mean ± SD. *P* values were calculated using a Scheffe's test as indicated; ** $0.001 < P < 0.001$, *** $P < 0.001$; *ns*, not significant. (B) Quantification of the diffusion coefficients of PSI (*n* = 30), PSII (*n* = 45), ATPase (*n* = 35) and Cyt b_6f (*n* = 30) in individual GFP-fused cells. The box shows the standard deviation, the whisker shows data from 5 to 95% range, the dot represents the average, the line is the median value.

PSII (75 ± 12%, *n* = 45), ATPase (76 ± 18%, *n* = 35) and Cyt b_6f (78 ± 15%, *n* = 30) complexes exhibit relatively higher mobile fractions than PSI (60 ± 17%, *n* = 30), probably ascribed to the larger dimension of trimeric PSI particles (see section 5.1) (Table 3.4).

The diffusion coefficients (*D*), derived from one-dimensional diffusion measurements, represent the average diffusion rates of photosynthetic membrane components over micron-scale

distances [181]. We found that the PSI, PSII and ATPase particles have similar *D* (Figure 3-16B), which are roughly consistent with LHCII antenna's *D* in grana membranes [224]. By contrast, the Cyt b_6f's *D* presents a one-fold increase compared with those of the other three photosynthetic components (Figure 3-16B) and is comparable to that of the Cyt *c* in mitochondrial membranes [225]. All four photosynthetic membrane-integrated complexes exhibit significantly reduced diffusion rates than lipids in the thylakoid membranes of Syn7942 ($3x10^{-9}$ cm^2/s) [184].

3.6 Discussion

A fundamental question about the cyanobacterial photosynthetic membrane is how their photosynthetic complexes are organised and structurally coordinated in the thylakoid membrane to construct the functional machinery for efficient photosynthetic energy transduction. In this chapter, we characterised the spatial distribution and mobility of photosynthetic complexes within the cyanobacterial thylakoid membrane, using a combination of AFM, TIRF, live-cell confocal microscopy and FRAP. To our knowledge, it is the first time to observe the patchy distribution and mobile features of Cyt b_6f and ATPase complexes in living cyanobacterial cells.

3.6.1 Organization of native thylakoid membranes

The cyanobacterial thylakoid membrane represents an interesting paradigm with highly dense protein arrangement in the membrane lipid bilayer. The components of both photosynthetic and respiratory electron transport chains are accommodated in cyanobacterial thylakoid membranes [18, 20]. Likewise, there are also ion channel proteins within cyanobacterial thylakoid membranes, which are postulated to be key in the balance of trans-thylakoid proton gradient for ATP synthesis [226-228]. Our AFM data reveal that, at molecular level, over 75% of the thylakoid membrane surface area is occupied by membrane proteins. It is comparable to the

protein densities estimated in grana thylakoids (~80%) and the whole thylakoid membranes (~70%) of higher plants and inner mitochondrial membranes (lipid:protein ratio = 0.34)[75, 219, 229, 230]. It is notably higher than those of stroma lamellae membranes (~50%) in higher plants and the plasma membrane (~23%)[231, 232]. Macromolecular crowding in thylakoid membranes could be essential to retaining strong protein-protein interactions between complexes and a high concentration of chlorophylls to ensure high quantum yields of photosynthetic energy transduction.

Given that many thylakoid complexes possess large dimensions within the lipid bilayer, it is plausible that the lipid space of the cyanobacterial thylakoid membrane will be further restricted. It remains unclear how electron carriers diffuse rapidly in the thylakoid lipids and mediate large-scale electron transport between thylakoid membrane complexes. The pathway of electron flux could be determined by the specific local protein environment and long-range protein organisation in membranes, as deduced in purple photosynthetic bacteria [52] and higher plants [75]. Our AFM images (Figure 3-9F) and previous EM results [233, 234] indicate that PSII particles tend to form regular arrays in cyanobacterial thylakoid membranes, which could potentially facilitate the long-range diffusion of small electron carrier molecules. Despite the PSI-enriched domains seen by confocal/TIRF microscopy in the present work and by structured illumination microscopy in a previous study on *Synechocystis* 6803 [235], we did not observe PSI-only membrane patches as reported recently [235]. This is probably due to the absence of detergent treatment during our membrane preparation, different growth conditions or the species-dependent variation. By contrast, AFM images show that PSI complexes are intermixed with PSII (Figure 3-9D). The PSI-PSII membrane regions have also been observed in other cyanobacteria such as *Synechocystis* 6803, *Thermosynechococcus* and *Synechococcus* sp. PCC 7002 [235]. The integration of PSI and PSII within the same thylakoid membrane regions in cyanobacteria could be structurally fundamental to state transitions, a mechanism for modulating the energy transfer from phycobilisomes to PSI and PSII balancing the energy

captured by phycobilisomes between PSI and PSII in response to changing conditions [85]. It provides the architectural basis for the movement of phycobilisomes between PSI and PSII [93] or local conformational changes of phycobilisome-PSI-PSII domains [91]. We also tentatively observed some Cyt b_6f complexes are spread in the PSII domains using AFM (Figure 3-9F). It is unclear whether Cyt b_6f are close to PSI since the two photosynthetic complexes have opposite protrusions above the thylakoid surfaces. No ATPase complexes were identified in AFM images, probably due to the weak association of the whole complex and their specific membrane locations that may not be accessible to the AFM probe [174]. Molecular organisations of Cyt b_6f and ATPase in the thylakoid membrane require further exploration.

3.6.2 Properties of the GFP-tagged strains

Most of what is known about distribution and mobility of transmembrane proteins in TMs it been achieved by techniques such as fluorescence microscopy [183, 236], hyperspectral confocal fluorescence [178] transmission electron microscopy [126] but not without some difficulties or inaccuracies. In our work, we took a different approach using fluorescence labelling. The benefit of the technique is that it easily permits in *vivo* detections. The disadvantage is that the GFP presence could have an impact on the physiology of the cells. Thus we ruled out this eventuality by a meticulous screening of the GFP-labelled strains. GFP-tagged photosynthetic complexes were analysed by purification techniques confirming that the recombinant proteins were incorporated in complete photosynthetic complexes and supercomplexes (Figure 3-4). Metabolic activities, pigment composition and electron flow around PSI shown no changes from the WT strain (Figure 3-5 and Figure 3-6). Coupling between phycobilisome and the photosystems was preserved with marginal differences in PSI-eGFP, the PSII-eGFP and the ATPase (sub β)-eGFP strains (Figure 3-7).

The stoichiometry of PSI and PSII presented significative differences just in the ATPase (sub ε)-eGFP and ATPase (sub γ)-eGFP strains (Figure 3-7). Finally, PSII activity was preserved at least for its 70% in all the mutants (Figure 3-8).

Given the above evaluations, all the strains produced were suitable for localisation and dynamic tracking. However, the ATPase (sub ε)-eGFP and ATPase (sub γ)-eGFP strains were not used for further studies since confocal fluorescence pictures evidenced a low fluorescence signal (data not shown) and they show a higher PSI:PSII ratio compared with WT strain.

3.6.3 Distribution of the four main photosynthetic complexes

Previous studies characterizing the large-scale distribution and dynamics of phycobilisomes, PSI and PSII in cyanobacterial cells were based on the natural fluorescence of phycobilins and chlorophylls [92, 178]. However, the extremely high concentration and fluctuation of pigments could largely restrict the sensitivity of fluorescence detection. Intense laser on phycobilins and chlorophylls which closely interact with each other may result in intrinsic photoprocesses of these pigments [96]. Moreover, accurate distinction of PSI and PSII is challenging based on only chlorophyll fluorescence. This is due to the notable overlap of PSII and PSII fluorescence, the low and rapid decay of PSI fluorescence at room temperature as well as the high PSI/PSII ratio in cyanobacteria [172, 220, 237]. To overcome this issue, we tagged eGFP to PSI, PSII, Cyt b_6f and ATPase, respectively, and used live-cell TIRF and confocal microscopy to probe their location and diffusion dynamics *in vivo*. Direct detection of eGFP fluorescence allows us to exclude any photochemical processes occurring in photosynthesis, i.e. quenching of fluorescence.

All the four complexes have inhomogeneous distribution in the thylakoid membrane. Apart from those widespread over the thylakoid membrane, PSI and PSII complexes tend to aggregate within large membrane domains. It was shown that PSI complexes present a higher heterogeneity than PSII, probably implying that PSI complexes are more abundant than others

in certain regions of the thylakoid membrane (Figure 3-13). How photosynthetic complexes are organised within these membrane domains await further investigation.

The different distribution patterns of photosynthetic complexes may indicate the functional and structural segregation of thylakoid membrane zones, to fulfil distinct roles in photosynthetic electron transport. In line with the heterogeneous organisation of photosynthetic complexes, the respiratory complexes, NDH-1 and SDH, have been reported to present the spatial segregation (on the scale of 100–300 nm) within the thylakoid membrane of Syn7942 [21]. Reorganization of respiratory NDH-1 complexes in thylakoid membranes, triggered by different light intensity, could serve as a physiological mechanism to channel the pathways of electron flow. Taken together, it appears that cyanobacterial thylakoid membranes possess specific domains to accommodate functionally relevant bioenergetic components and compartmentalise metabolism. Partitioning of bioenergetic complexes has also been observed in other membrane systems. For instance, in the primordial cyanobacterium *Gloeobacter violaceus* that has no internal thylakoid membranes, both the photosynthetic and the respiratory complexes are concentrated in two distinct plasma membrane domains [238]; the photosynthetic components are spatially separated in the thylakoid membranes of higher plants − PSII and light-harvesting complex II in grana stacks, whereas most of the PSI, light-harvesting complex I and ATPase in unstacked membrane regions [176]; the oxidative phosphorylation enzymes are clustered in specific zones within the plasma membranes of Gram-negative *Escherichia coli* (*E. coli*) and Gram-positive *Bacillus subtilis* [194, 239, 240]; different respiratory complexes are asymmetrically distributed in the mitochondrial inner membranes [241, 242]. The structural and functional segregation of membrane proteins appears to be a general characteristic of any biological membranes.

3.6.4 Mobility features of the photosynthetic complexes

Theoretical approaches to microscopically describe the motion of a protein in biological membranes have been attempted [243]. Then, modifications to the models were made accordingly with empirical evidences [244, 245]. It is experimentally established that D increases with the kinetic energy of the particles and temperature but is inversely proportional to the viscosity of the medium. Also, D is inversely proportional to the size of the particle. Beside these physical-chemical parameters, long-range diffusion can be facilitated or retarded by the tuning of the protein composition, the protein amount or the size of the supercomplexes (see section 5.1). Finally, any association event between the mobile molecule and any immobile scaffolds could change the D [245]. So, it could be inferred to specific interactions or regulation of the complex under study. Given the complexity of the system we decided to use an experimental approach to study the protein dynamics.

We characterised the diffusional fingerprints of the four photosynthetic complexes within thylakoid membranes. Over 60% of photosynthetic complexes are mobile in the crowded membrane environment under physiological conditions (Table 3.4), resembling the mobility of chlorophyll-protein complexes in isolated grana membranes from spinach [224]. By monitoring directly eGFP fluorescence, we found that about 75% of PSII are mobile under physiological conditions, with a diffusion coefficient of 0.98×10^{-10} $cm^2 \cdot s^{-1}$. It differs from the previous study that suggested the immobility of PSII in Syn7942 by tracking *Chl* fluorescence [246]. For comparison, we performed FRAP measurements on PSI-eGFP cells to detect *Chl* fluorescence recovery (Figure 3-17) by using a 633nm laser.

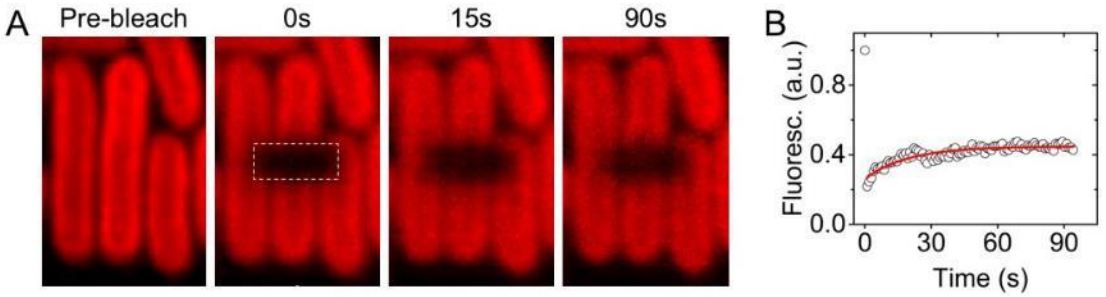

Figure 3-17 Confocal FRAP analysis of Chlorophyll fluorescence in WT Syn7942. (A) Representative FRAP sequence images. (B) Time course of fluorescence recovery of the bleached cell region (white square in A). Fluorescence values are relative to fluorescence prior to the bleach. The recovery of *Chl* fluorescence is presented as circles and fitted to an exponential function (red line).

The results show greatly restricted *Chl* diffusion in the same Syn7942 cell that we used for FRAP analysis on eGFP fluorescence, ruling out the possibilities that the mobility of photosynthetic complexes determined by FRAP on eGFP fluorescence arises from different growth conditions or is strain-dependent. Functional fluorescence tagging allows us to determine the diffusion coefficients of PSI, ATPase and Cyt b_6f in thylakoid membranes for the first time (PSI − 0.83×10^{-10} $cm^2 \cdot s^{-1}$, ATPase − 0.83×10^{-10} $cm^2 \cdot s^{-1}$, Cyt b_6f − 1.62×10^{-10} $cm^2 \cdot s^{-1}$, Table 3.4). The diffusion rates of PSI, PSII, ATPase and Cyt b_6f are in the same magnitude as the diffusion rates of IsiA in cyanobacterial thylakoid membranes [183] and LHCII in both grana and stroma membranes [224, 247]. However, the diffusion coefficients of cyanobacterial photosynthetic complexes are roughly more than one order of magnitude lower than those of membrane proteins in the eukaryotic plasma membrane [248], endoplasmic reticulum membrane [249] and mitochondrial membrane [250]. It further corroborates the high protein-density of thylakoid membranes. From these results, we can also appreciate that the diffusion coefficients are indiscernibly affected by the size of the complex (to be intended as the area of the transmembrane domain). In fact, retrieving the crystal structures from PDB database and reproducing it in Pymol it is possible to have a 3D view of the complexes. An approximate area of the transmembrane domain can be extrapolated to have a comparison between the complexes considered. The

smallest dimensions are ascribable to ATPase and Cyt b_6f dimer meanwhile, the PSI and PSII's dimensions of monomers and multimers, range from 3 to 9 times more than the Cyt b_6f. If the diffusivity was correlated with the dimension we should aspect higher values in Cyt b_6f and ATPase, but this is not respected. We, therefore, assume that the protein-protein or protein-lipid interactions with the immobile fraction have a substantial impact on the mobility.

The diffusion dynamics of photosynthetic complexes represents the combination of the mobility of photosynthetic complexes within the complex-enriched membrane regions and between the patches. It is feasible that the immobile photosynthetic complexes are concentrated mainly within the discrete membrane zones, whereas the mobile photosynthetic complexes can diffuse between each membrane zone. Recently, increasing experimental evidence has proven the occurrence of photosynthetic/respiratory supercomplexes in cyanobacteria, for instance, PSII–PSI [251], PSI–PSII–phycobilisome [99], PSI–phycobilisome [100] and NDH-1–PSI [252]. Concomitantly, the bioenergetic supercomplexes have also been characterised in chloroplasts and mitochondria [253, 254]. The observed bioenergetic membrane domains may act as the pools where functionally relevant complexes physically associate to form electron transport supercomplexes. However, a recent study has reported that mobile domains of different oxidative phosphorylation enzymes in the *E. coli* plasma membrane do not co-localize, in contrast to the "respirazones" notion [240]. Whether the structural association of different photosynthetic complexes in cyanobacteria is transient or dynamic in response to changes in the environmental conditions, as described in the "plasticity model" [255], is a subject for future study, e.g. visualisation of pairs of fluorescently tagged photosynthetic complexes.

By using the combination of AFM, TIRF, confocal microscopy and FRAP, our study provides deeper insight into the spatial organisation and mobility of photosynthetic complexes in the cyanobacterial thylakoid membrane. The thylakoid membrane possesses a high protein density which could potentially promote electron transduction. Rather than evenly located within the

native thylakoid membrane, the photosynthetic complexes tend to possess clustering distribution and are mobile in thylakoids, suggesting the specific organisation and functional compartmentalisation of the thylakoid membrane.

Chapter 4

Reorganization and dynamics of photosynthetic complexes triggered by intense red light

4.1 Introduction

Cyanobacteria are common residents of a broad range of habitats across all the latitudes [256]. This versatile ability is due to a fine response of their photosynthetic machinery to light (see section 1.4). Cyanobacteria have evolved sophisticated ways to sense the intensity, direction [257], duration, and wavelength of the light [258, 259]. Meanwhile, they also developed a dynamic feedback response, which adopts specific regulatory strategies on time scales ranging from hours/days (long-term [260]) to minutes/seconds or less (short-term [258]). A relevant factor in the growth conditions of photosynthetic organisms is the light spectra available in the environment (see section 1.4.2). Several experiments in high plants and cyanobacteria revealed that selective exposure to blue, red, or green light affects their phenotypic and/or genotypic traits [260-262]. However, while most of the plants receive all the spectrum of the solar light, seawater and freshwater organisms have at disposition wavelengths from the blue-green region to red depending on the depth in which they float in the water column. Since the ability of light to penetrate water decreases from red to blue light, cyanobacteria constantly perceive light quality and adjust themselves to capture the most available wavelength and maintain an efficient photosynthetic rate and a balanced cellular redox state (see section 1.6). Light sensing can involve the activation of specific photoreceptors, called phytochromes (absorbing in the red/far-red, blue/near-ultraviolet, and ultraviolet spectral ranges [263]) which, controlling signal transduction elements, lead the modulation of gene expressions, molecular and morphological responses (see section 1.4.2) [264]. Among the different light sources, perhaps, the better studied is the red light and its impact on the photosynthetic organisms. One of the most obvious long-term effects of red light exposure is the enhanced expression of genes related to translation (such as ribosomal proteins, RNA polymerase), genes related to tRNA processing and RNA

binding, genes related to photosynthesis, CO_2 fixation, and processes like biosynthesis of amino acids, fatty acids, purines, and pyrimidines) [260]**.** These data suggest a general stimulatory effect of red light on the cellular metabolism. Thus it is possible to consider the red light an optimal light quality for energy production and growth of cyanobacteria [260]. Along with regulation at the level of gene expression, other intriguing ways to control the cellular redox state exist, such as the supercomplex formation (association between two more electron transport complexes) and the lateral segregation (complexes involved in a particular pathway agglomerate in islands in the TMs). Both these strategies are usually fast responses that require the long-range diffusion of transmembrane proteins on the TMs. Despite detailed knowledge about long-term effects, we still know very little about fast protein dynamics in general responses to light quality changes and in particular to red light. Previous works in Syn7942 tracked the natural fluorescence of the chlorophyll, to show a redistribution of PSII in specific zones in response to the red light [172]. They proposed that these rearrangements be due to the photodamaged centres which diffuse in specialised repairing zone in the TMs. However, later studies on the respiratory pathway have proven that the redistribution of the transmembrane complexes (specifically Complex 1) balance the changes in the cellular redox state caused by the light variations [155]. Specifically, they found that the lateral segregation of supercomplexes may help to redirect the electrons towards certain acceptors rather than others. This strategy could perhaps be valid also for the photosynthetic electron transport pathways.

Given the importance of the localisation of the transmembranal supercomplexes and their dynamics, in the following sections we will focalise our attention on:

- the reorganisation of cyanobacterial photosynthetic apparatus (PSI, PSII, ATPase, Cyt b_6f) in response to intense red light on a minute timescale.

- the diffusion of these complexes in the thylakoid membranes by FRAP.

- the different motions of the supercomplexes clusters over the time of 13 minutes.

These results will help to extend previous observations in the cyanobacterial literature about red light responses and expand our knowledge on how/if same light stimulus lead different responses from the four central photosystem complexes.

4.2 Results

4.2.1 Distribution of photosynthetic complexes after red light

How the thylakoid membrane organisation is modulated in response to environmental stress is still enigmatic. It has been shown that intense red light can trigger the mobility and redistribution of *Chl* fluorescence to specific zones within the thylakoid membranes, referring to the reorganisation and mobility of PSII complexes in Syn7942 [172]. Here, we explore precisely the effects of red light on the distribution and diffusion of four photosynthetic components using the eGFP-tagged strains. Based on previous work [172], the red light source of our choice was an intense red light source (a 633-nm HeNe laser), which, although less close to physiological conditions, stimulates a fast response from the cells. Cells were exposed to red light by illuminating a field of 22 × 22 µm using a 633-nm laser (2 µW) for 1.5 min. eGFP and *Chl* fluorescence of the four eGFP-fused Syn7942 cells were detected in the regions of 500-520 nm and 670-720 nm, respectively. After red-light treatment, *Chl* fluorescence was enriched in localized zones within thylakoid membranes (Figure 4-1, *Chl* channels, arrows), consistent with the previous observation [172]. eGFP channels show specifically the redistribution of individual photosynthetic components triggered by red light. PSI complexes concentrate into one large membrane patch on one end of the cell (Figure 4-1A).

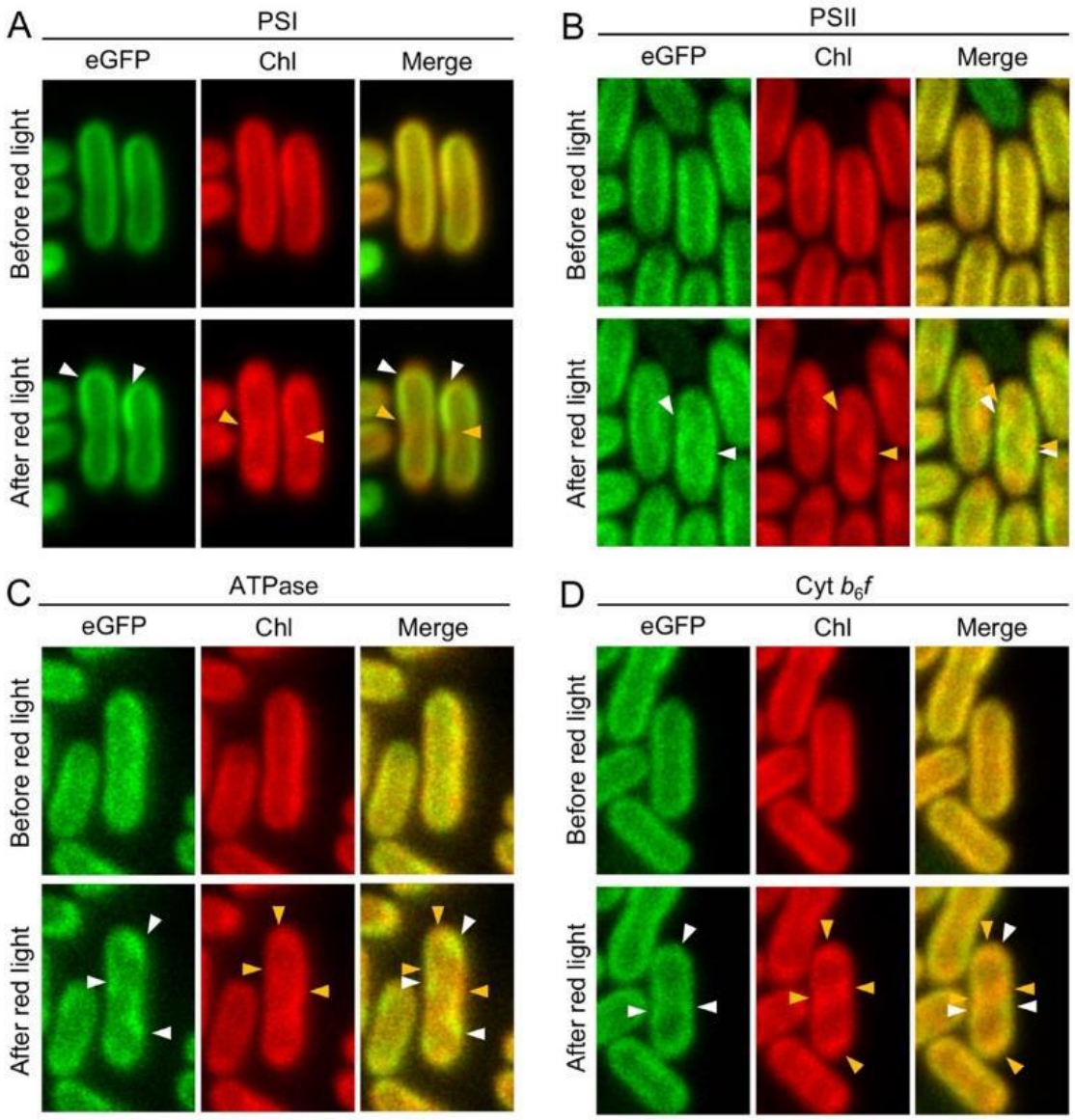

Figure 4-1 Reorganization of photosynthetic complexes triggered by intense red light. GFP-fused Syn7942 cells (A, PSI; B, PSII; C, ATPase; D, Cyt b_6f) were illuminated by intense red light of 633 nm for 1.5 mins. GFP fluorescence before and after red-light treatment was recorded. Patchy organisation of eGFP-tagged photosynthetic complexes and chlorophyll fluorescence after red light are indicated by white and orange triangles respectively.

PSII spots were often observed at the centre of the cell (Figure 4-1B), reminiscent of the uneven distribution of PSII complexes seen by TIRF (Figure 3-11B and Figure 3-11F). Significant spotty zones of ATPases in thylakoid membranes were visualised (Figure 4-1C). The ATPase membrane "domains" and *Chl* fluorescence intersperse (Figure 4-1C, merged channel), suggesting to some extent the independent localisation patterns of ATPase and PSII complexes. Similar segregation

was also observed for Cyt b_6f where *Chl* and Cyt b_6f domains localise in different regions (Figure 4-1D white and orange triangles). This change of distribution is further highlighted by the fluorescence profile displayed in Figure 4-2 and the fluorescence profile analysis in Figure 4-3. In Figure 4-2 the fluorescence profiles before and after red light of the GFP-tagged transformants (cells in Figure 4-1) were collected and displayed as described previously (see section 2.8.1).

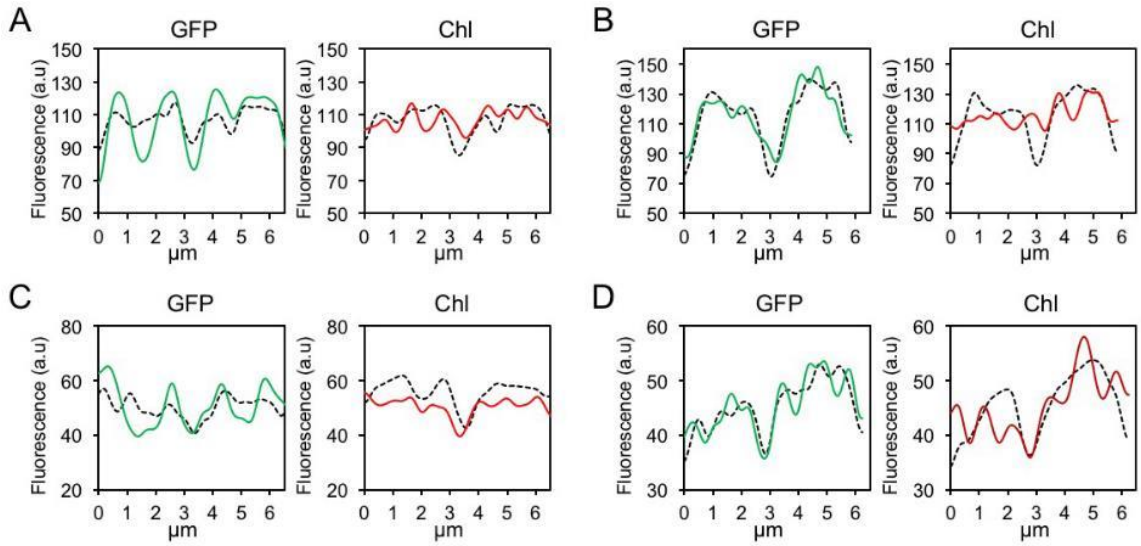

Figure 4-2 Profile changes of GFP and Chlorophyll fluorescence before and after red-light treatment of cells shown in Figure 4-1. Fluorescence profiles before red-light treatment are shown using black dashed lines. GFP and *Chl* fluorescence profiles after red-light treatment are shown in green and red, respectively. (A) PSI:eGFP. (B) PSII:eGFP. (C) ATPase:eGFP. (D) Cyt b_6f:eGFP. Variations of the peak to peak distance, peak amplitude, peak number or localisation are an index of a redistribution of the fluorescent complexes.

Our results reveal the presence of specific membrane domains for distinct photosynthetic complexes within the thylakoid membrane. It is notable that, after exposure to red light, the peak location, number, shape and peak to peak distance present variations which reveal a rearrangement of *Chl* and GFP-tagged complexes.

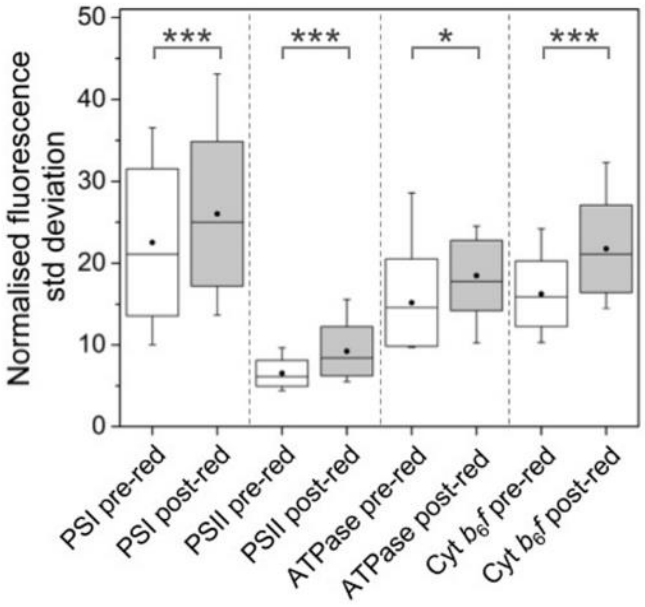

Figure 4-3 GFP fluorescence profile analysis comparison of the distribution of photosynthetic complexes in the thylakoid membranes. Normalized fluorescence profile SDs of GFP-tagged cells before (pre-red) and after red (post-red) light treatment. The box shows the standard deviation, the whisker shows data from 5 to 95% range, the dot represents the average, the line is the median value. The number of cells studied before red light treatment were n=30 for PSI; n=45 for PSII; n=35 for ATPase; n=30 for Cyt b_6f.The number of cells studied after red light treatment were n=26 for PSI; n=24 for PSII; n=28 for ATPase; n=28 for Cyt b_6f.

The peak to peak distance and the number of the peaks appear generally increasing after red-light exposure. In Figure 4-3 we calculated the standard deviations of the fluorescence profiles as an index of the distribution of the GFP-tagged complexes and *Chl*, where a higher std deviation value correlates with a less uniform fluorescence distribution. It is evident that all the fluorescence standard deviations undergo a significant increment in value. Given these observations, we can conclude that red light can trigger the redistribution of these photosynthetic components and their further segregation into specific membrane “zones”.

4.2.2 Mobility of photosynthetic complexes after red light by FRAP

To unravel the diffusion dynamics of photosynthetic complexes during redistribution triggered by red light, we performed FRAP measurements (with blue laser at 488 nm) on the cells directly following red-light treatment. Figure 4-4 shows typical FRAP image sequences of eGFP fluorescence in the four eGFP-labelled strains after red light illumination. Diffusion of the photosynthetic components, monitored by repeatedly imaging the same cell and recording the spread and recovery of the bleached area, leads to partial fluorescence recovery in the bleached zone (Figure 4-5).

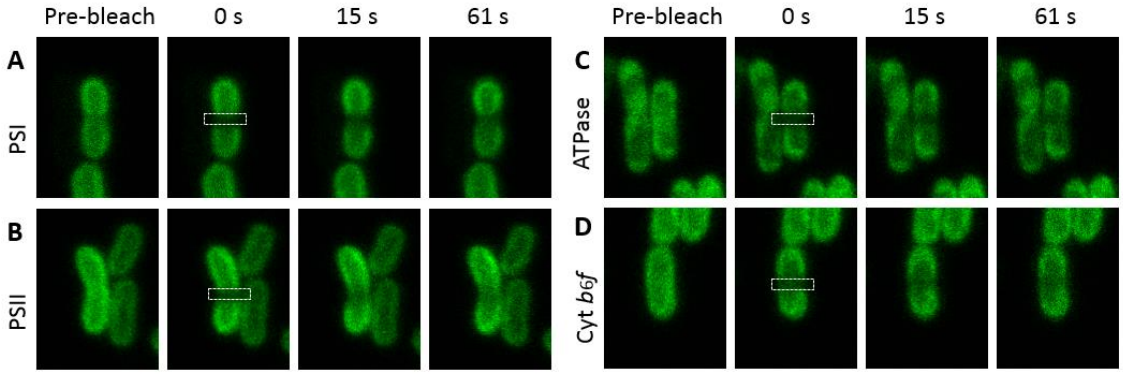

Figure 4-4 Representative FRAP image sequence of GFP fluorescence in individual GFP-tagged Syn7942 cells after red-light treatment. Snapshots of cells during data acquisition. In the panel labelled ‘‘pre-bleach’’ is showed the cell before photobleaching, the following snapshots show the cells after the photobleaching pulse. The white rectangles indicate the position of the area bleached. Either recovery of the fluorescence in the bleached area or expansion of the bleached area are an index of proteins diffusion along the TMs (A) PSI:eGFP. (B) PSII:eGFP. (C) ATPase:eGFP. (D) Cyt b_6f:eGFP.

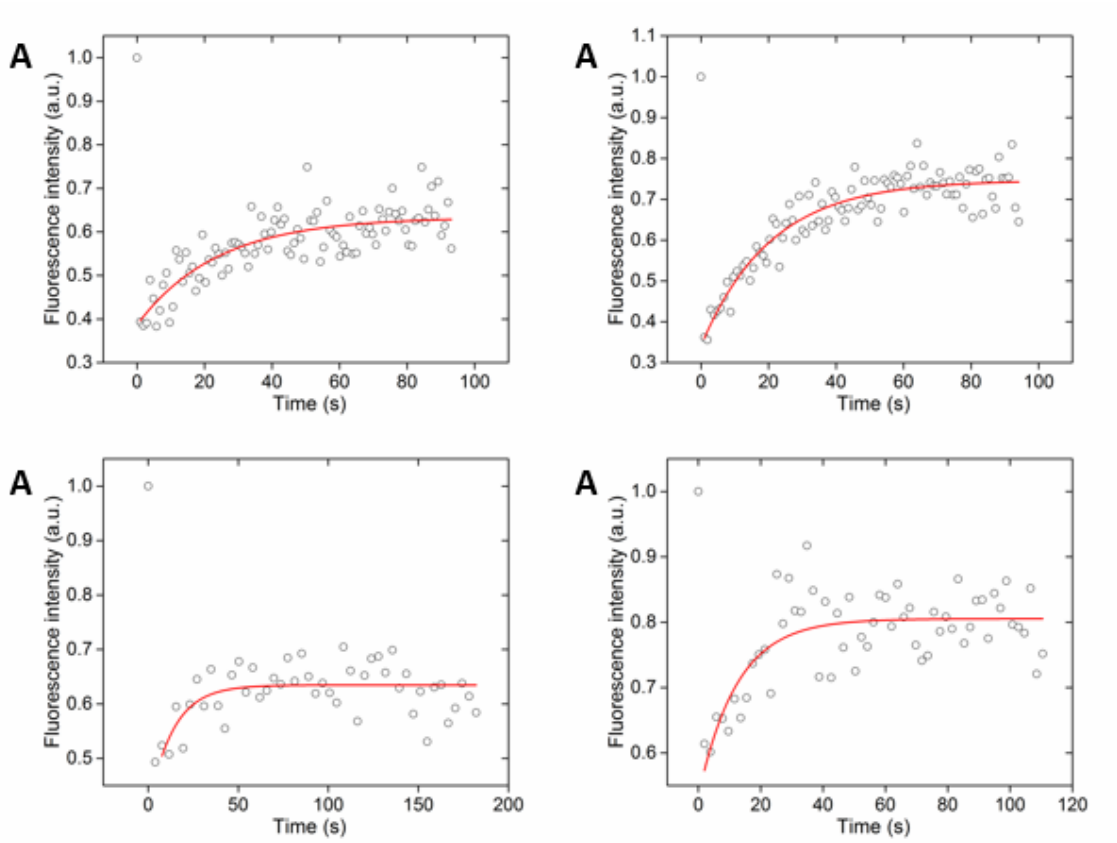

Figure 4-5 Representative fluorescence recovery curves of GFP fluorescence in individual GFP-tagged Syn7942 cells after red-light treatment. Time course of fluorescence recovery of the bleached cell regions (see white squares in Figure 4-4) for GFP fluorescence. The recovery of the GFP fluorescence is presented as circles and fitted to an exponential function (red lines). (A) PSI:eGFP. (B) PSII:eGFP. (C) ATPase:eGFP. (D) Cyt *b6f*:eGFP. See appendix L for additional recovery curves.

As shown in Figure 4-6A, the proportions of mobile PSI and PSII particles appear to be comparable before and after red light treatment, whereas the mobile fractions of ATPase and Cyt b_6f complexes are reduced by ~50% and 36%, respectively.

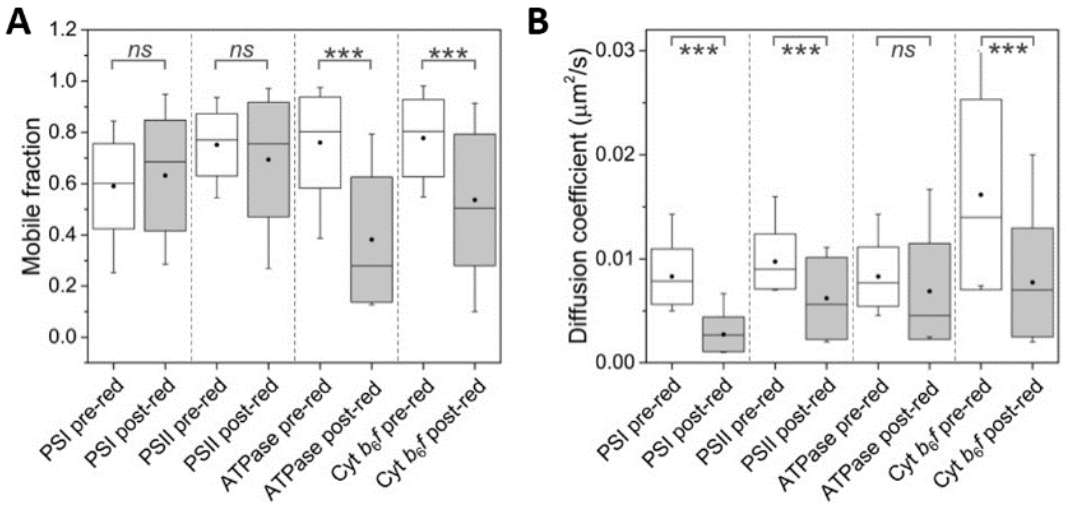

Figure 4-6 Quantification of the organisation and mobility of photosynthetic complexes before and after red-light treatment. (A) Quantification of the mobile fractions of photosynthetic complexes before (n_{PSI}= 34, n_{PSII}= 43, n_{ATPase}= 26, n_{cytb6f}= 27) and after red light treatment (n_{PSI}= 26, n_{PSII}= 24, n_{ATPase}= 28, n_{cytb6f}= 28). Data are obtained from a minimum of 7 independent replicas. (B) Quantification of the diffusion coefficients of photosynthetic complexes before and after red-light treatment. The box plots show the standard deviation, the whisker shows data from 5 to 95% range, the dot represents the average, the line is the median value. *P* values were calculated using a Scheffe's test as indicated; *** $P < 0.001$; *ns*, not significant.

In addition, red light led to the decrease of the diffusion coefficients of PSI, PSII and Cyt b_6f complexes by 65%, 34% and 49%, respectively (Figure 4-6B). It is plausible that after red light treatment a large proportion of these photosynthetic complexes are concentrated and immobilized into specific membrane regions. In contrast, the diffusion coefficient of ATPase complexes is not significantly affected by red-light treatment.

4.2.3 Dynamic characterisation of the red-light-induced clusters by time lapse

We further recorded the diffusion dynamics of photosynthetic complexes *in vivo* after red light treatment using time-lapse fluorescence microscopy (Figure 4-7). To visualise the movements of the fluorescence signal over the time of 12 min, we produced a kymograph from the time-lapse microscopy of the distribution of each photosynthetic complex after red light. Kymographs

are space-time plots which display fluorescence intensity values along a predefined path (x-axes) over time (y-axes). In the kymographs showed in Figure 4-7 in the x-axes is represented the TMs fluorescent profile of the cell considered (extracted as described in section 2.8.1), and its evolution over the time is displayed going from the top to the bottom.

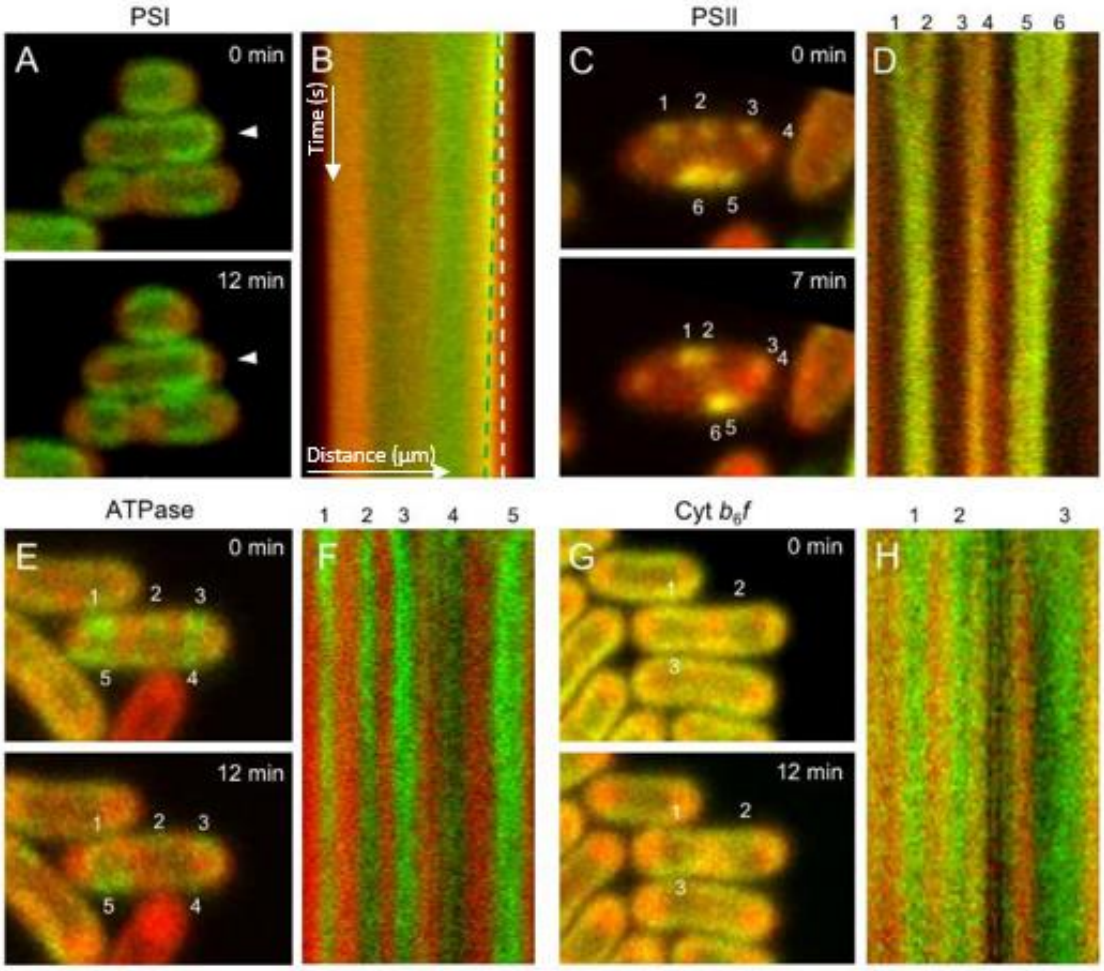

Figure 4-7 Time-lapse confocal microscopy imaging of the redistribution and dynamics of photosynthetic complexes induced by red light. (A, C, E, and G) Confocal images of GFP-tagged PSI, PSII, ATPase, and Cyt b_6f Syn7942 cells at 0 min and 12 min (7 min for PSII) after red light. White arrowhead in (A) indicates the ''shrinking'' of PSI-eGFP fluorescence profile. (B, D, F, and H) Kymographs taken from time-lapse microscopy of the distribution of photosynthetic complexes after red light. Kymographs start from the top at t=0 and end at t=12 min or t=7 min at the bottom as indicated by the white arrows in (B). The green and white dashed lines in (B) represent the edges of PSI-eGFP and *Chl* fluorescence, respectively. Spots of GFP fluorescence in cells were labelled with numbers, corresponding to the spots shown in (A), (C), (E), and (G) and were monitored as a function of time.

Within 12 minutes after red-light illumination, the PSI-eGFP fluorescence moved toward the cytosol of the cell in contrast to *Chl* fluorescence (Figure 4-7A). It is confirmed by the kymograph of eGFP and *Chl* fluorescence (Figure 4-7B). By contrast, no significant "shrinking" of PSII-eGFP fluorescence profile was observable. Instead, the PSII spots are laterally mobile along the thylakoid membrane. It was seen that two distinct PSII spots could merge into one spot within the same membrane patch (Figure 4-7C and 4-7D). The different redistribution features of PSI and PSII triggered by red light likely indicate the distinct subcellular locations of the two photosynthetic complexes. PSI complexes seem to have a preferential location at the inner layers of cyanobacterial thylakoid membranes which might be able to bend into the central cytoplasm after red-light treatment. Indeed, it has been demonstrated by neutron scattering experiments that thylakoid membranes in *Synechocystis* 6803 can be quite flexible [182]. By contrast, PSII complexes are located at the peripheral layers of thylakoid membranes which have more restricted space for conformational changes. Our results are in line with the previous data acquired from hyperspectral fluorescence microscopy imaging of *Synechocystis* 6803 [178, 179]. Moreover, ATPase complexes were enriched into specific membrane regions after red-light treatment (Figure 4-7E, Figure 4-1C). Time-lapse confocal imaging revealed explicitly that these ATPase patches intersperse between *Chl* fluorescence spots and appear immobile within 12 minutes (Figure 4-7F). Similarly, no visible mobility of Cyt b_6f patches was discerned (Figure 4-7G and 4-7H). In contrast to the mobile photosynthetic complex patches after red light, the lateral diffusion of photosynthetic complex domains before red-light treatment is restricted (Figure 4-8).

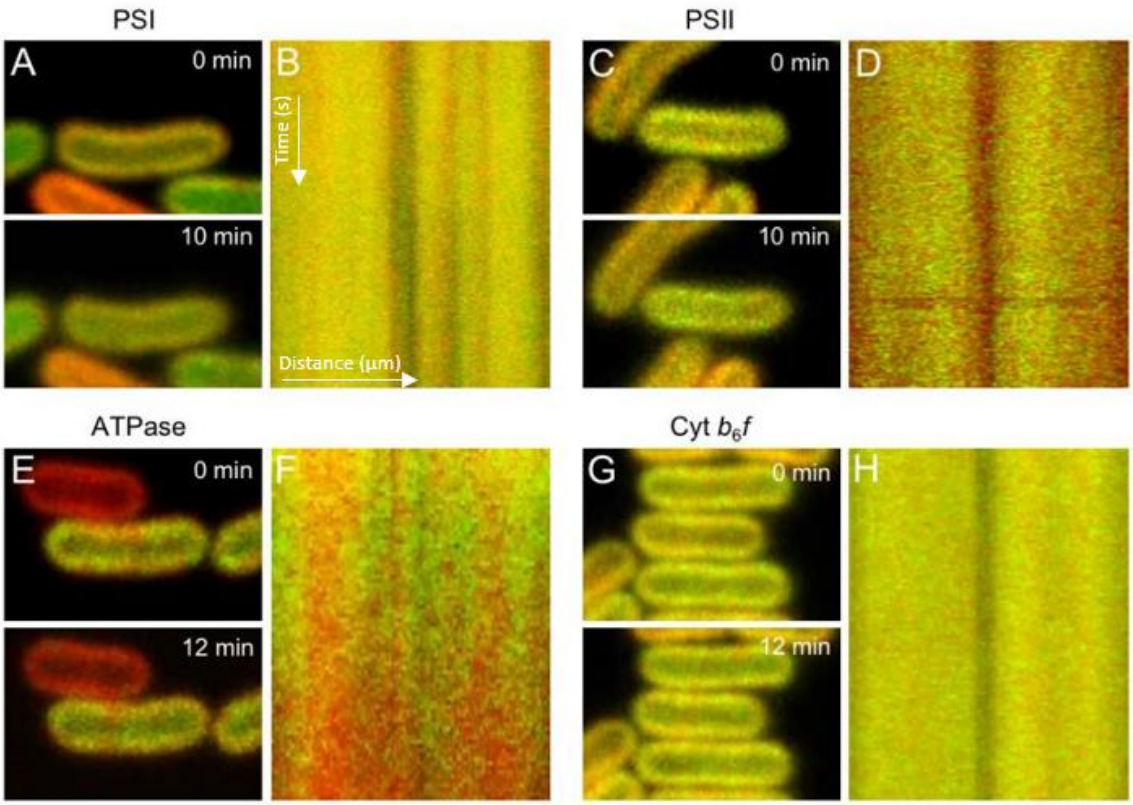

Figure 4-8 Time-lapse confocal microscopy imaging of the distribution and dynamics of photosynthetic complexes without red-light treatment. (A, C, E, G) Confocal images of GFP-tagged PSI, PSII, ATPase and Cyt b_6f Syn7942 cells at 0 min and 10 min (for PSI and PSII) or 12 min (for ATPase and Cyt b_6f). (B, D, F, H) Kymographs of the distribution of photosynthetic complexes, based on the confocal images shown in A, C, E, G. Kymographs start from top at t=0 and end at t=12 min (for ATPase and Cyt b_6f) or t=10 min (for PSI and PSII) at the bottom as indicated by the white arrows in (B).

4.3 Discussion

4.3.1 Distribution and dynamics of the red-light-induced clusters

In this chapter, we characterised a short-term adaptation to red light which is still poorly studied and described in the literature. In our experimental design, the Syn7924 cells were exposed for 1,5 min to intense red light. Soon after the treatment, fluorescent pictures were taken to visualise the localisation of the GFP-tagged complexes, FRAP analysis was carried out for 90 s to study the mobility of the tagged complexes and time-lapses over 12 min were used to monitor

the localisation of the complexes in a longer timescale. Our results, during the 12 min after red light treatment, showed that red light could induce the reorganisation of protein complexes in thylakoid membranes, which may represent a combination of protein mobility within membranes and the structural reorganisation of thylakoid membranes [172, 265]. The finding has categorical implications for the dynamic organisation of cyanobacterial thylakoid membranes, which is instrumental in environmental acclimation. The different reorganization features of PSI and PSII complexes, triggered by red light, suggest the non-uniform localization of PSI and PSII in different thylakoid membrane sacs in Syn7942: PSI complexes appear to be located mainly at the inner layers of thylakoid membranes, and PSII complexes are likely distributed at the peripheral layers of thylakoid membranes (Figure 4-7). It is consistent with previous hyperspectral confocal microscopy results obtained from *Synechocystis* 6803 [178, 179]. Also, ATPase and Cyt b_6f complexes showed the peculiar and differential distribution in patches along the TMs. However, while PSII spots are highly mobile, ATPase and Cyt b_6f appear more stable in their positions.

FRAP experiments, carried out over 90 s after the red-light treatment, further revealed that once the complexes rearrangement occurred, the diffusion rates of PSII, as well as PSI and ATPase are reduced, while it has the undetectable effect on the mobility of Cyt b_6f (Figure 4-6). However, we do not know how fast the rearrangements occur during the 1.5 min of red light treatment, and it would require further investigations with different experimental settings (using same laser power and shorter times prior FRAP measurements). Interestingly, the PSII patches, once formed, do not disassemble but show motility with merging and splitting events (Figure 4-7), reminiscent of the previous finding that PSII mobility could be induced by red light [172]. It is also important to mention that similar laser intensities of blue light or green light on Syn7942 cells did not trigger the redistribution of the chlorophyll signal (from a previous publication [172]). In this contest, we did not investigate the effects of other light wavelengths on the GFP-

labelled strains, which in future experiments could give us more information about the signal specificity of the response and the complexes involved.

A natural question that arises from our findings is whether there is a minimum light intensity to induce the redistribution of the photosynthetic complexes and if this is comparable to outdoor physiological conditions. The experimental settings in our studies were chosen to stimulate a strong cell response in a short time and be able to monitor the cells immediately under the microscope. However, confocal fluorescence microscopy operates with light intensities (0.9 kW/cm^2 or 4.46 10^7 $\mu E/(s*m^2)$) always many magnitudes higher than natural outdoor irradiations (which are around 10^{-4} kW/cm^2) [266]. Consequently, more physiological conditions to observe the phenomena in laboratory should make use of a broadband red light illumination to cells in bulk liquid culture. Under such conditions, previous FRAP experiments on PSII autofluorescence showed a decreased mobile fraction compared to the one red-laser induced [172]. Further experiments confirmed that the percentage of the mobile fraction is dependent on the time of red light exposition [172]. It was explicit that lower red light intensity (1200 $\mu E/(s*m^2)$) needs an increase of exposure time (3 hours) to induce the mobilisation of chlorophyll fluorescence [172]. Given these considerations, it is plausible to hypothesise that the effects here reported can also be relevant with the modest red-light intensity in natural conditions, providing that the exposure time is sufficiently long.

Taken together, our results indicate that the distribution and mobility of photosynthetic complexes in cyanobacterial thylakoid membranes are variable in response to environmental changes, to probably act as the molecular “tuners” for manipulating the pathways and performance of electron transport in cyanobacteria.

Still, many questions remain open about the mechanisms behind the phenomena and how this redistribution and clusterisation will affect the photosynthetic andrespiratory rate.

Possible processes involved in this response, as previously proposed ([172]), could be the perception of the red light from a specific receptor and the creation of a redox signal. In the first case, the red light activates a photoreceptor, leading to a signal transduction pathway and the mobilisation of the photosynthetic complexes throughout the TMs. It is probable that the receptors involved in the light sensing process are red/far-red phytochromes.

In the second case, the exposure to particular light can trigger an imbalance on the redox state of the cell as previously observed in low light on cyanobacterial respiratory complexes (Complex I) [155] and photosynthetic complexes (PSI and PSII) in plants [267]. As we illuminate with a 633 nm laser, we excite preferentially the PBsomes which are associated with PSII (although they can release energy also to PSI). An over-excitation of one photosystem over the other cause an imbalance in the electron pathways and can also damage the photosynthetic apparatus. The homeostasis of the redox state is then maintained by TMs remodelling and/or the change in the complexes localization [155] [267]. Based on these observations, more experiments to look in details the structure of TMs and the role of photoreceptors could give us a better understanding of the cellular response to red light.

Still, with our finding, we emphasised the importance of the light power, the settings and timing used during FRAP experiments especially using naturally fluorescence complexes (see Figure 3-17). Which could explain discrepancies of PSII mobility with previous works and will help for future experiment design.

Chapter 5

Factors determining the dynamics of PSI and PSII complexes: protein size, supercomplexes and temperature

5.1 Introduction

The photosynthetic energy conversion in cyanobacteria occurs in the TM. That membrane is a complex environment where the lateral diffusion processes play an essential role in several cellular functions (e.g. complexes repair, membrane biogenesis, electron transport) [22]. In previous chapters, we estimated the diffusion coefficients of the photosynthetic complexes and its change upon adaptation to red light. Here, we will take a closer look at the molecular and physical basis that regulate the diffusion of transmembrane proteins. We investigate the in *vivo* effect of factors as dimension of the proteins, their supramolecular organisation and temperature, on the regulation of the lateral mobility of PSI and PSII. For a better understanding of the experiment design and results in this chapter, we will briefly describe the parameters involved in the tuning of the protein dynamics.

The dynamics of molecules in the biological membranes is described quantitatively by the diffusion coefficient (D), which has dimension [L^2*t^{-1}], and the mobile fraction (see section 2.8.3). To simplify the model, we first consider a case of protein diffusion due to random movements (Brownian motion), that is when no protein-protein or protein-lipid interactions occur (Einstein's diffusion theory). The theoretical prediction of the diffusion coefficient affirms that D is directly proportional the kinetic energy (E_k) of the particles, inversely proportional to the size (thus the diameter) of the particle and inversely proportional to the viscosity of the medium. All these parameters are taken into account in the equation of Stokes-Einstein for a spherical particle [268]:

$$D = \frac{kT}{6\pi r\mu}$$

where k is the Boltzmann's constant, T the absolute temperature, r the radius of the particle and μ is the viscosity of the medium. The constant kT is directly proportional to E_k of the particle. Since both kinetic energy and μ are dependent on the temperature (E_k is proportional to T while μ decreases with higher T), also D increases upon raise of the temperature. However, upon warming above normal growth conditions, all biological membranes undergo different adaptive mechanisms altering membrane fluidity and protein and lipids compositions [269]. Subsequently, the prediction of the effect of the temperature on the membrane proteins is not straightforward.

It is also possible to infer from this equation that a larger radius of a particle results in a decreased diffusion coefficient. However, due to the peculiar properties of the biological membranes, precise mathematical predictions are often not entirely reflected in the experimental analysis [244-246]. The Einstein's diffusion theory is valid for very "diluted" membranes in contrast with most biological membranes [270]. On the contrary, real TMs appear very densely packed of proteins (see section 3.3) which have well-documented interactions lipid-protein and protein-protein [35, 45, 271-273]. Such conditions increase the viscosity of the membrane and at the same time alter the free diffusion of the transmembrane proteins. Therefore, protein diffusion in crowded and structured membrane can be very different from a standard model (Einstein's diffusion theory). A new representation, called the percolation model, has been developed to consider the impact of protein density and protein aggregations in diffusive processes in the TMs. According to this theory, the structural parameters controlling the lateral diffusion can be divided into four main groups:

- TMs structure (stacked or unstacked membranes, Figure 1-10),
- TM's protein density,
- supercomplexes
- protein supramolecular organisation [270].

We will briefly describe the known effect of these parameters. For a detailed study of the TMs structure, we refer to publications elsewhere [245, 270] since it is not the object of our studies. The protein density, or macromolecular crowding, indicates the quantity of the membrane integral protein complexes. As we calculated and discussed in chapter 3**,** cyanobacterial TMs, as all other photosynthetic membranes, have one of the highest protein density. The physiological advantage of macromolecular crowding is that it enables to high probability for absorbing and process sunlight. However, macromolecular crowding can considerably delay lateral diffusion due to an increment of the membrane viscosity [274]. A high degree of crowding is usually linked to slower protein mobility, with the long-range movement of membrane proteins restricted [182, 275] [176]. However, once reached high protein densities (called percolation threshold), the spatial organisation of the proteins plays a role in the diffusional processes.

The second parameter mentioned is the protein organisation in supercomplexes, which can be assimilated as obstacles along the diffusion path. The presence of large supercomplexes in the photosynthetic membrane is a frequent feature found from plant to bacteria [270]. Examples of supercomplexes found in cyanobacteria are PSI trimers [276], PSII dimers [277], Cyt b_6f dimers [278], PSI–IsiA [279], phycobilisome–PSII–PSI [35], PSI-Ndh-1 [280]. An important question is whether their presence, in an already crowded environment, obstructs or facilitate the diffusion of the photosynthetic complexes. According to the percolation theory, for small hydrophobic molecules, the presence of large supercomplexes do not obstruct the lateral diffusion, but on the contrary, they facilitate the transit through crowded thylakoid membranes [281, 282]. Even if, big supercomplexes are tightly packed, they are unable to fill all the space in the surrounding area, leaving empty a, so-called, interstitial space available for small particles. Monte Carlo simulations have proven this theory for plastoquinone and xanthophylls moving in the TMs [270].

The last parameter considered is the supramolecular organisation which is defined as spatial arrangements of many supercomplexes in a larger scale (between nm-scale and μm-scale). The

effect of these arrangements can be variable for different protein size, so our knowledge about transmembranal protein diffusion is still partial.

In this contest of theoretical uncertainty, we adopted an experimental approach to determine the diffusion parameters of transmembrane complexes with the alteration three factors: particle size, supercomplex formation and temperature.

In our study, we attempted to reduce the size of the PSI by two thirds through the inhibition of the trimerisation of PSI and follow up the lateral diffusion of its monomers. The size effect on the particle diffusion was then monitored by FRAP. Our investigations further considered the role of the supramolecular organisation in the lateral diffusion of PSII. Specifically, we monitored by FRAP the PSII diffusion rate in a PSI trimer-free mutant.

Finally, we examined the effects of the temperature on photosynthetic complexes dynamics (PSI, PSII and ATPase). In this experiment, the cyanobacterial growth temperature was raised of 4 °C, and the protein diffusion was monitored by FRAP.

5.2 Results

5.2.1 Genomic and structural characterisation of the PSI trimer-free strains

The structure of PSI consists of numerous subunits, *AChl* molecules, carotene molecules and other cofactors [283]. While the PSI complex of algae and higher plant is present exclusively in the form of a monomer, in cyanobacteria, it can also be found under a trimeric form. The process of trimerisation is ascribed to the presence of the PsaL subunit, a polypeptide of 166 amino acids located in the centre of the PSI homotrimer (Figure 5-1A) [284]. Two hydrophobic regions in the PsaL subunits, highly conserved among several cyanobacterial strains, take interaction from neighbouring PSI monomers while the subunit PsaI stabilises the connections [44]. Since the PsaL subunit is necessary for the structural stability of the PSI trimers, we have cloned and

sequenced the gene encoding the PsaL subunit and then inactivated it by the insertion of a chloramphenicol resistance cassette. In the end, the fully segregated KO strains should lack PSI-trimers.

The strategy to construct the Δ*psaL* mutants used is shown in Figure 2-2. The segregation of the KO strains produced in our work was verified by PCR (Figure 5-1B) using primers specific for the *psaL* gene (segregation primer listed in Table 2.3). The replacement of the *psaL* gene with the spectinomycin resistance gene was complete in the PSII:eGFP, ATPase:eGFP and Cyt b_6f:eGFP strains showing a unique band at 1500 bp which confirm the full segregation of the spectinomycin resistance cassette. The WT Syn7942 strain was used as negative control of the PCR, which shows a unique band at 800 bp consistent with the presence of the *psaL* gene. However, we did not obtain an entire removal of the *psaL* coding sequence in the PSI:eGFP+Δ*psaL* and Δ*psaL* strains.

Further characterisation was carried out using a BN-gel to evaluate the content of the PSI trimers (Figure 5-1C). It is possible to see the complete absence of the PSI trimer band in the Δ*psaL* and PSII:eGFP+Δ*psaL* strains but not in PSI:eGFP+Δ*psaL* strain. In the BN-PAGE it is also possible to discern the band corresponding to the dimeric PSII (green arrows). It may seem that a decreased amount of PSII dimers could be simultaneous to the absence of PSI trimers, as previously reported by Kłodawska et al. [43]. However, due to the lack of a WT control and the low-resolution image (taken with transmission light of ImageQuant LAS 4000) we cannot confirm this observation and further analysis is required. Also, BN-gels on the ATPase(subβ):eGFP+Δ*psaL* and Cyt b_6f:eGFP+Δ*psaL* strains are to be carried out for future experiments.

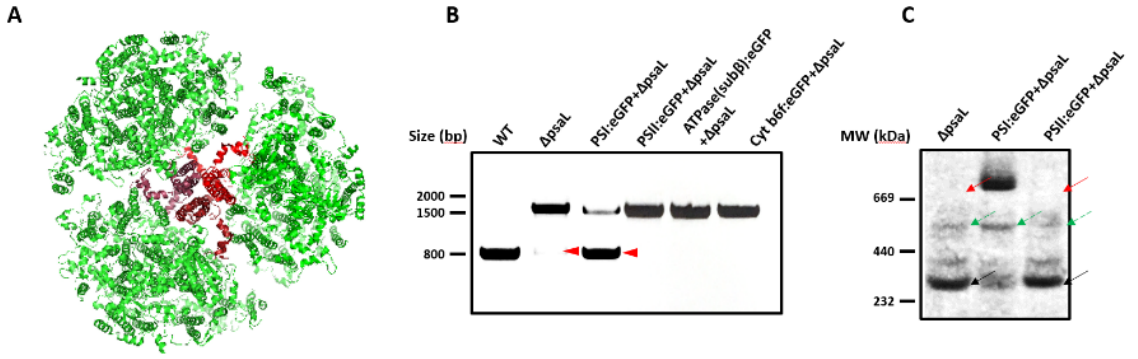

Figure 5-1 Structural model of PSI trimer and characterisation of the *psaL* knock out mutants. (A) View along the membrane normal from the stromal side of a PSI trimer, in red are highlighted the three PsaL subunits responsible of the PSI trimerization. (B) PCR verification of the segregation of *PsaL* knock out strains. The red arrowheads indicate the presence of *psaL* genes in the Syn7942 strains, in particular, a meagre amount is detected in the Δ*psaL* mutant and a consistent amount in the PSI:eGFP+Δ*psaL* mutant. (C) Greyscale image of a BN-gel on Δ*psaL*, PSI:eGFP+Δ*psaL*, PSII:eGFP+Δ*psaL* strains. It shows the absence of the PSI trimers (red arrows) and the localisation of the PSI monomers (black arrows) and PSII dimers (green dashed arrows).

5.2.2 Distribution of photosynthetic complexes in cyanobacterial thylakoid membranes

Distribution of the GFP tagged photosynthetic complexes were visualised by TIRF microscopy and confocal fluorescence microscopy in the PsaL-less strains. eGFP and *Chl* fluorescence of the four eGFP-fused+Δ*psaL* cells were detected using TIRF microscopy (Figure 5-2A). eGFP fluorescence is visible along the cell membrane, and still, it is possible to discern a heterogeneous distribution of the tagged complexes. All these observations are in line with the localisation of the GFP-fused strains in Chapter 3. The global distribution of the photosynthetic complexes in Δ*psaL* cells was further checked using confocal fluorescence microscopy (Figure 5-2B). All strains show the GFP signal localised in the TM as previously found (3.4.2). The distribution of PSI and PSII appear more uniformly distributed along the TM than ATPase and Cyt b_6f, which shows clear patches, as previously observed. Additional TIRF and confocal pictures

are needed for statistical analysis and more quantitative evaluation of the complexes distribution.

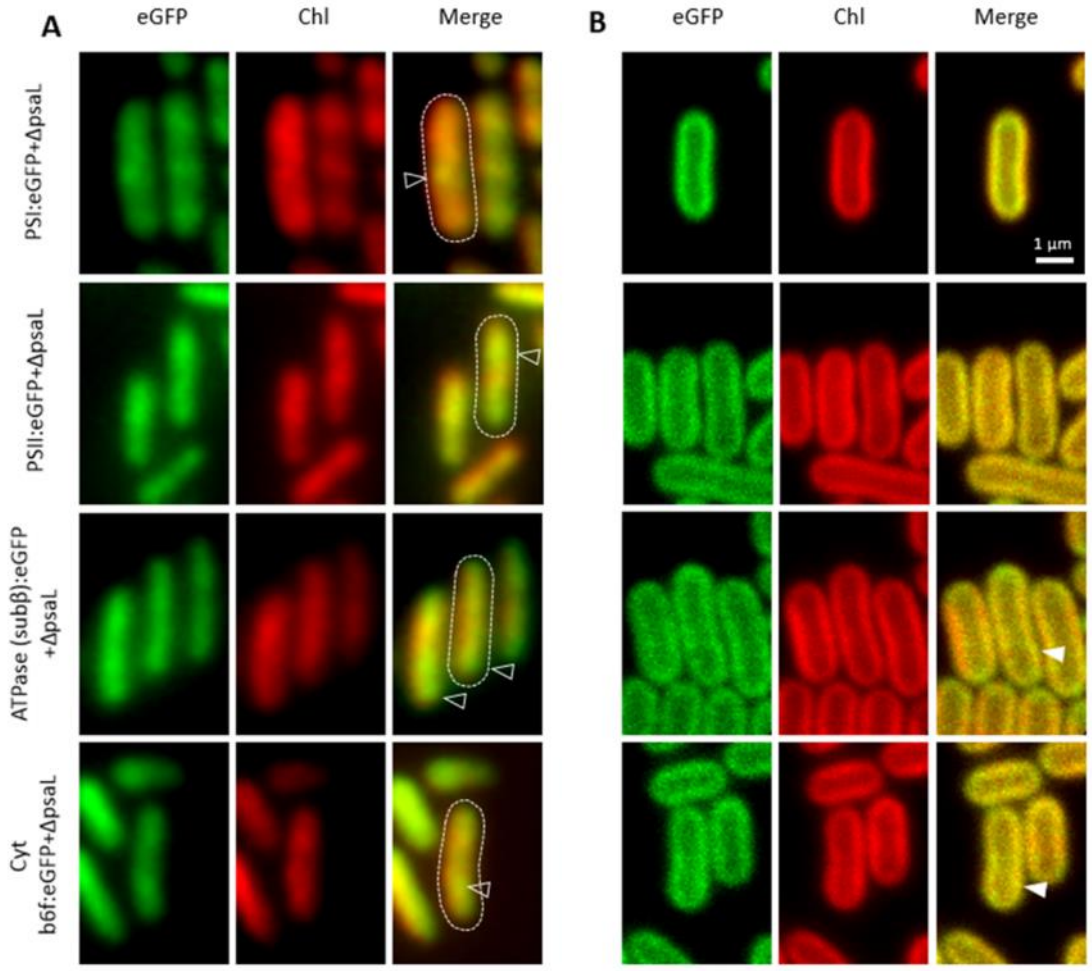

Figure 5-2 Distribution of the photosynthetic complexes in the Δ*psaL* mutants. (A) Single near-TIRF images of PSI:eGFP+Δ*psaL*, PSII:eGFP+Δ*psaL*, ATPase (subβ):eGFP+Δ*psaL*, Cyt b_6f:eGFP+Δ*psaL* double mutants. In the merged channel, the distinct fluorescent patches were indicated (white triangles), and cell body borders were outlined based on bright-field images (white dashed lines). (B) Confocal microscopy images of PSI:eGFP+Δ*psaL*, PSII:eGFP+Δ*psaL*, ATPase (subβ):eGFP+Δ*psaL*, Cyt b_6f:eGFP+Δ*psaL* double mutants. Fluorescence spots of photosynthetic complexes, as indicated by white arrowheads, illustrate the heterogeneous distribution of photosynthetic complexes in thylakoid membranes. Additional images in appendix M.

5.2.3 Mobility of photosynthetic complexes in cyanobacterial thylakoid membranes

The PSI monomerization effects on the diffusion dynamic of eGFP:PSI and eGFP:PSII complexes, were investigated using confocal FRAP analysis. Figure 5-3A and 5-3B show typical FRAP image

sequences of PSI:eGFP+Δ*psaL* and PSII:eGFP+Δ*psaL* mutants. Diffusion of the photosynthetic components, monitored by repeatedly imaging the same cell and recording the spread and recovery of the bleached area, leads to partial fluorescence recovery in the bleached zone (Figure 5-3C and 5-3D).

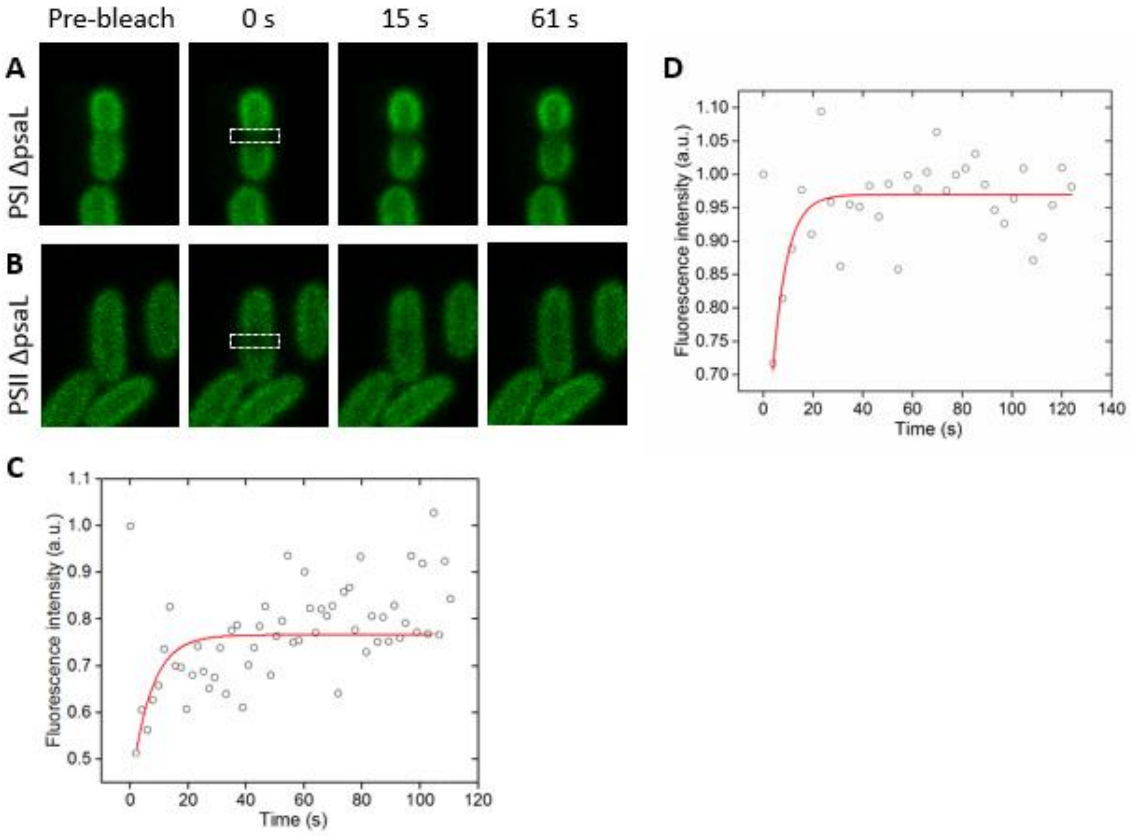

Figure 5-3 FRAP analysis of GFP fluorescence in PSI:eGFP+Δ*psaL* and PSII:eGFP+Δ*psaL* mutants. (A-B) Representative FRAP sequence images of PSI:eGFP+Δ*psaL* and PSII:eGFP+Δ*psaL* mutants. (C-D) Time course of fluorescence recovery of the bleached cell regions (white squares as shown in A-B) for GFP fluorescence. Fluorescence values (in arbitrary unit) are relative to fluorescence before the bleach. The recovery of GFP fluorescence is presented as circles and fitted to an exponential function (red lines). Additional recovery curves are shown in appendix N.

Effect of the size reduction – Tuning the size of transmembrane complexes provides a way to investigate the effect on the protein mobility in TMs. For this purpose, we chose to alter the size of the PSI complexes and measure its long-range diffusion by using FRAP. A similar approach was used previously with PBsomes [246]. We expected to monitor and compare the diffusion of

PSI:eGFP in both its monomeric and trimeric forms. However, in the PSI:eGFP+Δ*psaL* strain produced the PSI mainly appeared as trimers in the BN-PAGE. Despite incomplete segregation of the strain we proceeded to track the PSI complex by FRAP, under normal growth conditions (50 µE/(s*m^2)).

We found that the diffusion coefficient of PSI is not altered in PSI:eGFP+Δ*psaL* cells (Figure 5-4B). However, we also observed a shift of mobile fraction (Mf) of PSI from 60 ± 17% (n=30) in the WT membrane to 67 ± 14% (n=38), in the PSI:eGFP+Δ*psaL* strain (Figure 5-4). This last observation is coherent with the PCR results (Figure 5-1) which show an unidentified number of *psaL* genes successfully knocked out (band at 1500 bp). Thus, we could presume a slight increase of PSI monomers or a change in the PSII oligomerisation which is not detectable in the BN-PAGE due to its poor quality. Further analysis would be necessary to quantify the exact amount of monomeric PSI and PSII in the PSI:eGFP Δ*psaL* strain compared to WT.

Effect of obstacle size – Mutants lacking PSI trimers provide a further opportunity to explore the role of the supramolecular organisation on the diffusion of other transmembrane complexes. We have used a PSII:eGFP+Δ*psaL* mutant to track the movements of PSII in the complete absence of PSI trimers. In this strain, the inactivation of the *psaL* gene, involved in the process of PSI trimerisation, successfully produced PSI trimer–free strains as previously reported [284, 285] and confirmed by PCR and BN-PAGE.

The size reduction of the PSI supercomplexes is expected to decrease the diffusion coefficient of smaller complexes [270]. However, we do not know which effect this will cause to a big size complex such as the PSII.

We found that PSII has a 2-fold increase in the D value when PSI is under the monomeric form. Moreover, PSII has a decrease of Mf from 75 ± 12% (n=45), in the WT membranes, to 65 ± 16% (n=45) in the PSI trimer-free membranes (Figure 5-4). FRAP data on PSII provided evidence that

in a PSI trimer-free membranes PSII diffusion is facilitated and its interactions with the immobile scaffold are weakened. Further analysis is needed to investigate the multimeric form of PSII.

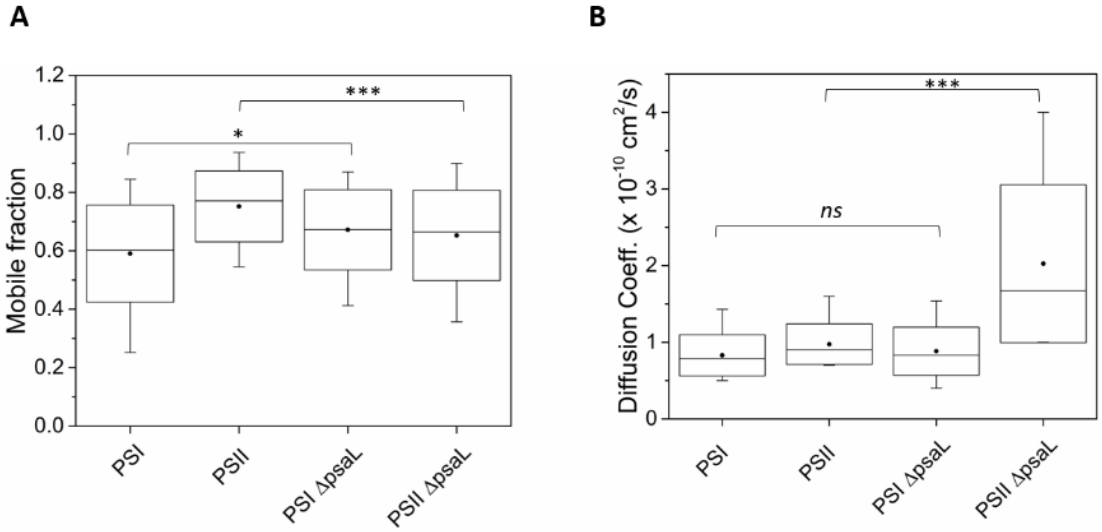

Figure 5-4 Mobility features of the GFP-tagged PSI and PSII in WT and Δ*psaL* strains. (A) Quantification of the mobile fractions in PSI and PSII complexes. GFP-tagged complexes were monitored in WT's and Δ*psaL* strains. (B) Quantification of the diffusion coefficient of PSI and PSII complexes. GFP-tagged complexes were monitored in a WT's TMs and in a Δ*psaL* TM. (eGFP:PSI+Δ*psaL* n= 38) (eGFP:PSII+Δ*psaL* n= 45). The box shows the standard deviation; the whisker shows data from 5 to 95% range; the dot represents the average; the line is the median value. P values were calculated using a Student T-test as indicated; * 0.01 < P < 0.05, *** P < 0.001; ns, not significant. Note that eGFP:PSI+Δ*psaL* mutant is not fully segregated.

Effect of the temperature- We aimed to unravel the effects of temperature on the transmembrane protein dynamics by increasing the growth temperature of Syn7942 cells from 30°C to 34°C for five days. We used the eGFP as a fluorescent marker to individually track PSI, PSII and ATPase in single labelled strains. Then, by FRAP analysis, we determined the thermal dependence of the diffusion of PSI, PSII and ATPase complexes (Figure 5-5).

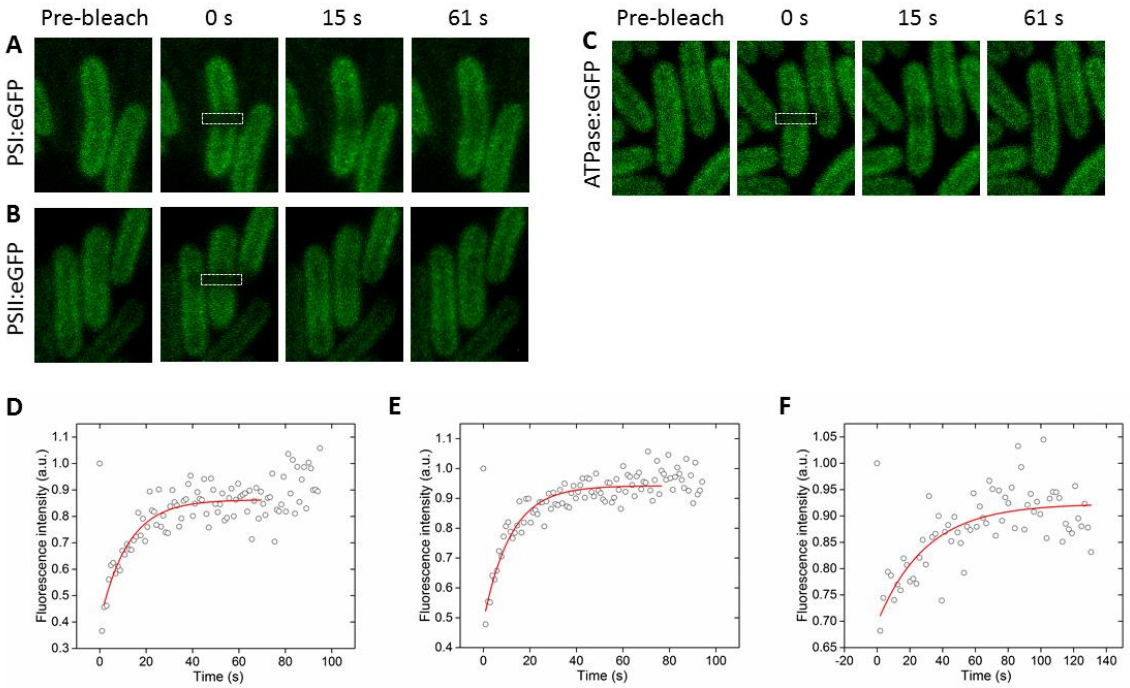

Figure 5-5 FRAP analysis of GFP fluorescence in PSI:eGFP, PSII:eGFP and ATPase:eGFP cells adapted at 34 °C for five days. (A-C) Representative FRAP sequence images of PSI:eGFP, PSII:eGFP and ATPase:eGFP cells. (C-F) Time course of fluorescence recovery of the bleached cell regions (white squares as shown in A-C) for GFP fluorescence. Fluorescence values (in arbitrary unit) are relative to fluorescence prior to the bleach. The recovery of GFP fluorescence is presented as circles and fitted to an exponential function (red lines). Additional recovery curves are shown in appendix O.

FRAP data revealed an increased mobile fraction of PSI and PSII complexes (Figure 5-6A), but no significant changes in the Mf of the ATPase complex. Interestingly, at 34 °C, the mobile fraction of all the three complexes have less dispersion of the values with a tendency to an upper common value. In contrast, the diffusion coefficients appear to react differently to the increased temperature. The PSII complex has a distinct increase of the D coefficient, but the D coefficient of PSI and ATPase did not present any significant changes between 30°C to 34°C (Figure 5-6B). Differential alteration of the diffusion coefficients among the photosynthetic complexes could be an index of different interaction with proteins and lipids or evidence of selective control.

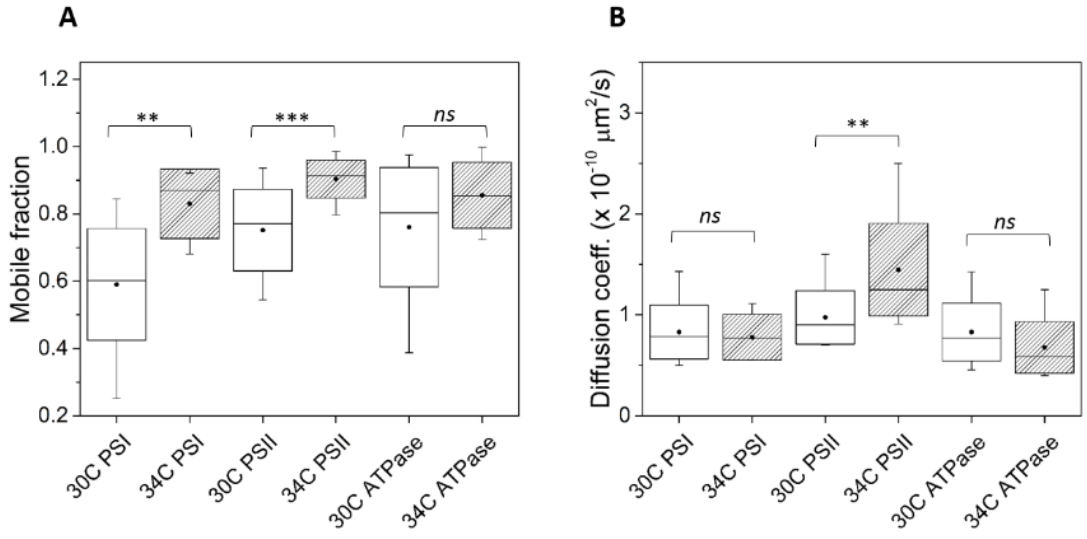

Figure 5-6 Mobility feature of the GFP-tagged PSI, PSII and ATPase cells adapted at 30 °C and 34 °C for five days. (A) Quantification and comparison of the mobile fractions between cells grown at 34 °C (PSI=5; PSII=12; ATPase=11) and 30 °C (PSI=34; PSII=43; ATPase=26). (B) Quantification of the diffusion coefficients between cells grown at 30 °C and 34 °C. The box shows the standard deviation, the whisker shows data from 5 to 95% range, the dot represents the average, the line is the median value. P values were calculated using a Student T-test as indicated; ** 0.001 < P < 0.001, *** P < 0.001; ns, not significant.

5.3 Discussion

Lateral migration of transmembrane proteins in the TMs is of vital importance for acclimation of the photosynthetic apparatus in response to external cues. As we discussed in section 5.1, protein dynamics are modulated by several physicochemical (temperature, the viscosity of the medium, the radius of the diffusing protein) and structural parameters (protein aggregation) [270]. However, the quantitative effect of these factors on the differential protein mobility is unknown for most of the transmembrane proteins in the TM compartment [286].

In this chapter, our purpose was to examine the effect of the temperature, the protein size and the supramolecular organisation on the photosynthetic protein lateral diffusion.

Effect of the size reduction on PSI – The diffusion of transmembrane proteins is strongly influenced by interactions with an immobile scaffold (lipids or proteins) and molecular crowding, in which the diffusion of large molecules should be more impeded compared to small molecules [282]. The importance of the size in the protein mobility was also verified in the cytoplasmic phase, where phycobilisome reduced in size diffuses faster than their regular counterpart [246, 287]. To explore the impact played by the size of a molecule into its lateral diffusion, we chosen to monitor the PSI:eGFP under its monomeric form (Δ*psaL* strain). Accordingly to the model discussed by Camley *et al.* [244], the coefficient of diffusivity of a particle is inversely proportional to its radius. Thus we should expect that the PSI diffusion coefficient increase by three times when it is under the monomeric form.

However, despite other Δ*psaL* strains fully segregate, the PSI:eGFP+Δ*psaL* strain maintained part of its *PsaL* genes, still showing PSI trimers on BN-PAGE (Figure 5-1). We can speculate that the GFP fused on the PsaE subunit and the simultaneous deletion of PsaL subunit may cause abnormalities in the cyclic electron flow around PSI which are not compatible with vital cells [42, 44]. However, also the Δ*psaL* strain failed to fully segregate in the time we had available (although previously done elsewhere). It is possible that this batch of cells did not have the suitable conditions for a good transformation. Future experiments are required to verify the efficiency of the cyclic electron flow by $P700^+$ re-reduction kinetics (see section 2.7.4).

In line with this result, we found that PSI's diffusion coefficients did not show a significant difference in wild-type and Δ*psaL* cells (Figure 5-4B). However, the PSI's mobile fraction appeared increased, leading to a supposedly less stable contact between PSI and the immobile scaffold. It needs to be verified if the exiguous number of *PsaL* gene inactivated in the PSI:eGFP+Δ*psaL* strain can have this substantial effect on the mobile fraction of PSI.

Thus, it remains unclear if the diffusion rate of PSI is affected by size reduction and in which extend it influences mobile fractions. It could be possible, for future studies, attempt to build a

PSI:eGFP+Δ*psaL* strain positioning the GFP tag in a different PSI subunit or track the mobility of another photosynthetic complex.

Effect of obstacle size – It is generally accepted that, although high protein density impedes lateral diffusion, the organisation of membrane proteins in aggregates could produce more compact obstacles which maximise the volume available for the movement of smaller molecules such as plastoquinol [282]. However, the qualitative impact of the size of the obstacles on larger photosynthetic complexes has not been addressed.

To explore the impact played by the size the supercomplexes in the overall diffusion of transmembrane proteins, we chosen to monitor the diffusion of PSII:eGFP in a Δ*psaL* strain. We successfully deleted all the copies of the *PsaL* gene obtaining a fully segregated double mutant PSI:eGFP+Δ*psaL*, as proven by PCR. Moreover, the mutant did not show PSI trimers on BN-PAGE (Figure 5-1). Our FRAP experiments on this mutant showed a decrease of the PSII's mobile fraction but an increase of its diffusion coefficient in the PSI trimer-free TMs. Our data suggest that the presence of the PSI trimers in wild-type TMs restrains the diffusion of PSII. Generalising we could infer that the reduction of large obstacles in the TMs facilitates the diffusion rate of complexes with comparable size. However, it was previously reported that the PSI monomerisation could also cause a decrease of PSII monomers and dimers [43]. In this latter scenario, the increased diffusion coefficient of PSII to values like Cyt b_6f (see section3.5), could be due also to decreased crowding and PSII complexes size reduction in TMs. Additional experiments studying the mobility of ATPase and Cyt b_6f in a PsaL-less strain should test the influence of the PSI monomerisation on other transmembrane proteins. Finally, our FRAP experiments also showed a decreased PSII mobile fraction. Thus, we can suppose that the local environment of PSII changes in response to the PSI's monomerisation, allowing more contacts with the surround. In this sense, further experiments to disclose changes in the protein

interactions in the PSI:eGFP+Δ*psaL* strain could help to have a better understanding of the dynamics of the protein in TMs.

Effect of the temperature – The effects of the temperature on the solar energy conversion efficiency and growth performance of photosynthetic organisms have been under study for decades [288, 289]. According to the literature [269], the increase of the temperature produces a series of changes in the TMs environment which have contrasting effects on the protein mobility. Among the transitions occurring in response to higher temperature, we can cite the increase of membrane fluidity, the decrease of unsaturated fatty acid [290], the change of protein quantity and type, formation of active oxygen radicals [291], reduction of carotenoids synthesis [292]. It is also being reported that higher temperature (35 °C) lead an increase of the photosynthetic electron flow and lead the PSII reaction centres in an oxidised state [289]. All these simultaneous changes make challenging to formulate theoretical predictions on the dynamics of transmembrane proteins.

In this chapter, we studied the thermal adaptation of photosynthetic complexes dynamics upon heating from 30 °C to 34 °C. Our FRAP experiments showed an increased D coefficient of PSII while PSI and ATPase maintain a constant behaviour. We also observed a significant increase of the mobile fraction in PSI and PSII, but no changes were detected in the ATPase. Only PSII showed a distinctive increment of both mobile fraction and diffusion rate which could be imputable to weaker interactions with the surrounding less-mobile proteins or stronger interaction with the more fluid lipid environment. Perhaps specific lipids or the general lipid environment of the membrane play a crucial role in mediating interactions between photosynthetic complexes. In other words, we found that there is a selective increase in the mobile fractions and diffusion coefficients of the photosynthetic complexes. Thus, protein dynamics do not passively reflect the TMs fluidity, but their lateral displacement is a controlled mechanism.

Chapter 6

Conclusions

6.1 Introduction

This research focuses on the dynamics and distribution of the photosynthetic complexes in the thylakoid membrane of the cyanobacteria *Synechococcus elongatus* PCC 7942. Specifically, we investigated the density, localisation and diffusivity of the four main complexes: PSI, PSII, ATPase and Cyt b_6f. Since it is known that the photosynthetic and respiratory machinery of cyanobacteria has a dynamic and flexible equilibrium, we hypothesised that the proteins complexes should be highly mobile. The focus of the presented experiments was on examining the organization and mobility feature of the photosynthetic complexes and the interferences on these dynamics form external and internal parameters. Here, we studied the response to the variation two relevant factors, red light and temperature. We also described the influence of internal parameters like the supramolecular organisation and the protein size on the complex motility. The principal techniques used were confocal and TIRF microscopies; both required the use of fluorescent-tagged complexes, which were not available. For that reason, the experiments performed in this work range from the design of new strains and physiological assays, to localization and mobility analyses.

In the subsequent sections, the most important results from previous chapters will be separated in two main sections:

- TMs composition and spatial distribution of the photosynthetic complexes
- Dynamics of the photosynthetic transmembrane proteins.

We will briefly summarise and comment our findings, with an outlook on possible future work.

6.2 TMs composition and their spatial distribution

The spatial and supramolecular organisation of the TMs are essential in maintaining high efficiency of photosynthetic processes and a correct redox state of its components (see section 1.5.2). Moreover, the TMs has also to respond to the changing environmental conditions by altering these arrangements. Knowledge of the localisation of the supercomplexes in TMs is therefore essential for understanding the function and the homeostasis of this highly complex and dynamic system. In the third and fourth chapters, we determined the protein density and relative abundance of the four central photosynthetic complexes (PSI, PSII, ATPase and Cyt b_6f). We also localise these complexes in standard growth conditions (30 °C, 50 µE/(m2*s)) and in presence of red light, providing a high-resolution description of TMs at nm and µm scale.

Protein crowding and disposition, in the TMs of wild-type Syn7942, were determined by using AFM. We calculated that the 75% of the TMs is composed of proteins, which is in line with other functional membranes such as the inner membrane of mitochondria and grana thylakoids chloroplasts [75, 219, 293, 294]. This protein concentration makes the cyanobacterial TMs among the most crowded biological membrane in nature [224]. We also observed an interspersed arrangement of PSI and PSII oligomers together with Cyt b_6f, but it was not possible to identify ATPase or PSI/PSII monomers due to lack of typical features.

Our visualisation of the GFP fluorescence by confocal and TIRF microscopy gave a new description of the distribution of the GFP-tagged PSI, PSII, ATPase and Cyt b_6f. Specifically, it appears that ATPase and Cyt b_6f have distinguishable small patches along the TM, while PSI forms large aggregations in an extremity of the cell and PSII has a more uniform arrangement. Using quantitative analysis of fluorescence images, the relative ratio of the four photosynthetic complexes was further calculated. ATPase showed to be the less abundant, followed in order by Cyt b_6f, PSII and PSI with a stoichiometry of 1:1.9:2.3:10 respectively.

We further proceeded our studies on the effect of red light on the localisation of the photosynthetic complexes. Previous authors examined the photosynthetic performance of cyanobacteria under various light quantities and qualities [295]. Although light responses either increase or decrease overall cellular productivity [296], it appears that the red light, not just has the most intrigued light sensing mechanism, but also maximise the growth rate and also the photosynthetic efficiency [295]. Exploring the effect of red light could be essential for further development of cyanobacterial production system and could provide us with a tool for tuning cell responses (for example to channel the conversion of the chemical energy to biomass).
Analysis of confocal pictures shown a remarked rearrangement of all the GFP-tagged complexes after red light treatment: PSII, ATPase and Cyt b_6f concentrate in distinctive patches; PSI appears distributed in all the TMs but, in specific areas, it localises in the inner layer of the TMs which seems bent. More information about the remodelling of the TMs red light adapted cells could be provided in future by electron microscopy, which has a higher resolution than confocal microscopy.

We have seen how in both standard growth conditions and after red light treatment, in general, the distribution of the photosynthetic complexes is tendentially uneven and sometimes perceptibly organised in agglomerations (the patches or spots). This is not a prerogative of cyanobacterial photosynthetic membranes. In other equally relevant membranes (such as the mitochondrial cristae membrane [297], the mammalian plasma membrane [298], the TMs of chloroplasts [299], the plasma membrane in E.Coli [239]) there are evidence of supercomplexes and also higher-level organizations (called patches, strings, arrays or domains), both in term of lipids and proteins. It is clear that ordered distribution is required for specific functions. Investigations in mitochondrial and photosynthetic membranes, where the electron pathways cover a central role, found that the super-assembling could be implied in the enhancement of the flow of electrons by reducing the distance of diffusion of the mobile electron carriers (e.g. ubiquinone and cytochrome)[300, 301]. It was also proposed that domains are essential in

preventing excess oxygen radical production [302]. However, the occurrence of several specific supercomplexes and higher ordered oligomers must have other functional purposes. In mitochondria, for example, it has been found that is essential for the assembly and stability of the individual complexes and the local curvature of the cristae membrane [303-305]. Several studies have been performed to describe the respiratory and the photosynthetic electron transports and their regulation. Missing information was often completed by looking at TMs (in cyanobacteria, algae and plants) and the mitochondrial inner membrane since they share significant similitudes.

Our results of spatial mapping of the protein stoichiometry and localisation, just summarised, allowed us to refine further the picture of the thylakoid membrane organisation and response. However, information on the subunit interaction and superassembly are still necessary to have a complete description of the electron transport machinery. In future experiments, it would be interesting to explore the patches composition in cyanobacteria. Confocal pictures of double labelled strains (GFP, YFP) could elucidate protein interactions and colocalizations. Recently advances in the pull-down assay coupled to mass spectrometry are promising to determine the composition of the photosynthetic patches in native conditions.

6.3 Mobility of PSI, PSII, ATPase and Cyt b_6f in the cyanobacterial thylakoid membrane

In the previous section, we have seen how the supramolecular organisation and localisation of the photosynthetic complexes is a mechanism highly regulated in cyanobacteria. Nevertheless, it is also dynamic because it adjusts continuously to the external stimuli optimising the light-energy conversion (see sections 1.4, 1.5, 1.6). However, the basic information about the mobility of the major membrane complexes are fragmentary and accurate models of the TMs activities

cannot be built. Thus, many functions of the TMs cannot be fully understood (electron transport regulation, protein biosynthesis, protein turnover and repair).

Therefore, we studied the photosynthetic dynamics in standard growth conditions and in response to the variation of three relevant factors: red light, temperature and supramolecular organisation.

Standard growth conditions – Our FRAP experiments conducted in standard conditions (30 °C and 50 µE/(m^2*s)), provided information about the mobility features of the photosynthetic complexes, providing further evidence that the photosynthetic complexes are a dynamic, rather than a static, configuration. A low percentage of PSI appeared to be mobile (60%) compared with PSII (75%), ATPase (76%) and Cyt b_6f (78%). The diffusion rates of PSI, PSII and ATPase are lower compared to Cyt b_6f, but still in the same order of magnitude of 10^{-10} cm^2/s. Comparison of our results with the literature (Table 6.1) shows that the photosynthetic complexes are ten times slower than the surrounding lipids in TMs measured in Syn7942 [306]. Despite the recognised influence of the protein size on the diffusion coefficient, our results showed no appreciable variations of diffusion rates accordingly with the complexes dimensions. In fact, the areas occupied by the ATPase in the TM is nine times smaller than PSI and PSII, but it exhibits a similar diffusion coefficient. We could instead postulate a critical role played by different interactions between proteins and immobile fraction which has not been tested for thylakoid proteins in details.

Red-light adaptation – We further proceeded our studies exploring and characterised the photosynthetic dynamics of PSI, PSII, ATPase and Cyt b_6f complexes in response to intense red-light. Our FRAP analysis of treated cells shows that PSI and PSII mobile fractions values are similar before and after the treatment, while Cyt b_6f and ATPase mobile fractions show a significant decrease. Moreover, decreased diffusion rates were observed in PSI and PSII and Cyt b_6f except for ATPase which does not show any significant change. Time lapses carried out over 13 min displayed that spots of PSII are highly mobile, but patches of ATPase and Cyt b_6f appeared quite

static. Again, PSI appears localised more in the inner layer of the TM, where probably the TMs structure is reorganised. The identification of the criteria behind the patches distribution and eventual colocalizations may be identified by further work on strains containing multiple tagged complexes. We hypothesised two possible processes involved in this red-light response: the activation of photoreceptors or an alteration of the redox state of an intermediary of the electron chain. It would be worth to explore these mechanisms and know how they can affect the efficiency of the light harvesting.

Effect of obstacle size – Influence of the supramolecular organisation on the lateral diffusion of PSII was investigated in PsaL-free strains, where the formation of PSI trimers was prevented. In this case, the size of the obstacle (PSI trimers) was reduced by two third. We demonstrated, by FRAP experiments, that PSII has a two-fold increase of D coefficient in the PSI trimer-free TMs, but the percentage of mobile PSII is decreased. This finding supports the idea that the presence of the PSI trimers restrains the diffusion of PSII. Generalising we could infer that the size reduction of large obstacles facilitates the diffusion rate of complexes with comparable dimensions. However, since the PSI monomerisation could also cause a decrease of PSII monomers and dimers [43], the increased diffusion coefficient of PSII could be due also to decreased TMs crowding and PSII complexes size reduction. Our data also suggest that, in response to the PSI's monomerisation, the contacts of PSII with the surround is stronger. However, we cannot infer that these changes are due exclusively to the PSI trimer-free environment. Further investigations need to elucidate if the PSI monomerisation could affect other supramolecular assemblies or alter protein density in the TMs.

Effect of the temperature – The thermal adaptation of photosynthetic complexes dynamics was probed upon heating from 30 °C to 34 °C the cell cultures. The increase of the growth temperature in cyanobacteria produces a series of changes in the TMs which have contrasting effects on the protein mobility. Thus, predictions of the protein diffusion are challenging. Our

FRAP experiments showed an increased diffusion coefficient of PSII while PSI and ATPase maintain a constant behaviour. We also observed a significant increase of the mobile fraction in PSI and PSII, but no changes were detected in the ATPase. These data show a diverse increment of mobile fractions and diffusion rates among the photosynthetic complexes which perhaps reflect changes in their specific interactions with the surrounding area.

The summary of the studies addressing the mobility of protein and lipids in literature (in black) and our results (in red) are presented in Table 6.1. As we can see, there is a limited number of studies about the mobility of photosynthetic complexes not provided of autofluorescence.

Table 6.1 Summary of diffusion coefficients in literature. In black are listed diffusion coefficient from previous publications [142, 270]. In red are written the diffusion coefficient values calculated in our studies. Abbreviations: SPT-single particle tracking; FRAP- fluorescence recovery after photobleaching; FCS- fluorescence correlation spectroscopy.

Compartment	Technique	Diffusion coefficient ($\mu m^2/s$)	Ref.
Cell compartments			
Water (GFP)	FRAP	87	[307]
Plant cytoplasm (GFP)	FCS	40	[308]
Animal cytoplasm (GFP)	FRAP	25	[307]
Mitochondrial matrix (GFP)	FRAP	20-30	[309]
Prokaryotic cytoplasm (GFP)	FRAP	6-9	[310]
Prokaryotic periplasm (GFP) *Ecoli*	FRAP	2.6	[310]
Chloroplast stroma (GFP)	FCS	0.9	[308]
Cyanobacteria cytoplasm (based on PBS)	FRAP	0.03	[246]
Thylakoid lumen (Phycoerythrin)	FRAP	~0	[311]
Eukaryotic membranes			
Plasma membrane (protein)	FRAP	0.25-0.75	[312]

Endoplasmatic reticulum (protein)	FRAP	0.26-0.49	[313]
Lipids	FRAP	1-4	[314]
Mitochondria membranes			
Cytochrome bc_1	FRAP	0.1-1	[315]
F_1F_0-ATPase	FRAP	0.1	[315]
Cytochrome c	FRAP	0.016	[316]
Photosynthetic proteins of thylakoid membranes			
Cytochrome b_6f (GFP)	FRAP	0.0162	[317]
F_1F_0-ATPase (GFP)	FRAP	0.0083	[317]
Plastocyanin		Unknown values	
PSI (GFP) (GFP)	FRAP	0.0083	[317]
PSII (GFP) (GFP)	FRAP	0.0098	[317]
Phycobilisomes core	FRAP	0.07	[246]
Phycobilisomes	FRAP	0.004-0.03	[246] [92]
Phycoerythrins	FRAP	~0	[311]
LHCIIp—in stroma	SPT	0.03	[247]
LHCII in stroma	SPT	0.003	[247]
LHCII in grana	FRAP	0.005	[224]
IsiA—cyanobacteria	FRAP	0.003	[318]
Photosystem II—red light (Chl fluorescence)	FRAP	0.023	[172]
Photosystem II—dark (Chl fluorescence)	FRAP	~0.00002	[92] [318]
PSII grana	Simulation	<0.000001	[294]
Lipids	FRAP	0.06-1	[306]
PQ thylakoids (plants)	Pyrene fluorescence quenching	0.01-0.3	[319]

PQ liposomes	Pyrene fluorescence quenching	10-30	[320, 321]
LHCII grana	Simulation	0.000013	[322]
PSI- red light (GFP)	FRAP	0.0054	[317]
PSII-red light (GFP)	FRAP	0.0088	[317]
ATPase-red light (GFP)	FRAP	0.0054	[317]
Cyt b_6f-red light (GFP)	FRAP	0.0083	[317]
PSII-with monomeric PSI (GFP)	FRAP	0.0202	Section 5.3
PSI (GFP)	FRAP at 34 °C	0.0078	Section 5.3
PSII (GFP)	FRAP at 34 °C	0.0145	Section 5.3
ATPase (GFP)	FRAP at 34 °C	0.0068	Section 5.3

There is a whole range of different fluorescence microscopic methods that can be used (FRAP, FCS, FRET) which are suitable to track the protein mobility on a single cell level. However, the most intensively adopted is the FRAP method. According to these values, computer simulations predict diffusion coefficients always much lower than experimental data. It suggests that simulations are not able to reproduce what is realised in native TMs. It is possible that the difference between experimental data and computer simulation is due to the supramolecular organisation of the proteins. According to the percolation theory (see section 5.1), once the protein density reaches a certain value (called percolation threshold), the existence of ordered arrays of proteins creates more diffusive space available for small proteins. However, larger proteins have still constrained mobility (as supported by our FRAP results). Moreover, stoichiometry, protein distribution and packing can change during the adaptation processes in ways and timing not well characterised [270]. Then we can presume that simulation models need further descriptive parameters of the TMs organisation to reach a higher accuracy. Another simplified system to track long-term protein diffusion is the use of artificial lipid bilayer, however

in this case protein movement appear 50-500 times faster than within the plasma membrane [323].

From Table 6.1 we also learn that the diffusivity changes in distinct compartments. The protein diffusion is higher in eukaryotic plasma membranes compared to TMs (of cyanobacteria and chloroplast). This could be due to the higher protein crowding in TMs [142] but also on specific lipid-protein and protein-protein interactions.

Elucidating the precise protein density, their diffusivity and complexes assembling gave us more understanding about the effect they could have on diffusion dependent-processes in TMs. Leading us a step ahead on efficient theoretical modelling of biomembranes.

6.4 Final conclusions

During the past decades, cyanobacteria have been identified as a suitable organism for biotechnological applications as well as renewable biofuels. Due to their high photosynthetic rates and their ability to be easily genetically modified to produce compounds of interest, they are considered valuable organisms for economical, industrial-scale production processes [295, 324]. Consequently, it is crucial to elucidate the mechanisms behind the acclimation responses, which have a substantial impact in either promoting photoprotection (energy dissipation) or enhancing the production of desired end-products [296].

In conclusion, our work provided a more detailed picture of the cyanobacterial photosynthetic complexes organisation (in term of protein quantity ad stoichiometry, lateral segregation) and their plasticity (response to red light, temperature, supramolecular organisation). The characterisation of the diffusivity of these photosynthetic complexes and their reorganisation represents a novelty in cyanobacterial physiology. Quantifying the numerous dynamic phenomena will be an essential step to clarify the lateral diffusion's crucial role in the regulation of numerous cellular processes. Our findings and others can perhaps be synergistically used to

improve the adaptation of these strains to conditions more suitable for industrial productions and their use as cell factories.

Bibliography

1. Keeling, R.F., et al., *What atmospheric oxygen measurements can tell us about the global carbon cycle.* Global Biogeochemical Cycles, 1993. **7**: p. 37-67.
2. Falkowski, P.G. and Y. Isozaki, *The Story of O₂.* Science, 2008. **322**(5901): p. 540-542.
3. Falkowski, P.G., et al., *The rise of oxygen over the past 205 million years and the evolution of large placental mammals.* Science, 2005. **309**(5744): p. 2202-4.
4. Blankenship, R.E. and H. Hartman, *The origin and evolution of oxygenic photosynthesis.* Trends in Biochemical Sciences, 1998. **23**(3): p. 94-97.
5. Falkowski, P.G. and A.H. Knoll, *CHAPTER 1 - An Introduction to Primary Producers in the Sea: Who They Are, What They Do, and When They Evolved*, in *Evolution of Primary Producers in the Sea*. 2007, Academic Press: Burlington. p. 1-6.
6. Raven, J.A. and J.F. Allen, *Genomics and chloroplast evolution: what did cyanobacteria do for plants?* Genome Biology, 2003. **4**(3): p. 209-209.
7. Martin, W., et al., *Evolutionary analysis of Arabidopsis, cyanobacterial, and chloroplast genomes reveals plastid phylogeny and thousands of cyanobacterial genes in the nucleus.* Proc Natl Acad Sci U S A, 2002. **99**(19): p. 12246-51.
8. Giovannoni, S.J., et al., *Evolutionary relationships among cyanobacteria and green chloroplasts.* Journal of Bacteriology, 1988. **170**(8): p. 3584-3592.
9. Pisciotta, J.M., Y. Zou, and I.V. Baskakov, *Light-dependent electrogenic activity of cyanobacteria.* PLoS One, 2010. **5**(5): p. e10821.
10. Wang, B., et al., *Application of synthetic biology in cyanobacteria and algae.* Front Microbiol, 2012. **3**: p. 344.
11. Kaneko, T., et al., *Structural analysis of four large plasmids harboring in a unicellular cyanobacterium, Synechocystis sp. PCC 6803.* DNA Res, 2003. **10**(5): p. 221-8.
12. McConnell, I., G. Li, and G.W. Brudvig, *Energy Conversion in Natural and Artificial Photosynthesis.* Chemistry & biology, 2010. **17**(5): p. 434-447.
13. Grätzel, M., *The Artificial Leaf, Molecular Photovoltaics Achieve Efficient Generation of Electricity from Sunlight.* Comments on Inorganic Chemistry, 1991. **12**(2-3): p. 93-111.
14. Styring, S., *Artificial photosynthesis for solar fuels.* Faraday discussions, 2012. **155**: p. 357-376.
15. Wang, B., et al., *Application of synthetic biology in cyanobacteria and algae.* Frontiers in microbiology, 2012. **3**.
16. DeRuyter, Y.S. and P. Fromme, *Molecular structure of the photosynthetic apparatus*, in *The Cyanobacteria: Molecular Biology, Genomics, and Evolution*, A. Herrero and E. Flores, Editors. 2008, Caister Academic Press: Norfolk, UK. p. 217-270.
17. Kern, J., et al., *Purification, characterisation and crystallisation of photosystem II from Thermosynechococcus elongatus cultivated in a new type of photobioreactor.* Biochim Biophys Acta, 2005. **1706**(1-2): p. 147-57.
18. Vermaas, W.F., *Photosynthesis and respiration in cyanobacteria*, in *Encyclopedia of Life Sciences*. 2001, Nature Publishing Group: London. p. 245-251.
19. Lea-Smith, D.J., et al., *Thylakoid terminal oxidases are essential for the cyanobacterium Synechocystis sp. PCC 6803 to survive rapidly changing light intensities.* Plant Physiol, 2013. **162**(1): p. 484-95.
20. Mullineaux, C.W., *Co-existence of photosynthetic and respiratory activities in cyanobacterial thylakoid membranes.* Biochim Biophys Acta, 2014. **1837**(4): p. 503-11.

21. Liu, L.N., et al., *Control of electron transport routes through redox-regulated redistribution of respiratory complexes.* Proc Natl Acad Sci U S A, 2012. **109**(28): p. 11431-11436.
22. Liu, L.N., *Distribution and dynamics of electron transport complexes in cyanobacterial thylakoid membranes.* Biochim Biophys Acta, 2016. **1857**(3): p. 256-65.
23. Cogdell, R.J., A. Gall, and J. Kohler, *The architecture and function of the light-harvesting apparatus of purple bacteria: from single molecules to in vivo membranes.* Q Rev Biophys, 2006. **39**(3): p. 227-324.
24. Liu, L.N. and S. Scheuring, *Investigation of photosynthetic membrane structure using atomic force microscopy.* Trends in Plant Sciences, 2013. **18**(5): p. 277-286.
25. Liu, L.N., et al., *Forces guiding assembly of light-harvesting complex 2 in native membranes.* Proc Natl Acad Sci U S A, 2011. **108**(23): p. 9455-9.
26. Croce, R. and H. van Amerongen, *Natural strategies for photosynthetic light harvesting.* Nat Chem Biol, 2014. **10**(7): p. 492-501.
27. Minagawa, J., *Dynamic reorganization of photosynthetic supercomplexes during environmental acclimation of photosynthesis.* Front Plant Sci, 2013. **4**: p. 513.
28. Adir, N., *Elucidation of the molecular structures of components of the phycobilisome: reconstructing a giant.* Photosynth Res, 2005. **85**(1): p. 15-32.
29. Liu, L.N., et al., *Characterization, structure and function of linker polypeptides in phycobilisomes of cyanobacteria and red algae: An overview.* Biochimica et Biophysica Acta-Bioenergetics, 2005. **1708**(2): p. 133-142.
30. Watanabe, M. and M. Ikeuchi, *Phycobilisome: architecture of a light-harvesting supercomplex.* Photosynth Res, 2013. **116**(2-3): p. 265-76.
31. Zhang, J., et al., *Structure of phycobilisome from the red alga Griffithsia pacifica.* Nature, 2017. **551**(7678): p. 57-63.
32. Liu, L.N., et al., *Light-induced energetic decoupling as a mechanism for phycobilisome-related energy dissipation in red algae: a single molecule study.* PLoS One, 2008. **3**(9): p. e3134.
33. Arteni, A.A., et al., *Structure and organization of phycobilisomes on membranes of the red alga Porphyridium cruentum.* Photosynth Res, 2008. **95**(2-3): p. 169-74.
34. Wolfe, G.R., et al., *Evidence for a common origin of chloroplasts with light-harvesting complexes of different pigmentation.* Nature, 1994. **367**(6463): p. 566-568.
35. Liu, H., et al., *Phycobilisomes supply excitations to both photosystems in a megacomplex in cyanobacteria.* Science, 2013. **342**(6162): p. 1104-1107.
36. Liu, L.N., et al., *One-step chromatography method for efficient separation and purification of R-phycoerythrin from Polysiphonia urceolata.* Journal of Biotechnology, 2005. **116**(1): p. 91-100.
37. Liu, L.N., et al., *Light-induced energetic decoupling as a mechanism for phycobilisome-related energy dissipation in red algae: a single molecule study.* PLoS ONE, 2008. **3**(9): p. e3134.
38. Olson, J.M. and R.E. Blankenship, *Thinking about the evolution of photosynthesis.* Photosynth Res, 2004. **80**(1-3): p. 373-86.
39. Hohmann-Marriott, M.F. and R.E. Blankenship, *Evolution of photosynthesis.* Annu Rev Plant Biol, 2011. **62**: p. 515-48.
40. Schubert, W.D., et al., *A common ancestor for oxygenic and anoxygenic photosynthetic systems: a comparison based on the structural model of photosystem I.* J Mol Biol, 1998. **280**(2): p. 297-314.
41. Lushy, A., L. Verchovsky, and R. Nechushtai, *The stable assembly of newly synthesized PsaE into the photosystem I complex occurring via the exchange mechanism is facilitated by electrostatic interactions.* Biochemistry, 2002. **41**(37): p. 11192-11199.

42. Xu, W., et al., *Proteins of the cyanobacterial photosystem I.* Biochimica et Biophysica Acta (BBA) - Bioenergetics, 2001. **1507**(1–3): p. 32-40.
43. Kłodawska, K., et al., *Elevated growth temperature can enhance photosystem I trimer formation and affects xanthophyll biosynthesis in cyanobacterium Synechocystis sp. PCC6803 cells.* Plant and Cell Physiology, 2014. **56**(3): p. 558-571.
44. MacGregor-Chatwin, C., et al., *Lateral segregation of photosystem I in cyanobacterial thylakoids.* Plant Cell, 2017.
45. Karapetyan, N.V., A.R. Holzwarth, and M. Rögner, *The photosystem I trimer of cyanobacteria: molecular organization, excitation dynamics and physiological significance.* FEBS letters, 1999. **460**(3): p. 395-400.
46. Zouni, A., et al., *Crystal structure of photosystem II from Synechococcus elongatus at 3.8 angstrom resolution.* Nature, 2001. **409**(6821): p. 739.
47. Ferreira, K.N., et al., *Architecture of the photosynthetic oxygen-evolving center.* Science, 2004. **303**(5665): p. 1831-8.
48. Aro, E.-M., et al., *Dynamics of photosystem II: a proteomic approach to thylakoid protein complexes.* Journal of Experimental Botany, 2005. **56**(411): p. 347-356.
49. Berry, E., et al., *Structural and Mutational Studies of the Cytochrome bc 1 Complex*, in *The Purple Phototrophic Bacteria*, C.N. Hunter, et al., Editors. 2009, Springer Netherlands. p. 425-450.
50. Shikanai, T., *Central role of cyclic electron transport around photosystem I in the regulation of photosynthesis.* Curr Opin Biotechnol, 2014. **26**: p. 25-30.
51. Rexroth, S., et al., *Functional Characterization of the Small Regulatory Subunit PetP from the Cytochrome b6f Complex in Thermosynechococcus elongatus.* The Plant Cell, 2014. **26**(8): p. 3435-3448.
52. Liu, L.N., et al., *Quinone pathways in entire photosynthetic chromatophores of Rhodospirillum photometricum.* J Mol Biol, 2009. **393**(1): p. 27-35.
53. Scheuring, S. and J.N. Sturgis, *Chromatic adaptation of photosynthetic membranes.* Science, 2005. **309**(5733): p. 484-7.
54. Grossman, A.R., et al., *The phycobilisome, a light-harvesting complex responsive to environmental conditions.* Microbiological reviews, 1993. **57**(3): p. 725-749.
55. Murakami, A. and Y. Fujita, *Regulation of Photosystem Stoichiometry in the Photosynthetic System of the Cyanophyte Synechocystis PCC 6714 in Response to Light-Intensity.* Plant and Cell Physiology, 1991. **32**(2): p. 223-230.
56. Li, H. and L.A. Sherman, *A redox-responsive regulator of photosynthesis gene expression in the cyanobacterium Synechocystis sp. Strain PCC 6803.* J Bacteriol, 2000. **182**(15): p. 4268-77.
57. Hihara, Y., K. Sonoike, and M. Ikeuchi, *A novel gene, pmgA, specifically regulates photosystem stoichiometry in the cyanobacterium Synechocystis species PCC 6803 in response to high light.* Plant Physiol, 1998. **117**(4): p. 1205-16.
58. Kehoe, D.M. and A. Gutu, *Responding to color: the regulation of complementary chromatic adaptation.* Annu Rev Plant Biol, 2006. **57**: p. 127-50.
59. Grossman, A.R., et al., *The phycobilisome, a light-harvesting complex responsive to environmental conditions.* Microbiol Rev, 1993. **57**(3): p. 725-49.
60. Federspiel, N.A. and A.R. Grossman, *Characterization of the light-regulated operon encoding the phycoerythrin-associated linker proteins from the cyanobacterium Fremyella diplosiphon.* J Bacteriol, 1990. **172**(7): p. 4072-81.
61. Conley, P.B., P.G. Lemaux, and A. Grossman, *Molecular characterization and evolution of sequences encoding light-harvesting components in the chromatically adapting cyanobacterium Fremyella diplosiphon.* J Mol Biol, 1988. **199**(3): p. 447-65.

62. Oelmuller, R., A.R. Grossman, and W.R. Briggs, *Role of Protein Synthesis in Regulation of Phycobiliprotein mRNA Abundance by Light Quality in Fremyella diplosiphon.* Plant Physiol, 1989. **90**(4): p. 1486-91.
63. Oelmuller, R., et al., *Changes in Accumulation and Synthesis of Transcripts Encoding Phycobilisome Components during Acclimation of Fremyella diplosiphon to Different Light Qualities.* Plant Physiol, 1988. **88**(4): p. 1077-83.
64. Jiang, Z., et al., *Bacterial photoreceptor with similarity to photoactive yellow protein and plant phytochromes.* Science, 1999. **285**(5426): p. 406-9.
65. Hoff, W.D., Matthijs, H.C.P., Schubert, H., Crielaard, W., Hellingwerf, K.J., *Rhodopsin(s) in eubacteria.* Biophys Chem, 1995. **56**: p. 193-199.
66. Bezy, R.P., L. Wiltbank, and D.M. Kehoe, *Light-dependent attenuation of phycoerythrin gene expression reveals convergent evolution of green light sensing in cyanobacteria.* Proceedings of the National Academy of Sciences, 2011. **108**(45): p. 18542-18547.
67. Gutu, A. and D.M. Kehoe, *Emerging Perspectives on the Mechanisms, Regulation, and Distribution of Light Color Acclimation in Cyanobacteria.* Molecular Plant, 2012. **5**(1): p. 1-13.
68. Dong, G. and S.S. Golden, *How a cyanobacterium tells time.* Curr Opin Microbiol, 2008. **11**(6): p. 541-6.
69. Dong, G., Y.I. Kim, and S.S. Golden, *Simplicity and complexity in the cyanobacterial circadian clock mechanism.* Curr Opin Genet Dev, 2010. **20**(6): p. 619-25.
70. Golden, S.S., *Light-responsive gene expression in cyanobacteria.* J Bacteriol, 1995. **177**(7): p. 1651-4.
71. Dodd, A.N., et al., *Plant circadian clocks increase photosynthesis, growth, survival, and competitive advantage.* Science, 2005. **309**(5734): p. 630-3.
72. Noordally, Z.B., et al., *Circadian control of chloroplast transcription by a nuclear-encoded timing signal.* Science, 2013. **339**(6125): p. 1316-9.
73. Gould, P.D., et al., *Delayed fluorescence as a universal tool for the measurement of circadian rhythms in higher plants.* Plant J, 2009. **58**(5): p. 893-901.
74. Baena-González, E., R. Barbato, and E.-M. Aro, *Role of phosphorylation in the repair cycle and oligomeric structure of photosystem II.* Planta, 1999. **208**(2): p. 196-204.
75. Kirchhoff, H., U. Mukherjee, and H.J. Galla, *Molecular architecture of the thylakoid membrane: lipid diffusion space for plastoquinone.* Biochemistry, 2002. **41**(15): p. 4872-82.
76. Liu, L.-N., et al., *Control of electron transport routes through redox-regulated redistribution of respiratory complexes.* Proceedings of the National Academy of Sciences, 2012.
77. Dekker, J.P. and E.J. Boekema, *Supramolecular organization of thylakoid membrane proteins in green plants.* Biochim Biophys Acta, 2005. **1706**(1-2): p. 12-39.
78. Kirchhoff, H., *Structural changes of the thylakoid membrane network induced by high light stress in plant chloroplasts.* Philos Trans R Soc Lond B Biol Sci, 2014. **369**(1640): p. 20130225.
79. Kirchhoff, H., et al., *Dynamic control of protein diffusion within the granal thylakoid lumen.* Proc Natl Acad Sci U S A, 2011. **108**(50): p. 20248-53.
80. Gonçalves, R.P., et al., *Architecture of the native photosynthetic apparatus of Phaeospirillum molischianum.* J Struct Biol, 2005. **152**(3): p. 221-228.
81. Scheuring, S., et al., *The photosynthetic apparatus of Rhodopseudomonas palustris: structures and organization.* J Mol Biol, 2006. **358**(1): p. 83-96.
82. Adams, P.G. and C.N. Hunter, *Adaptation of intracytoplasmic membranes to altered light intensity in Rhodobacter sphaeroides.* Biochim Biophys Acta, 2012. **1817**(9): p. 1616-27.
83. Scheuring, S., et al., *Watching the photosynthetic apparatus in native membranes.* Proc Natl Acad Sci U S A, 2004. **101**(31): p. 11293-11297.

84. Mullineaux, C.W. and J.F. Allen, *State 1-State 2 transitions in the cyanobacterium Synechococcus 6301 are controlled by the redox state of electron carriers between Photosystems I and II.* Photosynth Res, 1990. **23**(3): p. 297-311.
85. Mullineaux, C.W. and D. Emlyn-Jones, *State transitions: an example of acclimation to low-light stress.* J Exp Bot, 2005. **56**(411): p. 389-93.
86. Staehelin, L.A. and C.J. Arntzen, *Regulation of chloroplast membrane function: protein phosphorylation changes the spatial organization of membrane components.* The Journal of cell biology, 1983. **97**(5): p. 1327-1337.
87. Allen, J.F. and N.G. Holmes, *A general model for regulation of photosynthetic unit function by protein phosphorylation.* FEBS Letters, 1986. **202**(2): p. 175-181.
88. Rakhimberdieva, M.G., et al., *Interaction of Phycobilisomes with Photosystem II Dimers and Photosystem I Monomers and Trimers in the Cyanobacterium Spirulina platensis†.* Biochemistry, 2001. **40**(51): p. 15780-15788.
89. Biggins, J. and D. Bruce, *Regulation of excitation energy transfer in organisms containing phycobilins.* Photosynth Res, 1989. **20**(1): p. 1-34.
90. Bruce, D., S. Brimble, and D.A. Bryant, *State transitions in a phycobilisome-less mutant of the cyanobacterium Synechococcus sp. PCC 7002.* Biochim Biophys Acta, 1989. **974**(1): p. 66-73.
91. McConnell, M.D., et al., *Regulation of the distribution of chlorophyll and phycobilin-absorbed excitation energy in cyanobacteria. A structure-based model for the light state transition.* Plant Physiol, 2002. **130**(3): p. 1201-12.
92. Mullineaux, C.W., M.J. Tobin, and G.R. Jones, *Mobility of photosynthetic complexes in thylakoid membranes.* Nature, 1997. **390**(6658): p. 421-424.
93. Joshua, S. and C.W. Mullineaux, *Phycobilisome diffusion is required for light-state transitions in cyanobacteria.* Plant Physiol, 2004. **135**(4): p. 2112-9.
94. Joshua, S., et al., *Involvement of phycobilisome diffusion in energy quenching in cyanobacteria.* Plant Physiol, 2005. **138**(3): p. 1577-85.
95. Kana, R., et al., *Phycobilisome Mobility and Its Role in the Regulation of Light Harvesting in Red Algae.* Plant Physiol, 2014. **165**(4): p. 1618-1631.
96. Liu, L.N., et al., *FRAP analysis on red alga reveals the fluorescence recovery is ascribed to intrinsic photoprocesses of phycobilisomes than large-scale diffusion.* PLoS One, 2009. **4**(4): p. e5295.
97. Mustardy, L., F.X. Cunningham, Jr., and E. Gantt, *Photosynthetic membrane topography: quantitative in situ localization of photosystems I and II.* Proc Natl Acad Sci U S A, 1992. **89**(21): p. 10021-5.
98. Bald, D., J. Kruip, and M. Rogner, *Supramolecular architecture of cyanobacterial thylakoid membranes: How is the phycobilisome connected with the photosystems?* Photosynth Res, 1996. **49**(2): p. 103-18.
99. Liu, H., et al., *Phycobilisomes supply excitations to both photosystems in a megacomplex in cyanobacteria.* Science, 2013. **342**(6162): p. 1104-7.
100. Watanabe, M., et al., *Attachment of phycobilisomes in an antenna-photosystem I supercomplex of cyanobacteria.* Proc Natl Acad Sci U S A, 2014. **111**(7): p. 2512-7.
101. Llorente-Garcia, I., et al., *Single-molecule in vivo imaging of bacterial respiratory complexes indicates delocalized oxidative phosphorylation.* Biochimica et Biophysica Acta (BBA) - Bioenergetics, 2014. **1837**(6): p. 811-824.
102. Allahverdiyeva, Y., et al., *Flavodiiron proteins Flv1 and Flv3 enable cyanobacterial growth and photosynthesis under fluctuating light.* Proceedings of the National Academy of Sciences, 2013. **110**(10): p. 4111-4116.
103. Zhang, P., et al., *Operon flv4-flv2 provides cyanobacterial photosystem II with flexibility of electron transfer.* Plant Cell, 2012. **24**(5): p. 1952-71.

104. Bailey, S. and A. Grossman, *Photoprotection in cyanobacteria: regulation of light harvesting.* Photochem Photobiol, 2008. **84**(6): p. 1410-20.
105. El Bissati, K., et al., *Photosystem II fluorescence quenching in the cyanobacterium Synechocystis PCC 6803: involvement of two different mechanisms.* Biochim Biophys Acta, 2000. **1457**(3): p. 229-42.
106. Gorbunov, M.Y., et al., *A kinetic model of non-photochemical quenching in cyanobacteria.* Biochim Biophys Acta, 2011. **1807**(12): p. 1591-9.
107. Wilson, A., et al., *A soluble carotenoid protein involved in phycobilisome-related energy dissipation in cyanobacteria.* Plant Cell, 2006. **18**(4): p. 992-1007.
108. Kerfeld, C.A., et al., *The crystal structure of a cyanobacterial water-soluble carotenoid binding protein.* Structure, 2003. **11**(1): p. 55-65.
109. Kirilovsky, D. and C.A. Kerfeld, *The Orange Carotenoid Protein: a blue-green light photoactive protein.* Photochem Photobiol Sci, 2013. **12**(7): p. 1135-43.
110. Gwizdala, M., et al., *Characterization of the Synechocystis PCC 6803 Fluorescence Recovery Protein involved in photoprotection.* Biochim Biophys Acta, 2013. **1827**(3): p. 348-54.
111. Stoitchkova, K., et al., *Heat- and light-induced reorganizations in the phycobilisome antenna of Synechocystis sp. PCC 6803. Thermo-optic effect.* Biochim Biophys Acta, 2007. **1767**(6): p. 750-6.
112. Six, C., et al., *UV-induced phycobilisome dismantling in the marine picocyanobacterium Synechococcus sp. WH8102.* Photosynth Res, 2007. **92**(1): p. 75-86.
113. Rinalducci, S., J.Z. Pedersen, and L. Zolla, *Generation of reactive oxygen species upon strong visible light irradiation of isolated phycobilisomes from Synechocystis PCC 6803.* Biochim Biophys Acta, 2008. **1777**(5): p. 417-24.
114. Wyman, M., R.P. Gregory, and N.G. Carr, *Novel Role for Phycoerythrin in a Marine Cyanobacterium, Synechococcus Strain DC2.* Science, 1985. **230**(4727): p. 818-20.
115. Knoll, A.H., *Cyanobacteria and earth history.* The Cyanobacteria: Molecular Biology, Genomics, and Evolution, 2008. **484**.
116. Stanier, R.Y. and G. Cohen-Bazire, *Phototrophic prokaryotes: the cyanobacteria.* Annu Rev Microbiol, 1977. **31**: p. 225-74.
117. Van De Meene, A.M., et al., *The three-dimensional structure of the cyanobacterium Synechocystis sp. PCC 6803.* Archives of Microbiology, 2006. **184**(5): p. 259-270.
118. Nevo, R., et al., *Thylakoid membrane perforations and connectivity enable intracellular traffic in cyanobacteria.* The EMBO Journal, 2007. **26**(5): p. 1467-1473.
119. Pisareva, T., et al., *Model for membrane organization and protein sorting in the cyanobacterium Synechocystis sp. PCC 6803 inferred from proteomics and multivariate sequence analyses.* Journal of proteome research, 2011. **10**(8): p. 3617-3631.
120. Mullineaux, C.W., *Function and evolution of grana.* Trends Plant Sci, 2005. **10**(11): p. 521-5.
121. Vothknecht, U.C. and P. Westhoff, *Biogenesis and origin of thylakoid membranes.* Biochimica et Biophysica Acta (BBA) - Molecular Cell Research, 2001. **1541**(1): p. 91-101.
122. Knoot, C.J., et al., *Cyanobacteria: promising biocatalysts for sustainable chemical production.* Journal of Biological Chemistry, 2018. **293**(14): p. 5044-5052.
123. Williams, J.G.K., *[85] Construction of specific mutations in photosystem II photosynthetic reaction center by genetic engineering methods in Synechocystis 6803*, in *Methods in Enzymology*. 1988, Academic Press. p. 766-778.
124. Jordan, P., et al., *Three-dimensional structure of cyanobacterial photosystem I at 2.5 A resolution.* Nature, 2001. **411**(6840): p. 909-17.
125. Mullineaux, C.W., *Co-existence of photosynthetic and respiratory activities in cyanobacterial thylakoid membranes.* Biochimica et Biophysica Acta (BBA) - Bioenergetics, 2014. **1837**(4): p. 503-511.

126. Sherman, D.M., T.A. Troyan, and L.A. Sherman, *Localization of membrane proteins in the cyanobacterium Synechococcus sp. PCC7942 (radial asymmetry in the photosynthetic complexes).* Plant physiology, 1994. **106**(1): p. 251-262.
127. Peschek, G.A., et al., *Life Implies Work: A Holistic Account of Our Microbial Biosphere Focussing on the Bioenergetic Processes of Cyanobacteria, the Ecologically Most Successful Organisms on Our Earth*, in *Bioenergetic Processes of Cyanobacteria: From Evolutionary Singularity to Ecological Diversity*, G.A. Peschek, C. Obinger, and G. Renger, Editors. 2011, Springer Netherlands: Dordrecht. p. 3-70.
128. Magidson, V. and A. Khodjakov, *Circumventing photodamage in live-cell microscopy.* Methods in cell biology, 2013. **114**: p. 10.1016/B978-0-12-407761-4.00023-3.
129. Lippincott-Schwartz, J., E. Snapp, and A. Kenworthy, *Studying protein dynamics in living cells.* Nat Rev Mol Cell Biol, 2001. **2**(6): p. 444-456.
130. Wombacher, R. and V.W. Cornish, *Chemical tags: applications in live cell fluorescence imaging.* J Biophotonics, 2011. **4**(6): p. 391-402.
131. Swedlow, J.R. and M. Platani, *Live cell imaging using wide-field microscopy and deconvolution.* Cell structure and function, 2002. **27**(5): p. 335-341.
132. Minsky, M., *Memoir on inventing the confocal scanning microscope.* Scanning, 1988. **10**(4): p. 128-138.
133. Krichevsky, O. and G. Bonnet, *Fluorescence correlation spectroscopy: the technique and its applications.* Reports on Progress in Physics, 2002. **65**(2): p. 251.
134. Dinant, C., et al., *Fluorescence resonance energy transfer of GFP and YFP by spectral imaging and quantitative acceptor photobleaching.* Journal of microscopy, 2008. **231**(1): p. 97-104.
135. Mullineaux, C.W. and M. Sarcina, *Probing the dynamics of photosynthetic membranes with fluorescence recovery after photobleaching.* Trends in plant science, 2002. **7**(6): p. 237-240.
136. Palmer, A.G. and N.L. Thompson, *Molecular aggregation characterized by high order autocorrelation in fluorescence correlation spectroscopy.* Biophysical Journal, 1987. **52**(2): p. 257-270.
137. Ankers, J.M., et al., *Spatio-temporal protein dynamics in single living cells.* Curr Opin Biotechnol, 2008. **19**(4): p. 375-80.
138. Haustein, E. and P. Schwille, *Single-molecule spectroscopic methods.* Current opinion in structural biology, 2004. **14**(5): p. 531-540.
139. Day, C.A., et al., *Analysis of protein and lipid dynamics using confocal fluorescence recovery after photobleaching (FRAP).* Current protocols in cytometry / editorial board, J. Paul Robinson, managing editor ... [et al.], 2012. **CHAPTER**: p. Unit2.19-Unit2.19.
140. Sprague, B.L., et al., *Analysis of binding reactions by fluorescence recovery after photobleaching.* Biophys J, 2004. **86**(6): p. 3473-95.
141. Häder, D.P., *The Molecular Biology of Cyanobacteria. Edited by Donald A. Bryant.* Plant Ecology, 1997. **133**(2): p. 236-238.
142. Kana, R., *Mobility of photosynthetic proteins.* Photosynth Res, 2013. **116**(2-3): p. 465-79.
143. Mattheyses, A.L., S.M. Simon, and J.Z. Rappoport, *Imaging with total internal reflection fluorescence microscopy for the cell biologist.* J Cell Sci, 2010. **123**(Pt 21): p. 3621-8.
144. Whited, A.M. and P.S. Park, *Atomic force microscopy: a multifaceted tool to study membrane proteins and their interactions with ligands.* Biochim Biophys Acta, 2014. **1838**(1 Pt A): p. 56-68.
145. Binnig, G., C.F. Quate, and C. Gerber, *Atomic force microscope.* Phys Rev Lett, 1986. **56**(9): p. 930-933.
146. Liu, L.-N. and S. Scheuring, *Investigation of photosynthetic membrane structure using atomic force microscopy.* Trends in plant science, 2013. **18**(5): p. 277-286.

147. Williams, D.B. and C.B. Carter, *The transmission electron microscope*, in *Transmission electron microscopy*. 1996, Springer. p. 3-17.
148. Luft, J.H., *Improvements in epoxy resin embedding methods.* The Journal of Cell Biology, 1961. **9**(2): p. 409-414.
149. Tandeau de Marsac, N. and J. Houmard, *Adaptation of cyanobacteria to environmental stimuli: new steps towards molecular mechanisms*. Vol. 10. 1993. 119-189.
150. Schindelin, J., et al., *Fiji: an open-source platform for biological-image analysis.* Nat Meth, 2012. **9**(7): p. 676-682.
151. Grenier, F., et al., *Complete Genome Sequence of Escherichia coli BW25113.* Genome Announcements, 2014. **2**(5): p. e01038-14.
152. Gust, B., T. Kieser, and K.F. Chater, *REDIRECT Technology: PCR-targeting System in Streptomyces coelicolor*. 2002, Norwich: John Innes Centre.
153. Gust, B., et al., *Lambda red-mediated genetic manipulation of antibiotic-producing Streptomyces.* Adv Appl Microbiol, 2004. **54**: p. 107-28.
154. Rippka, R., et al., *Generic Assignments, Strain Histories and Properties of Pure Cultures of Cyanobacteria.* Microbiology, 1979. **111**(1): p. 1-61.
155. Liu, L.-N., et al., *Control of electron transport routes through redox-regulated redistribution of respiratory complexes.* Proceedings of the National Academy of Sciences, 2012. **109**(28): p. 11431-11436.
156. Gust, B., et al., *PCR-targeted Streptomyces gene replacement identifies a protein domain needed for biosynthesis of the sesquiterpene soil odor geosmin.* Proc Natl Acad Sci U S A, 2003. **100**(4): p. 1541-6.
157. Murphy, K.C., *Use of bacteriophage lambda recombination functions to promote gene replacement in Escherichia coli.* J Bacteriol, 1998. **180**(8): p. 2063-71.
158. Murphy, K.C., K.G. Campellone, and A.R. Poteete, *PCR-mediated gene replacement in Escherichia coli.* Gene, 2000. **246**(1-2): p. 321-30.
159. Golden, S.S., *Mutagenesis of cyanobacteria by classical and gene-transfer-based methods.* Methods Enzymol, 1988. **167**: p. 714-27.
160. Griese, M., C. Lange, and J. Soppa, *Ploidy in cyanobacteria.* FEMS Microbiol Lett, 2011. **323**(2): p. 124-31.
161. SAMBROOK, H., *Molecular cloning: a laboratory manual. Cold Spring Harbor, NY.* 1989.
162. Golden, S.S. and L.A. Sherman, *Optimal conditions for genetic transformation of the cyanobacterium Anacystis nidulans R2.* Journal of Bacteriology, 1984. **158**(1): p. 36-42.
163. Zhang, P., et al., *Expression and Functional Roles of the Two Distinct NDH-1 Complexes and the Carbon Acquisition Complex NdhD3/NdhF3/CupA/Sll1735 in Synechocystis sp PCC 6803.* The Plant Cell, 2004. **16**(12): p. 3326-3340.
164. Komenda, J. and J. Barber, *Comparison of psbO and psbH deletion mutants of Synechocystis PCC 6803 indicates that degradation of D1 protein is regulated by the QB site and dependent on protein synthesis.* Biochemistry, 1995. **34**(29): p. 9625-31.
165. Cameron, Jeffrey C., et al., *Biogenesis of a Bacterial Organelle: The Carboxysome Assembly Pathway.* Cell, 2013. **155**(5): p. 1131-1140.
166. Strasser, R.J., A. Srivastava, and M. Tsimilli-Michael, *The fluorescence transient as a tool to characterize and screen photosynthetic samples.* Probing photosynthesis: mechanisms, regulation and adaptation, 2000: p. 445-483.
167. Goedheer, J., *On the low-temperature fluorescence spectra of blue-green and red algae.* Biochimica et Biophysica Acta (BBA)-Bioenergetics, 1968. **153**(4): p. 903-906.
168. Veerman, J., et al., *The PsbU Subunit of Photosystem II Stabilizes Energy Transfer and Primary Photochemistry in the Phycobilisome− Photosystem II Assembly of Synechocystis sp. PCC 6803.* Biochemistry, 2005. **44**(51): p. 16939-16948.
169. Böddi, B., M. Ryberg, and C. Sundqvist, *Identification of four universal protochlorophyllide forms in dark-grown leaves by analyses of the 77 K fluorescence*

emission spectra. Journal of Photochemistry and Photobiology B: Biology, 1992. **12**(4): p. 389-401.
170. Murakami, A., *Quantitative analysis of 77K fluorescence emission spectra in Synechocystis sp. PCC 6714 and Chlamydomonas reinhardtii with variable PS I/PS II stoichiometries.* Photosynthesis research, 1997. **53**(2): p. 141-148.
171. Mimuro, M., A. Murakami, and Y. Fujita, *Studies on spectral characteristics of allophycocyanin isolated from Anabaena cylindrical: Curve-fitting analysis.* Archives of Biochemistry and Biophysics, 1982. **215**(1): p. 266-273.
172. Sarcina, M., N. Bouzovitis, and C.W. Mullineaux, *Mobilization of photosystem II induced by intense red light in the Cyanobacterium Synechococcus sp PCC7942.* Plant Cell, 2006. **18**(2): p. 457-64.
173. Fish, K.N., *Total Internal Reflection Fluorescence (TIRF) Microscopy.* Current protocols in cytometry / editorial board, J. Paul Robinson, managing editor ... [et al.], 2009. **0 12**: p. Unit12.18-Unit12.18.
174. Liu, L.N. and S. Scheuring, *Investigation of photosynthetic membrane structure using atomic force microscopy.* Trends Plant Sci, 2013. **18**(5): p. 277-86.
175. Ishikawa-Ankerhold, H.C., R. Ankerhold, and G.P. Drummen, *Advanced fluorescence microscopy techniques--FRAP, FLIP, FLAP, FRET and FLIM.* Molecules, 2012. **17**(4): p. 4047-132.
176. Kirchhoff, H., *Molecular crowding and order in photosynthetic membranes.* Trends Plant Sci, 2008. **13**(5): p. 201-7.
177. Agarwal, R., et al., *Heterogeneity in thylakoid membrane proteome of Synechocystis 6803.* J Proteomics, 2010. **73**(5): p. 976-91.
178. Vermaas, W.F., et al., *In vivo hyperspectral confocal fluorescence imaging to determine pigment localization and distribution in cyanobacterial cells.* Proc Natl Acad Sci U S A, 2008. **105**(10): p. 4050-5.
179. Collins, A.M., et al., *Photosynthetic pigment localization and thylakoid membrane morphology are altered in Synechocystis 6803 phycobilisome mutants.* Plant Physiol, 2012. **158**(4): p. 1600-9.
180. Sherman, D.M., T.A. Troyan, and L.A. Sherman, *Localization of membrane proteins in the cyanobacterium Synechococcus sp. PCC7942 (Radial asymmetry in the photosynthetic complexes).* Plant Physiol, 1994. **106**(1): p. 251-262.
181. Mullineaux, C.W., *FRAP analysis of photosynthetic membranes.* J Exp Bot, 2004. **55**(400): p. 1207-11.
182. Stingaciu, L.R., et al., *Revealing the Dynamics of Thylakoid Membranes in Living Cyanobacterial Cells.* Sci Rep, 2016. **6**: p. 19627.
183. Sarcina, M. and C.W. Mullineaux, *Mobility of the IsiA chlorophyll-binding protein in cyanobacterial thylakoid membranes.* J Biol Chem, 2004. **279**(35): p. 36514-8.
184. Sarcina, M., et al., *Lipid diffusion in the thylakoid membranes of the cyanobacterium Synechococcus sp.: effect of fatty acid desaturation.* FEBS Lett, 2003. **553**(3): p. 295-8.
185. Mackle, M.M. and B.A. Zilinskas, *Role of signal peptides in targeting of proteins in cyanobacteria.* Journal of bacteriology, 1994. **176**(7): p. 1857-1864.
186. Palmer, T. and B.C. Berks, *The twin-arginine translocation (Tat) protein export pathway.* Nature Reviews Microbiology, 2012. **10**(7): p. 483.
187. Frain, K.M., et al., *Protein translocation and thylakoid biogenesis in cyanobacteria.* Biochim Biophys Acta, 2016. **1857**(3): p. 266-73.
188. Kosemund, K., I. Geiger, and H. Paulsen, *Insertion of light-harvesting chlorophyll a/b protein into the thylakoid topographical studies.* Eur J Biochem, 2000. **267**(4): p. 1138-45.

189. Kubota, H., et al., *Purification and characterization of photosystem I complex from Synechocystis sp. PCC 6803 by expressing histidine-tagged subunits.* Biochim Biophys Acta, 2010. **1797**(1): p. 98-105.
190. Wongratana, J., et al., *Generation and characterization of His-tagged-PsbA-expressing transformants of Chlamydomonas reinhardtii that are capable of photoautotrophic growth.* Journal of applied phycology, 2013. **25**(2): p. 445-452.
191. Gulis, G., et al., *Purification of His6-tagged Photosystem I from Chlamydomonas reinhardtii.* Photosynthesis research, 2008. **96**(1): p. 51-60.
192. Li, Z.-L., T.M. Bricker, and R. Burnap, *Kinetic characterization of His-tagged CP47 Photosystem II in Synechocystis sp. PCC6803.* Biochimica et Biophysica Acta (BBA)-Bioenergetics, 2000. **1460**(2): p. 384-389.
193. Sugiura, M. and Y. Inoue, *Highly purified thermo-stable oxygen-evolving photosystem II core complex from the thermophilic cyanobacterium Synechococcus elongatus having His-tagged CP43.* Plant and cell physiology, 1999. **40**(12): p. 1219-1231.
194. Johnson, A.S., S. van Horck, and P.J. Lewis, *Dynamic localization of membrane proteins in Bacillus subtilis.* Microbiology, 2004. **150**(Pt 9): p. 2815-24.
195. Patterson, G.H. and J. Lippincott-Schwartz, *A photoactivatable GFP for selective photolabeling of proteins and cells.* Science, 2002. **297**(5588): p. 1873-1877.
196. Düser, M.G., et al., *The proton-translocating a subunit of F0F1-ATP synthase is allocated asymmetrically to the peripheral stalk.* Journal of Biological Chemistry, 2008. **283**(48): p. 33602-33610.
197. Zhang, M., et al., *Rational design of true monomeric and bright photoactivatable fluorescent proteins.* Nature methods, 2012. **9**(7): p. 727-729.
198. Jordan, P., et al., *Three-dimensional structure of cyanobacterial photosystem I at 2.5 angstrom resolution.* Nature, 2001. **411**(6840): p. 909.
199. Biesiadka, J., et al., *Crystal structure of cyanobacterial photosystem II at 3.2 Å resolution: a closer look at the Mn-cluster.* Physical Chemistry Chemical Physics, 2004. **6**(20): p. 4733-4736.
200. Young, I.D., et al., *Structure of photosystem II and substrate binding at room temperature.* Nature, 2016. **540**(7633): p. 453-457.
201. Vinothkumar, K.R., et al., *Structure of the mitochondrial ATP synthase from Pichia angusta determined by electron cryo-microscopy.* Proceedings of the National Academy of Sciences, 2016: p. 201615902.
202. Baniulis, D., et al., *Structure-function, stability, and chemical modification of the cyanobacterial cytochrome b6f complex from Nostoc sp. PCC 7120.* Journal of Biological Chemistry, 2009. **284**(15): p. 9861-9869.
203. Royant, A. and M. Noirclerc-Savoye, *Stabilizing role of glutamic acid 222 in the structure of Enhanced Green Fluorescent Protein.* J Struct Biol, 2011. **174**(2): p. 385-90.
204. Battchikova, N., M. Angeleri, and E.M. Aro, *Proteomic approaches in research of cyanobacterial photosynthesis.* Photosynth Res, 2015. **126**(1): p. 47-70.
205. Herranen, M., et al., *Towards functional proteomics of membrane protein complexes in Synechocystis sp. PCC 6803.* Plant Physiology, 2004. **134**(1): p. 470-481.
206. Zhang, P., et al., *Isolation, subunit composition and interaction of the NDH-1 complexes from Thermosynechococcus elongatus BP-1.* Biochem J, 2005. **390**(Pt 2): p. 513-20.
207. Watanabe, M., et al., *Novel supercomplex organization of photosystem I in Anabaena and Cyanophora paradoxa.* Plant and cell physiology, 2010. **52**(1): p. 162-168.
208. Watanabe, M., et al., *Is the photosystem II complex a monomer or a dimer?* Plant and cell physiology, 2009. **50**(9): p. 1674-1680.
209. Du, W., et al., *Photonfluxostat: A method for light-limited batch cultivation of cyanobacteria at different, yet constant, growth rates.* Algal research, 2016. **20**: p. 118-125.

210. Murakami, A., et al., *Absorption spectrum of allophycocyanin isolated from Anabaena cylindrica: variation of the absorption spectrum induced by changes of the physico-chemical environment.* J Biochem, 1981. **89**(1): p. 79-86.
211. Shen, G., S. Boussiba, and W.F. Vermaas, *Synechocystis sp PCC 6803 strains lacking photosystem I and phycobilisome function.* Plant Cell, 1993. **5**(12): p. 1853-63.
212. Walker, D. and I.R. Walker, *The use of the oxygen electrode and fluorescence probes in simple measurements of photosynthesis.* 1987.
213. Zhang, P., et al., *Expression and functional roles of the two distinct NDH-1 complexes and the carbon acquisition complex NdhD3/NdhF3/CupA/Sll1735 in Synechocystis sp PCC 6803.* Plant Cell, 2004. **16**(12): p. 3326-40.
214. Umena, Y., et al., *Crystal structure of oxygen-evolving photosystem II at a resolution of 1.9 Å.* Nature, 2011. **473**(7345): p. 55-60.
215. Engel, B.D., et al., *Native architecture of the Chlamydomonas chloroplast revealed by in situ cryo-electron tomography.* Elife, 2015. **4**: p. e04889.
216. Kruip, J., et al., *Structural organization of the major subunits in cyanobacterial photosystem 1. Localization of subunits PsaC, -D, -E, -F, and -J.* J Biol Chem, 1997. **272**(27): p. 17061-9.
217. Phuthong, W., et al., *The use of contact mode atomic force microscopy in aqueous medium for structural analysis of spinach photosynthetic complexes.* Plant Physiol, 2015. **169**(2): p. 1318-32.
218. Johnson, M.P., et al., *Nanodomains of cytochrome b6f and photosystem II complexes in spinach grana thylakoid membranes.* Plant Cell, 2014. **26**(7): p. 3051-61.
219. Tremmel, I.G., et al., *Dependence of plastoquinol diffusion on the shape, size, and density of integral thylakoid proteins.* Biochim Biophys Acta, 2003. **1607**(2-3): p. 97-109.
220. Joshua, S. and C.W. Mullineaux, *The rpaC gene product regulates phycobilisome-photosystem II interaction in cyanobacteria.* Biochim Biophys Acta, 2005. **1709**(1): p. 58-68.
221. Fujita, Y. and A. Murakami, *Regulation of electron transport composition in cyanobacterial photosynthetic system: Stoichiometry among photosystem I and II complexes and their light-harvesting antennae and cytochrome b_6/f complex.* Plant Cell Physiol, 1987. **28**(8): p. 1547-1553.
222. Fraser, J.M., et al., *Photophysiological and photosynthetic complex changes during iron starvation in Synechocystis sp. PCC 6803 and Synechococcus elongatus PCC 7942.* PLoS One, 2013. **8**(3): p. e59861.
223. Mullineaux, C.W. and M. Sarcina, *Probing the dynamics of photosynthetic membranes with fluorescence recovery after photobleaching.* Trends Plant Sci, 2002. **7**(6): p. 237-40.
224. Kirchhoff, H., et al., *Protein diffusion and macromolecular crowding in thylakoid membranes.* Plant Physiol, 2008. **146**(4): p. 1571-8.
225. Hochman, J.H., et al., *Lateral mobility of cytochrome c on intact mitochondrial membranes as determined by fluorescence redistribution after photobleaching.* Proc Natl Acad Sci U S A, 1982. **79**(22): p. 6866-70.
226. Kuo, M.M., et al., *Prokaryotic K^+ channels: from crystal structures to diversity.* FEMS Microbiol Rev, 2005. **29**(5): p. 961-85.
227. Zanetti, M., et al., *A novel potassium channel in photosynthetic cyanobacteria.* PLoS One, 2010. **5**(4): p. e10118.
228. Checchetto, V., et al., *Thylakoid potassium channel is required for efficient photosynthesis in cyanobacteria.* Proc Natl Acad Sci U S A, 2012. **109**(27): p. 11043-8.
229. Ardail, D., et al., *Mitochondrial contact sites. Lipid composition and dynamics.* J Biol Chem, 1990. **265**(31): p. 18797-802.

230. Kirchhoff, H., et al., *Supramolecular photosystem II organization in grana thylakoid membranes: evidence for a structured arrangement.* Biochemistry, 2004. **43**(28): p. 9204-13.
231. Dupuy, A.D. and D.M. Engelman, *Protein area occupancy at the center of the red blood cell membrane.* Proc Natl Acad Sci U S A, 2008. **105**(8): p. 2848-52.
232. Murphy, D.J., *The molecular organisation of the photosynthetic membranes of higher plants.* Biochimica et Biophysica Acta (BBA) - Reviews on Biomembranes, 1986. **864**(1): p. 33-94.
233. Folea, I.M., et al., *Domain organization of photosystem II in membranes of the cyanobacterium Synechocystis PCC6803 investigated by electron microscopy.* FEBS Lett, 2008. **582**(12): p. 1749-54.
234. Mörschel, E. and G.H. Schatz, *Correlation of photosystem-II complexes with exoplasmatic freeze-fracture particles of thylakoids of the cyanobacterium Synechococcus sp.* Planta, 1987. **172**(2): p. 145-154.
235. MacGregor-Chatwin, C., et al., *Lateral segregation of photosystem I in cyanobacterial thylakoids.* Plant Cell, 2017. **29**(5): p. 1119-1136.
236. Aspinwall, C.L., M. Sarcina, and C.W. Mullineaux, *Phycobilisome mobility in the cyanobacterium Synechococcus sp. PCC7942 is influenced by the trimerisation of photosystem I.* Photosynthesis research, 2004. **79**(2): p. 179.
237. Turconi, S., G. Schweitzer, and A.R. Holzwarth, *Temperature dependence of picosecond fluorescence kinetics of a cyanobacterial photosystem I particle.* Photochem Photobiol, 1993. **57**(1): p. 113-119.
238. Rexroth, S., et al., *The plasma membrane of the cyanobacterium Gloeobacter violaceus contains segregated bioenergetic domains.* Plant Cell, 2011. **23**(6): p. 2379-90.
239. Lenn, T., M.C. Leake, and C.W. Mullineaux, *Clustering and dynamics of cytochrome bd-I complexes in the Escherichia coli plasma membrane in vivo.* Mol Microbiol, 2008. **70**(6): p. 1397-407.
240. Llorente-Garcia, I., et al., *Single-molecule in vivo imaging of bacterial respiratory complexes indicates delocalized oxidative phosphorylation.* Biochim Biophys Acta, 2014. **1837**(6): p. 811-24.
241. Wilkens, V., W. Kohl, and K. Busch, *Restricted diffusion of OXPHOS complexes in dynamic mitochondria delays their exchange between cristae and engenders a transitory mosaic distribution.* J Cell Sci, 2013. **126**(Pt 1): p. 103-16.
242. Vogel, F., et al., *Dynamic subcompartmentalization of the mitochondrial inner membrane.* J Cell Biol, 2006. **175**(2): p. 237-47.
243. Saffman, P.G. and M. Delbrück, *Brownian motion in biological membranes.* Proceedings of the National Academy of Sciences, 1975. **72**(8): p. 3111-3113.
244. Camley, B.A. and F.L. Brown, *Contributions to membrane-embedded-protein diffusion beyond hydrodynamic theories.* Physical Review E, 2012. **85**(6): p. 061921.
245. Gambin, Y., et al., *Lateral mobility of proteins in liquid membranes revisited.* Proc Natl Acad Sci U S A, 2006. **103**(7): p. 2098-102.
246. Sarcina, M., M.J. Tobin, and C.W. Mullineaux, *Diffusion of phycobilisomes on the thylakoid membranes of the cyanobacterium Synechococcus 7942. Effects of phycobilisome size, temperature, and membrane lipid composition.* J Biol Chem, 2001. **276**(50): p. 46830-4.
247. Consoli, E., et al., *Diffusion of light-harvesting complex II in the thylakoid membranes.* EMBO Rep, 2005. **6**(8): p. 782-6.
248. Frick, M., K. Schmidt, and B.J. Nichols, *Modulation of lateral diffusion in the plasma membrane by protein density.* Curr Biol, 2007. **17**(5): p. 462-7.
249. Nehls, S., et al., *Dynamics and retention of misfolded proteins in native ER membranes.* Nat Cell Biol, 2000. **2**(5): p. 288-95.

250. Gupte, S.S., et al., *Two-dimensional diffusion of F_1F_0-ATP synthase and ADP/ATP translocator. Testing a hypothesis for ATP synthesis in the mitochondrial inner membrane.* Biochimica et Biophysica Acta (BBA) - Biomembranes, 1991. **1069**(2): p. 131-138.
251. Bečková, M., et al., *Association of Psb28 and Psb27 proteins with PSII-PSI supercomplexes upon exposure of Synechocystis sp. PCC 6803 to high light.* Mol Plant, 2017. **10**(1): p. 62-72.
252. Gao, F., et al., *The NDH-1L-PSI Supercomplex Is Important for Efficient Cyclic Electron Transport in Cyanobacteria.* Plant Physiol, 2016. **172**(3): p. 1451-1464.
253. Lapuente-Brun, E., et al., *Supercomplex assembly determines electron flux in the mitochondrial electron transport chain.* Science, 2013. **340**(6140): p. 1567-70.
254. Iwai, M., et al., *Isolation of the elusive supercomplex that drives cyclic electron flow in photosynthesis.* Nature, 2010. **464**(7292): p. 1210-3.
255. Acin-Perez, R., et al., *Respiratory active mitochondrial supercomplexes.* Mol Cell, 2008. **32**(4): p. 529-39.
256. Kulasooriya, S., *Cyanobacteria: pioneers of planet earth.* Ceylon Journal of Science (Biological Sciences), 2012. **40**(2).
257. Schuergers, N., et al., *Cyanobacteria use micro-optics to sense light direction.* Elife, 2016. **5**: p. e12620.
258. Fankhauser, C. and J. Chory, *Light control of plant development.* Annual review of cell and developmental biology, 1997. **13**(1): p. 203-229.
259. Montgomery, B.L., *Sensing the light: photoreceptive systems and signal transduction in cyanobacteria.* Molecular microbiology, 2007. **64**(1): p. 16-27.
260. Hubschmann, T., et al., *Red and far-red light alter the transcript profile in the cyanobacterium Synechocystis sp. PCC 6803: impact of cyanobacterial phytochromes.* FEBS Lett, 2005. **579**(7): p. 1613-8.
261. Zheng, J., M. Hu, and Y. Guo, *Regulation of photosynthesis by light quality and its mechanism in plants.* Ying yong sheng tai xue bao= The journal of applied ecology, 2008. **19**(7): p. 1619-1624.
262. Singh, A.K., et al., *A systems-level analysis of the effects of light quality on the metabolism of a cyanobacterium.* Plant physiology, 2009. **151**(3): p. 1596-1608.
263. Dijkwel, P.P., et al., *Sucrose control of phytochrome A signaling in Arabidopsis.* The Plant Cell, 1997. **9**(4): p. 583.
264. Lamparter, T., *Evolution of cyanobacterial and plant phytochromes.* FEBS letters, 2004. **573**(1-3): p. 1-5.
265. Iwai, M., M. Yokono, and A. Nakano, *Toward understanding the multiple spatiotemporal dynamics of chlorophyll fluorescence.* Plant Signal Behav, 2015. **10**(6): p. e1022014.
266. Stelzer, E.H.K., *Light-sheet fluorescence microscopy for quantitative biology.* Nat Meth, 2015. **12**(1): p. 23-26.
267. Wood, W.H., et al., *Dynamic thylakoid stacking regulates the balance between linear and cyclic photosynthetic electron transfer.* Nature plants, 2018. **4**(2): p. 116.
268. Shire, S.J., *9 - The molecular basis of high viscosity of monoclonal antibodies (mAbs) at high concentration*, in *Monoclonal Antibodies*. 2015, Woodhead Publishing. p. 163-192.
269. Inoue, N., et al., *Acclimation to the growth temperature and the high-temperature effects on photosystem II and plasma membranes in a mesophilic cyanobacterium, Synechocystis sp. PCC6803.* Plant and Cell Physiology, 2001. **42**(10): p. 1140-1148.
270. Kirchhoff, H., *Diffusion of molecules and macromolecules in thylakoid membranes.* Biochimica et Biophysica Acta (BBA) - Bioenergetics, 2014. **1837**(4): p. 495-502.
271. Iwai, M., et al., *Isolation of the elusive supercomplex that drives cyclic electron flow in photosynthesis.* Nature, 2012. **464**(7292): p. 1210.

272. Watanabe, M., et al., *Attachment of phycobilisomes in an antenna–photosystem I supercomplex of cyanobacteria.* Proceedings of the National Academy of Sciences, 2014. **111**(7): p. 2512-2517.
273. Li, M., et al., *Characterization and evolution of tetrameric photosystem I from the thermophilic cyanobacterium Chroococcidiopsis sp TS-821.* The Plant Cell, 2014. **26**(3): p. 1230-1245.
274. Jeon, J.-H., et al., *Protein crowding in lipid bilayers gives rise to non-Gaussian anomalous lateral diffusion of phospholipids and proteins.* Physical Review X, 2016. **6**(2): p. 021006.
275. Mullineaux, C.W., *FRAP analysis of photosynthetic membranes.* Journal of Experimental Botany, 2004. **55**(400): p. 1207-1211.
276. Boekema, E., et al., *Evidence for a trimeric organization of the photosystem I complex from the thermophilic cyanobacterium Synechococcus sp.* Febs Letters, 1987. **217**(2): p. 283-286.
277. Boekema, E.J., et al., *Supramolecular structure of the photosystem II complex from green plants and cyanobacteria.* Proceedings of the National Academy of Sciences, 1995. **92**(1): p. 175-179.
278. Poggese, C., et al., *Cytochrome b 6/f complex from the cyanobacterium Synechocystis 6803: evidence of dimeric organization and identification of chlorophyll-binding subunit.* FEBS letters, 1997. **414**(3): p. 585-589.
279. Kouřil, R., et al., *Structure and functional role of supercomplexes of IsiA and Photosystem I in cyanobacterial photosynthesis.* FEBS Letters, 2005. **579**(15): p. 3253-3257.
281. Minton, A.P., *The influence of macromolecular crowding and macromolecular confinement on biochemical reactions in physiological media.* Journal of biological chemistry, 2001. **276**(14): p. 10577-10580.
282. Ellis, R.J., *Macromolecular crowding: obvious but underappreciated.* Trends in biochemical sciences, 2001. **26**(10): p. 597-604.
283. Schubert, W.-D., et al., *Photosystem I of Synechococcus elongatus at 4 Å resolution: comprehensive structure analysis.* Journal of molecular biology, 1997. **272**(5): p. 741-769.
284. Chitnis, V.P. and P.R. Chitnis, *PsaL subunit is required for the formation of photosystem I trimers in the cyanobacterium Synechocystis sp. PCC 6803.* FEBS letters, 1993. **336**(2): p. 330-334.
285. Schluchter, W.M., et al., *Characterization of psaI and psaL mutants of Synechococcus sp. strain PCC 7002: a new model for state transitions in cyanobacteria.* Photochem Photobiol, 1996. **64**(1): p. 53-66.
286. Liu, L.-N., *Distribution and dynamics of electron transport complexes in cyanobacterial thylakoid membranes.* Biochimica et Biophysica Acta (BBA)-Bioenergetics, 2016. **1857**(3): p. 256-265.
287. Nenninger, A., G. Mastroianni, and C.W. Mullineaux, *Size dependence of protein diffusion in the cytoplasm of Escherichia coli.* Journal of bacteriology, 2010. **192**(18): p. 4535-4540.
288. Hikosaka, K., *Modelling optimal temperature acclimation of the photosynthetic apparatus in C 3 plants with respect to nitrogen use.* Annals of Botany, 1997. **80**(6): p. 721-730.
289. Mackey, K.R., et al., *Effect of temperature on photosynthesis and growth in marine Synechococcus.* Plant physiology, 2013: p. pp. 113.221937.
290. Balogi, Z., et al., *"Heat shock lipid" in cyanobacteria during heat/light-acclimation.* Archives of biochemistry and biophysics, 2005. **436**(2): p. 346-354.
291. Murata, N., et al., *Photoinhibition of photosystem II under environmental stress.* Biochimica et Biophysica Acta (BBA)-Bioenergetics, 2007. **1767**(6): p. 414-421.

292. Liu, B.-H. and Y.-K. Lee, *Secondary carotenoids formation by the green alga Chlorococcum sp.* Journal of applied phycology, 2000. **12**(3-5): p. 301-307.
293. Ardail, D., et al., *Mitochondrial contact sites. Lipid composition and dynamics.* Journal of Biological Chemistry, 1990. **265**(31): p. 18797-18802.
294. Kirchhoff, H., et al., *Supramolecular photosystem II organization in grana thylakoid membranes: evidence for a structured arrangement.* Biochemistry, 2004. **43**(28): p. 9204-9213.
295. Zavřel, T., et al., *Characterization of a model cyanobacterium Synechocystis sp. PCC 6803 autotrophic growth in a flat-panel photobioreactor.* Engineering in Life Sciences, 2015. **15**(1): p. 122-132.
296. Montgomery, B.L., *The Regulation of Light Sensing and Light-Harvesting Impacts the Use of Cyanobacteria as Biotechnology Platforms.* Front Bioeng Biotechnol, 2014. **2**: p. 22.
297. Dudkina, N.V., et al., *Structure and function of mitochondrial supercomplexes.* Biochimica et Biophysica Acta (BBA)-Bioenergetics, 2010. **1797**(6-7): p. 664-670.
298. Engelman, D.M., *Membranes are more mosaic than fluid.* Nature, 2005. **438**(7068): p. 578.
299. Dekker, J.P. and E.J. Boekema, *Supramolecular organization of thylakoid membrane proteins in green plants.* Biochimica et Biophysica Acta (BBA)-Bioenergetics, 2005. **1706**(1-2): p. 12-39.
300. Heinemeyer, J., et al., *A structural model of the cytochrome c reductase/oxidase supercomplex from yeast mitochondria.* Journal of Biological Chemistry, 2007. **282**(16): p. 12240-12248.
301. Schägger, H., *Respiratory chain supercomplexes.* IUBMB life, 2001. **52**(3-5): p. 119-128.
302. Lenaz, G. and M.L. Genova, *Structural and functional organization of the mitochondrial respiratory chain: a dynamic super-assembly.* The international journal of biochemistry & cell biology, 2009. **41**(10): p. 1750-1772.
303. Paumard, P., et al., *The ATP synthase is involved in generating mitochondrial cristae morphology.* The EMBO journal, 2002. **21**(3): p. 221-230.
304. Giraud, M.-F., et al., *Is there a relationship between the supramolecular organization of the mitochondrial ATP synthase and the formation of cristae?* Biochimica et Biophysica Acta (BBA)-Bioenergetics, 2002. **1555**(1-3): p. 174-180.
305. Stroh, A., et al., *Assembly of respiratory complexes I, III, and IV into NADH oxidase supercomplex stabilizes complex I in Paracoccus denitrificans.* Journal of Biological Chemistry, 2004. **279**(6): p. 5000-5007.
306. Sarcina, M., et al., *Lipid diffusion in the thylakoid membranes of the cyanobacterium Synechococcus sp.: effect of fatty acid desaturation.* FEBS letters, 2003. **553**(3): p. 295-298.
307. Swaminathan, R., C.P. Hoang, and A. Verkman, *Photobleaching recovery and anisotropy decay of green fluorescent protein GFP-S65T in solution and cells: cytoplasmic viscosity probed by green fluorescent protein translational and rotational diffusion.* Biophysical journal, 1997. **72**(4): p. 1900-1907.
308. Kohler, R., et al., *Active protein transport through plastid tubules: velocity quantified by fluorescence correlation spectroscopy.* Journal of cell science, 2000. **113**(22): p. 3921-3930.
309. Partikian, A., et al., *Rapid diffusion of green fluorescent protein in the mitochondrial matrix.* The Journal of cell biology, 1998. **140**(4): p. 821-829.
310. Mullineaux, C.W., et al., *Diffusion of green fluorescent protein in three cell environments in Escherichia coli.* Journal of bacteriology, 2006. **188**(10): p. 3442-3448.
311. Kaňa, R., O. Prášil, and C.W. Mullineaux, *Immobility of phycobilins in the thylakoid lumen of a cryptophyte suggests that protein diffusion in the lumen is very restricted.* FEBS letters, 2009. **583**(4): p. 670-674.

312. Frick, M., K. Schmidt, and B.J. Nichols, *Modulation of lateral diffusion in the plasma membrane by protein density.* Current biology, 2007. **17**(5): p. 462-467.
313. Nehls, S., et al., *Dynamics and retention of misfolded proteins in native ER membranes.* Nature cell biology, 2000. **2**(5): p. 288.
314. Fulbright, R.M., et al., *Fatty acid alteration and the lateral diffusion of lipids in the plasma membrane of keratinocytes.* Experimental cell research, 1997. **233**(1): p. 128-134.
315. Gupte, S.S., et al., *Two-dimensional diffusion of F1F0-ATP synthase and ADP/ATP translocator. Testing a hypothesis for ATP synthesis in the mitochondrial inner membrane.* Biochimica et Biophysica Acta (BBA)-Biomembranes, 1991. **1069**(2): p. 131-138.
316. Hochman, J.H., et al., *Lateral mobility of cytochrome c on intact mitochondrial membranes as determined by fluorescence redistribution after photobleaching.* Proceedings of the National Academy of Sciences, 1982. **79**(22): p. 6866-6870.
317. Casella, S., et al., *Dissecting the native architecture and dynamics of cyanobacterial photosynthetic machinery.* Molecular Plant, 2017.
318. Sarcina, M. and C.W. Mullineaux, *Mobility of the IsiA chlorophyll-binding protein in cyanobacterial thylakoid membranes.* Journal of Biological Chemistry, 2004. **279**(35): p. 36514-36518.
319. Blackwell, M., et al., *The plastoquinone diffusion coefficient in chloroplasts and its mechanistic implications.* Biochimica et Biophysica Acta (BBA)-Bioenergetics, 1994. **1183**(3): p. 533-543.
320. Blackwell, M.F., et al., *A method for estimating lateral diffusion coefficients in membranes from steady-state fluorescence quenching studies.* Biophysical journal, 1987. **51**(5): p. 735-744.
321. Blackwell, M.F. and J. Whitmarsh, *Effect of integral membrane proteins on the lateral mobility of plastoquinone in phosphatidylcholine proteoliposomes.* Biophysical journal, 1990. **58**(5): p. 1259-1271.
322. Drepper, F., et al., *Lateral diffusion of an integral membrane protein: Monte Carlo analysis of the migration of phosphorylated light-harvesting complex II in the thylakoid membrane.* Biochemistry, 1993. **32**(44): p. 11915-11922.
323. Sukhorukov, V.M., et al., *Determination of protein mobility in mitochondrial membranes of living cells.* Biochimica et Biophysica Acta (BBA) - Biomembranes, 2010. **1798**(11): p. 2022-2032.
324. Lindberg, P., S. Park, and A. Melis, *Engineering a platform for photosynthetic isoprene production in cyanobacteria, using Synechocystis as the model organism.* Metabolic engineering, 2010. **12**(1): p. 70-79.

Appendix

Appendix for chapter 2

Appendix A

Table of the antibodies' concentrations used for western blot

Component description	Concentration	Expected band size
Goat anti-mouse IgG, Promega	1:2500	
Goat Anti-rabbit, Agrisera	1:25000	
Anti eGFP-tag, Invitrogen	1:2500	27 kDa
Anti PsaC (PSI complex), host: rabbit, Agrisera	1:1000	9 kDa
Anti D2 (PsbD, PSII complex), host: rabbit, Agrisera	1:5000	39.4 kDa
Anti cyt f (Cyt b_6f complex), host: rabbit, Agrisera	1:10000	31 kDa
Anti AtpB (sub β ATPase complex), host: rabbit, Agrisera	1:5000	51.7 kDa

Appendix B

List the components of the resuspension and the solubilization buffers used for BN-gel.

Buffer	Components	Stock concentration	Tot volume
Resuspension buffer			100 µL
	50BTH40G	50 mM BisTris-HCl, 40% (w/v) Glycerol	50 µL
	Pefabloc	10 mg/ml	2.5 µL
	MgCl2	1M	1 µL
	RQ1 (DNase)		4 µL
	H2O		42.5 µL
Solubilization buffer			100 µL

	50BTH40G	50 mM BisTris-HCl, 40% (w/v) Glycerol	50 µL
	Pefabloc	10 mg/ml	2.5 µL
	MgCl2	1M	1 µL
	RQ1 (DNase)		4 µL
	DM (dodecyl maltoside)	10%	30 µL
	H2O		12.5 µL

Appendix C

The following Matlab script uses the fluorescence profile values extracted by ImageJ to estimate the mobile fraction, the bleach depth and the bleach width of the frapped cells. It also provides the experimental fluorescence recovery curve and the experimental difference bleaching profile used to run the simulation in Sigma plot (see appendix D). The number of pictures taken before the bleaching, the time interval between frames and the pixel size of the images needed to be adapted for each FRAP experiment. See section 2.8.3 for details.

1D FRAP analysis

```
%-- Script to calculate the 1D FRAP recovery and provide Diffusion
coefficient and mobile fraction
%
%   ver 1: First working. Takes output from ImageJ macro and calculates
Diffusion Coefficient
%   ver 2: tried to incorporate the curve fitting to extract parameters
but does not resolve with complex equation
%
%                                                  Written By Dave Mason
[dnmason@liv.ac.uk], Nov 2015
%
%-------------------------------------------------------------------------
----------------------------
%clearvars -except inFile inPath

sizePreBleach=3; %-- How many prebleach values?
timeInterval= 0.970036364; %-- seconds between frames
xyCalib=0.0415; %-- pixel size (um/pixel)
-- Runtime options
showGraphs=1; %-- Display graphs? [0/1] (may help with debugging
problems)
chooseCentre=1; %-- Interactively select centre of bleach region? [0/1]
```

```
approveFit=1; %-- Interactively select centre of bleach region? [0/1]


inPath=uigetdir;
fileList=dir(fullfile(inPath,'*.csv'));
fileNum=0;
%-- returns a structured array where size(fileList,1) equals the number
of files ending in csv

for myFile = fileList';
inFile=myFile.name;
%clearvars -except showGraphs chooseCentre inPath fileList approveFit
sizePreBleach timeInterval xyCalib outData outNames fileNum inFile
myFile

%close all

%-- Only pick the bleach sheets from the list to prevent double
processing
if strfind(inFile,'_bleach') %-- remember that it may have a timestamp
on it
    %--Record number of files
    fileNum=fileNum+1;
    data_bleach=importdata([inPath '\' inFile]);
    %-- should probably check this even exits!
    data_ctrls=importdata([inPath                                    '\'
strrep(inFile,'_bleach','_ctrls')]);
else
    continue %-- Break to next file in list
end
disp('--------------------------------------');
disp(['Processing : ' inPath '\' inFile]);
disp('--------------------------------------');

%-- should have both datasets in at this point so pull some parameters
sizeT=length(data_ctrls(:,1));
sizeX=length(data_bleach(:,1))/sizeT;
-- Arrange the bleach data into a matrix of (Length x Timepoint)
data_array=data_bleach(((1-1)*sizeX)+1:((1-1)*sizeX)+sizeX);
for i=2:sizeT
    data_array=horzcat(data_array,data_bleach(((i-1)*sizeX)+1:((i-
1)*sizeX)+sizeX));
end
-- Background subtract the matrix per position
data_array_bgsub=data_array(1,:) - data_ctrls(:,2)';
for i=2:sizeX
data_array_bgsub=vertcat(data_array_bgsub,data_array(i,:)            -
data_ctrls(:,2)');
end
-- Correct for nonspecific bleaching
data_array_bgsub_cor=data_array(1,:) ./ data_ctrls(:,1)';
for i=2:sizeX
data_array_bgsub_cor=vertcat(data_array_bgsub_cor,data_array(i,:)   ./
data_ctrls(:,1)');
```

```
end
-- calculate the sum of the pre-bleach values and take the mean
avgSumPreBleach=mean(sum(data_array_bgsub_cor(:,1:sizePreBleach)));
-- calculate the sum of the first post-bleach values
avgSumPostBleach=sum(data_array_bgsub_cor(:,sizePreBleach+1));
-- scaled pre-bleach values: average multiplied by the ratio of the sum
of the post bleach and the sum of the pre-bleach
scaledPreBleach=data_array_bgsub_cor(:,sizePreBleach)*(avgSumPostBleac
h/avgSumPreBleach);
-- Difference profile: subtract each of the values for the first post-
bleach from the scaled pre-bleach column
differenceProfile=data_array_bgsub_cor(:,sizePreBleach+1)-
scaledPreBleach;
-- Look at the first post-bleach value and find the closest position to
the maxima of the gaussian fit
differenceProfileSmoothed=smooth(differenceProfile);
[tmp                                                peakVal]=findpeaks(-
differenceProfileSmoothed,'MinPeakDistance',floor(sizeX*0.5),'MinPeakH
eight',(range(differenceProfileSmoothed)/2)+min(-
differenceProfileSmoothed) );

if chooseCentre==1
    h0=figure('Color',[1 1 1]);
    plot(differenceProfile)
    hold on
    plot(differenceProfileSmoothed,'r-')
    for j=1:length(peakVal)
        plot([peakVal(j) peakVal(j)],[-0.6 0.3],'g-')
    end
    title(['Raw (blue) and Smoothed (red) Difference Profile (Peak = '
num2str(peakVal) ')'])
    xlabel 'Distance (pixels)';
    ylabel 'Difference Profile';


    peakVal_user=inputdlg('Select          X          position','Peak
Val',1,{num2str(peakVal)});
    %-- no error catching non-numeric input
    peakVal=str2num(peakVal_user{1});
    close(h0);

end

if showGraphs==1
    h1=figure('Color',[1 1 1]);
    plot(differenceProfile)
    hold on
    plot(differenceProfileSmoothed,'r-')
    for j=1:length(peakVal)
        plot([peakVal(j) peakVal(j)],[-0.6 0.3],'g-')
    end
    title(['Raw (blue) and Smoothed (red) Difference Profile (Peak = '
num2str(peakVal) ')'])
    xlabel 'Distance (pixels)';
```

```
    ylabel 'Difference Profile';
end
-- pull the intensity versus time for the mid-gauss point
expFluorRecovery=data_array_bgsub_cor(peakVal,sizePreBleach+1:end)';
tempOutPut=data_array_bgsub_cor(peakVal,:)';
expFluorRecovery_time=[timeInterval:timeInterval:length(expFluorRecove
ry)*timeInterval]';
expFluorRecoveryForSigmaPlot=expFluorRecovery-
scaledPreBleach(peakVal);
-- Concatenate the scaled Pre-Bleach Value (at Peak) with the normalised
recovery data
outputGraphY=[scaledPreBleach(peakVal) expFluorRecovery(:)'];
outputGraphYnorm=(outputGraphY/outputGraphY(1));
outputGraphX=[timeInterval:timeInterval:(length(expFluorRecovery)+1)*t
imeInterval]';
outputGraphData=[outputGraphX outputGraphYnorm'];
csvwrite(strrep(fullfile(inPath,inFile),'.csv','_outputGraphData.csv')
,outputGraphData);

if showGraphs==1
h2=figure('Color',[1 1 1]);
plot(expFluorRecovery_time,expFluorRecovery,'bo');
hold on
plot([expFluorRecovery_time(1)
expFluorRecovery_time(end)],[mean(expFluorRecovery(end-5:end))
mean(expFluorRecovery(end-5:end))],'r-');
plot([expFluorRecovery_time(1)
expFluorRecovery_time(end)],[expFluorRecovery(1)
expFluorRecovery(1)],'r:');
title 'Normalised Recovery'
xlabel 'Time (seconds)';
ylabel 'Fractional Recovery';
end
-- estimate the Mobile Fraction by fitting
%-- First create fit options
%-- order: a (base), b (plateau), c (rate)
%-- Half time is calculated as 1/c
fo = fitoptions('Method','NonlinearLeastSquares',...
               'Lower',[0,0,0],...
               'Upper',[2,2,Inf],...
               'StartPoint',[0.1,1,0.1]);

fitEqu='(a-b)*exp(-c*x)+b';
[fit1a                                                          fit1b
fit1c]=fit(expFluorRecovery_time,expFluorRecovery,fitEqu,fo);
disp(['Half Time of recovery = ' num2str(1/fit1a.c) ' seconds'])
%-- Check to see if the fit converges (if not exitflag is negative)
if fit1c.exitflag<0
    %-- Hasn't fit, so do a rough and ready calculation
    CalcPlateau=mean(expFluorRecovery(end-5:end));
else
    %-- Assume the fit has worked so pull the parameters from the fit
    CalcPlateau=fit1a.b;
    %-- Also add the fit to the graph
```

```
    plot(fit1a,'g');
    legend off
end
-- Save the image of the Mf estimate parameters. If the fit has worked,
this will include the fit line
        saveFrame=getframe(h2);

imwrite(saveFrame.cdata,strrep(fullfile(inPath,inFile),'.csv','_Mf_Fig
.png'));
        clearvars saveFrame;

%-----------------------------------------------------------------------

Mf1=(CalcPlateau-expFluorRecovery(1))/(scaledPreBleach(peakVal)-
expFluorRecovery(1));
disp('--- Recovery Parameters: ---');
if fit1c.exitflag<0
disp('Curve Fit Failed - Used last 5 values to estimate plateau')
else
    disp('Curve Fit Successful')
end
disp(['Calculated Plateau: ' num2str(CalcPlateau)] )
disp(['Calculated Mobile Fraction: ' num2str(Mf1)] )

if approveFit==1
    inputPlateau=inputdlg(['The     Calculated     Plateau     is     '
num2str(CalcPlateau)       '.       Optionally       change       this
below:'],'Input',1,{num2str(CalcPlateau)});
    inputPlateau=str2num(inputPlateau{:});
else
    inputPlateau=CalcPlateau;
end
Mf2=(inputPlateau-expFluorRecovery(1))/(scaledPreBleach(peakVal)-
expFluorRecovery(1));
disp(['Estimated Plateau: ' num2str(inputPlateau)] )
disp(['Estimated Mobile Fraction: ' num2str(Mf2)] )

%-----------------------------------------------------------------------
-- First calculate the width of the bleach profile
a=data_array_bgsub_cor(:,sizePreBleach+1);
numVals=length(a);
b=[xyCalib:xyCalib:length(a)*xyCalib]';
c=smooth(a);
d=max(c)-c;
[fit3a                                                              fit3b
fit3c]=fit(b(round(numVals*0.3):round(numVals*0.7)),d(round(numVals*0.
3):round(numVals*0.7)),'gauss1');
-- read out the depth and HW
e=fit3a.a1;
-- but this is the full depth, so we need to subtract from this the
inverted BG (for which we've used the mean of the first 10% of values)
e=e-mean(d(1:round(numVals*0.2)));
-- record the SD
f=fit3a.c1;
```

```
if showGraphs==1
    h4=figure('Color',[1 1 1]);
    plot(fit3a,b,d);
    title 'Fitted Data'
    legend off
    hold on
    plot(b,mean(d(1:round(numVals*0.1))),'r:');
    xlabel 'Distance (um)';
    ylabel 'Inverted Intensity';
end

g=(2.3548*fit3a.c1)/2; %-- Fit gives sigma, calculate the FWHM and
divide by two to get HW@HM
-- Output values
disp('--- Bleaching Parameters: ---');
disp(['Depth: ' num2str(e)]);
disp(['Half-width: ' num2str(g) 'um']);
%disp('--- Other Parameters: ---');
%disp(['Mean         Intensity         along         profile:         '
num2str(mean(data_array_bgsub(:,1))/(sizeX*xyCalib))]);
%disp(['Standard        Deviation        along        profile:        '
num2str(std(data_array_bgsub(:,1)))]);

if fileNum<2
    outData=[fileNum inputPlateau Mf2 e g peakVal numVals];
    outNames={inFile};
else
    outData=vertcat(outData,[fileNum  inputPlateau  Mf2  e  g  peakVal
numVals]);
    outNames=[outNames;inFile]; %-- Vert cat two cell arrays
end
-- Save out the parameters for sigmaplot
csvwrite([inPath                                                    '\'
strrep(inFile,'.csv','_expFluor.csv')],expFluorRecoveryForSigmaPlot);
csvwrite([inPath                                                    '\'
strrep(inFile,'.csv','_diffProf.csv')],differenceProfile);
end %-- Close 'for' loop
-- Add the data to the cell array
outData=num2cell(outData);
outCell=[outNames,outData];
%-- add headers
outTitles={'FileName','Index','Plateau','Mf','Depth','HalfWidth','Peak
','NumVal'};
outCell=[outTitles;outCell];
-- Write out the data in rows of:
fID = fopen([inPath '\OutputData.csv'], 'wt') ;
%-- print title
fprintf(fID, '%s,%s,%s,%s,%s,%s,%s,%s\n', outCell{1,:});
fclose(fID);
fID = fopen([inPath '\OutputData.csv'], 'a') ;
for i=2:size(outCell,1)
    fprintf(fID, '%s,%f,%f,%f,%f,%f,%f,%f\n', outCell{i,:});
end
```

```
fclose(fID);
%clearvars -except outCell
```

Appendix D

Iterative computer routine to predict the evolution of fluorescence profile during diffusion events and calculate the diffusion coefficient value. This routine uses the values of mobile fraction and the experimental difference bleaching profile calculated in Matlab. The code is shown in red, while values that should be adjusted are shown in blue. Abbreviations: D= diffusion coefficient, in $\mu m^2 s^{-1}$; F= experimental value for the mobile fraction (between 0 and 1); T= timespan for the simulation (in seconds); s= size of dataset (i.e. number of X-points in the profile); i= X-increment (in microns). See section 2.8.3 for details.

SIGMAPLOT ROUTINE

```
D=0.01
F=0.5
T=200
s=256
i=0.02146
E=0.00001
k=D/((i^2)*100)
l= E/((i^2)*100)
for q=1 to 100 do
block(q+1,2,q+1,s)=block(q,1,q,s-1)
block(q+2,1,q+2,s-1)=block(q,2,q,s)
cell(q+1,1)=cell(q+1,2)
cell(q+2,s)=cell(q+2,s-1)
col(q+1)=col(q)+(l*(col(q+1)+col(q+2)-2*col(q)))
end for
col(105)=col(102)
col(111)=col(1)
col(1)=F*col(111)
for m=1 to T do
for n=1 to 100 do
block(n+1,2,n+1,s)=block(n,1,n,s-1)
block(n+2,1,n+2,s-1)=block(n,2,n,s)
```

```
cell(n+1,1)=cell(n+1,2)
cell(n+2,s)=cell(n+2,s-1)
col(n+1)=col(n)+(k*(col(n+1)+col(n+2)-2*col(n)))
end for
col(m+111)=col(101)
col(1)=col(101)
end for
col(1)=col(105)*(1-F)
for p=112 to (T+111) do
col(p)=col(p)+col(1)
end for
```

Appendix E

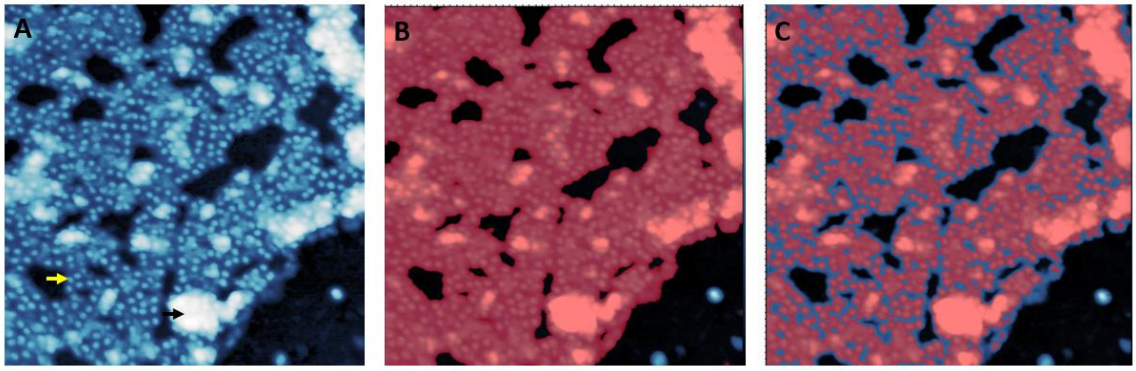

Figure A 1 Estimation protein density from AFM images. (A) Topography image of a thylakoid membrane patch on mica. The protein appears as little cyan dots (white arrow) or larger cyan aggregates (black arrow). The lipids (blue) surrounds the proteins. (B) The area covered by the membrane (masked in red) occupies 82% of the image. The mask is a function of the Gwyddion software that allows, among other properties, to estimate the area of the region of interest. (C) The protein region (61% of the image) can be masked because the protein protrudes from the lipid layer. We can have a rough estimation of the protein content by the protein area/membrane area ratio; in this case, 0.61/0.82 = 0.74 (i.e., the protein content is 74%).

Appendix for chapter 3

Appendix F

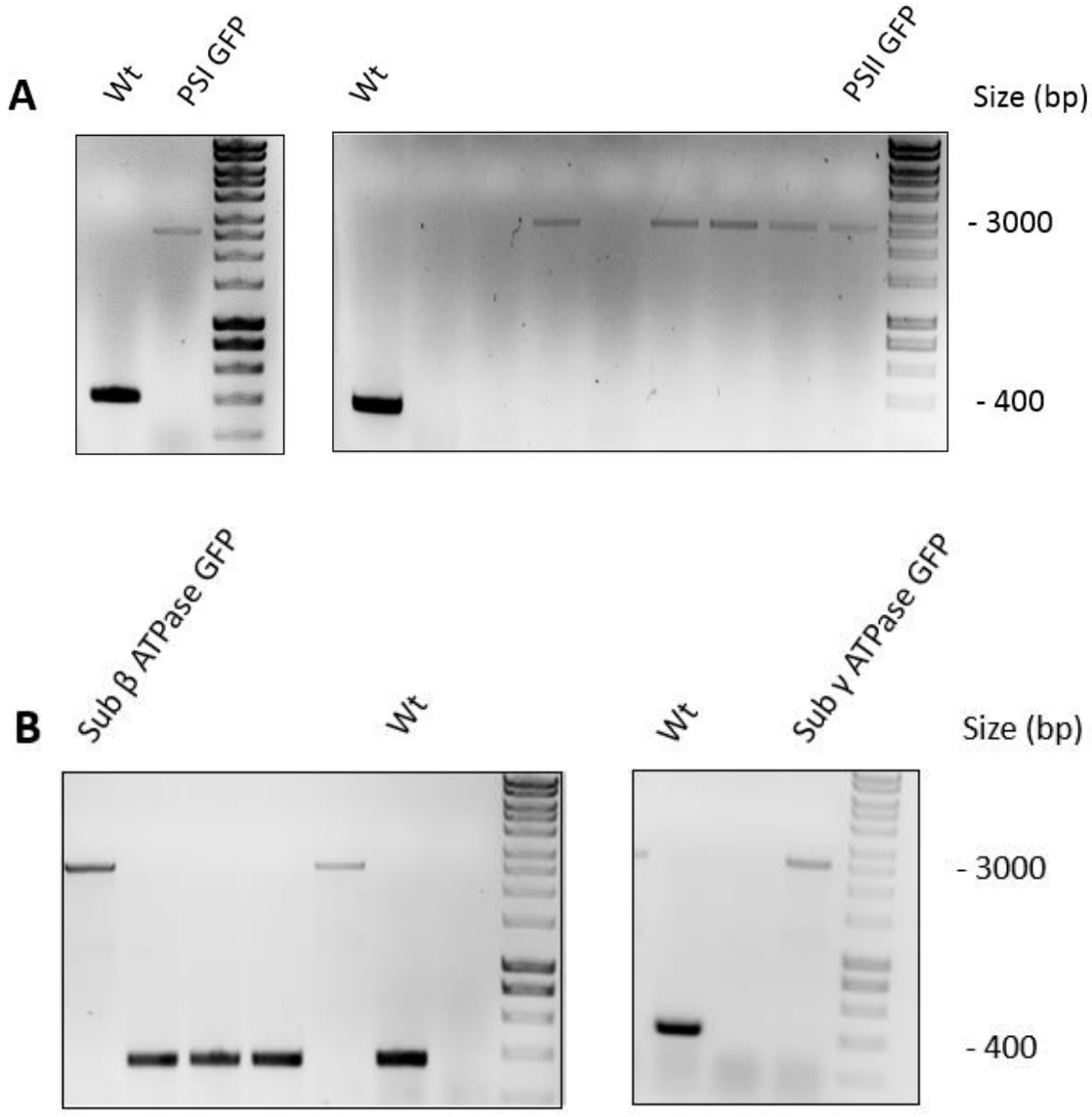

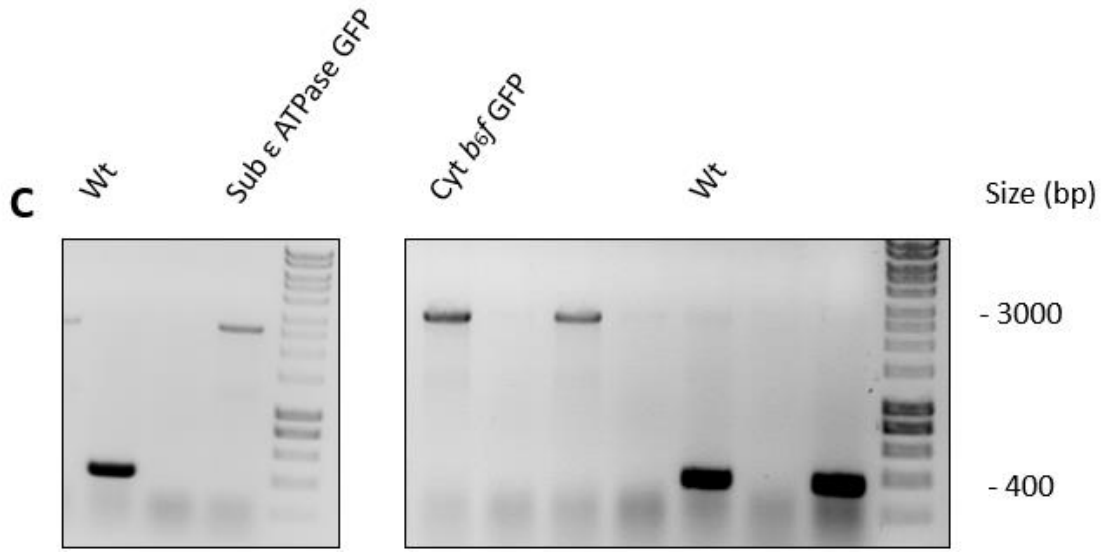

Figure A 2 PCR verification of the full segregation of the mutants. Original gels for the evaluation of the GFP fusion strains by segregation PCR. All primer pairs have been tested on both WT and mutant DNA (GFP segregation primers are listed in Table 2.3). The fragments amplified from a WT strain not containing GFP insertion are 380 bp. Each gel show the strains PSI:eGFP (A), PSII:eGFP (A), Cyt b_6f:eGFP (C), sub γ ATPase:eGFP (B), sub β ATPase:eGFP (B) and sub ε ATPase:eGFP (C) full segregated into the Syn 7942 genome (fragment size of 3000 bp).

Appendix G

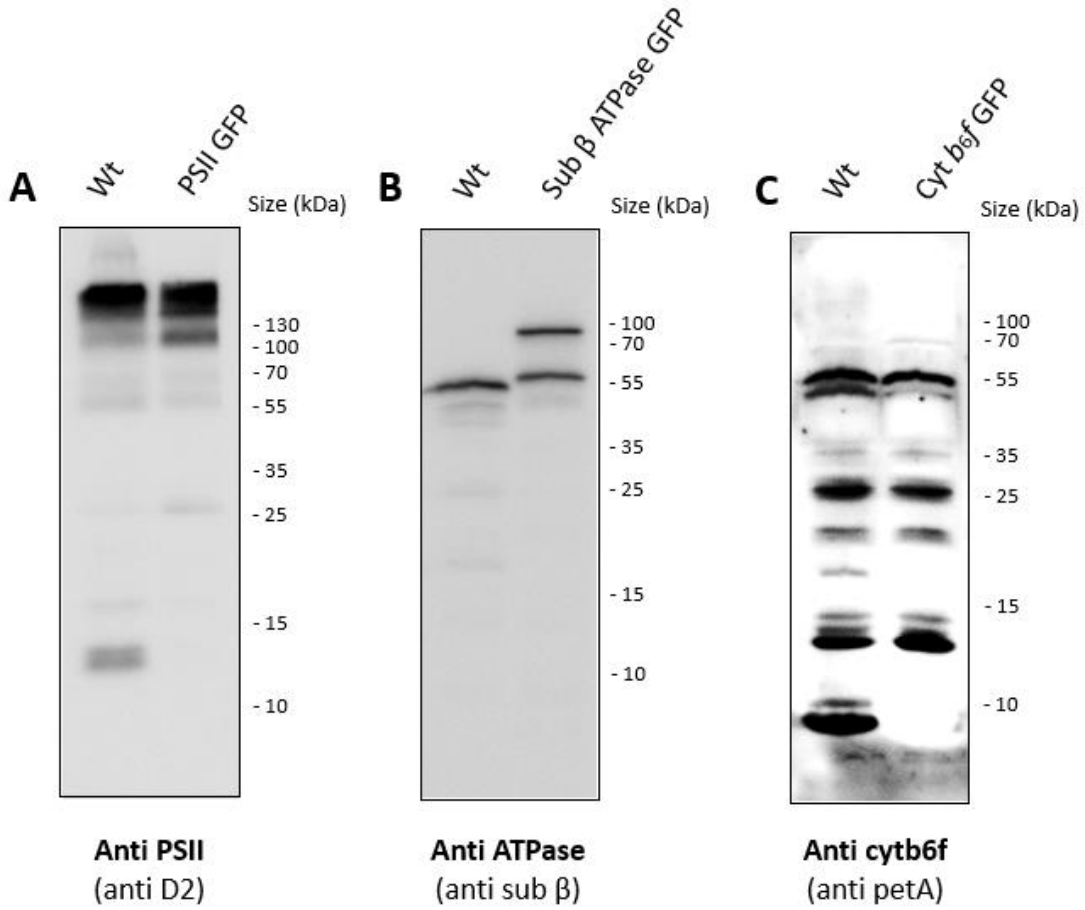

Figure A 3 Characterization of the GFP fusion mutants with SDS page and immunoblot analysis. Immunoblots on SDS page using anti-PSII (A), anti-ATPase (B) and anti-Cyt b_6f (C) antibody. The band size predicted for each targeted subunit are as follow: 39 kDa (D2), 51.7 kDa (sub β) and 34 kDa (petA). Samples were loaded in equal protein amount.

Appendix H

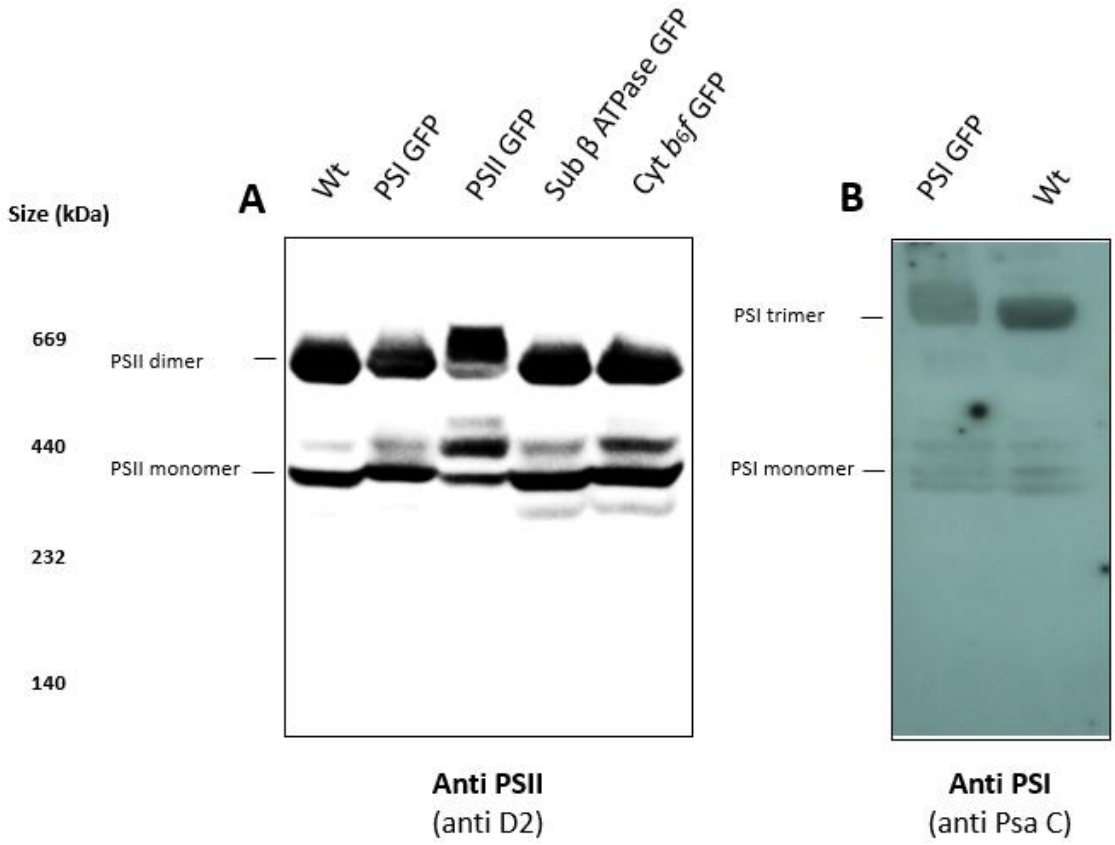
A
Wt
PSI GFP
PSII GFP
Sub β ATPase GFP
Cyt b6f GFP
Size (kDa)
669
440
232
140
PSII dimer
PSII monomer
Anti PSII
(anti D2)
B
PSI GFP
Wt
PSI trimer
PSI monomer
Anti PSI
(anti Psa C)

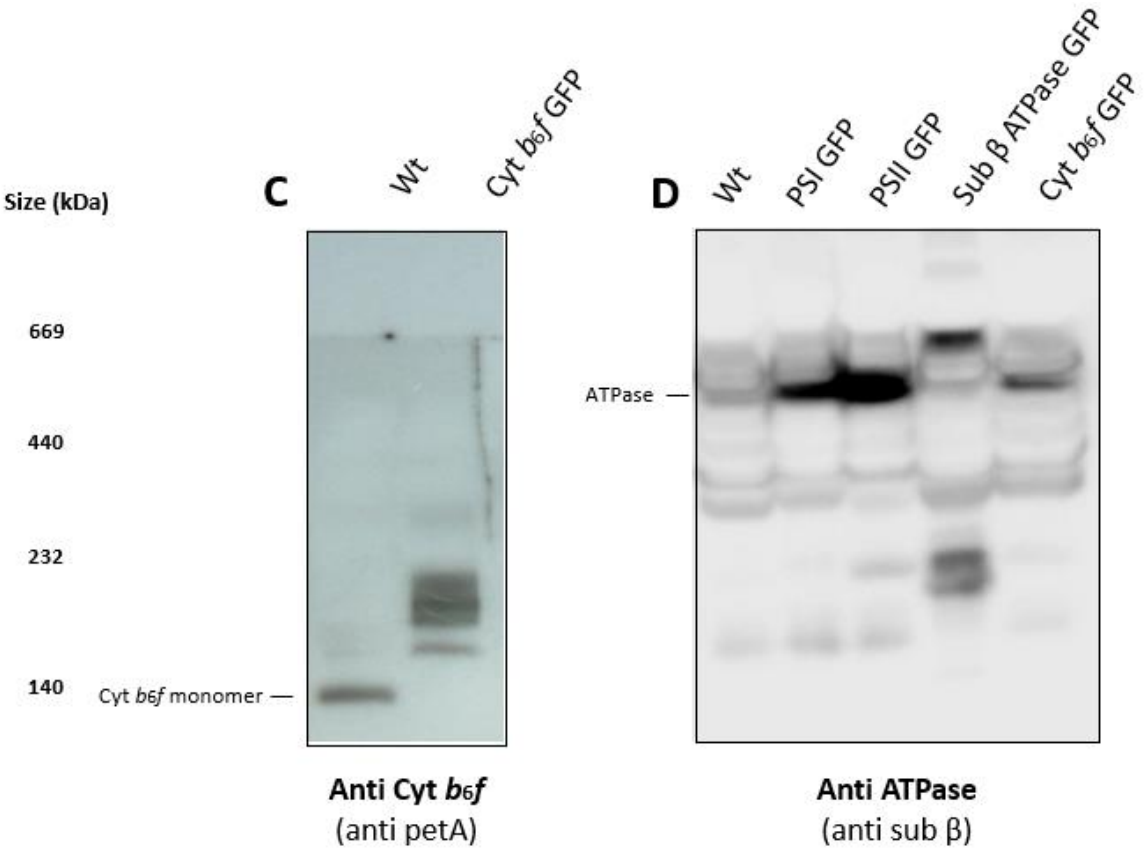

Figure A 4 Characterization of the GFP fusion mutants with BN-PAGE and immunoblot analysis. Immunoblot analysis on BN-PAGE using anti-PSII (A), anti-PSII (B), anti-Cyt b6f (C) and anti-ATPase (D) antibody. The band size predicted for each targeted complex are shown on the left of each gel. Samples were loaded in equal chlorophyll amount.

Appendix I

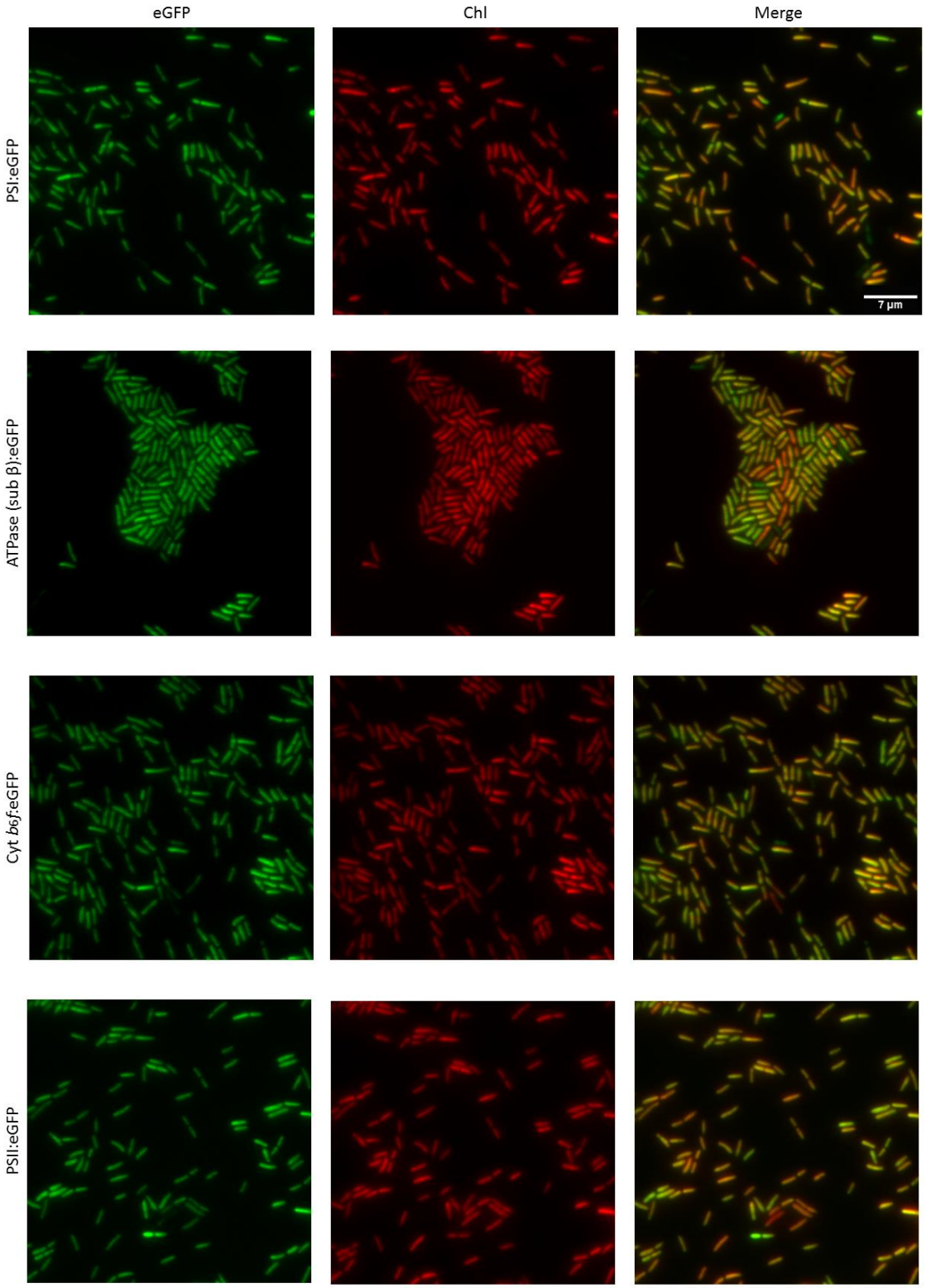

Figure A 5 Overview of photosynthetic complexes in Syn7942 by TIRF microscopy. Single near-TIRF image frames of PSI:eGFP, PSII:eGFP, ATPase:eGFP and Cyt b_6f:eGFP Syn7942 cells.

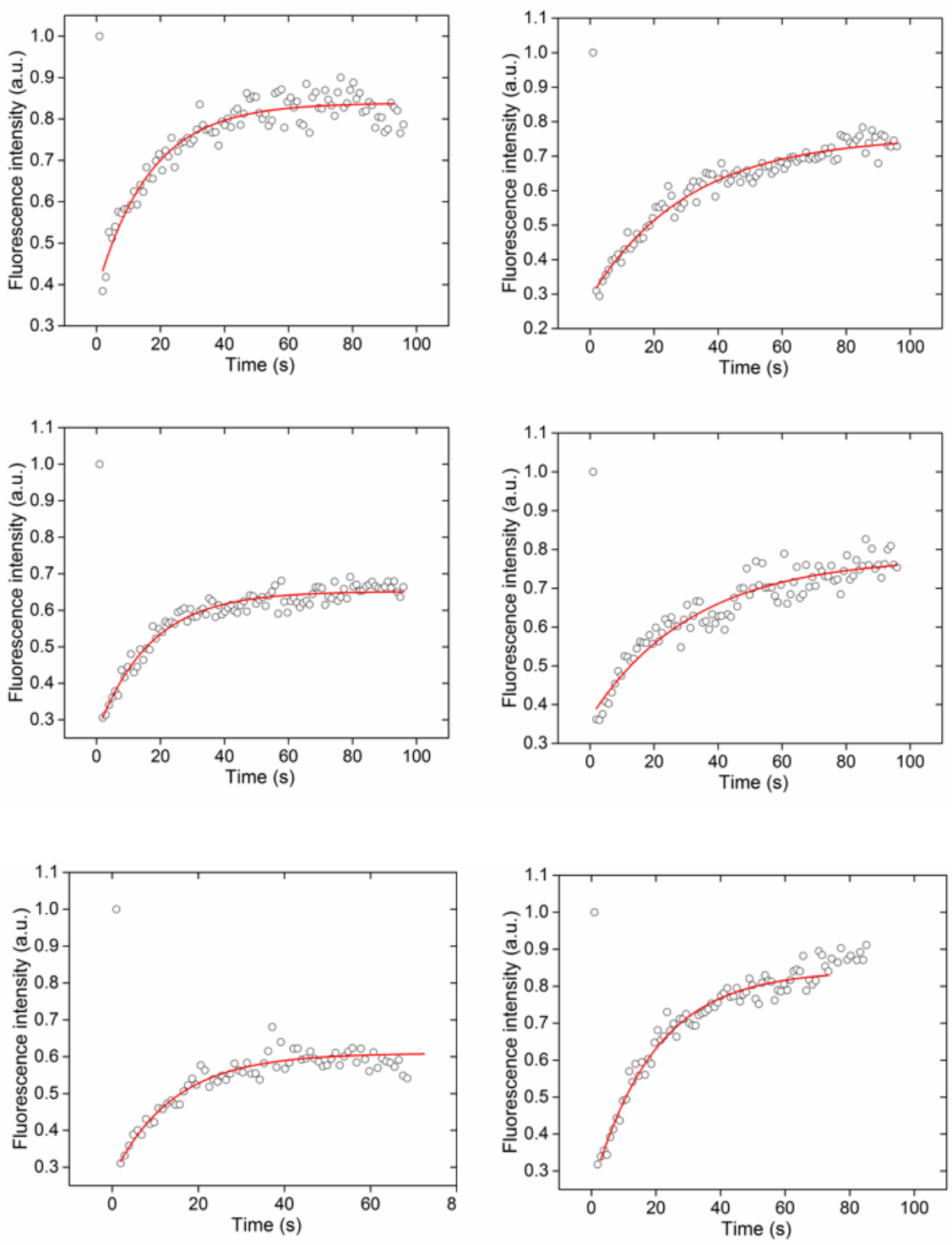

Figure A 6 Additional fluorescence recovery curves of GFP fluorescence in PSI:eGFP cells grown at 30 °C under white illumination (40-50 µE/m²*s)). Time course of fluorescence recovery of the bleached cell regions for GFP fluorescence. The recovery of the GFP fluorescence is presented as circles and fitted to an exponential function (red lines) to highlight the curve trend.

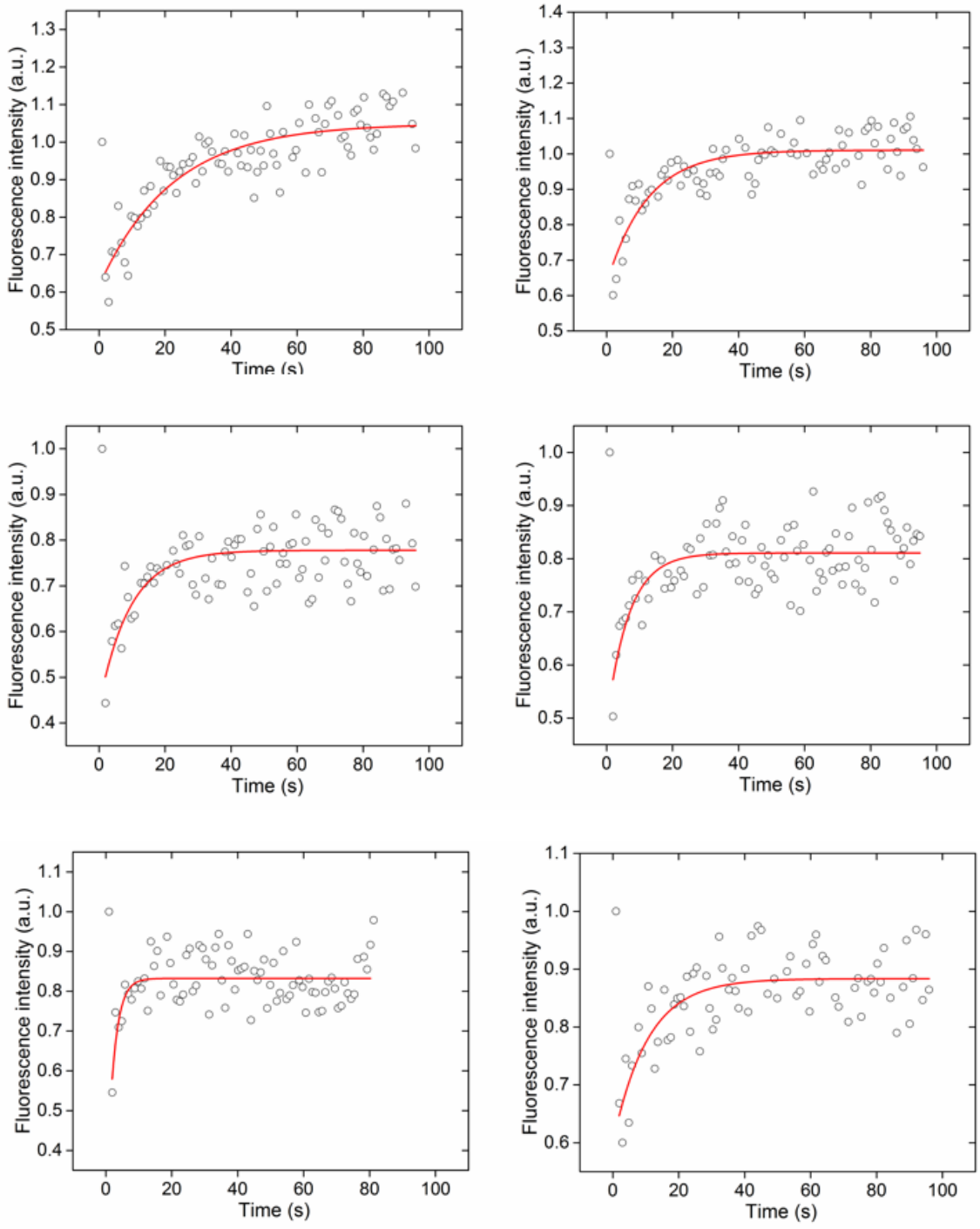

Figure A 7 Additional fluorescence recovery curves of GFP fluorescence in PSII:eGFP cells grown at 30 °C under white illumination (40-50 µE/m2*s)). Time course of fluorescence recovery of the bleached cell regions for GFP fluorescence. The recovery of the GFP fluorescence is presented as circles and fitted to an exponential function (red lines) to highlight the curve trend.

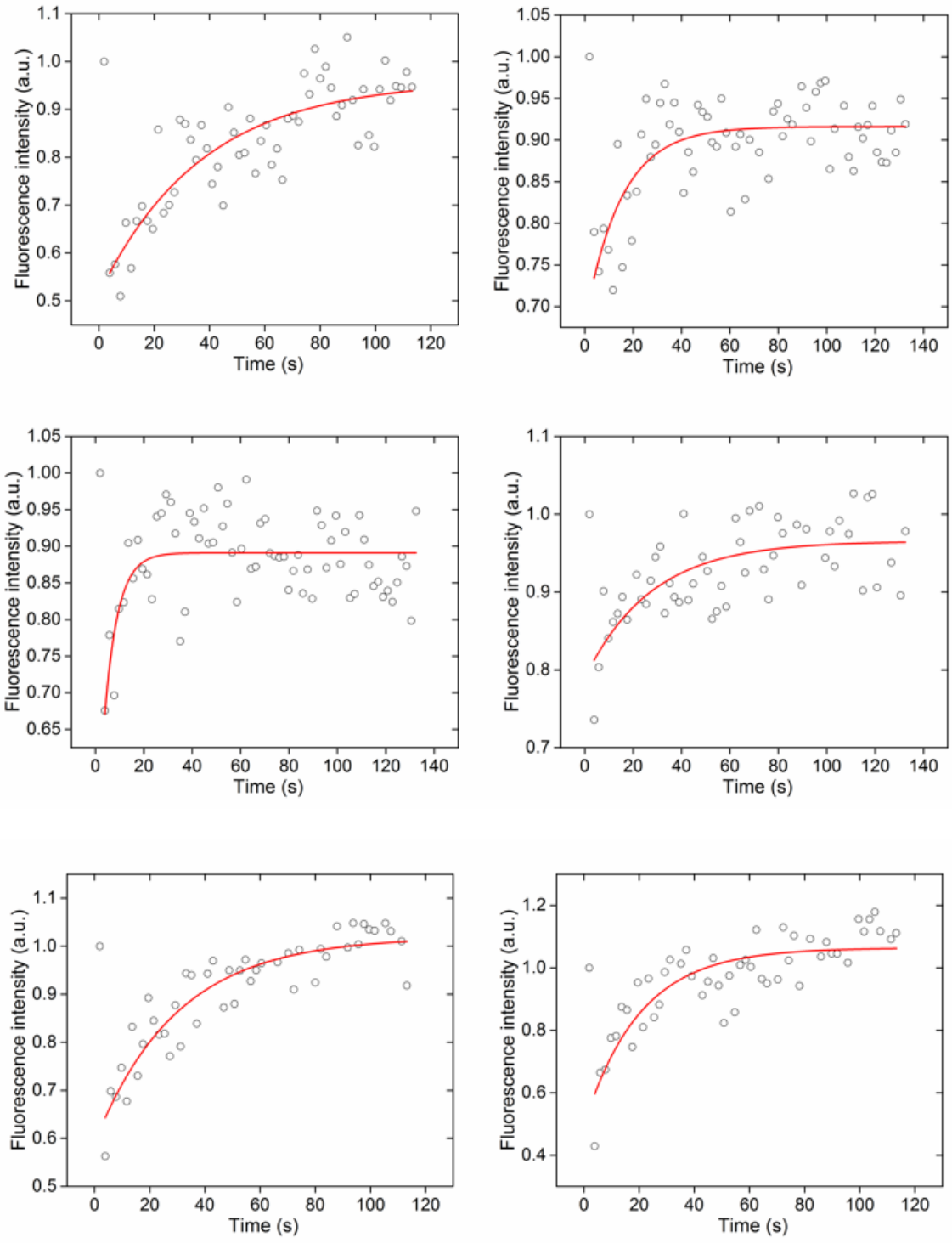

Figure A 8 Additional fluorescence recovery curves of GFP fluorescence in ATPase:eGFP cells grown at 30 °C under white illumination (40-50 µE/m2*s)). Time course of fluorescence recovery of the bleached cell regions for GFP fluorescence. The recovery of the GFP fluorescence is presented as circles and fitted to an exponential function (red lines) to highlight the curve trend.

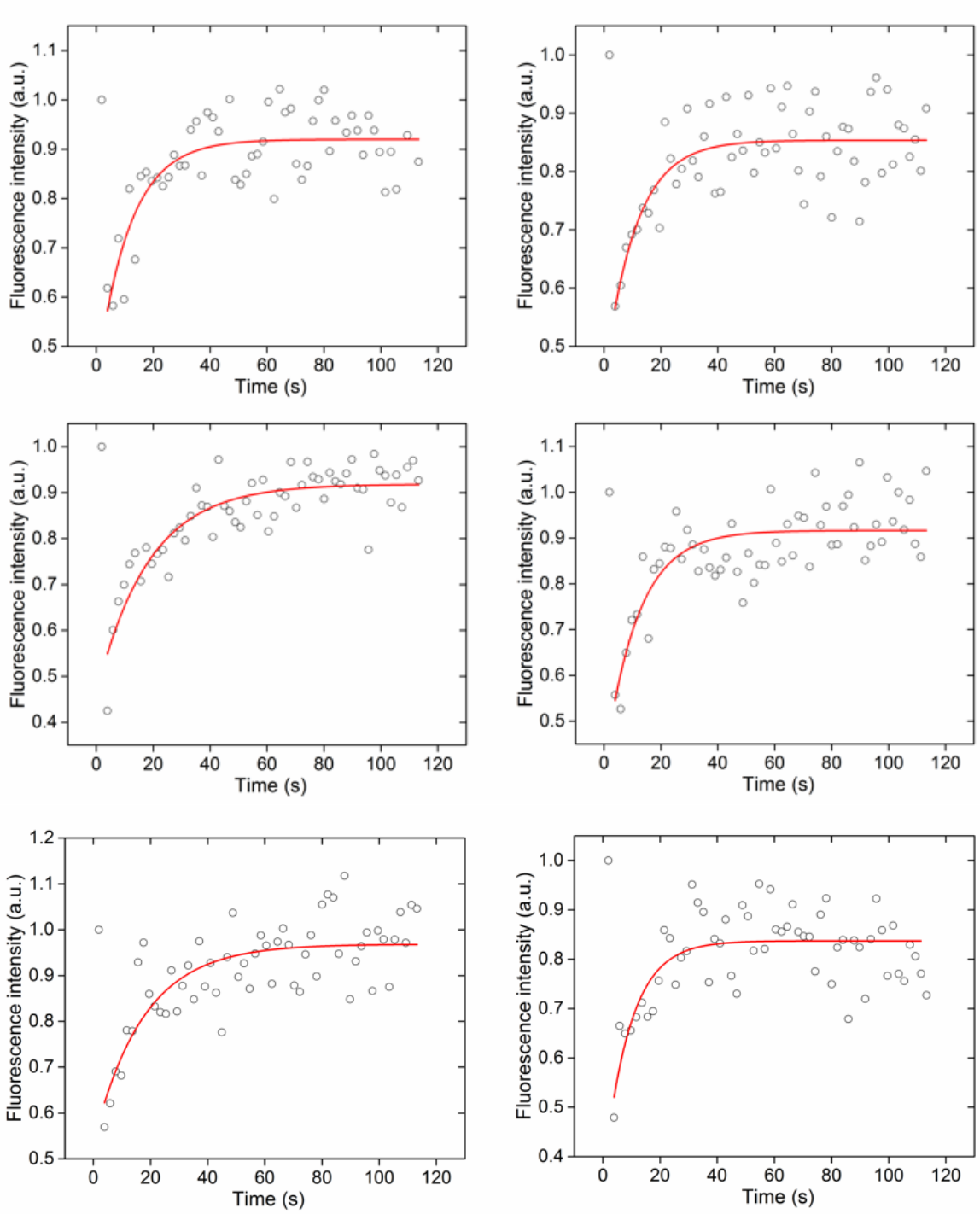

Figure A 9 Additional fluorescence recovery curves of GFP fluorescence in Cyt b_6f:eGFP cells grown at 30 °C under white illumination (40-50 µE/m2*s)). Time course of fluorescence recovery of the bleached cell regions for GFP fluorescence. The recovery of the GFP fluorescence is presented as circles and fitted to an exponential function (red lines) to highlight the curve trend.

Appendix for chapter 4

Appendix L

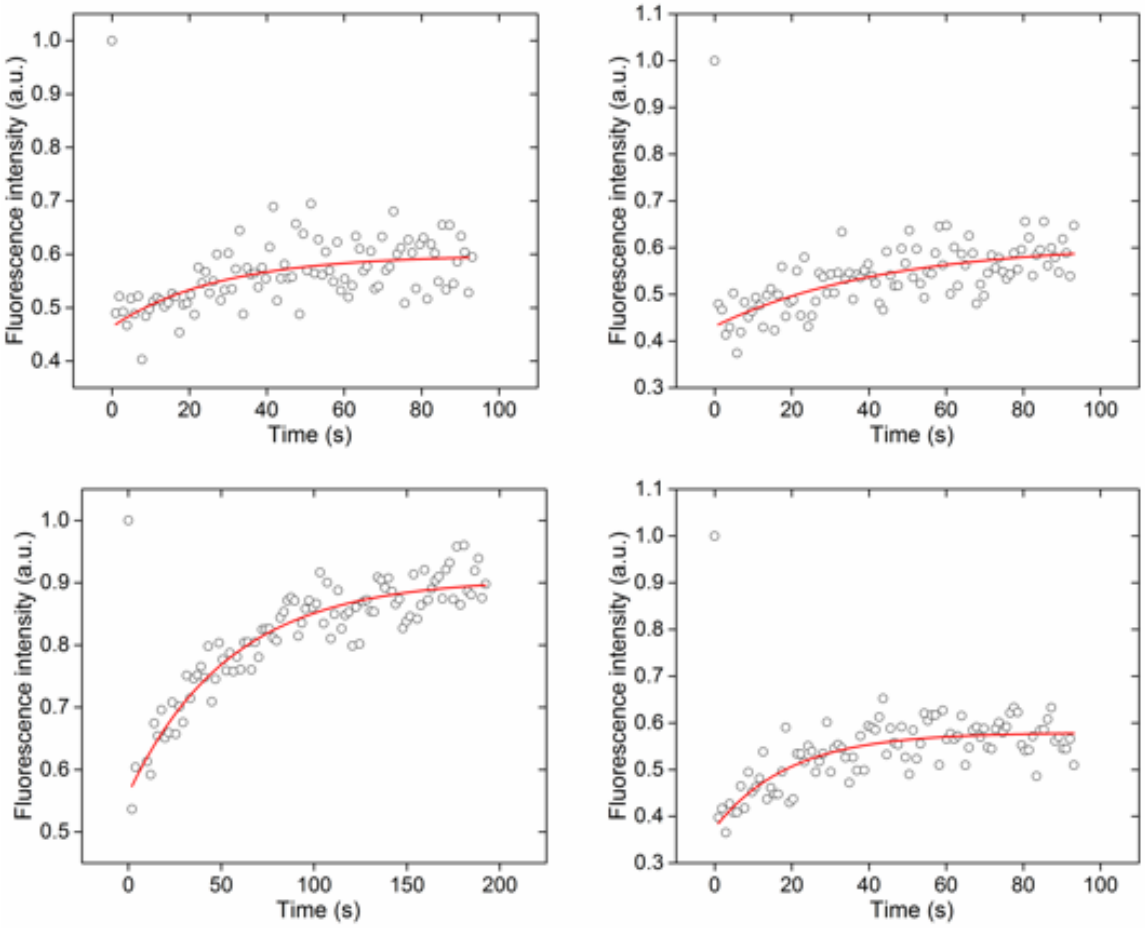

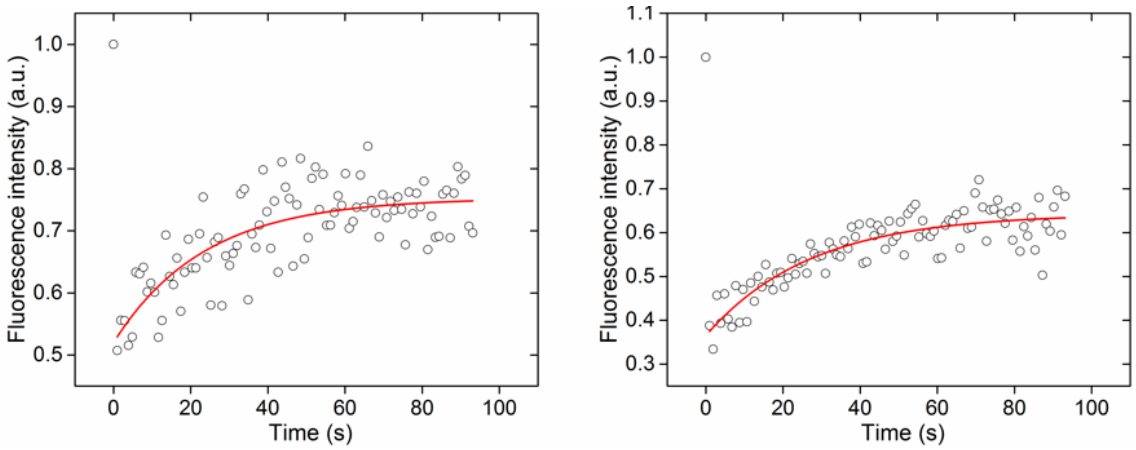

Figure A 10 Additional fluorescence recovery curves of GFP fluorescence in PSI:eGFP cells after red light treatment. Time course of fluorescence recovery of the bleached cell regions for GFP fluorescence. The recovery of the GFP fluorescence is presented as circles and fitted to an exponential function (red lines) to highlight the curve trend.

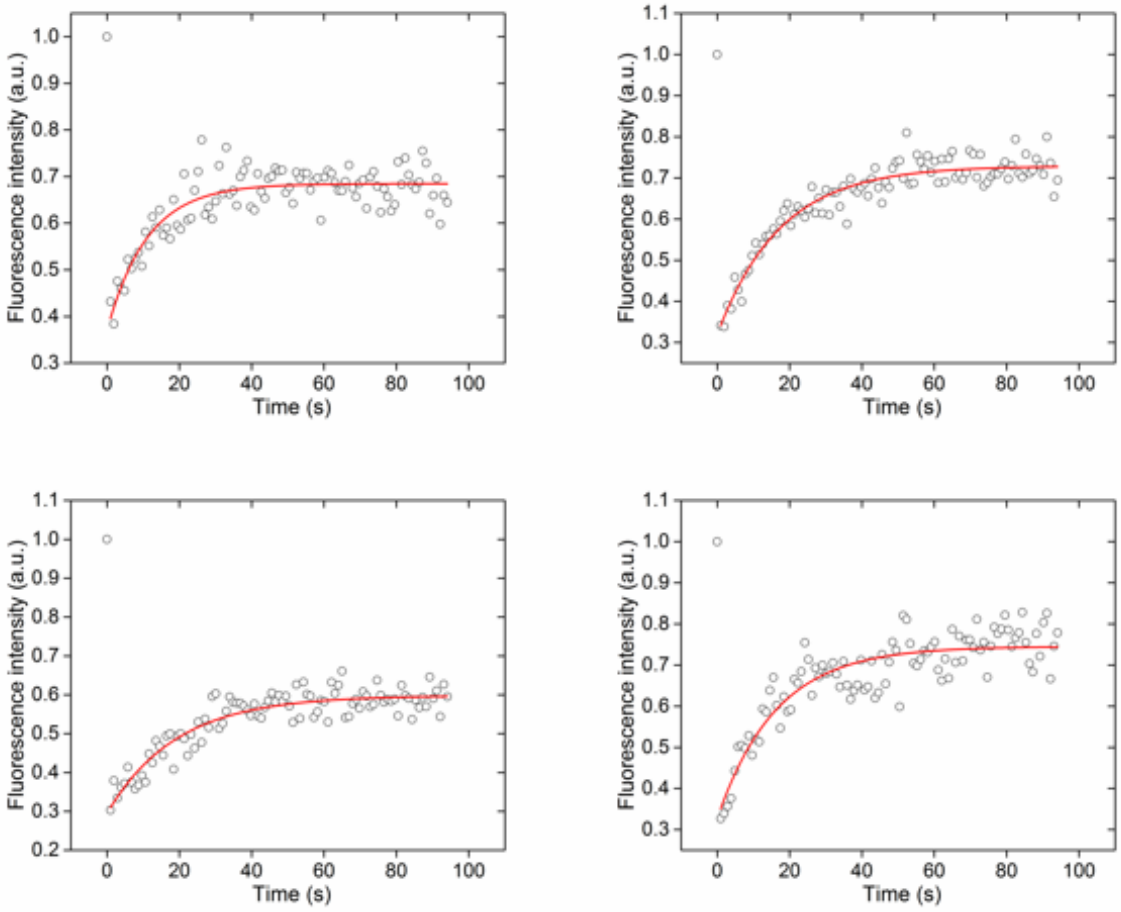

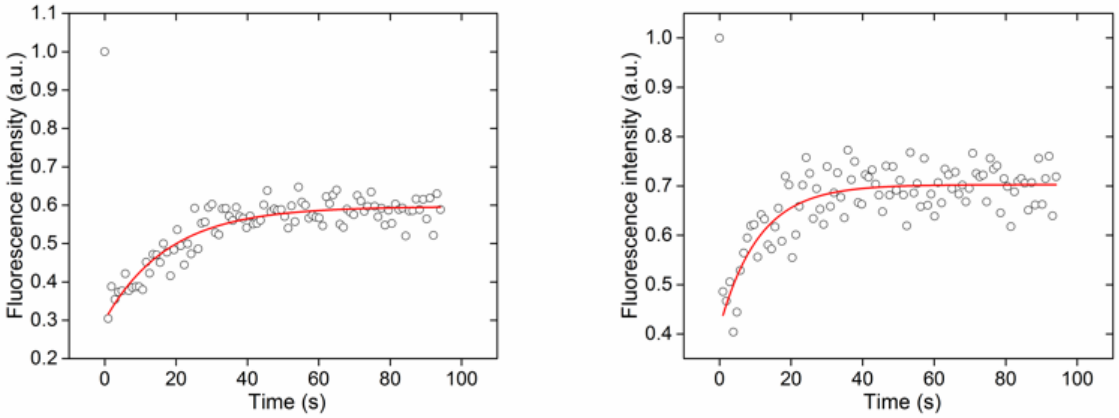

Figure A 11 Additional fluorescence recovery curves of GFP fluorescence in PSII:eGFP cells after red light treatment. Time course of fluorescence recovery of the bleached cell regions for GFP fluorescence. The recovery of the GFP fluorescence is presented as circles and fitted to an exponential function (red lines) to highlight the curve trend.

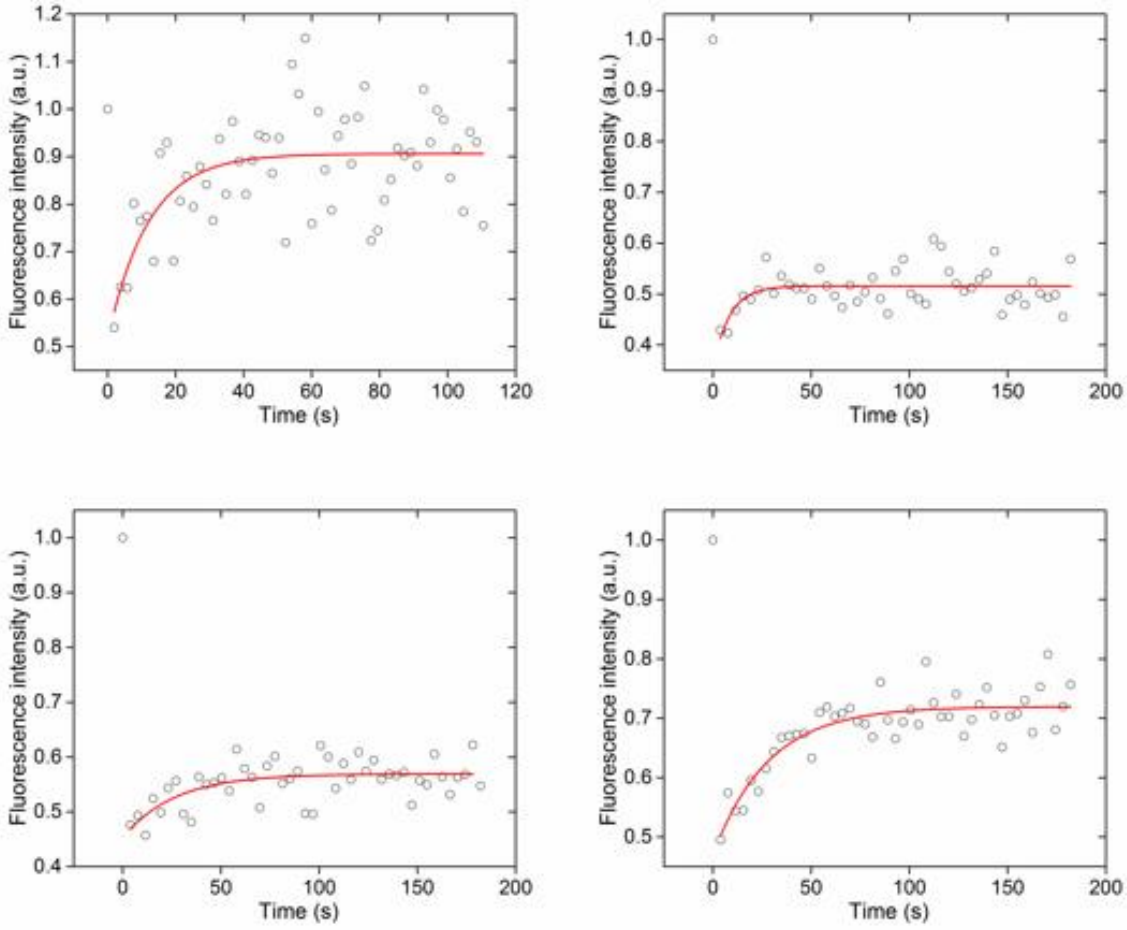

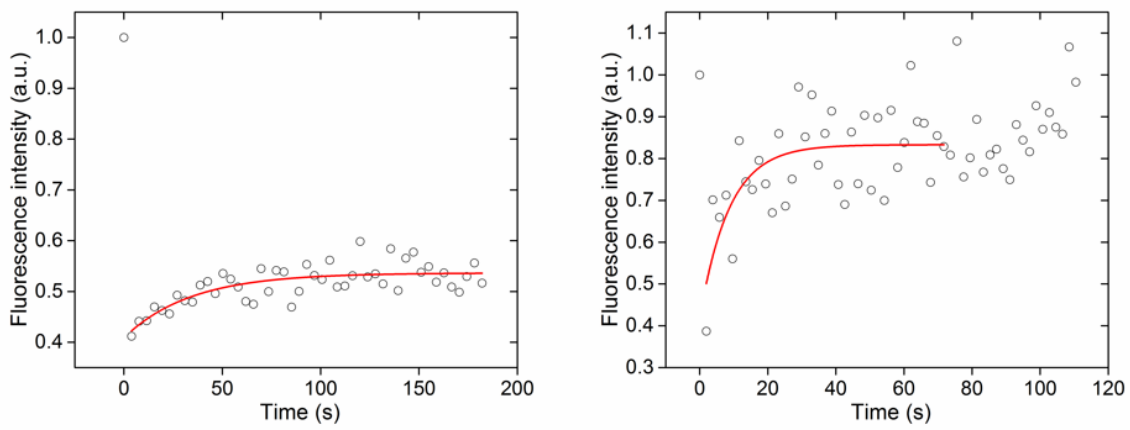

Figure A 12 Additional fluorescence recovery curves of GFP fluorescence in ATPase:eGFP cells after red light treatment. Time course of fluorescence recovery of the bleached cell regions for GFP fluorescence. The recovery of the GFP fluorescence is presented as circles and fitted to an exponential function (red lines) to highlight the curve trend.

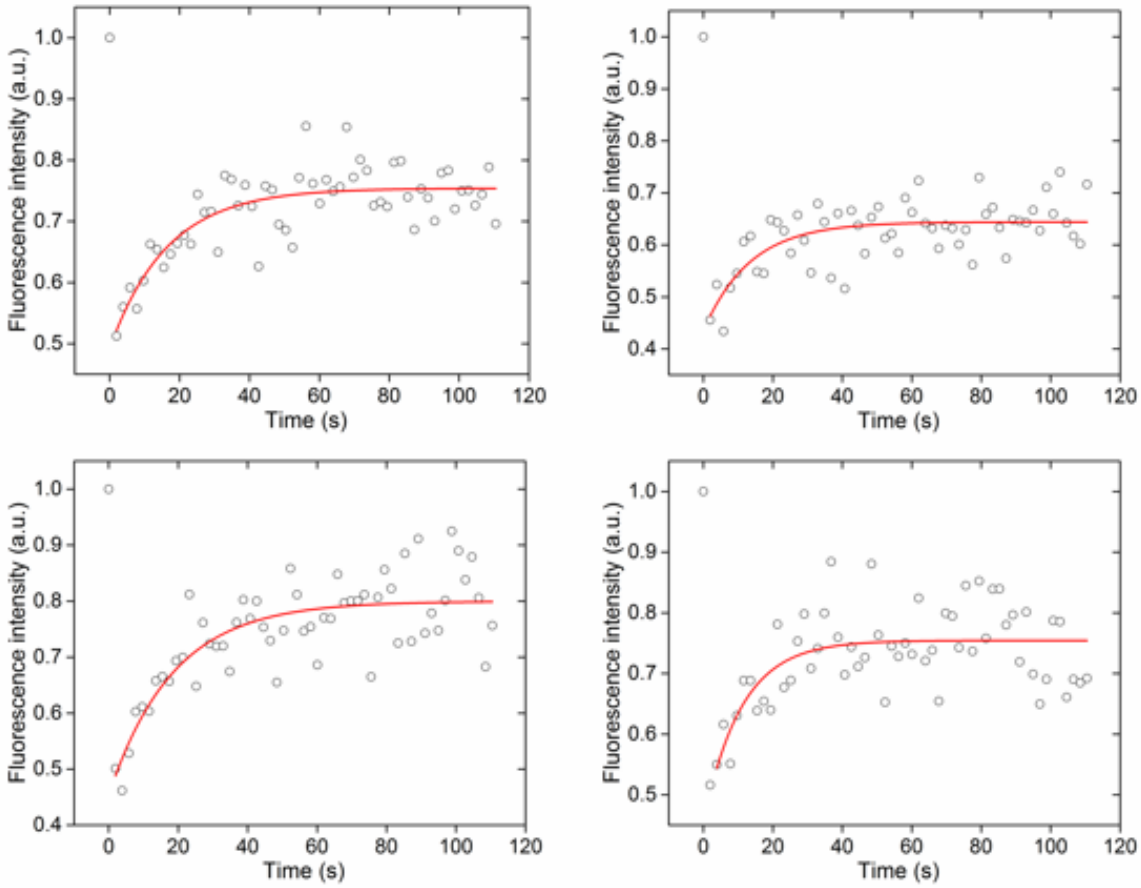

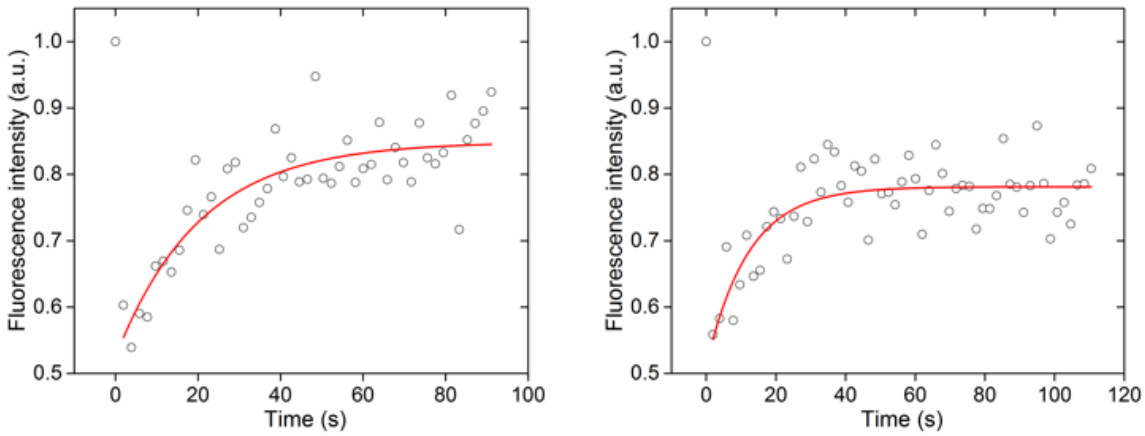

Figure A 13 Additional fluorescence recovery curves of GFP fluorescence in Cyt b_6f:eGFP cells after red light treatment. Time course of fluorescence recovery of the bleached cell regions for GFP fluorescence. The recovery of the GFP fluorescence is presented as circles and fitted to an exponential function (red lines) to highlight the curve trend.

Appendix for chapter 5

Appendix M

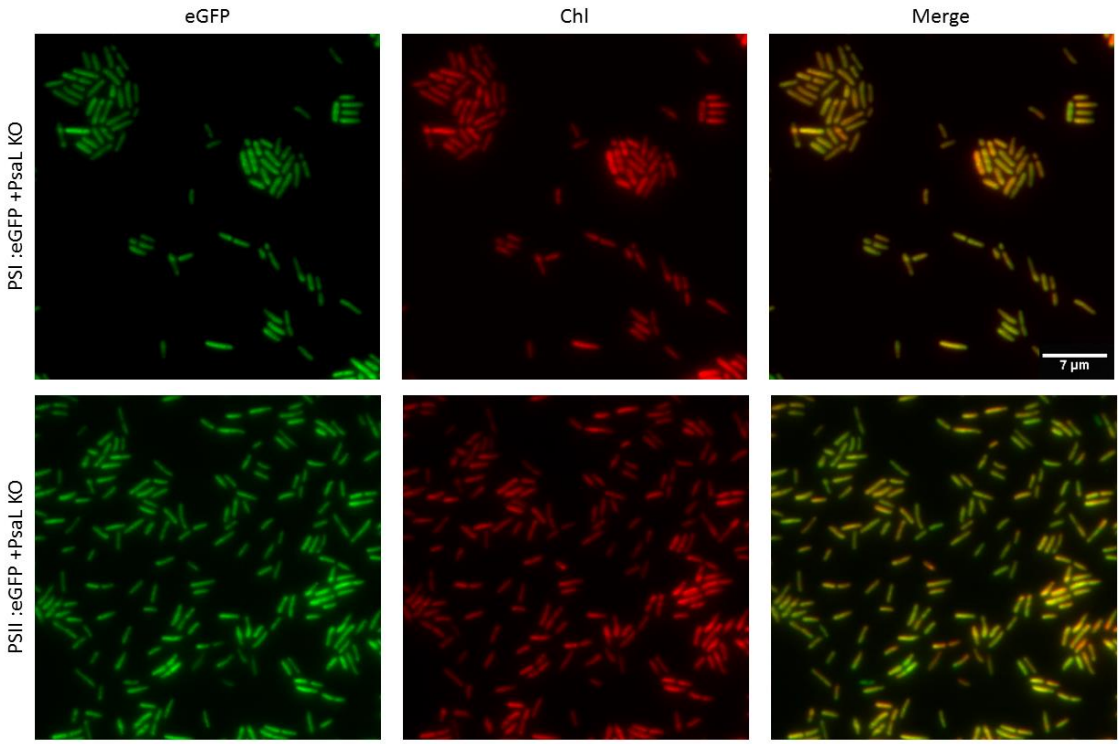

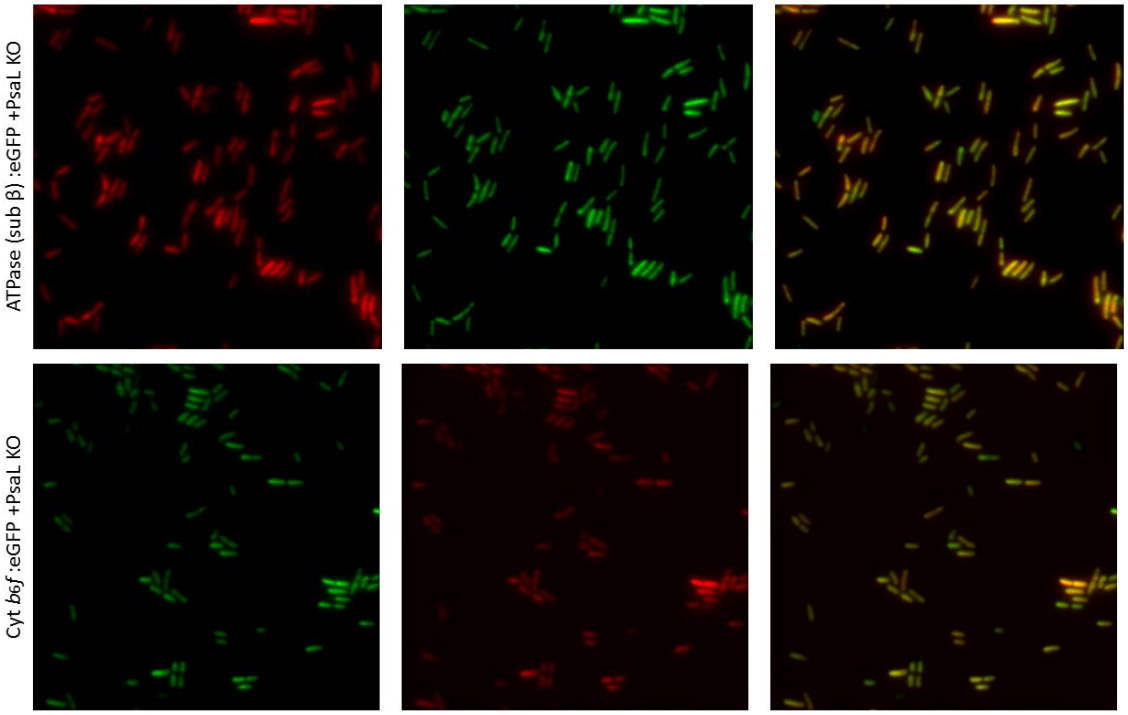

Figure A 14 Distribution of the photosynthetic complexes in the ΔPsaL mutants. Single near-TIRF images of PSI:eGFP+ΔPsaL, PSII:eGFP+ΔPsaL, ATPase (subβ):eGFP+ΔPsaL, Cyt b_6f:eGFP+ΔPsaL double mutants.

Appendix N

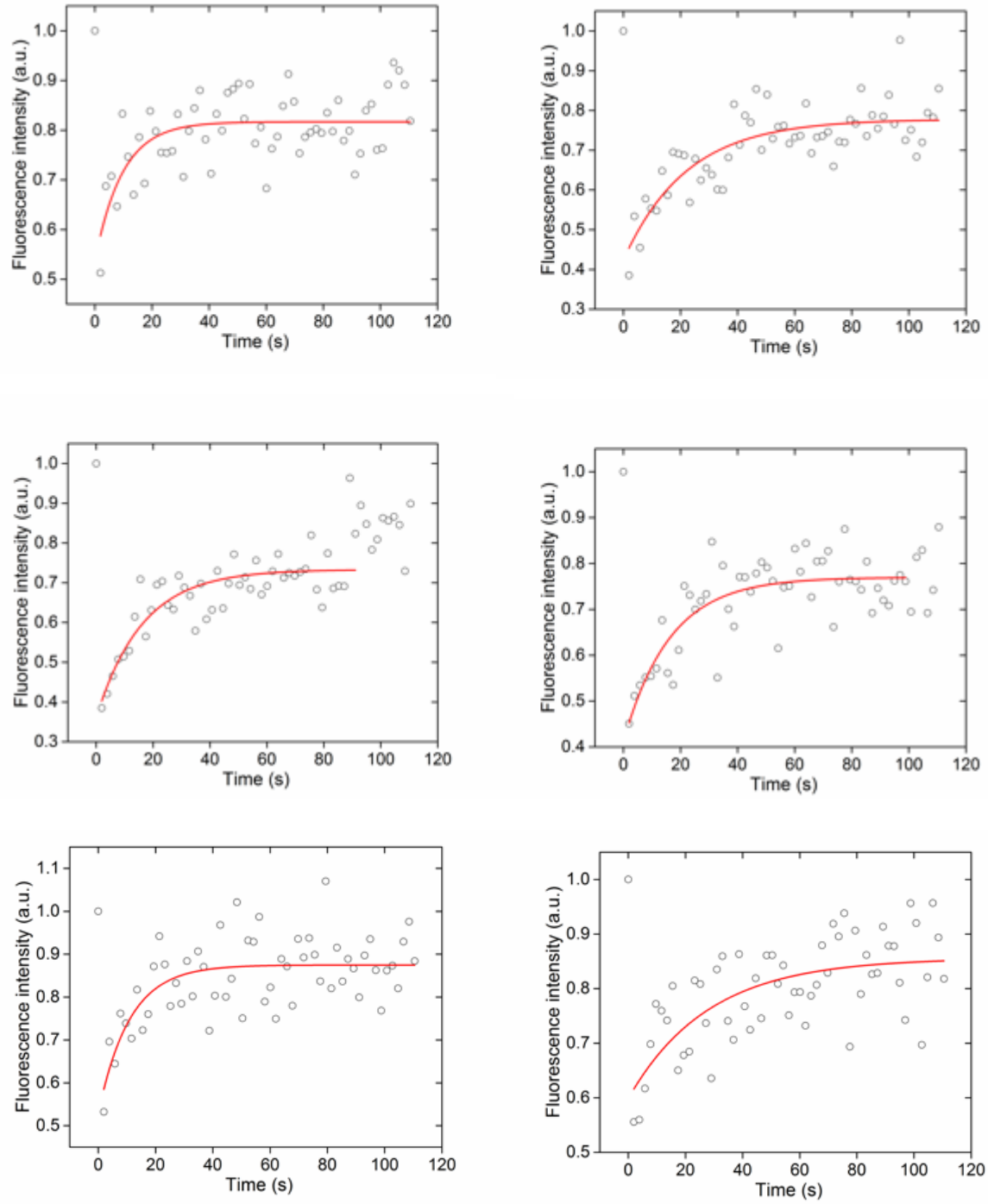

Figure A 15 Additional fluorescence recovery curves of GFP fluorescence in PSI:eGFP+ΔPsaL the mutant. Time course of fluorescence recovery of the bleached cell regions for GFP fluorescence. The recovery of the GFP fluorescence is presented as circles and fitted to an exponential function (red lines) to highlight the curve trend.

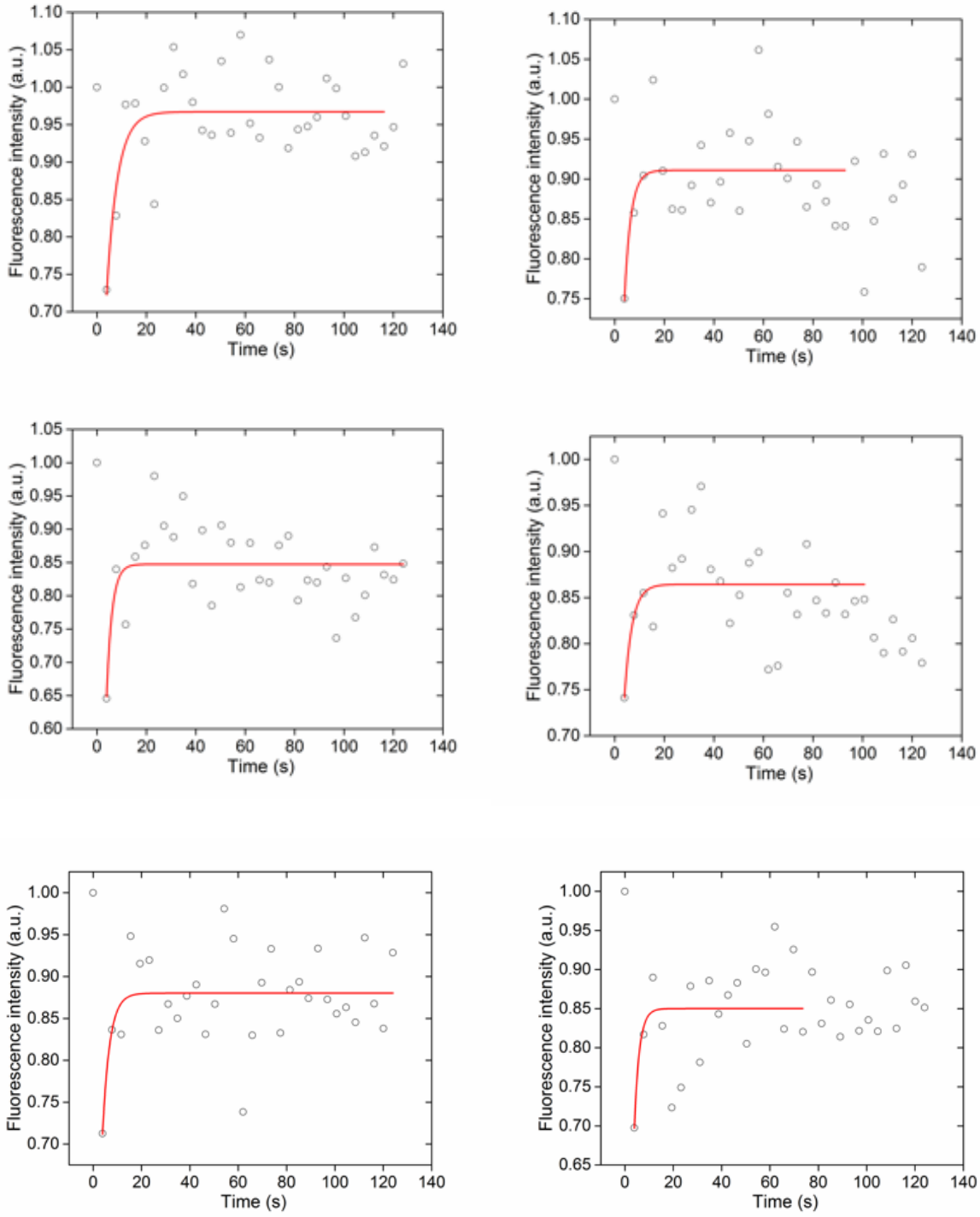

Figure A 16 Additional fluorescence recovery curves of GFP fluorescence in the PSII:eGFP+ΔPsaL mutant. Time course of fluorescence recovery of the bleached cell regions for GFP fluorescence. The recovery of the GFP fluorescence is presented as circles and fitted to an exponential function (red lines) to highlight the curve trend.

Appendix O

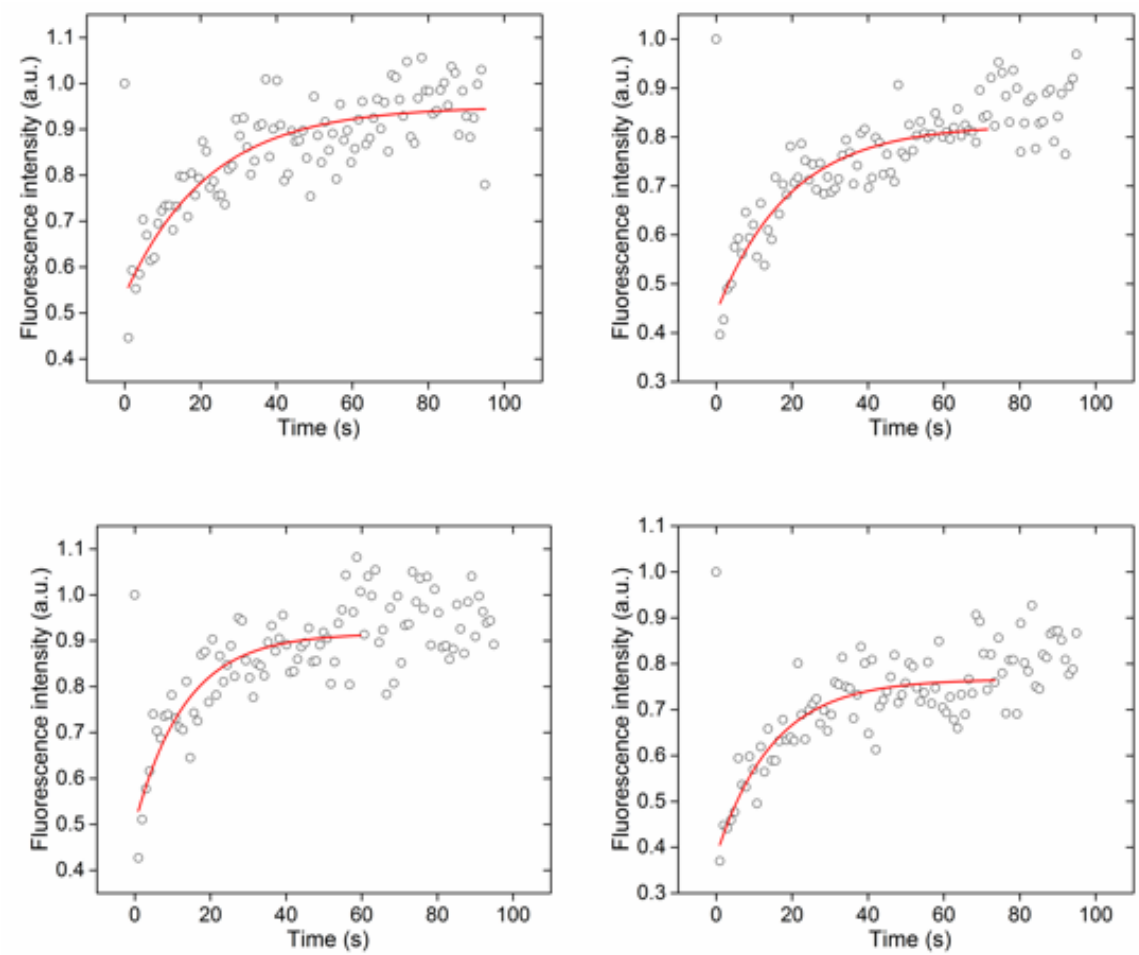

Figure A 17 Additional fluorescence recovery curves of GFP fluorescence in the PSI:eGFP cells grown at 34 °C. Time course of fluorescence recovery of the bleached cell regions for GFP fluorescence. The recovery of the GFP fluorescence is presented as circles and fitted to an exponential function (red lines) to highlight the curve trend.

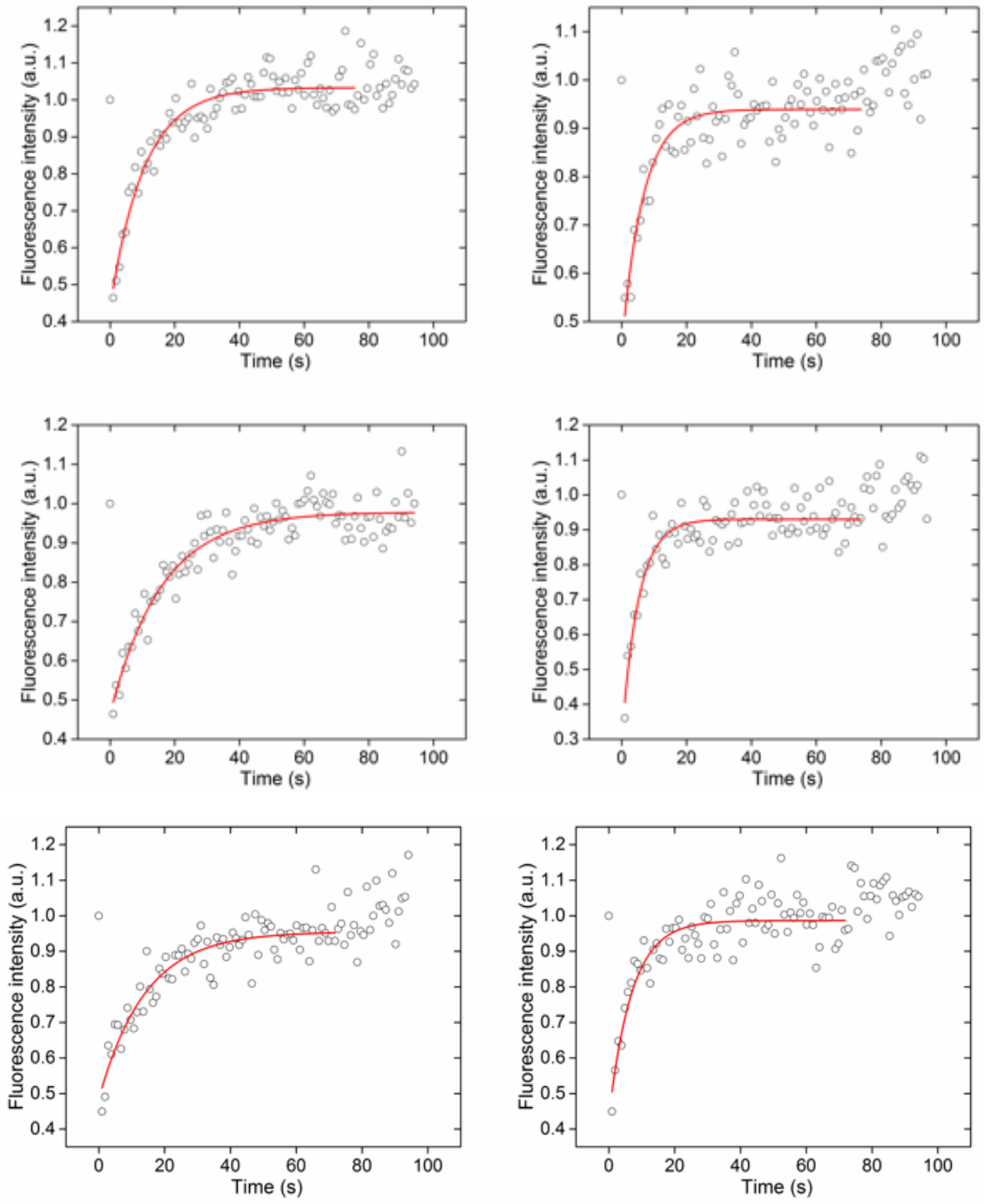

Figure A 18 Additional fluorescence recovery curves of GFP fluorescence in the PSII:eGFP cells grown at 34 °C. Time course of fluorescence recovery of the bleached cell regions for GFP fluorescence. The recovery of the GFP fluorescence is presented as circles and fitted to an exponential function (red lines) to highlight the curve trend.

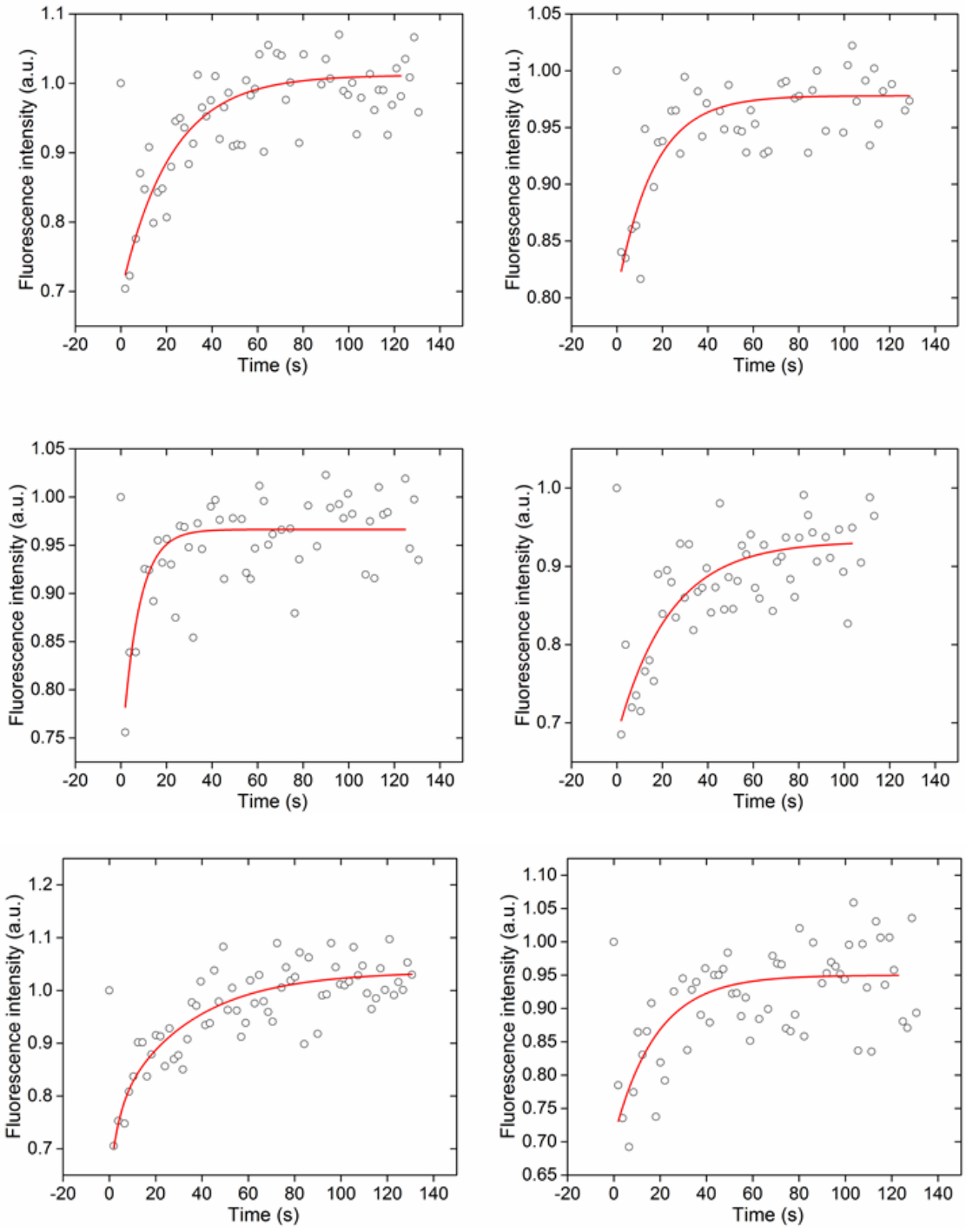

Figure A 19 Additional fluorescence recovery curves of GFP fluorescence in the ATPase(subβ):eGFP cells grown at 34 °C. Time course of fluorescence recovery of the bleached cell regions for GFP fluorescence. The recovery of the GFP fluorescence is presented as circles and fitted to an exponential function (red lines) to highlight the curve trend.